





von Karman Institute For Fluid Dynamics
Turbomachinery and Propulsion Department

Université Catholique de Louvain
Institute of Mechanics, Materials and Civil Engineering

"Experimental and numerical investigations of solidity effects on compressor performance and stability"

PhD Dissertation

Jérôme Sans

Promotors:

Pr. Tony Arts (UCL)
Pr. Philippe Chatelain (UCL)

Doctoral committee:

Dr. Jean-François Brouckaert (VKI)
Pr. Tom Verstraete (VKI)

Doctoral jury members:

Pr. Grégoire Winckelmans (UCL - Président du jury)
Pr. Hervé Jeanmart (UCL)
Dr. Stéphane Hiernaux (Techspace Aero)

Knowledge speaks, but wisdom listens.
Jimi Hendrix

Abstract

The present work addresses the issue of choosing the optimum solidity at the earliest stage of the aerodynamic design of axial compressors. The solidity in compressors is defined as the ratio of the aerodynamic chord over the peripheral distance between two adjacent blades, the pitch. The choice of the solidity occurs at the level of the meridional design. It represents a crucial step in the whole design process and is usually the result of a compromise between high efficiency and high stability margin.

To improve the current design practices, the present work, supported by Techspace Aero, investigates the solidity effects on compressor performance and stability through both numerical and experimental research. Setting the emphasis on a solidity reduction (i.e. a reduction of the blade number), the study aims at validating and updating the existing low-speed correlations to improve the current design practices.

The research is firstly approached with FINE/Turbo and examines solidity variations on two linear compressor cascades. The first geometry considers a state-of-the-art controlled diffusion low pressure compressor blade profile provided by TechSpace Aero. The second cascade involves a double circular arc blade that is extensively supported by literature data. While the standard double circular arc performance is in agreement with the correlations, the study reveals that correlations must be updated in terms of both deviation and losses to match the performance of the state-of-the-art controlled diffusion blade.

High-speed cascade measurement performed in the VKI-C3 facility are then presented and compared with pre-test and post-test numerical results. While the derived deviation rules offer very good agreement, the numerical losses are always higher than the experimental data. The off-design analysis also highlights strong discrepancies between the numerical and experimental results. Finally, the most important conclusion of this comparison is that the lower the solidity, the worse the numerical results.

The issue of the optimum solidity is also addressed by coupling the VKI meridional solver ACPreDesign and the VKI optimizer CADO. The maximum diffusion factor is varied and it appears that higher efficiencies are achieved for higher diffusion factors. Uncertainty quantification techniques such as Monte-Carlo sampling or stochastic collocation are then introduced to model the uncertainties inherently present in any correlations into ACPreDesign. While 3D blade design optimization chases 0.1% of efficiency enhancement, uncertainty quantification techniques underline non-negligible uncertainty bands of 1.0% to 2.0% that are disregarded by standard deterministic methods. Such additional information may push the designer to substantially increase the design targets to ensure that the final value meets the requirements. Robust design optimization is the final point that is approached but the comparison of optimizations

with or without uncertainty does not show any difference. It means that, in the case of solidity optimization with ACPreDesign, the optimum solidity distributions obtained with or without considering epistemic uncertainties can always be considered as robust solutions.

Acknowledgements

Before entering the core of the subject, I take here the opportunity to thank all those who made this work possible.

My first thanks go to Techspace Aero for supporting financially this research. Very special thanks also go to my supervisor, Jean-François Brouckaert, who believed in me and gave me the chance to accomplish this work. Every day he shared with me all his knowledge and his critical observations. I thank him for his generosity and his dedication to my work as well as for all the very interesting and fruitful discussions about compressors, pressure and temperature transducers but also about wine or music. Everything I have learned from him will be of great help in my future career.

I do not forget the rest of my doctoral committee and in particular, Tom Verstraete and Tony Arts to whom I am very grateful for their help, their availability and their very relevant and critical interventions which definitely contributed to improve the completeness and the quality of this thesis.

Some special thanks also go to Matteo Resmini and Nadège Henault who helped me respectively during the numerical and the experimental parts of this research. Regarding my lab experience, I must obviously express all my gratitude to Julien, Gérard, Térence, Walter, Bram, Pierre and Jean-Christophe without whom I would probably still be sitting in the lab. Similarly, my numerical research would not have been feasible without the work of the whole staff of the VKI computer center.

A PhD thesis also means a daily life full of challenges, bad and good news, distresses and joys. To go through the stressful moments, there are family and friends. I cannot forget my musical partners: Dave, Bernd, Imre, PaPa, Delphine, Alejandro and Alessia. I have been lucky to have you to cover my mistakes and to help me to always get back on track (especially rhythmically speaking). I must also thank the whole VKI family who transformed this thesis into an unforgettable and unique human experience: Justin, Laura, Marina, Tyler, Sophia, JB, Sergio, Bayindir, Clara, Fabrizzio, Giulia, Cis, Nicolas...(and probably even more, I owe a drink to all those that I forgot). But the support did not only come from inside the VKI walls but also from very faithful friends outside the VKI world. Without being exhaustive, I would like to thank *les vrais skieurs*, The Joggings, the Pukkelpop team, mi primo Alejandro and my ex-roommates Sophie and Laure.

Last but not least, I would like to thank my family: Jean-Marc, Georgette,

Jean, Lucie, Benoît, Julie, Gérard, Marie-Rose, Geneviève, Catherine, Eric, Alain and, finally, the most important, my sweet love, Hélène. Without her encouragements, her understanding and her smile, this work would not have been possible.

Jérôme Sans
Brussels, April 2015

Contents

1 Introduction **1**
1.1 Background and motivation 1
1.2 Objectives 3

2 Theoretical background **5**
2.1 Two-dimensional cascade investigations 5
2.1.1 Definitions and nomenclature 5
2.1.2 Incidence and deviation rules 8
2.1.3 Blade loading and losses 18
2.1.4 Compressibility effects 28
2.1.5 Stability 32
2.1.6 The effect of axial velocity-density ratio 36
2.2 Three-dimensional investigations 38
2.3 The optimum solidity 47
2.3.1 Direct methods 47
2.3.2 Meridional optimization 52

3 Numerical Investigation **53**
3.1 Motivation 53
3.2 Geometrical model 54
3.3 Numerical Model 55
3.3.1 Expected experimental uncertainty 56
3.3.2 Mesh sensitivity 57
3.3.3 Turbulence model effects 60
3.3.4 Numerical scheme effects 68
3.4 Results and discussion 72
3.4.1 Performance 72
3.4.2 Comparison with correlations 79
3.4.3 Isentropic Mach number 85
3.4.4 Stall margin 89
3.5 Conclusion 91

4 Experimental Investigation **95**
4.1 Introduction 95
4.2 Facility and test section 95
4.3 Instrumentation and probes 99
4.4 Test matrix 101
4.5 Periodicity and inlet conditions 101

4.6 Experimental results . . . 105
4.6.1 Mid-span performance . . . 105
4.6.2 Spanwise distributions . . . 110
4.6.3 Wakes . . . 112
4.7 Comparison with CFD and correlations . . . 114
4.7.1 Optimum incidence prediction . . . 115
4.7.2 Deviation rule . . . 126
4.7.3 Diffusion factor, AVDR and loss parameters . . . 129
4.7.4 Off-design correlations . . . 136
4.7.5 Stability margin . . . 140
4.8 Outlet flow topology . . . 141
4.8.1 Effects of incidence and solidity . . . 141
4.8.2 Comparison with CFD . . . 145
4.9 Conclusion . . . 149

5 Meridional optimization 153
5.1 Introduction . . . 153
5.2 Axial Compressor Pre-design tool . . . 154
5.2.1 Input . . . 154
5.2.2 Loss correlations . . . 155
5.3 Optimization . . . 156
5.3.1 Method and constraints . . . 156
5.3.2 Results . . . 159
5.4 Uncertainty quantification . . . 164
5.4.1 Sampling techniques . . . 164
5.4.2 Stochastic collocation . . . 165
5.4.3 Parametrization . . . 166
5.5 Uncertainty quantification results . . . 168
5.5.1 Full stage . . . 168
5.5.2 Single rotor . . . 173
5.6 Optimization under uncertainty . . . 174
5.7 Conclusion . . . 176

6 Conclusions and perspectives 179
6.1 Conclusions . . . 179
6.2 Perspectives . . . 182

A The DREAM project booster 185
A.1 Velocity triangles . . . 185
A.2 Preliminary study of the blade number effect . . . 186
A.2.1 Influence of rotor blade number . . . 186
A.2.2 Influence of stator blade number . . . 188

B Probe calibration and uncertainty calculation 191
B.1 Kiel probe calibration . . . 191
B.2 Three-hole probe calibration . . . 191

B.3 Uncertainty analysis . . . 193
B.3.1 Systematic and random uncertainties . . . 193
B.3.2 Pressure uncertainty . . . 194
B.3.3 Derived quantities . . . 197

C Experimental investigation - Complementary results 207
C.1 Spanwise distributions . . . 207
C.2 Wakes . . . 209
C.2.1 Total pressure loss wakes . . . 209
C.2.2 Yaw angle wakes . . . 210
C.3 Numerical parameter effects . . . 213
C.3.1 Outlet flow topology . . . 213
C.3.2 Total pressure loss wakes . . . 222

D Meridional Optimization - Complementary results 229
D.1 Additional optimization constraint . . . 229
D.2 Single rotor solidity optimization . . . 231
D.3 Uncertainty quantification . . . 232
D.3.1 Full stage results with two uncertain parameters . . . 232
D.3.2 Single rotor results with three uncertain parameters . . . 233

Bibliography 237

List of Figures 247

List of Tables 257

Nomenclature

Roman Symbols

A	Area	[m^2]
C_p	Pressure coefficient	[-]
D	Diffusion factor	[-]
H	Shape factor	[-]
H_n	n-order Hermite's polynomial	[-]
K	Three-hole probe Calibration coefficient	[-]
K_i	Incidence-rule thickness correction coefficient	[-]
K_δ	Deviation-rule thickness correction coefficient	[-]
M	Mach number	[-]
P	Pressure	[mbar]
Re	Reynolds number	[-]
T	Temperature	[K]
Tu	Turbulence intensity	[%]
U	Peripheral speed	[m/s]
	or uncertain parameter	[ ]
U_{95}	Total uncertainty at 95% confidence level	[ ]
V	Absolute velocity	[m/s]
W	Relative velocity	[m/s]
Z	Blade number	[-]
b	Deviation-rule exponent	[-]
	or systematic uncertainty	[ ]
c	aerodynamic chord	[m]
f	Probability density function	[-]
g	Staggered spacing	[m]
h	Blade height	[m]
i	Incidence	[°]
k	Turbulence kinetic energy	[m^2/s^2]
l	Turbulence length scale	[m]
m	Deviation-rule slope factor	[-]
m_c	Carter's rule slope factor	[-]
n	Incidence-rule slope factor	[-]
r	Radius	[m]
	or correlation coefficient	[-]
s	Pitch	[m]
t	Thickness	[m]
x	Spanwise coordinate	[m]
y	Pitchsiwe coordinate	[m]

z	Axial coordinate	[m]

Greek Symbols

α	Absolute flow angle	[°]
β	Relative flow angle	[°]
γ	Stagger angle	[°]
δ	Deviation	[°]
ϵ	Turbulence kinetic energy dissipation rate	[m^2/s^3]
ζ	Loss parameter	[-]
η	Efficiency	[-]
θ	Momentum thickness	[m]
κ	Metal angle	[°]
μ	Dynamic viscosity	[Pa·s]
	or Average	[ ]
ν	Kinematic viscosity	[Pa·s]
ν_T	Turbulent kinematic viscosity	[Pa·s]
ξ	Random variable	[-]
π	Pressure ratio	[-]
ρ	Density	[kg/m^3]
σ	Solidity	[-]
	or Standard deviation	[ ]
ϕ	Camber angle	[°]
ψ	Zweifel loading coefficient	[-]
ω	Total pressure loss coefficient	[-]
Δ	Variation, difference	[ ]
Γ	Circulation	[m^2/s]

Subscript

C	Center-hole pressure
L	Left-hole pressure
R	Right-hole pressure
cr	Critical conditions
fs	Free-stream
i	Ideal
is	Isentropic
loc	Local value
max	Maximum value
min	Minimum value
opt	Optimum condition
ref	Reference value
s	Static quantity

t	True total pressure
θ	Peripheral direction
0	Total quantity or Zero-camber quantity
1	Cascade inlet
2	Cascade outlet

Acronyms

AR	Aspect-Ratio
AVDR	Axial Velocity Density Ratio
B2B	Blade-to-Blade
BPF	Blade Passage Frequency
CDB	Controlled Diffusion Blade
CFD	Computational Fluid Dynamics
DCA	Double Circular Arc
IGV	Inlet Guide Vane
ISRE	Isentropic Simple Radial Equilibrium
LE	Leading Edge
LP	Low Pressure
NISRE	Non-Isentropic Simple Radial Equilibrium
PDF	Probability Density Function
PS	Pressure Side
RANS	Reynolds Averaged Navier-Stokes
SS	Suction Side
TE	Trailing Edge
VKI	von Karman Institute for Fluid Dynamics

Chapter 1

Introduction

1.1 Background and motivation

Aviation plays a crucial role in the greenhouse-gas emissions as well as in the local quality of air and the urban noise pollution. The Strategic Research & Innovation Agenda (SRIA) of the Advisory Council for Aeronautical Research in Europe (ACARE) reports that the aviation industry is responsible for 2% of the human-induced CO_2 emissions worldwide. Moreover, while the European air-traffic keeps growing continuously, more and more sectors tend to develop low carbon technologies and the proportion of the human-made CO_2 emissions due to aviation is expected to increase to 3% by 2050. Within those perspectives, ACARE has set up short- and long-term targets (established relatively to aircraft capabilities in 2000) that are:

- a reduction of 50% of the CO_2 emissions and the fuel consumption per passenger kilometre by 2020 (and 75% by 2050);
- a reduction of 80% of the NO_x emissions by 2020 (and 90% by 2050);
- a decrease of the perceived noise by 50% in 2020 (and 65% in 2050);
- a significant progress in the environmental impact of the manufacturing and maintenance of the aircraft and related products.

ACARE has also identified the main contributions in the above 50% of CO_2 reduction and 15 to 20% are expected to arise from more efficient engines. Therefore, for environmental as well as economical issues as low emissions go with low fuel consumption, the European aviation industry must develop new engine technologies to fulfill those requirements.

Over the last decades, tremendous efforts have been undertaken to decrease the fuel consumption of civil aircraft engines but the improvements were mainly relying on the growth of the bypass ratio (BPR) of the turbofan engines. A high BPR indeed contributes to increase the propulsive efficiency but it goes with heavy drag and weight penalties. For several years, the propulsive and thermal efficiency enhancements were sufficient to compensate the high weight and drag of the high BPR turbofan engines but, nowadays, the requirement of ACARE cannot be met with a standard turbofan architecture. This gave birth to many European research projects such as NEWAC, VITAL, DREAM or

LEMCOTEC, or more recently, the partnership between the European Commission and the Aeronautical Industry, Clean Sky. All those projects or joint initiatives aim at developing, validating and testing new engine architectures and components to substantially contribute to a greener aviation.

In that framework, specific attention must also be dedicated to decrease the engine weight and more precisely the weight of the low-pressure components that are bigger and heavier. The use of composite materials is a solution among others that can considerably contribute to reduce the weight of the engine. It also appears very attractive to simply reduce the number of blades of both compressor and turbine. Besides the reduction of weight, it also offers lower production and maintenance costs. However, this can have important aerodynamic consequences.

The aerodynamic parameter related to the blade number is the solidity. The solidity is defined as the ratio between the aerodynamic chord and the peripheral distance between two blades, i.e. the pitch, that is directly linked to the number of blades.

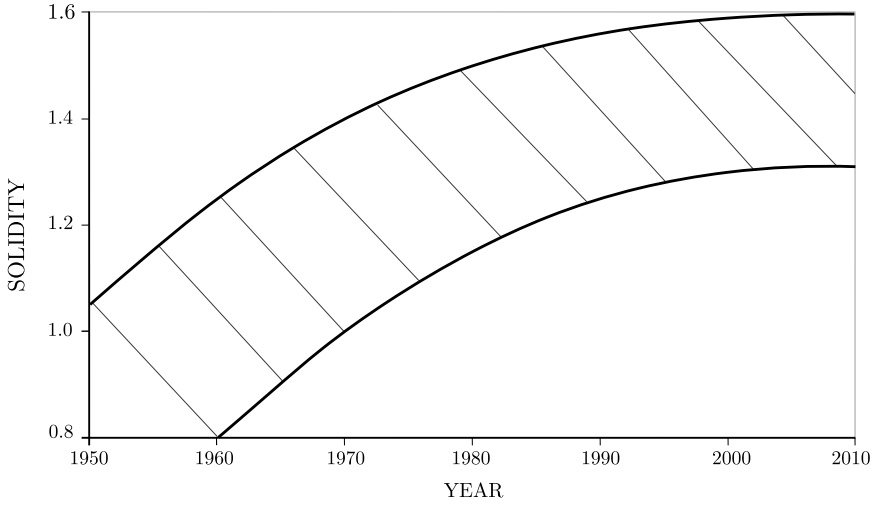


Figure 1.1: *Evolution of solidity in compressor design over the last decades*

Looking at the trend in compressor design, it can be observed in Fig. 1.1 (Obrecht, 2013, [1]) that the mean solidity constantly increased over the last 60 years but an asymptotic behaviour is noticed for the last 10 years. The increase of the number of blades allowed to increase the pressure ratio and consequently the thermal efficiency of the engine and/or reduce the number of stages. However, the severe constraints on consumption and pollutant emissions that appeared in the beginning of the 21^{st} century modified the trend in compressor design and, nowadays, manufacturers tend to decrease the number of blades in order to decrease the mass of the engine as well as the production

and maintenance costs. The present investigation focuses on the solidity effects on the compressor performance and stability in view of reducing the number of blades by 10% to 20%. It must also be mentioned that similar interests also exist for turbine design. This is especially true for the low pressure turbine since it represents 20% to 30% of the engine weight. But, despite the fact that the low pressure compressor represents about 10% of the engine weight compared to the low pressure turbine, the influence of solidity on the compressor stall margin results in a higher impact on the whole engine operability.

1.2 Objectives

Very early in the 1940's, Howell [2], Zweifel [3] or Carter [4] and, later, in the early 1950's, Lieblein et al. [5] identified the solidity as an important feature in compressor design that strongly affects the aerodynamic performance of the compressor, its loading and its stability. The solidity appears to be one of the most important factors in all the existing compressor correlations.

The solidity is selected very early in the design process and because of the important role played by the solidity in the loading assessment and the stability of the compressors, its determination represents a deciding factor and must be regarded with great care.

Driven by the need to improve the current design practices, Techspace Aero supported both numerical and experimental research at the von Karman Institute on the solidity effects in axial compressors. More precisely, the study is focused on a state-of-the-art blade profile, representative of a low-pressure compressor stator profile. Setting the emphasis on solidity reduction, the work aims at validating and updating the existing low-speed correlations both with numerical simulations and high-speed cascade tests in the VKI-C3 facility.

Before entering the core of the subject, it is essential to summarize the most important aspects that can influence the choice of solidity in compressor design. The second chapter covers the literature and the theoretical background required to address issues such as losses, loading, deviation or stability which are all intimately linked to the solidity. From various cascades tests, the establishment and the use of correlations is also commented. Finally, Chapter 2 addresses the definition of an optimum solidity.

The use of CFD is the current practice for compressor design. In order to prepare the experimental campaign and to assess the capability of CFD in validating the existing correlation data, Chapter 3 exposes the numerical investigation performed with FINE/Turbo (Numeca International) on two linear compressor cascades. While the first geometry involves a controlled diffusion blade (CDB) representing the state-of-the-art of Techspace Aero, the second profile is a standard double circular arc (DCA) blade. The choice of the latter

is motivated by the extensive amount of literature about this geometry that enables to evaluate and calibrate the CFD predictions. The variability of the results due to the turbulence model or the numerical scheme is also considered.

The experimental validation by high-speed cascade tests in the VKI-C3 facility is presented in Chapter 4. The considered airfoil is the controlled diffusion blade of Techspace Aero studied in Chapter 3. Solidity variations were only applied by changing the pitch to keep the chord-based Reynolds number constant (at given inlet Mach number) as well as the aspect ratio. Performance were measured in terms of total pressure losses and deviation for 3 solidities, 6 incidences, 2 inlet Mach numbers and at 4 span locations. Chapter 4 starts by describing the facility and the instrumentation used within the experimental campaign. After analyzing the measurement results on their own, they are compared with both the pre-test and the post-test numerical calculations. The post-test calculations were performed with the experimental boundary conditions and on a slightly different numerical model than in Chapter 3 to exactly match the experimental domain. Finally, the establishment of new correlations rules is developed for deviation and losses at design and off-design incidences.

Chapter 5 addresses the optimization of solidity at the level of the meridional design with and without the consideration of uncertainties. To support this investigation, the geometry of a low-pressure compressor studied at VKI within the European DREAM project is considered. The throughflow solver that is used, ACPreDesign, is a Non-Isentropic Simple Radial Equilibrium (NISRE) solver recently implemented at VKI. Since nowadays meridional calculations are very cheap in terms of computational time, they can then be combined with optimization tools and/or with uncertainty quantification (UQ) techniques which both require many evaluations. In that framework, ACPreDesign was firstly coupled with the VKI optimizer CADO (based on an Evolutionary Algorithm) to perform solidity optimizations. Various optimum solidity distributions were analyzed and compared to identify the main parameters that influence the outcome of the optimization. On the other hand, the introduction of uncertainty quantification techniques such as Monte-Carlo sampling or stochastic collocation was also examined in order to take into account the epistemic uncertainties inherently related to the empirical correlations of ACPreDesign. The results were examined in terms of efficiency probability density functions as well as efficiency means and standard deviations. Finally, the issue of optimization under uncertainty, also known as robust design optimization, was addressed to highlight the possible existence of an optimum in terms of performance parameters as well as sensitivities to uncertain inputs.

The work ends with Chapter 6 that gathers the main conclusions of this investigation and presents the future experimental and numerical perspectives.

Chapter 2

Theoretical background

This chapter covers the main required theoretical background and available literature to address the effect of solidity. Firstly, correlations from cascade tests are analyzed. Despite the fact that the flow in axial compressors is primarily three-dimensional and unsteady, two-dimensional cascade approach allows to shed light on the physical phenomena taking place in the blade-to-blade plane. These correlations mainly come from the 1960's and may have been corrected since then by engine manufacturer internal experience. However, it is undeniable that all compressor designers once dealt with the works of Howell [2], Carter [4] or Lieblein et al. [5]. After cascade experiments, some measurements performed on real compressor geometries are also presented. Such three-dimensional investigations are less frequent because of their complexity and costs but some examples were found. Finally, the specific issue of the optimum solidity is addressed.

2.1 Two-dimensional cascade investigations

Cascade tests have been used for decades to understand the flow field physics inside a compressor blade channel. They have lead to enormous compressor design improvements by the establishment of correlation data. After recalling the nomenclature of compressor cascade geometry, most of the correlations are examined setting the emphasis on the effect of solidity.

2.1.1 Definitions and nomenclature

The nomenclature for the flow and blade angles is defined in Fig. 2.1. It follows the standards of the well-known NASA SP-36 axial compressor design manual [6]. The incidence i is defined as the difference between the inlet flow angle β_1 and the inlet metal angle κ_1. The deviation δ is the difference between the outlet flow angle β_2 and the blade metal angle at the trailing edge κ_2. The blade metal angles κ_1 and κ_2 are sometimes referred to as $\beta_{m,1}$ and $\beta_{m,2}$. The angles are all measured with respect to the axial direction and usually given in degrees.

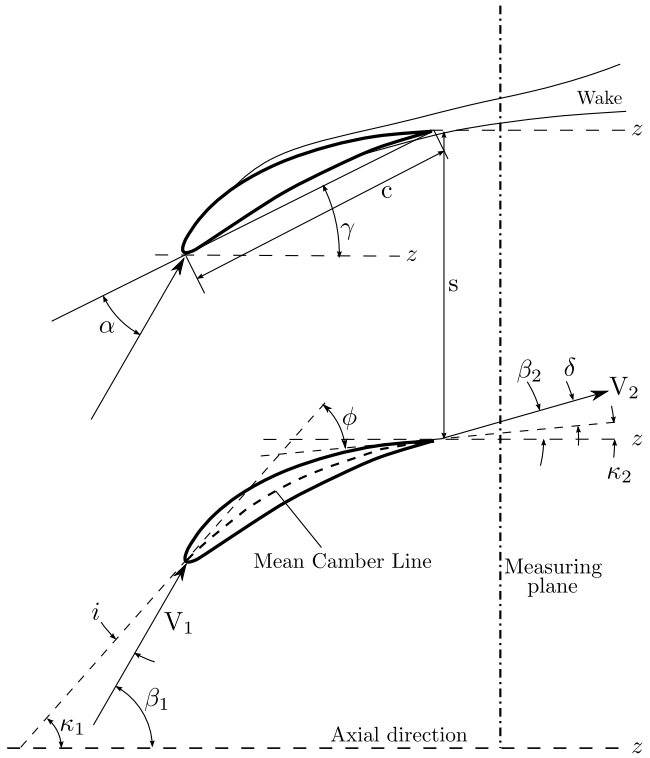


Figure 2.1: *Geometrical definition of a cascade*

- β_1 relative inlet flow angle;
- β_2 relative outlet flow angle;
- κ_1 inlet metal angle;
- κ_2 outlet metal angle;
- ϕ camber angle;
- i incidence angle;
- δ deviation angle;
- γ stagger angle;
- c aerodynamic chord;
- s pitch.

Following the nomenclature of Fig. 2.1, the solidity σ is defined by Eq. (2.1) as the ratio of the chord c over the pitch s.

$$\sigma = \frac{c}{s} \tag{2.1}$$

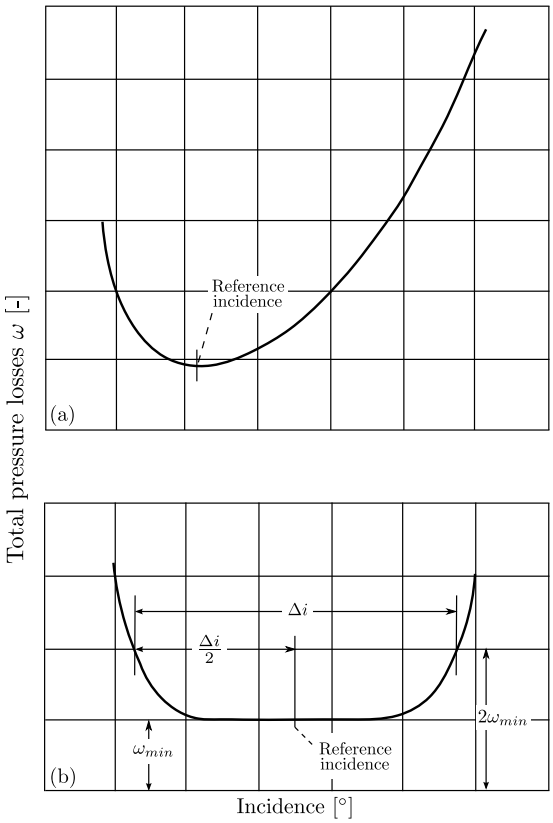


Figure 2.2: *Optimum incidence definition [6]: (a) minimum loss incidence; (b) mid-range incidence*

The performance parameters of a compressor profile are the deviation angle δ (cf. Fig. 2.1) and the total pressure losses ω, defined in Eq. (2.2).

$$\omega = \frac{p_{01} - p_{02}}{p_{01} - p_{s1}} \tag{2.2}$$

Most of the correlations only present the performance at a reference incidence. The reference incidence of a given profile is the incidence for which minimum total pressure losses (ω_{min}) are obtained. It is therefore called optimum incidence or minimum loss incidence. As illustrated in Fig. 2.2, the optimum incidence may also be defined as the mid-range incidence if the loss curve presents a very flat region.

As far as cascades are concerned, the stalling incidence refers to as the incidence yielding $2\omega_{min}$. Similarly, as indicated in Fig. 2.2, the incidence range Δi is then defined as the difference between the positive and negative incidences that both yield $2\omega_{min}$.

2.1.2 Incidence and deviation rules

As soon as engineers were interested in cascade performance, they attempted to approach the solidity effect. The first correlations came from Howell in 1945 [2]. He assessed the airfoil loading through a *nominal* turning, defined as 80% of the maximum turning. He found that the nominal tangential velocity difference was only depending on the solidity. This is illustrated in Fig. 2.3 where the nominal flow turning is plotted versus the outlet flow angle and the pitch-to-chord ratio s/c $(= 1/\sigma)$. Data of Fig. 2.3 are accurately approached by Eq. (2.3) for outlet flow angles β_2 between 0° and 40°.

$$\tan(\beta_1) - \tan(\beta_2) = \frac{1.55}{1 + \dfrac{1.5}{\sigma}} \tag{2.3}$$

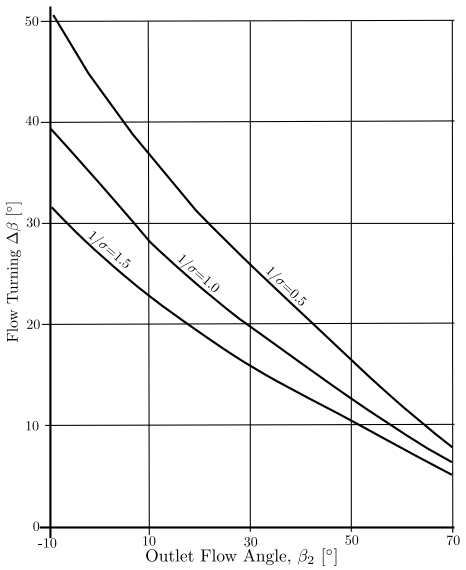


Figure 2.3: *Nominal flow turning as a function of outlet flow angle and pitch-to-chord ratio[2]*

Even though Howell's work was a breakthrough in compressor design, it remains not very practical for design purposes. In particular, no advice is given regarding the choice of the incidence and the camber effect is neglected.

Carter [4] considered the maximum lift/drag ratio as optimum condition. The influence of camber and stagger were also included. He also observed that the optimum flow conditions were linked to a specific location of the forward stagnation point which, for a given camber, depended on the pitch and thus on the solidity. He provided design curves giving the optimum incidence as a function of camber, turning and pitch-to-chord ratio $(s/c = 1/\sigma)$. An example

of such design curves is shown in Fig. 2.4 in which the optimum turning is referred to as ε_{opt}. However, the influence of thickness, stagger and inlet flow angle are still not taken into account.

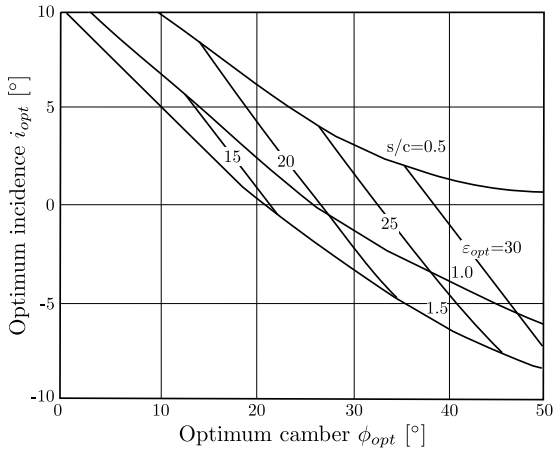


Figure 2.4: *Design curves for optimum conditions [7]*

The greatest development of Carter comes more from his deviation rule. To calculate the deviation, he offered an easy formula given in Eq. (2.4),

$$\delta = m_C \frac{\phi}{\sqrt{\sigma}} \tag{2.4}$$

where ϕ is the camber angle and the m_C coefficient is expressed by Carter as a function of the blading type and the stagger angle (Fig. 2.5).

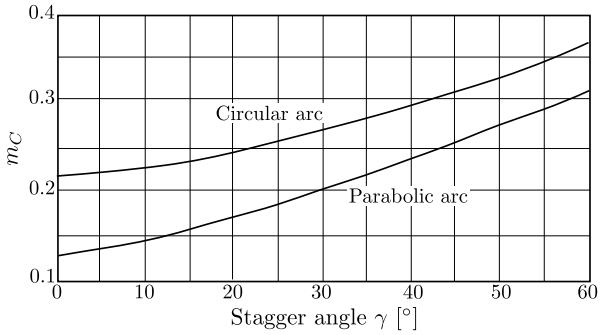


Figure 2.5: *m_C factor for Carter's deviation rule (Eq. (2.4))*

According to many sources (Cumpsty [8], Horlock [7] or Gostelow [9]), Eq. (2.4) originally comes from Constant's work published in 1937 in *Performance of cas-*

cade aerofoils[1]. Howell already proposed a new version in [2]. Carter finally brought in a really convenient form (as written in Eq. (2.4)) and mapped the m_C coefficient for different bladings and stagger angles [4]. Carter's rule sheds light on the physical effect of the solidity on cascade performance. For a given camber and stagger, the deviation is inversely proportional to the square root of the solidity. It means that the higher the solidity, the better the flow is following the blade and the bigger is the turning. For a rotor, since the turning is linked to the total pressure rise, more pressure ratio will be achieved if the solidity is increased.

Analyzing various experimental cascade tests of Herrig et al. [10], Lieblein built a correlation and gave design recommendations based on an optimum incidence angle, taken as the minimum loss incidence angle (Fig. 2.2). In the handbook of NASA [6], *Aerodynamic design of axial-flow compressors*, Lieblein tabulated all the correlation data and provided many design recommendations. Nonetheless, it must be said that those correlations are based on low-speed tests ($M \leq 0.3$).

For the prediction of the optimum incidence, Eq. (2.5) is used.

$$i_{opt} = \underbrace{i_0}_{\text{Zero-camber opt. incidence}} + \underbrace{n\phi}_{\text{Influence of camber on the opt. incidence}} \tag{2.5}$$

The first term is the optimum incidence for a zero-camber blade while the second one takes into account the influence of camber on optimum incidence. The zero-camber incidence depends on the thickness distribution (i.e NACA-65-A_{10} series or DCA) and the maximum thickness-chord ratio through the factors K_i. This is presented in [6] as follows:

$$i_0 = K_i \; i_{0,10} \tag{2.6}$$

where $i_{0,10}$ is the optimum incidence for a zero-camber NACA-65 blade with a thickness-to-chord ratio of 10%. The factor K_i, the zero-camber 10% thick incidence angle $i_{0,10}$ as well as the slope n from Eq. (2.5), are mapped as a function of the inlet flow angle in [6]. The effect of the solidity directly appears in $i_{0,10}$ and n as shown in Fig. 2.6 and Fig. 2.7. The K_i coefficient only depends on maximum thickness-to-chord ratio and the type of blade (Fig. 2.8).

[1] Unfortunately, a copy of Constant's original paper remains unobtainable.

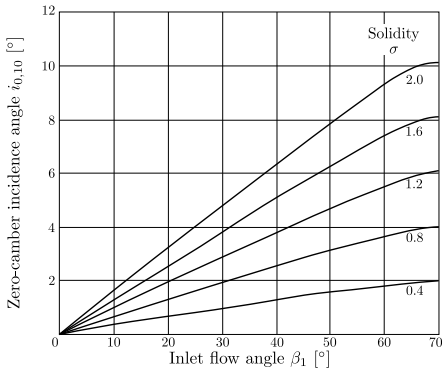


Figure 2.6: *Zero-camber incidence angle for blades of 10% maximum thickness [6]*

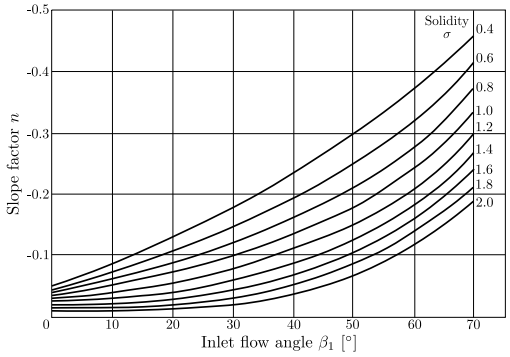


Figure 2.7: *Slope factor n for blades of 10% maximum thickness [6]*

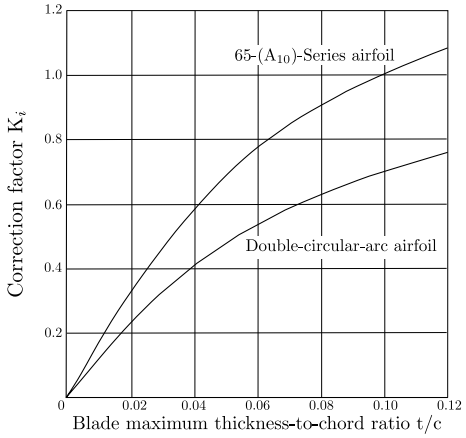


Figure 2.8: *Thickness correction for the zero-camber optimum incidence angle [6]*

Taking all the contributions required in Eq. (2.5), it appears that the optimum incidence increases with solidity. As this is not straightforward, the optimum incidence has been calculated for 5 solidities for a DCA blade with a maximum thickness-to-chord ratio of 6.5% and an inlet flow angle of 50°. The results are given at constant camber in Table 2.1 and at constant flow turning Table 2.2.

σ	$i_{0,10}$	K_i	n	ϕ	i_{opt}	$\Delta\beta$
1.0	3.9	0.57	-0.180	30°	-3.2°	17.5°
1.2	4.7	0.57	-0.152	30°	-1.9°	19.9°
1.4	5.5	0.57	-0.128	30°	-0.7°	21.8°
1.6	6.3	0.57	-0.108	30°	0.3°	23.5°
1.8	7.1	0.57	-0.089	30°	1.4°	25.0°

Table 2.1: *Optimum incidence calculation for different solidities at constant camber (DCA blade, $t/c_{max} = 6.5\%$, $\beta_1 = 50°$ and $\phi = 30°$)*

σ	$i_{0,10}$	K_i	n	$\Delta\beta$	i_{opt}	ϕ
1.0	3.9	0.57	-0.180	20°	-4.0°	34.7°
1.2	4.7	0.57	-0.152	20°	-1.9°	30.2°
1.4	5.5	0.57	-0.128	20°	-0.4°	27.1°
1.6	6.3	0.57	-0.108	20°	0.9°	24.9°
1.8	7.1	0.57	-0.089	20°	2.0°	23.0°

Table 2.2: *Optimum incidence calculation for different solidities at constant flow turning (DCA blade, $t/c_{max} = 6.5\%$, $\beta_1 = 50°$ and $\Delta\beta = 20°$)*

The same procedure can be applied to predict the deviation angle. The deviation at optimum incidence is given by:

$$\delta_{opt} = K_\delta \; \delta_{0,10} + \frac{m}{\sigma^b} \; \phi \tag{2.7}$$

where K_δ depends on the maximum thickness-to-chord ratio as well as the thickness distribution (Fig. 2.10), $\delta_{0,10}$ is a zero-camber deviation for a 10%-thick airfoil (function of β_1 and σ, Fig. 2.9), m depends on the blade type (also function of β_1, Fig. 2.11), b is an exponent depending on β_1 (Fig. 2.12) and ϕ is the camber. The influence of solidity on deviation directly appears in Eq. (2.7). It is very similar to the Carter's rule (cf. Eq. (2.4)) but it predicts a non-zero deviation for a zero-camber profile. This is a weakness of the Carter's rule since, even for a zero-camber profile, the optimum incidence increases with the solidity and consequently, the deviation at optimum incidence is also increasing.

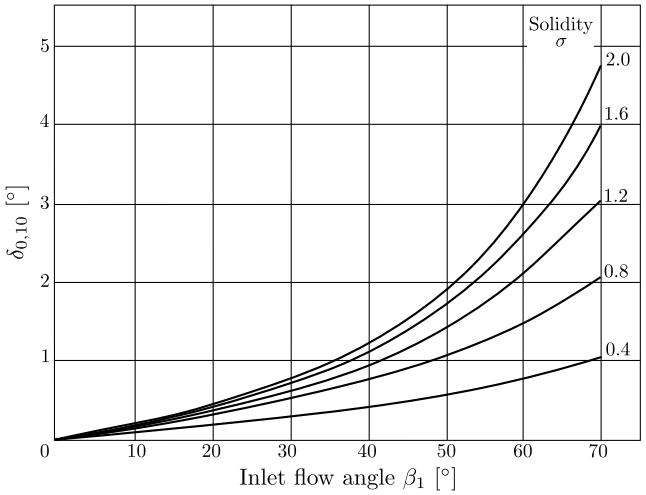


Figure 2.9: *Zero-camber deviation angle of Eq. (2.7) for blades of 10% maximum thickness [6]*

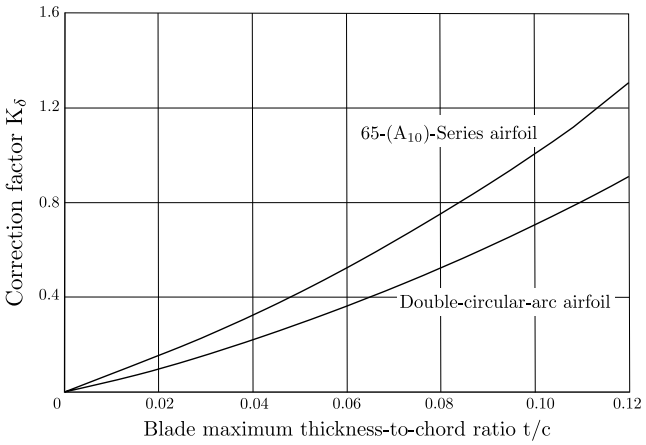


Figure 2.10: *Thickness correction for zero-camber deviation angle [6]*

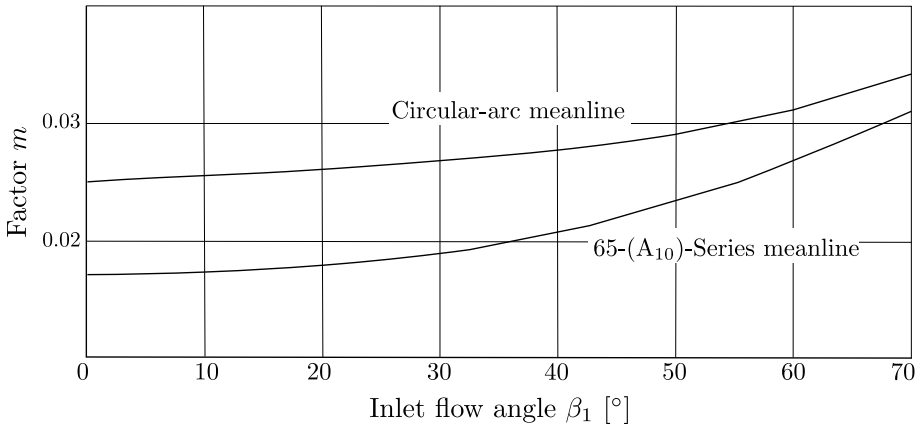


Figure 2.11: *m factor of Eq. (2.7) [6]*

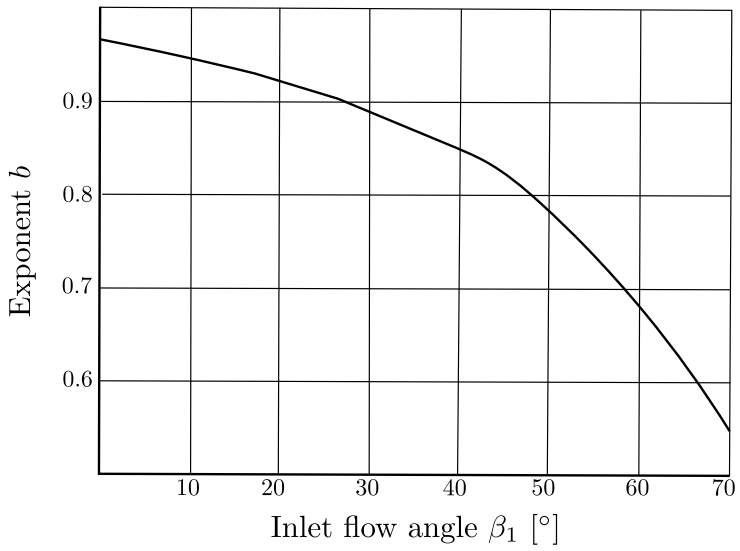


Figure 2.12: *b exponent of Eq. (2.7) [6]*

Examples of the NASA deviation prediction are presented in Table 2.3 and Table 2.3 respectively at constant camber and constant flow turning. It reveals the same trend as the Carter's rule: an increase of solidity reduces the deviation. Quantitatively, the predictions are very similar but the rules diverge towards low solidities. They reach closer agreement at high solidity. Further comparison of both rules will be shown in Chapter 3.

σ	$\delta_{0,10}$	K_δ	m	b	ϕ	δ_{opt}	$\Delta\beta$
1.0	1.2	0.40	0.29	0.78	30°	9.3°	17.5°
1.2	1.4	0.40	0.29	0.78	30°	8.2°	19.9°
1.4	1.6	0.40	0.29	0.78	30°	7.4°	21.8°
1.6	1.7	0.40	0.29	0.78	30°	6.8°	23.5°
1.8	1.8	0.40	0.29	0.78	30°	6.3°	25.0°

(a)

σ	δ_{opt}
1.0	8.8°
1.2	7.9°
1.4	7.2°
1.6	6.7°
1.8	6.3°

(b)

Table 2.3: *NASA (a) and Carter (b) deviation predictions for DCA blade with* $t/c_{max} = 6.5\%$ *and* $\beta_1 = 50°$ *at constant camber*

σ	$\delta_{0,10}$	K_δ	m	b	$\Delta\beta$	δ_{opt}	ϕ
1.0	1.2	0.40	0.29	0.78	20°	10.7°	34.7°
1.2	1.4	0.40	0.29	0.78	20°	8.3°	30.2°
1.4	1.6	0.40	0.29	0.78	20°	6.8°	27.1°
1.6	1.7	0.40	0.29	0.78	20°	5.7°	24.9°
1.8	1.8	0.40	0.29	0.78	20°	5.0°	23.0°

(a)

σ	δ_{opt}
1.0	10.0°
1.2	8.0°
1.4	6.6°
1.6	5.7°
1.8	4.9°

(b)

Table 2.4: *NASA (a) and Carter (b) deviation predictions for DCA blade with* $t/c_{max} = 6.5\%$ *and* $\beta_1 = 50°$ *at constant flow turning*

Another interesting feature is given in Fig. 2.13 that shows the variation of deviation with respect to a change of incidence (i.e. different from the reference minimum loss incidence) as a function of solidity. The slope of the deviation versus incidence is always positive but decreases with solidity. Going to an infinite solidity, the slope tends to zero. This highlights the guidance role of the solidity in cascades. The higher is the solidity, the better the flow is guided and the less sensitive is the deviation to any change of incidence. Finally, using the figures 2.9 to 2.13, the deviation at a slightly off-design positive incidence is given by:

$$\delta = \delta_{opt} + (i - i_{opt}) \left(\frac{d\delta}{di} \right)_{opt} \tag{2.8}$$

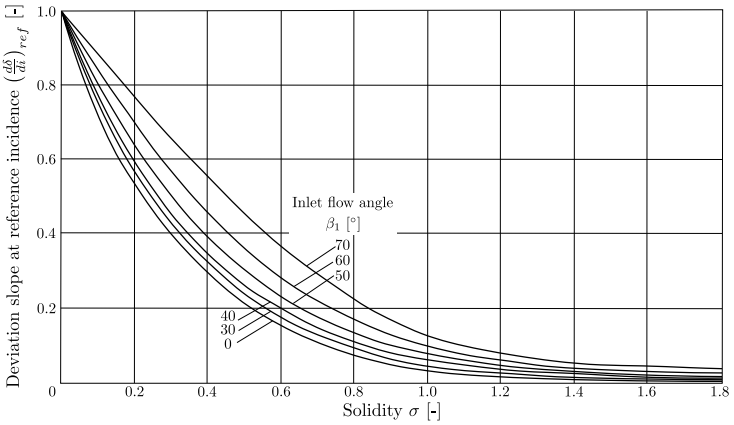


Figure 2.13: *Deviation angle slope at optimum incidence [6]*

To conclude this section, it must be mentioned that, physically, the influence of the solidity on both the incidence and the deviation can already be explained by an inviscid potential flow approach. As mentioned by Cumpsty in [8], it was recognized that optimum conditions were obtained when the stagnation conditions were sitting at the leading edge tip. From the 2D inviscid irrotational flow theory, it is known that, a cascade can be modeled by a distribution of circulation Γ on the pressure and suction sides. The situation is depicted in Fig. 2.14 but, for simplicity, the whole circulation is assumed to be concentrated in a single point P on the camberline. To satisfy the Kutta-Joukowsky condition, the value of Γ is the one that brings the rear stagnation point exactly at the trailing edge and moreover, the intensity of Γ is also proportional to $1/d$ where d is the distance to the vortex center P. Therefore, for an incoming mean flow at zero incidence, the induced velocity V_1^Γ due to Γ increases when approaching the leading edge and the resulting velocity V_1' gets more inclined with respect to the camberline. The position of the stagnation point does not fall exactly at the leading edge tip and to bring back the stagnation point close to the leading edge (i.e. to operate at optimum condition), the mean flow must attack the blade with a slightly negative incidence. Likewise, at the trailing edge, the resulting vector V_2' leaves the cascade tangent to the trailing edge by combination of the induced velocity V_2^Γ and the outlet velocity V_2^∞. In the far field, as the contribution of V_2^Γ decreases, the mean outlet flow does not follow the outlet direction of the camberline and a deviation is created.

To understand the influence of the solidity, one must go back to the definition of the circulation around the blade which, assuming a constant axial velocity, is given by Eq. (2.9).

$$\Gamma = \oint V.dl = V_{ax} \left(\tan\beta_1 - \tan\beta_2\right) \, s \tag{2.9}$$

Therefore, according to Eq. (2.9), decreasing the solidity (i.e. increasing the spacing) increases the circulation. As sketched in Fig. 2.15, keeping a mean

flow at zero incidence, the induced velocity will then be larger when the pitch increases from s_a to s_b and, as $V_1^{\Gamma_a} < V_1^{\Gamma_b}$, the stagnation point will move further down on the pressure side. Consequently, in order to bring the front stagnation point on the leading edge tip, the mean incidence flow must be more negative when the solidity decreases. Similarly, since $V_2^{\Gamma_a} < V_2^{\Gamma_b}$, the deviation angle increases with the spacing.

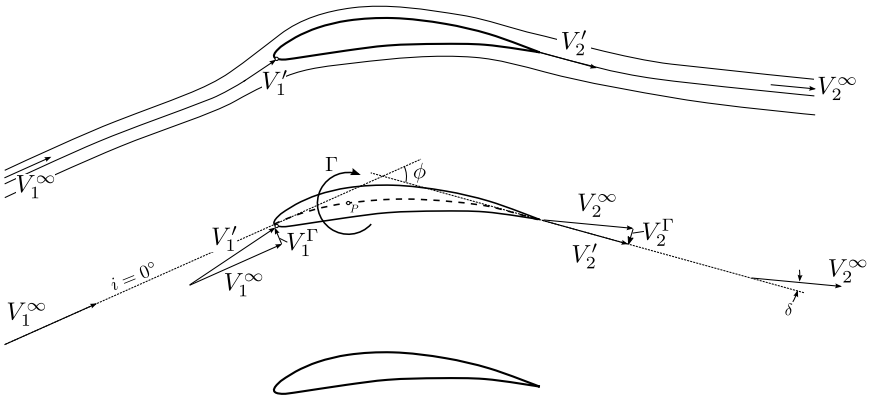


Figure 2.14: *Sketch of the influence of the blade circulation on an incoming flow at zero incidence*

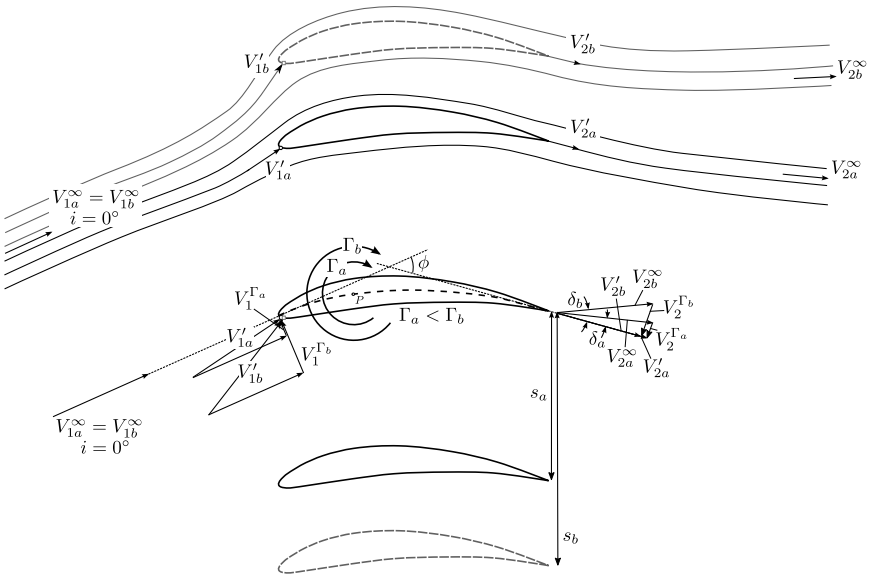


Figure 2.15: *Sketch of the influence of the solidity on incidence and deviation by potential flow theory*

The displacement of the stagnation point is also illustrated in Fig. 2.16 from [8] based on incompressible singularity method calculations. This confirms the results of Table 2.1 and Table 2.2 and as the solidity decreases, the optimum incidence decreases.

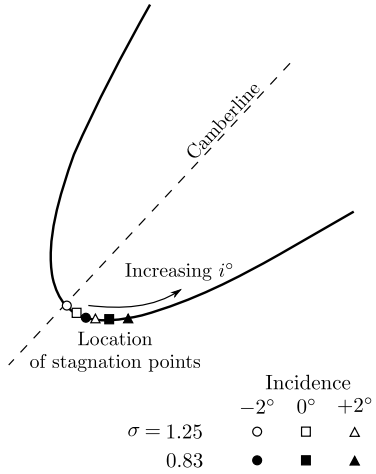


Figure 2.16: *Position of the stagnation points around the leading edge computed using an incompressible singularity method for a NACA-65 airfoil with different solidities [8]*

2.1.3 Blade loading and losses

The issues of blade loading assessment and prediction of losses are largely addressed in the literature. The designer must be able to characterize in which conditions the blade is operating and how far it is from stall. The loading criteria will thus be always related to the generated total pressure losses or the drag-lift ratio coefficient of the blade profile.

The first attempt in characterizing the loading came from Zweifel in 1945 [3]. He compared the lift of the blade to an ideal lift based on the outlet velocity. The Zweifel coefficient ψ is defined below:

$$\psi = \frac{\Delta V_\theta (V_1 + V_2)}{\sigma V_2^2} \tag{2.10}$$

To establish this coefficient, he relied on different cascade tests, from turbines and compressors. Surprisingly, this coefficient offers the remarkable property that for many different blades the minimum drag-lift ratio is independent from the inlet and outlet flow angles β_1 and β_2 and always lies between $\psi = 0.8$ and $\psi = 1$. This is illustrated in Fig. 2.17.

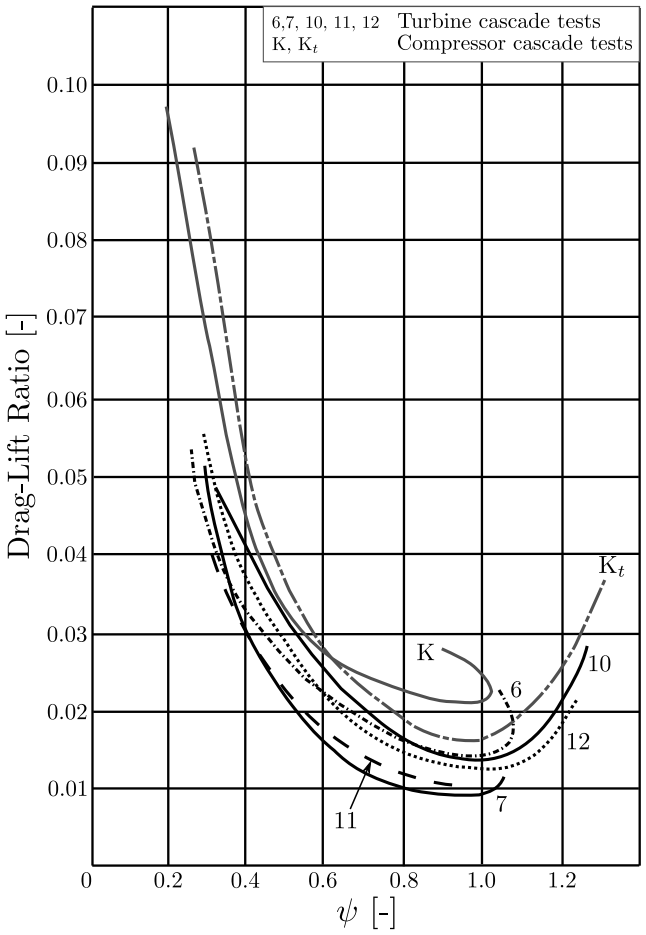


Figure 2.17: *Drag-lift ratio in function of the Zweifel loading factor ψ for different types of bladings*

This allows to define an optimum pitch distance to operate at maximum lift-drag ratio for given β_1 and β_2 values. For incompressible flow, the Zweifel coefficient can be written as follows:

$$\psi = \frac{(\cos(\beta_1) + \cos(\beta_2))(\tan(\beta_1) - \tan(\beta_2))}{\sigma \ \cos^2(\beta_2)} \tag{2.11}$$

Hence, given β_1 and β_2, the optimum pitch required for maximum lift-drag ratio (i.e. $\psi = 0.9$) can be determined. This method to select the optimum pitch can be used -at least as a first guess- in compressor blade design. Eck [11], Wallis [12] or Dixon [13] refer to Zweifel optimum pitch distance when designing optimum fans. This factor is also mentioned by Obrecht [1] to address the issues of loading and choice of the number of blades. Nevertheless, the data used by Zweifel mainly came from turbine cascade tests. Therefore, this pitch

selection method might not be trusted completely when designing compressor blades.

Regarding the assessment of loading and stability limit of cascades, the greatest advancement came from Lieblein and his diffusion factor in 1953 [5]. It is admitted that the suction side boundary layer, facing an adverse pressure gradient, is responsible for the limiting pressure rise and turning of the flow. Therefore, Lieblein linked the suction side deceleration of the flow to a local diffusion factor:

$$D_{loc} = \frac{V_{max} - V_2}{V_{max}} \tag{2.12}$$

where V_{max} is the peak suction side velocity and V_2 the outlet velocity. Under the form of Eq. (2.12), the calculation of the diffusion factor was very time-consuming and not practical. A more convenient diffusion factor was then defined to assess the loading of the blades:

$$D = (1 - \frac{V_2}{V_1}) + \frac{\Delta V_\theta}{2V_1\sigma} \tag{2.13}$$

This definition uses the outlet-inlet velocity ratio, the circumferential velocity difference as well as the solidity. This is still applicable for three-dimensional compressors. For a rotor, the relative velocities are considered. The change of radius can also be taken into account by considering the circulation around the blade. In the case of a rotor, the diffusion factor takes the form of Eq. (2.14):

$$D = (1 - \frac{W_2}{W_1}) + \frac{\Delta(rW_\theta)}{2\ r_m W_1 \sigma_m} \tag{2.14}$$

where r_m is the mean radius and σ_m, the mean solidity defined as $(\sigma_1 + \sigma_2)/2$. The solidities σ_1 and σ_2 are respectively based on rotor inlet and outlet radii, which are equal in the case of an axial machine. The solidity clearly appears as an important parameter in the appraisal of the loading. This offers a way to select the solidity or similarly to adapt the diffusion level.

Gathering the results of measurements performed on various types of bladings (DCA, NACA65 or British C4 among others [10]) having different solidities but also maximum thicknesses and camber angles, Lieblein linked the wake momentum thickness to the diffusion factor. This is illustrated in Fig. 2.18 from [6]. The wake momentum thickness starts to rise more steeply for diffusion factors above 0.6. It was therefore commonly accepted that a diffusion factor of 0.6 could be considered as the blade stall limit.

The wake momentum thickness is defined by Eq. (2.15), where V_2 is the outlet velocity and $V_{2,fs}$ is the outlet free-stream velocity as sketched in Fig. 2.19. Hence, by definition, the measurement of the wake momentum thickness is only feasible with hot-wires or more complex techniques such as Laser Doppler Velocimetry (LDV) or Particule Image Velocimetry (PIV) which both require

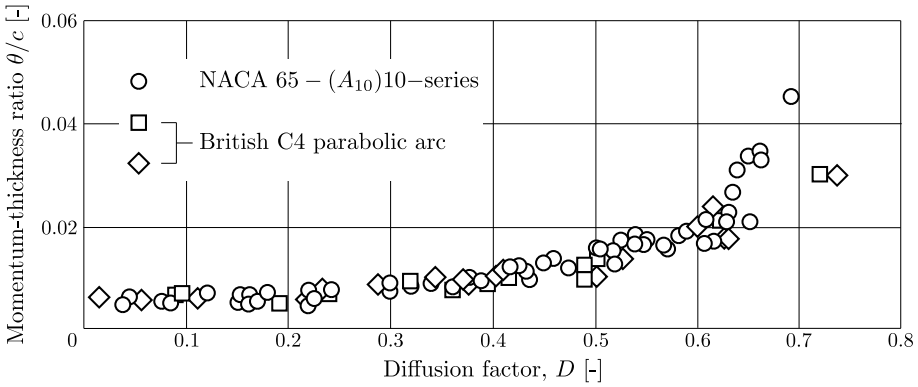


Figure 2.18: *Evolution of momentum thickness to chord ratio as a function of Lieblein diffusion factor of Eq. (2.13) [6]*

an optical access. It may also be possible with multi-hole pressure probes but measurements of total and static pressures as well as flow angle are very complicated in a blade wake [14]. They are subjected to blockage effects of the probe itself and require a lot of care in miniaturization to get accurate data.

$$\theta = \int_{-s/2}^{s/2} \left(1 - \frac{V_2}{V_{2,fs}}\right) \frac{V_2}{V_{2,fs}} dy \tag{2.15}$$

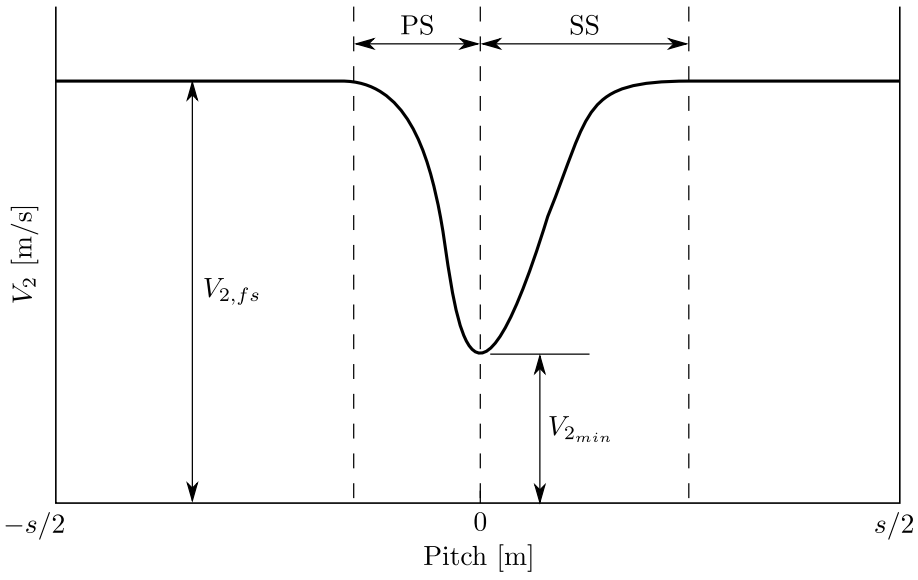


Figure 2.19: *Sketch of an outlet velocity wake for the calculation of the wake momentum thickness*

Since it is not always possible to measure the wake momentum thickness, Lieblein [15] derived the link between the momentum thickness to chord ratio and the total pressure losses, as shown in Eq. (2.16), where H is the wake shape factor.

$$\frac{\theta}{c} = \frac{\omega \cos\beta_2}{2\sigma} \left(\frac{\cos\beta_2}{\cos\beta_1}\right)^2 \left\{ \frac{3H-1}{2H} \left[1 - \frac{\theta}{c}\frac{H\sigma}{\cos\beta_2}\right]^3 \right\} \tag{2.16}$$

Lieblein observed in [15] and [16] that the last term within braces in Eq. (2.16) was close to 1 and not subject to strong variations over a wide diffusion range. Therefore, he suggested the use of loss parameters to approximate the wake momentum thickness. Those loss parameters are given in Eq. (2.17) and Eq. (2.18) and are referred to as ζ_1 and ζ_2 in the following. They present the strong advantage of relying only on total pressure losses and flow angle measurements. Plotted as a function of the diffusion factor, both loss parameters offer a good prediction of the wake momentum thickness. This is shown in Fig. 2.20.

$$\zeta_1 = \frac{\omega \cos\beta_2}{2\sigma} \approx \frac{\theta}{c} \tag{2.17}$$

$$\zeta_2 = \frac{\omega \cos\beta_2}{2\sigma} \left(\frac{\cos\beta_2}{\cos\beta_1}\right)^2 \approx \frac{\theta}{c} \tag{2.18}$$

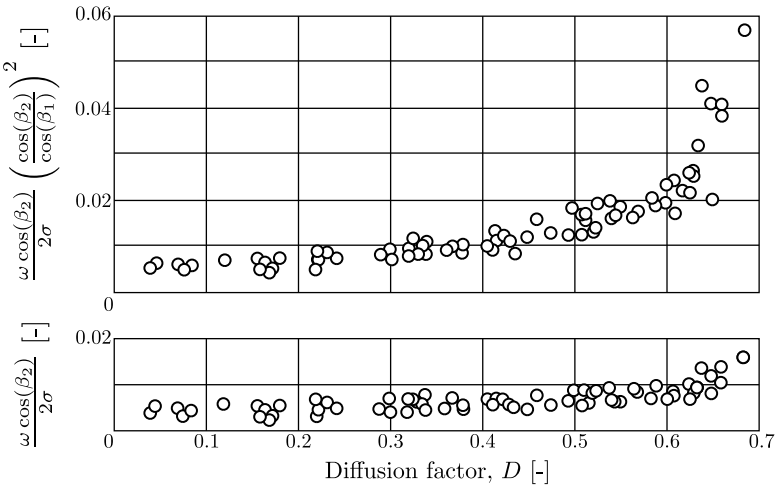


Figure 2.20: *Evolution of loss parameters ζ_1 and ζ_2 with diffusion factor [6]*

Lieblein continued his work and defined an equivalent diffusion ratio [17]. This equivalent diffusion ratio is closer to the original definition of the local diffusion factor and expresses the ratio of the peak suction side velocity to the outlet velocity.

$$D_{eq} = \frac{V_{max}}{V_2} \tag{2.19}$$

This approach encountered a great support and was adapted or improved by many such as Koch and Smith [18], Casey [19] or Wright and Miller [20]. Nonetheless, by definition, the determination of the equivalent diffusion ratio is based on the knowledge of the blade velocity distribution. This task is not straightforward as, on one hand, the maximum suction side velocity strongly depends on the cascade geometry which is not known at the level of the meridional design. Some models are then necessary to overcome this problem and provide the missing information. A very good example of such model is the generic velocity model described by Dickens and Day [21]. On the other hand, experimentally, the equivalent diffusion ratio still remains very difficult to measure. For NACA 65 and DCA airfoils, Lieblein [17] gave an empirical approximation shown in Eq. (2.20).

$$D_{eq} = \frac{V_{max}}{V_2} \approx \frac{\cos\beta_2}{\cos\beta_1}\left[1.12 + 0.61\frac{\cos^2\beta_1}{\sigma}(\tan\beta_1 - \tan\beta_2)\right] \tag{2.20}$$

Using Eq. (2.20), the same type of figure as Fig. 2.18 can be obtained. This is done in Fig. 2.21 where the wake momentum thickness to chord ratio is plotted as a function of D_{eq}. For a D_{eq} greater than 1.8 (or 2 depending on the source), the flow is considered to be separated on the suction surface.

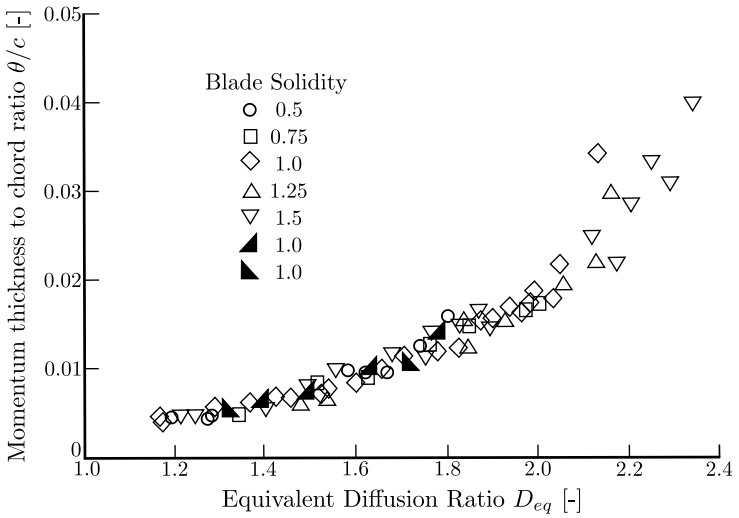


Figure 2.21: *Variation of wake momentum thickness to chord ratio as a function of the equivalent diffusion factor*

Casey [19] fitted the relation of D_{eq} and the pressure losses presented by Lieblein in [5]. This is given by Eq. (2.21).

$$\omega = 2\frac{0.0045}{1 - 0.95\ln(D_{eq})}\frac{\sigma}{\cos(\beta_2)}\left(\frac{\cos(\beta_1)}{\cos(\beta_2)}\right)^2 \tag{2.21}$$

Wright and Miller presented in [20] a performance prediction method used by Rolls-Royce and mainly based on Lieblein's work from [17]. However, they

completed Lieblein's expression (Eq. (2.20)) by adding a correction for maximum thickness and considering axial velocity ratios different than 1 by using velocities instead of flow angles. Their equivalent diffusion factor is given by Eq. (2.22). The correlation is shown in Fig. 2.22 for different Mach numbers.

$$D_{eq} = \left[1 - \frac{V_2}{V_1} + \left(1 + \frac{t_{max}}{c}(10.116 - 34.15\frac{t_{max}}{c})\right)\right]\frac{V_1}{V_2} + 1.0 \qquad (2.22)$$

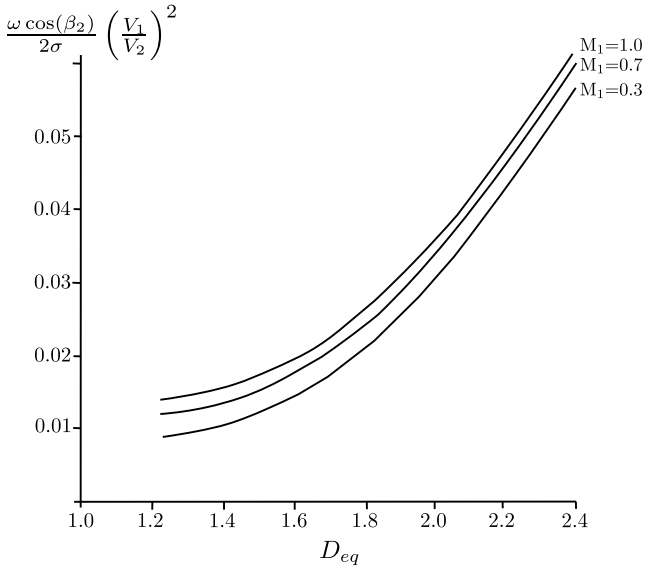


Figure 2.22: *Loss correlation of Wright and Miller [20] using D_{eq} of Eq. (2.22)*

Koch and Smith [18] developed the most complete loss prediction model. The model is in good agreement with Lieblein's data but it has the advantage to be more complete by taking into account many more effects such as axial velocity density ratio, Reynolds number or maximum thickness-to-chord ratio.

In order to build their blade profile loss correlation, Koch and Smith considered three values of diffusion ratio and theoretical blade velocity distributions. They are displayed in Fig. 2.23. Then, with the help of a compressible boundary layer code, they calculated the trailing edge momentum thickness over a wide range of streamtube contractions as well as Reynolds and Mach numbers. They also provided a more general formulation of the equivalent diffusion ratio valid for various types of profile, AVDR, Reynolds and Mach numbers. The whole derivation is not recalled here and is available in [18]. Some assumptions are done on the blade geometry as the throat position that is assumed to be located at one-third of the chord length. According to Koch and Smith, it is valid for high subsonic Mach numbers as long as no strong shock appears on the suction side. The comparison with Lieblein's correlation is shown in Fig. 2.24 at low Mach number ($M_1 = 0.05$) and AVDR=1 (no streamtube contraction).

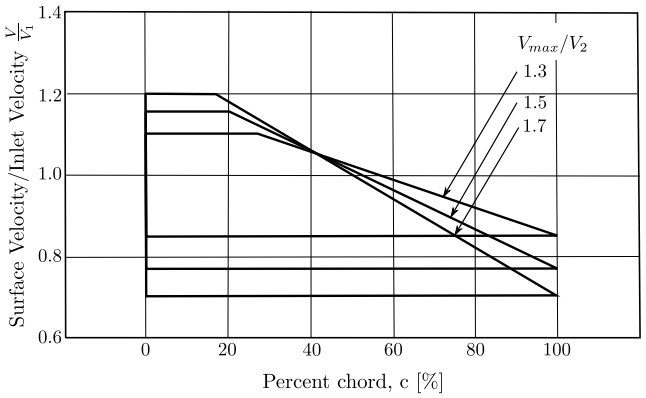


Figure 2.23: *Theoretical velocity distribution and diffusion ratios considered by Koch and Smith [18]*

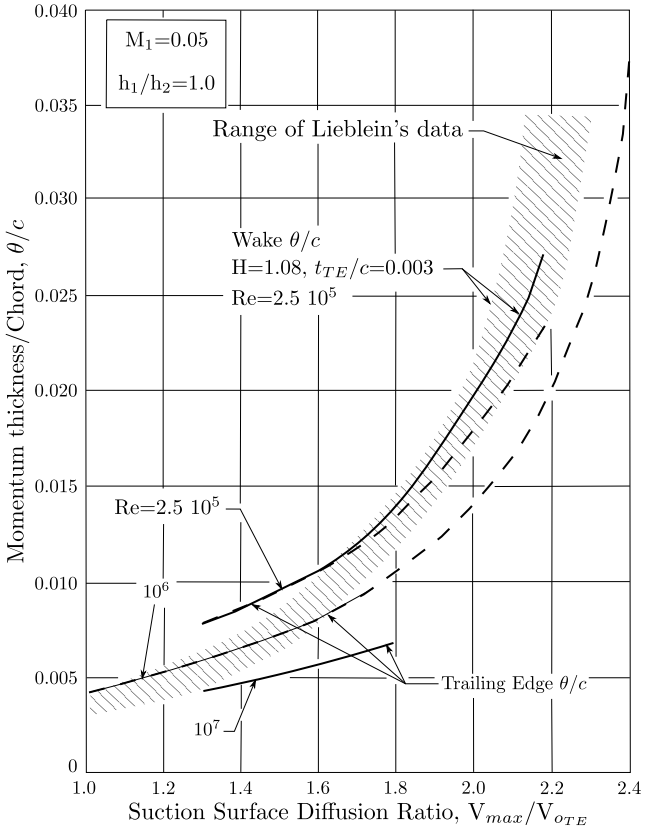


Figure 2.24: *Momentum thickness to chord ratio versus equivalent diffusion ratio at $M_1 = 0.05$ and AVDR=1 [18]*

Although methods like the ones of Lieblein [17], Koch and Smith [18] or Wright and Miller [20] may give good estimates of the momentum thickness, it is still required to convert the momentum thickness into total pressure losses for the meridional design. Therefore, a relation like the one derived by Lieblein for incompressible flow and given in Eq. (2.16) is necessary. It may be the weakness of such correlations as the final output required by the designer is the total pressure losses rather than the momentum thickness.

Regarding the choice of the solidity, it may be interesting to look if the minimum loss solidity can be extracted from those correlations. Indeed, for a given velocity triangle, the solidity is the only remaining parameter. As an example, with the mid-span inlet and outlet velocity triangles of a low-pressure compressor studied at VKI within the European DREAM project (cf. Appendix A), Fig. 2.25 and Fig. 2.26 respectively show the losses as a function of solidity using Lieblein's [6] or Koch's [18] correlations. Lines of constant diffusion factor or equivalent diffusion ratio are also indicated. Lieblein presented the same results in [17] (cf. Fig. 2.21). It is given in Fig. 2.27 where the white circles correspond to $D_{eq} = 2.0$, considered as the stall limit.

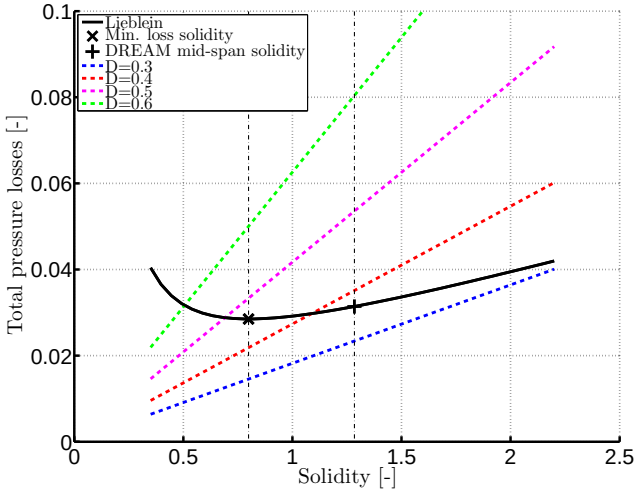


Figure 2.25: *Evolution of losses as a function of solidity using Lieblein's correlation [6] and the mid-span DREAM booster data*

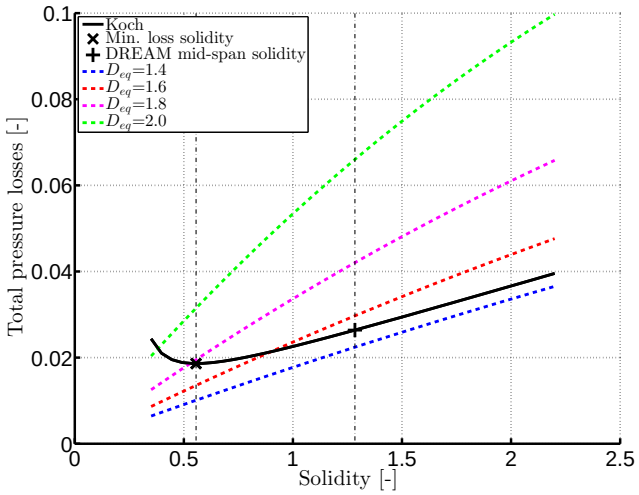


Figure 2.26: *Evolution of losses as a function of solidity using Koch and Smith correlation [18] and the mid-span DREAM booster data*

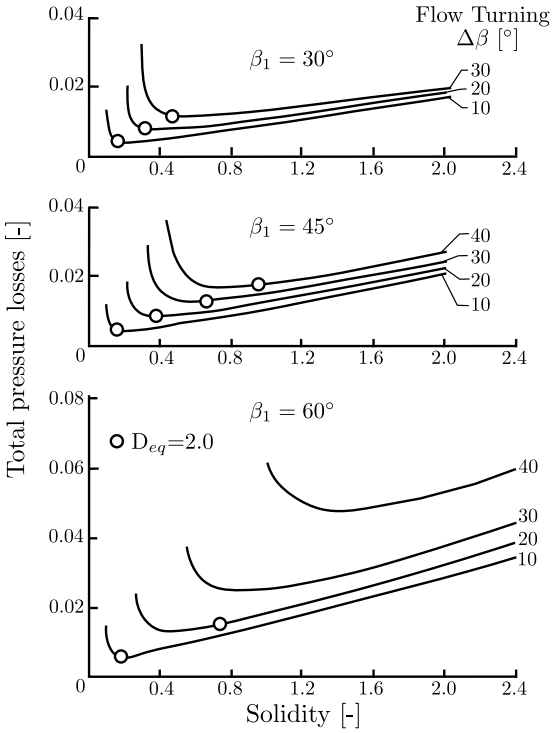


Figure 2.27: *Losses versus solidity for various inlet and outlet flow angles using Lieblein's correlation of [17]*

The issue of the optimum solidity will be addressed in a following section but Fig. 2.25, Fig. 2.26 and Fig. 2.27 show that a theoretical optimum exists. However, it appears that the solidity which gives the minimum losses is too low and leads to very high diffusion that would most probably cause flow separation. For solidities higher than the optimum, the losses increase with solidity. This trend can be explained by the growth of wetted area and friction losses when the number of blades (or the chord) increases.

2.1.4 Compressibility effects

In the previous section, except Koch and Smith or Wright and Miller, none of the correlations includes Mach number effects. More particularly, the results of Lieblein all come from low-speed tests[2]. Moreover, the expression of Eq. (2.16) derived by Lieblein in [15] relies on incompressible relations. In theory, the definition of the loss parameters is thus only valid for the incompressible regime.

Looking at high subsonic flow, a very important feature is the critical Mach number. The critical Mach number is the Mach number at which a sonic point appears along the blade suction side. It really depends on the profile geometry both in terms of camber and thickness distributions. Below that Mach number, many authors claim that no correction should be applied to incompressible correlations. Optimum incidence, deviation and losses can be predicted by the correlations presented in the previous sections. The manual of NASA [6] is stating that the compressibility corrections can be neglected and does not provide any correction. However, some work has been done to improve this lack and, above the critical Mach number, it is possible to find some corrections to the incompressible rules.

As an example, the work of Boyce [22] provides some corrections to Carter's rule for Mach number above an arbitrary Mach number level of 0.75 as it can be seen in Fig. 2.28. Some evidences can be found in the manual of NASA [6] showing that the Mach number does have an effect on the deviation already below an inlet Mach number of 0.75. The compressibility effect on deviation is displayed in Fig. 2.29 for a British C4 profile and a DCA blade. The effect of the inlet Mach number on the flow turning is also shown for a T1($18A_6I_{48}$)08 and a NACA 65-($12A_{10}$)10 in Fig. 2.30. In both figures, the influence of the inlet Mach number is very limited and consequently, it was admitted that the effect of compressibility on deviation could be neglected as long as critical conditions were not reached.

[2]The cascade wind tunnel that has been used for those tests is the actual VKI-C1 cascade wind tunnel and cannot exceed an inlet Mach number of 0.3.

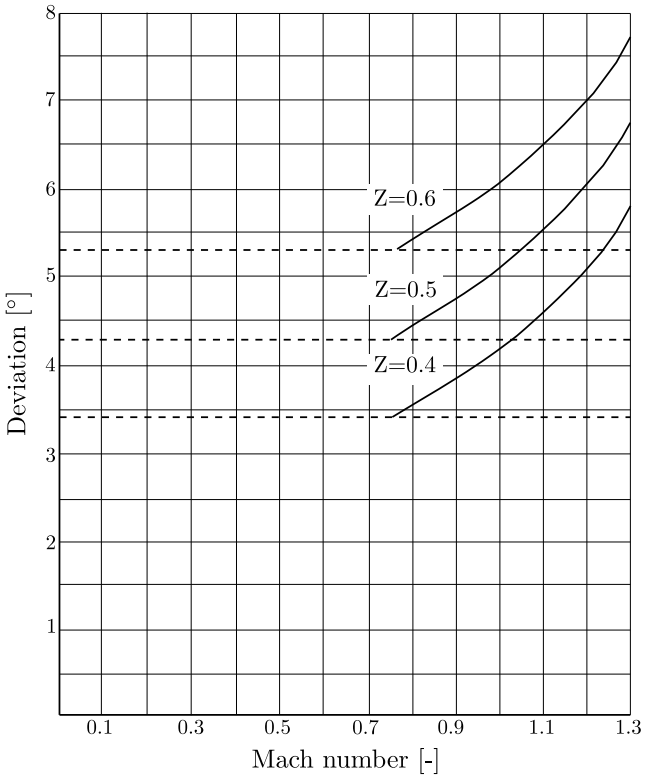


Figure 2.28: *Mach effect on deviation for various maximum thickness location Z [22]*

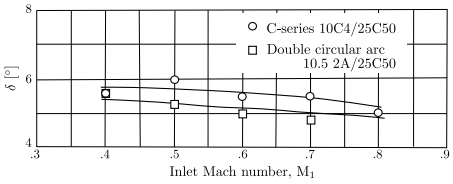


Figure 2.29: *Effect of Mach number on deviation on British C4 and DCA profiles [6]*

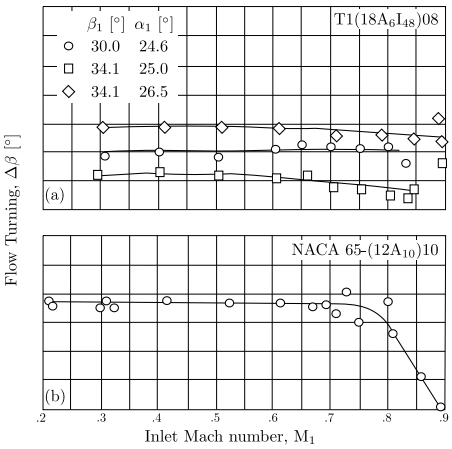


Figure 2.30: *Effect of Mach number on turning: (a) T1(18A_6I_{48})08 and (b) NACA 65-(12A_{10})10 [6]*

Regarding the losses, Jansen and Moffat [23] suggest that the incompressible losses may simply be corrected by Eq. (2.23) above the critical Mach number. According to Eq. (2.23), the losses increase linearly above the critical Mach number.

$$\omega_{comp} = \omega_{incomp}[2(M_1 - M_{cr}) + 1] \tag{2.23}$$

The determination of the critical Mach number remains a difficult task. Jansen and Moffat offer a method to predict the critical conditions based on NACA 65 series experimental results. It was observed that the pressure coefficient C_p corresponding to the minimum pressure point on the blade suction surface remained nearly unchanged until a sonic point appears on the suction side. The pressure coefficient is defined as:

$$C_{p,min} = \frac{p_{s,min} - p_{s1}}{p_{01} - p_{s1}} \tag{2.24}$$

When critical conditions are met, one can establish:

$$-\left(C_{p,min}\right)_{incomp} = -\left(C_{p,min}\right)_{comp} = \frac{1 - \left(\frac{2}{\gamma+1} + \frac{\gamma-1}{\gamma+1}M_{cr}^2\right)^{\gamma/\gamma-1}}{\left(1 + \frac{\gamma-1}{2}M_{cr}^2\right)^{\gamma/\gamma-1} - 1} \tag{2.25}$$

Eq. (2.25) may also be reversed and the critical Mach number may be written as a function of $C_{p,min}$ [24]:

$$M_{cr} = \sqrt{\frac{2}{\gamma - 1}\left[\left(\frac{1 - C_{p,min}}{\left(\frac{2}{\gamma+1}\right)^{\frac{\gamma}{\gamma-1}} - C_{p,min}}\right)^{\left(\frac{\gamma-1}{\gamma}\right)} - 1\right]} \tag{2.26}$$

Following that assumption, one can get a first guess of the critical Mach number of a cascade based on incompressible data. This is shown in Fig. 2.31.

A more sound estimation can only be obtained by predicting the velocity distribution but, at the level of meridional design, the profile is not known. For the NACA 65 series, Jansen and Moffat expressed $\frac{V_{max}}{V_1}$ as (cf. [23]),

$$\frac{V_{max}}{V_1} = 1 + (0.4 + \frac{t_{max}}{c})\left(\frac{\Delta V_\theta}{\sigma V_1}\right) + (0.03 + 0.7\frac{t_{max}}{c}) \tag{2.27}$$

and knowing that,

$$-\left(C_{p,min}\right)_{incomp} = \left(\frac{V_{max}}{V_1}\right)^2 - 1 \tag{2.28}$$

one can calculate the critical Mach number with Eq. (2.26).

For slightly supersonic flow (from M=1 to Mach=1.4), cascade measurement data were produced by Heilmann et al. [25]. They only deal with DCA profiles

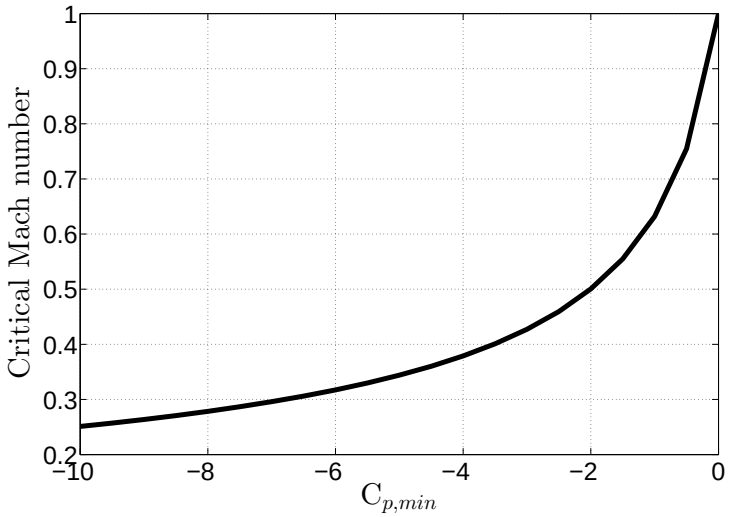


Figure 2.31: *Critical Mach number versus minimum pressure coefficient on suction side*

and consider solidity variation by changing the pitch length. These data are displayed in Fig. 2.32. For $M_1 < 1.2$, the losses increase with solidity. Heilmann et al. explain this behavior by arguing that, in this Mach number range, the profile losses are still predominant compared to the overall losses. For higher Mach numbers, the shock losses become more important. The loss reduction then comes from the lower Mach number achieved in front of the passage shock. By reducing the pitch distance, the distance between the leading edge and the passage shock location decreases. This reduces the expansion rate on the suction side and lowers the Mach number in front of the passage shock. The latter is weaker and induces less losses. The trend of losses in function of solidity is thus opposite for such Mach numbers and the losses decrease for higher solidities. This behavior was previously observed by Schwenk and al. ([26] and [27]) investigating the solidity effect in transonic compressors. This issue is commented in Sec. 2.2. It must be said that those observations really modified the trend in fan design of the 60's where the fan tip solidity was always close to 1 as quoted in the NASA manual [6] in 1965:

> *[...] Reasonable values of solidity for the transonic compressors appear to be in order of 1 at the tip section. Extremely low solidities lead to poor guidance and high losses, while extremely high solidities lead to hub choking problems and high losses.[...]*

Nowadays, in fan or booster designs, fan tip sections that experience (slightly) supersonic relative Mach numbers (1.2 - 1.4) always have solidities between 1.1 and 1.4. More precisely, for such cases, it is agreed that a good practice is to consider a tip solidity equal to the relative tip Mach number. In [28], Glassman

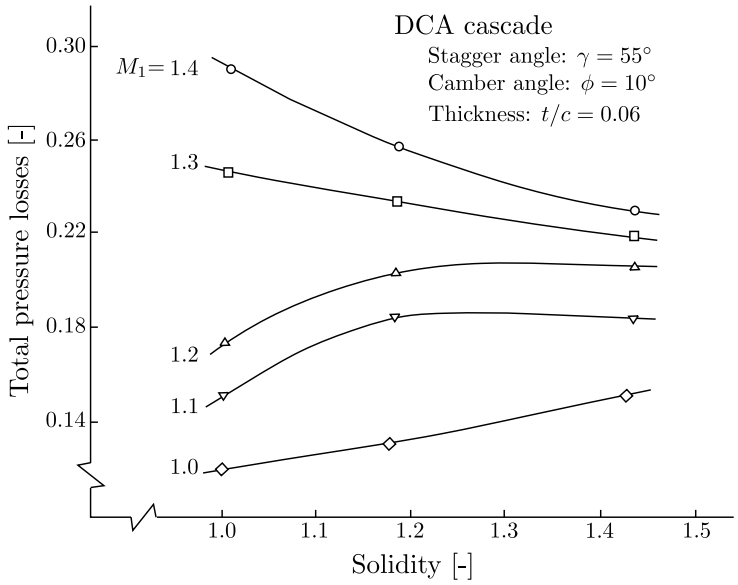


Figure 2.32: *Total pressure losses as a function of solidity and inlet Mach number*

and Lavelle found a linear relation between the rotor tip solidity and the inlet relative Mach number that appears to match quite well the rotor tip solidities of the NASA compressor database.

$$\sigma_{r,tip} = 0.5 M_{r,tip} + 0.7 \tag{2.29}$$

Eq. (2.29) may only be a first guess but it confirms that for supersonic inlet relative Mach numbers the tip solidity should be above 1.

2.1.5 Stability

It is commonly accepted that a decrease of solidity has a negative effect on the stability of a cascade or a compressor. It can be explained by analyzing the diffusion factor (Eq. (2.13)) or the Zweifel coefficient (Eq. (2.10)) that increases when the solidity decreases while a higher loading is more likely to cause to flow separation. The only attempt to quantify this trend comes from Koch and his analogy with 2D diffusers [29].

Koch used the work on diffusers of Sovran and Klomp [30] and applied it to compressors. Two-dimensional diffuser results from [30] relate the maximum static pressure rise to the ratio of the diffuser length over the diffuser inlet width (or inlet area in the case of 3D diffusers). For compressors, Koch suggests to use the outlet passage width (i.e. the staggered spacing between two blades) as the inlet streamtube width varies depending on the incoming incidence. The

geometrical analogy of a compressor passage with a two-dimensional diffuser is illustrated in Fig. 2.33.

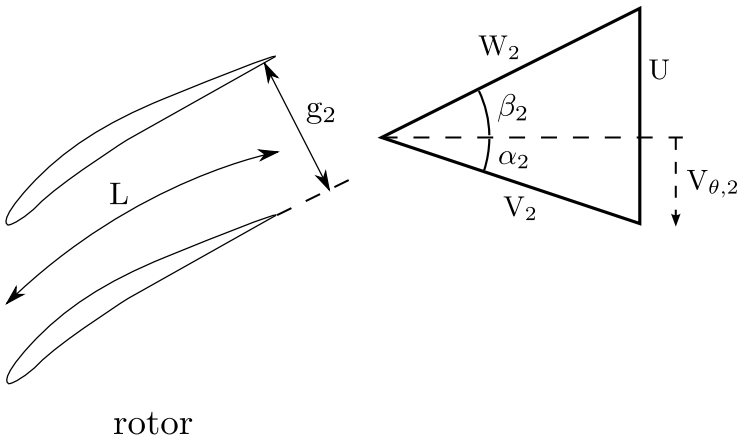


Figure 2.33: *Sketch of Koch's diffuser analogy of a compressor passage with L as the diffuser length and g_2 as the diffuser outlet width*

Sovran and Klomp results included the effect of the inlet boundary layer blockage. From their data, the maximum static pressure rise can be plotted as a function of the ratio L/g_2 (i.e. diffuser length over exit passage width) for different inlet boundary layer blockages. It is done in Fig. 2.34. It is interesting to observe that, over the range of boundary layer blockage, the minimum static pressure rise is achieved for an inlet blockage of 9%.

Against the 5% blockage curve of Fig. 2.34, Koch plotted the stalling effective static pressure rise coefficient of General Electric compressor test data. The final correlation is shown in Fig. 2.35[3].

[3]Even though Fig. 2.35 indicates a 9% inlet blockage, it seems that Koch most probably used the 5% inlet blockage diffuser correlation curve available in Fig. 2.34

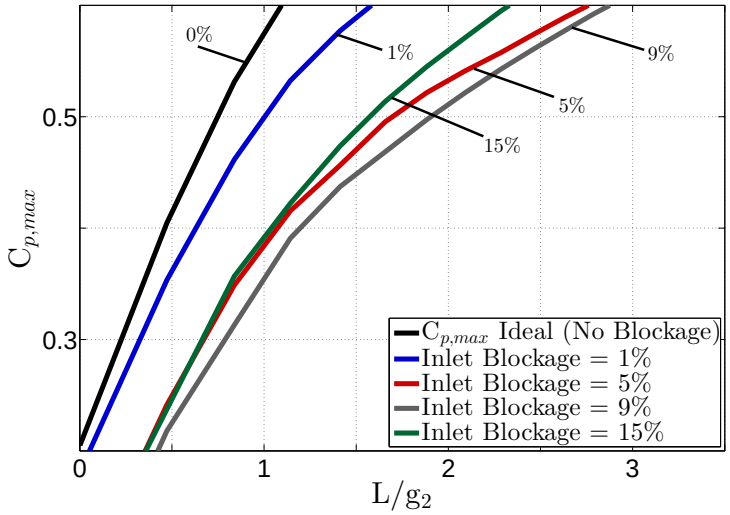


Figure 2.34: *Maximum diffuser static pressure rise for various values of inlet blockage in function of L/g_2*

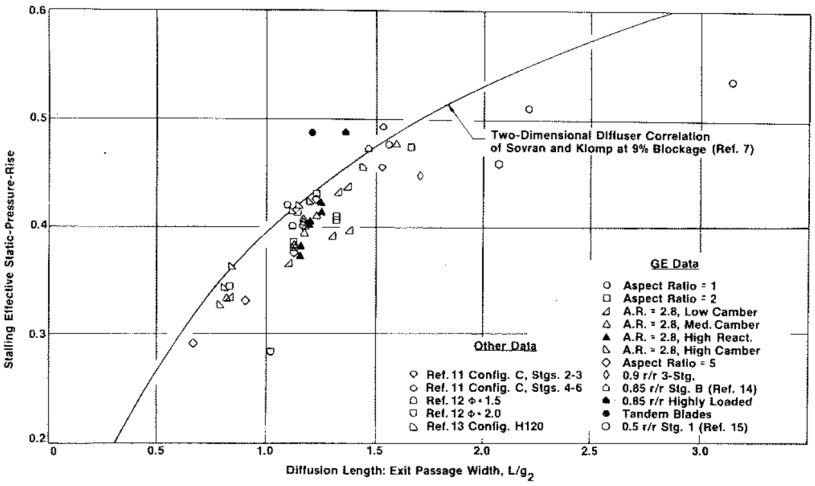
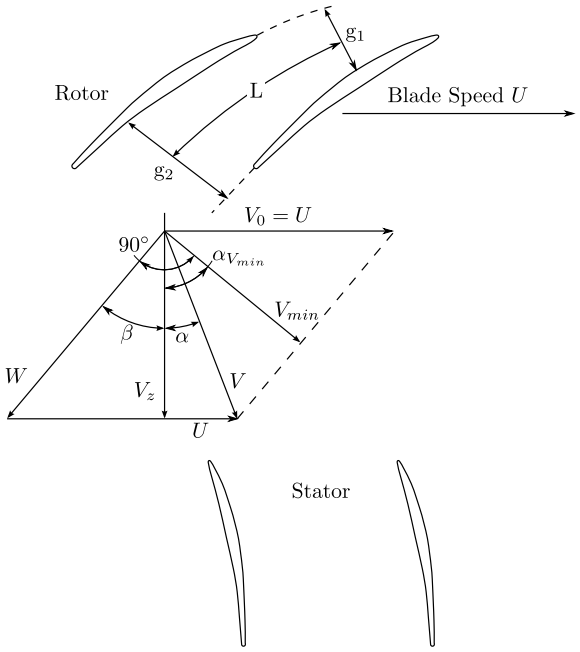


Figure 2.35: *Koch's correlation of stalling effective static pressure rise [29]*

The effective stalling pressure rise is a stage quantity defined as the stage static pressure rise at stall over an effective dynamic pressure. It is a stage quantity that is thus not defined for a simple compressor cascade. The effective dynamic pressure can be seen as the inlet dynamic pressure multiplied by an empirical factor based on the stage velocity triangle. The factor was introduced to explain the higher static pressure rise achieved for stages having high stagger angles. Fig. 2.36 shows how this weight factor is defined in [29] and reveals that

the calculation of the effective pressure rise is not unambiguous and not very physical. However, the strength of this model resides in the fact that it can give an estimate of the stalling capability of a given stage at the level of the meridional design. As mentioned by Cumpsty [8], many compressors have been observed to run below the correlation curve but very few were above.



For a stator:

$$\mathcal{F}_{eff} = \frac{V_{eff}^2}{V^2} = \frac{\left(V^2 + 2.5V_{min}^2 + 0.5V_0^2\right)}{4V^2}$$

$$\frac{V_{min}^2}{V^2} = \sin(\alpha + \beta), \text{ if } (\alpha + \beta) \leq 90^\circ \text{ and } \beta \geq 0^\circ$$

$$\frac{V_{min}^2}{V^2} = 1.0, \text{ if } (\alpha + \beta) > 90^\circ$$

$$\frac{V_{min}^2}{V^2} = \frac{V_0^2}{V^2}, \text{ if } \beta < 0^\circ$$

Figure 2.36: *Koch's definition of effective dynamic pressure factor [29]*

With this simple two-dimensional diffuser analogy, Koch could explain the better stability at high solidity. The diffuser length L is mainly a function of the aerodynamic chord and the profile camber while g_2 can be estimated as $s/\cos\gamma$. Finally, the quantity L/g_2 is proportional to $\sigma/\cos\gamma$. Such a correlation can at least provide an indication of the relative impact of a solidity change on the stability.

2.1.6 The effect of axial velocity-density ratio

In compressor design, the complex three-dimensional unsteady flow is often approximated by considering independently the steady two-dimensional flows on two different families of surfaces: the S1 or blade-to-blade (B2B) surfaces and the S2 or meridional flow surfaces. In both surfaces, the flow is assumed to be two-dimensional and axisymmetric. The losses (and deviation) of a given profile are firstly obtained in the B2B plane and are then used in the meridional plane to provide an estimation of the losses (and deviation) required for the meridional design. Correlations from cascade tests such as the ones exposed in the previous section are used to obtain the B2B performance. Following this design approach, it is essential to ensure that the B2B correlation data respect the two-dimensionality assumption. For cascade flows, the two-dimensionality of the flow is characterized by the axial velocity density ratio. It is defined by Eq. (2.30).

$$AVDR = \frac{\rho_2 \, V_{ax_2}}{\rho_1 \, V_{ax_1}} \tag{2.30}$$

The AVDR is an essential parameter in cascade investigations. If it is not controlled, the AVDR will typically be higher than 1 because of the growth of the end-wall boundary layers and the resulting contraction of the streamtube as well as because of the static pressure rise and the density increase across the passage. Nonetheless, nowadays, in new engine architectures, especially in the low-pressure turbomachinery components (turbines or compressors), the blades may operate at AVDR bigger than 1 simply because of a strong change of meanline radius or strong contraction.

During the cascade tests of Herrig et al. [10] on which Lieblein relied to build his correlations, it is mentioned that two-dimensionality (i.e. AVDR=1) was ensured by endwall boundary layer suction upstream of the blades. In the case of Carter [4], it is not specified but Cumpsty [8] says that the AVDR was most probably between 1.0 and 1.2.

Investigations were performed by many authors but no clear trend emerged. Most particularly, the experimental work of Starken et al. [31] tried to analyze the influence of the AVDR on losses and deviation. If a trend on losses did not clearly emerge, it appears that increasing the AVDR decreased the deviation by decreasing the outlet flow angle. This is shown in Fig. 2.37. The trend seems linear but changes with incidence and Mach number. The influence of AVDR on total pressure losses is not straightforward as it can be seen in Fig. 2.38. The trend is varying with the Mach number but also with inlet flow angle.

Another experimental work of Stark and Hoheisel [32] showed more obvious effects as displayed in Fig. 2.39. For a DCA blade with various aspect ratios, the deviation and the losses decrease when the AVDR increases at a constant inlet Mach number of 0.6. The same behaviour is observed at two other inlet Mach number levels of 0.3 and 0.8 as displayed in Fig. 2.40. It demonstrates that the AVDR must be accounted for the loss and deviation calculations. However, no correlation has been found that includes the effect of AVDR.

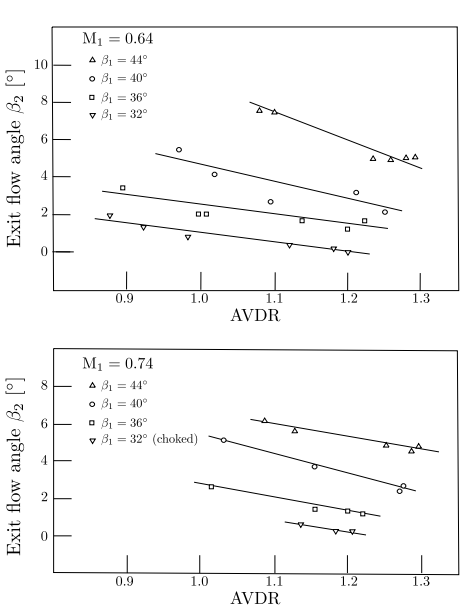


Figure 2.37: *Exit flow angle versus AVDR at various inlet flow angles and Mach numbers [31]*

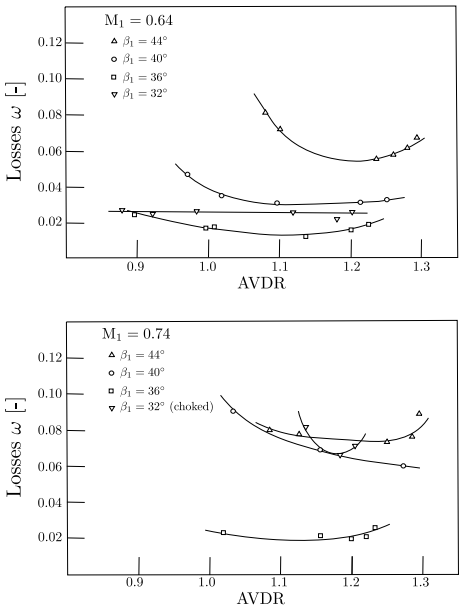


Figure 2.38: *Total pressure losses versus AVDR at various inlet flow angles and Mach numbers [31]*

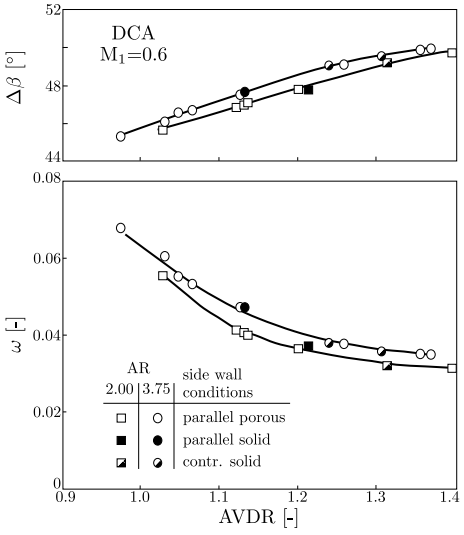


Figure 2.39: *Turning and losses versus AVDR at M=0.6 [32]*

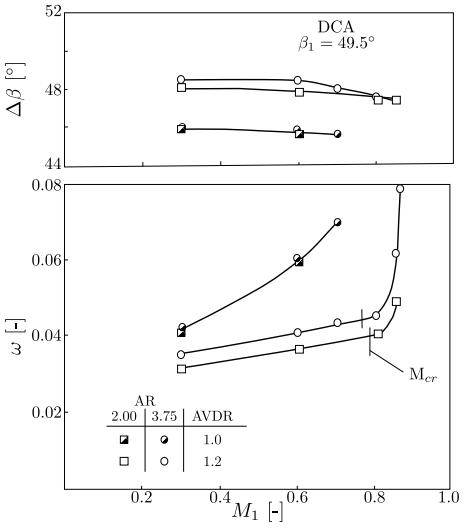


Figure 2.40: *Turning and losses versus Mach number for various AVDR and aspect ratios [32]*

More recently, Kumaran et al. [33] also investigated numerically the effect of AVDR on a linear cascade by considering convergent end-walls (instead of strictly parallel end-walls). The flow accelerates downstream of the blade and generates an AVDR higher than 1. It emerges that the losses decrease when the AVDR increases. This is explained by an increased outlet total pressure due to the outlet velocity re-distribution induced by the convergent channel.

Even though it is undeniable that the AVDR is an essential parameter of compressor performance, this issue has not been investigated extensively in the current research. Part of the work of Ozgen [34] performed at VKI was dedicated to the AVDR effects on the numerical performance of a linear compressor cascade based on the same model as the one presented in Chapter 3. Unfortunately, no real trend emerged from this investigation. As pointed out by Cumpsty [8], everybody agrees to say that the AVDR has an effect on the blade performance and that this parameter must be monitored during any experimental or numerical cascade investigation. However, the control of the AVDR while performing cascade measurements is not an easy task since it requires to adapt the end-wall boundary layer suction (upstream and downstream of the blades) iteratively depending on the incidence, the inlet Mach number, the Reynolds number, the solidity and the blade type. Finally, for compressor design applications, no general rule exists to predict the influence of the AVDR; it remains an open subject.

2.2 Three-dimensional investigations

Although Lieblein's correlations are quite reliable for two-dimensional designs, they show big discrepancies when they are compared with three-dimensional compressor tests. Lieblein's results only deal with cascades and therefore do not account for three-dimensional flow. Robbins et al. [35] offered corrections to the two-dimensional correlations based on annular cascade measurements which take into account three-dimensional losses. In Fig. 2.41, the discrepancies between annular and two-dimensional cascade tests are shown in terms of the loss parameter ζ_1 ($= \omega \cos\beta_2 / 2\sigma$) versus diffusion factor. It can be seen that the losses vary along the radius. The greatest discrepancies are observed at the rotor tip. Finally, some fitted curves which take into account three-dimensional effects are shown in Fig. 2.42, Fig. 2.43 and Fig. 2.44 respectively for losses, incidence and deviation corrections.

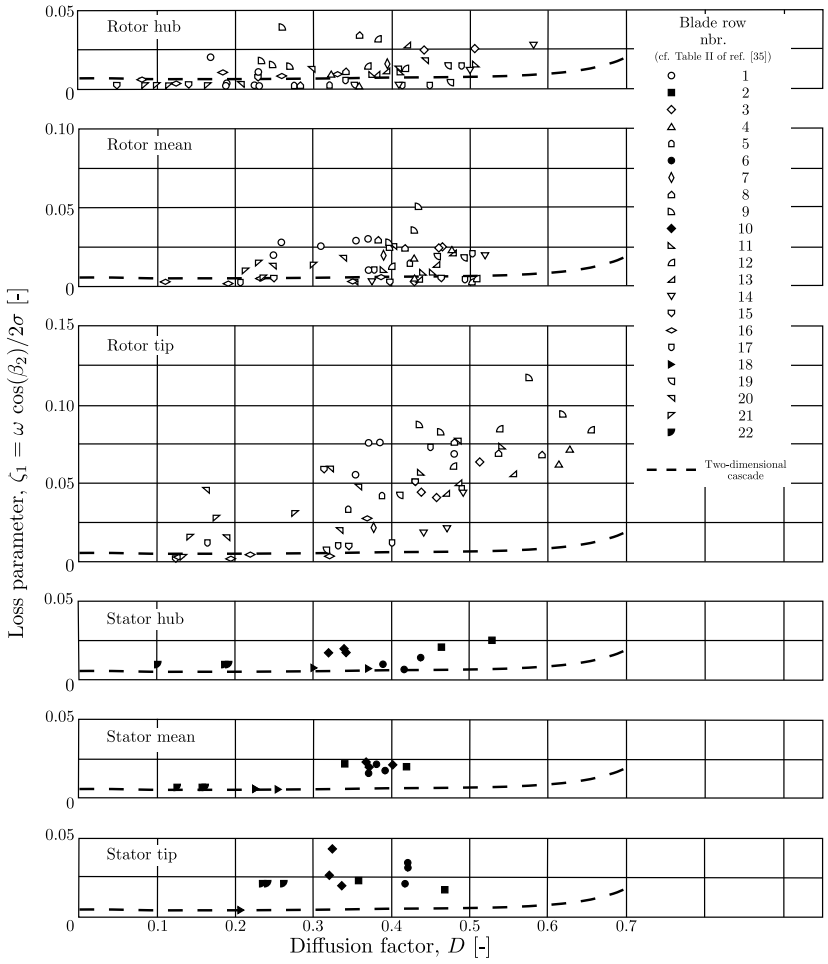


Figure 2.41: *Variation of loss parameter ζ_1 $(= \omega \cos \beta_2 / 2\sigma)$ as a function of diffusion factors for linear and annular cascade tests [35]*

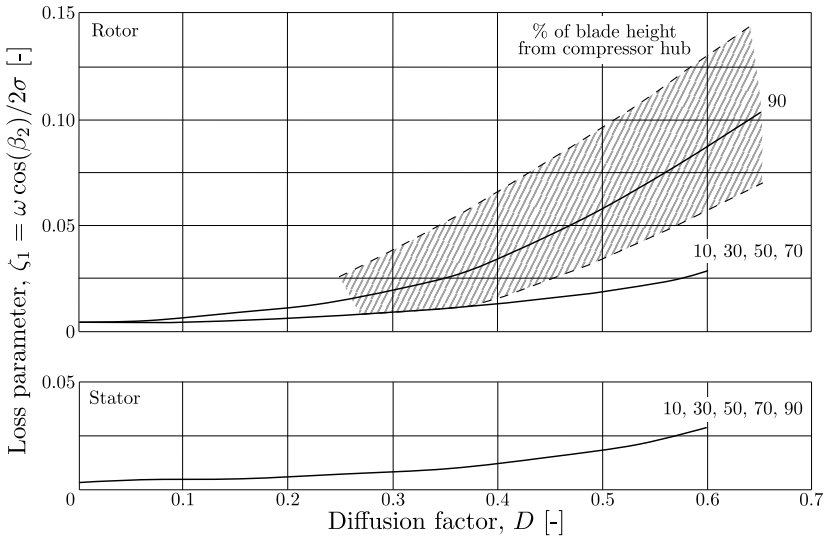


Figure 2.42: *Variation of ζ_1 with diffusion factor from annular cascade tests (fitted curves) [35]*

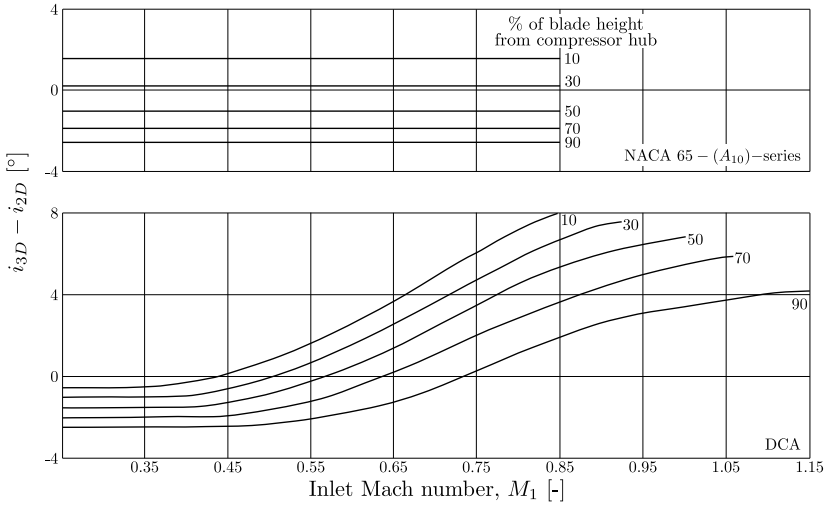


Figure 2.43: *Variation of optimum incidence between 2D and 3D tests versus Mach number (fitted curves) [35]*

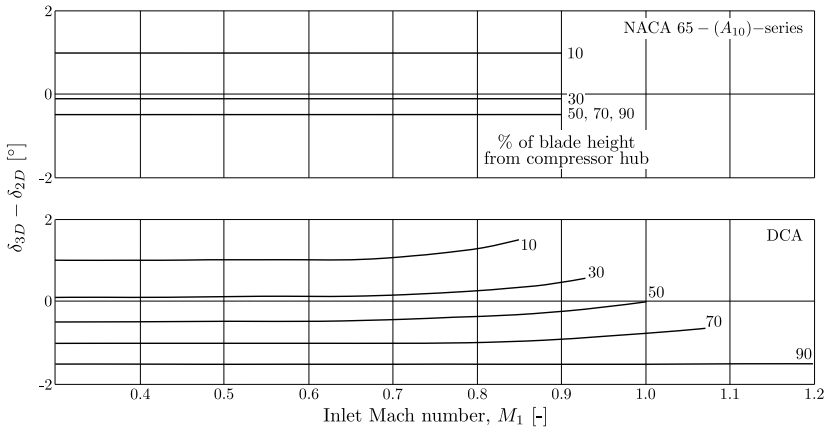


Figure 2.44: *Variation of deviation at optimum incidence between 2D and 3D tests versus Mach number (fitted curves) [35]*

Studies dedicated to the blade number effect on a full compressor stage are very rare since such investigations are very expensive. However, some examples may be found in the literature. In 1952, Standahar and Serovy [36] investigated the effect of changing the solidity by varying the blade number on a fan stage. The performance at nominal speed is shown in Fig. 2.45.

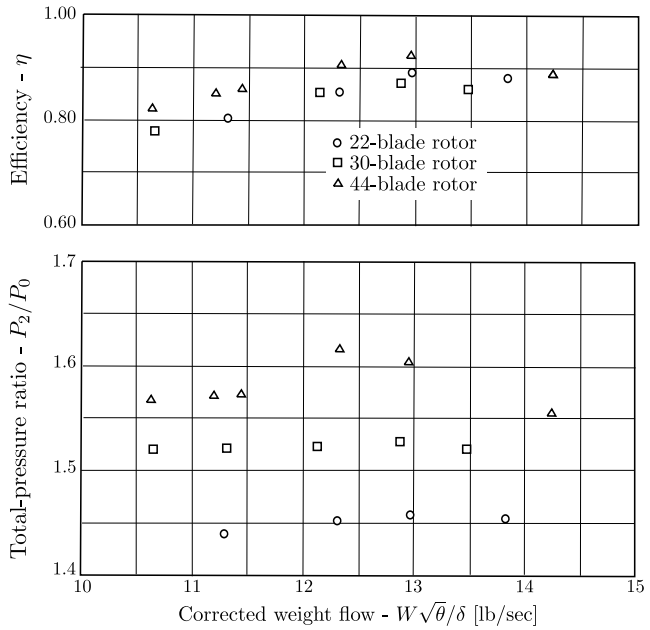


Figure 2.45: *Efficiency and pressure ratio for three rotors with different number of blades at nominal speed [36]*

The pressure ratio increased as solidity was increased. This trend was predictable by cascade test results as the turning increased for high solidity. For the same throttle condition, the high solidity compressor operated at lower mass flow. The mass-flow shift comes from higher blockage when more blades are mounted in the machine. The efficiency evolution is rather unexpected. Indeed, the efficiency was bigger for the high solidity while theoretically more blades induce more friction and more losses. This was confirmed a few years later by Schwenk and Lewis ([26] and [27]) or Heilmann et al. [25]. It could not be explained at the time but it is a typical result for a fan with supersonic rotor-tip relative Mach number.

In 1955 and 1956, Schwenk and Lewis ([26] and [27]) highlighted three-dimensional effects of the solidity on two different compressors. These compressors were representative of fan or low-pressure compressor designs with a global pressure ratio of $1.3 \sim 1.4$ and with sonic or slightly supersonic inlet Mach numbers at the tip. The main differences between both compressors are the mean chord length and the tip-section camber angle. Both compressors were designed with DCA blades. On each of these compressors, three levels of solidity were tested. Starting from a design tip solidity around 1.0 (common design practice at the time), they removed some blades to get tip solidities below 1.0. As expected, they observed that the pressure ratio decreased when solidity decreased. Moreover, since the blockage increased with the number of blades, the high solidity rotor worked at lower mass-flows. Regarding efficiencies and total pressure losses, an unexpected evolution was measured since the low solidity rotor, supposed to give the least friction losses, showed the poorest efficiency. Results are displayed in Fig. 2.46 for the compressor studied in [26]. At 80% of design speed, the efficiency is the same for the three rotors. At full speed, the efficiency falls in the tip region and the high solidity rotor gives the best efficiency. The effect of solidity is thus varying from hub to tip. The same behavior appeared on both compressors.

One explanation can be the suction-side Mach number which, as shown in the sketch of Fig. 2.47, is bigger when the pitch distance increases. In that situation, a stronger shock takes place and higher losses appear. This conclusion is supported by the work of Heilmann et al. mentioned earlier (cf. Fig. 2.32). This is also confirmed in [26] and [27] as for lower rotating speeds, the relative inlet Mach number becomes subsonic again and the high-loss level witnessed for the low solidity rotors disappeared. This underlines the importance of both compressibility and three-dimensionality effects in the behaviour of transonic compressors.

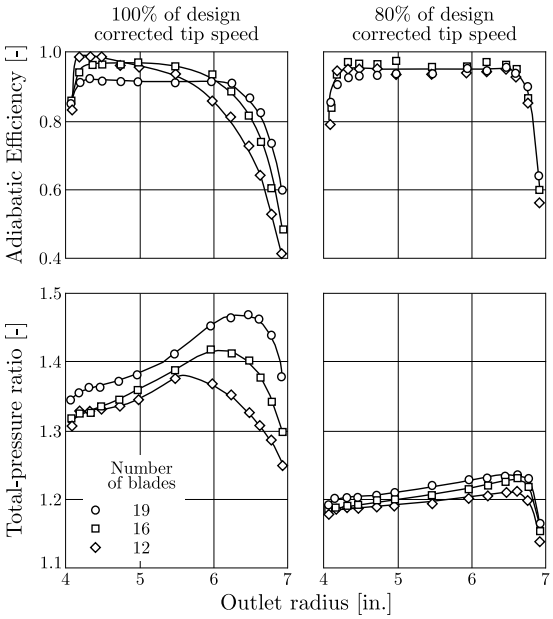


Figure 2.46: *Efficiency and pressure ratio distributions along the span for three rotors with different number of blades at nominal speed (a) and* 80% *of nominal speed (b) [26]*

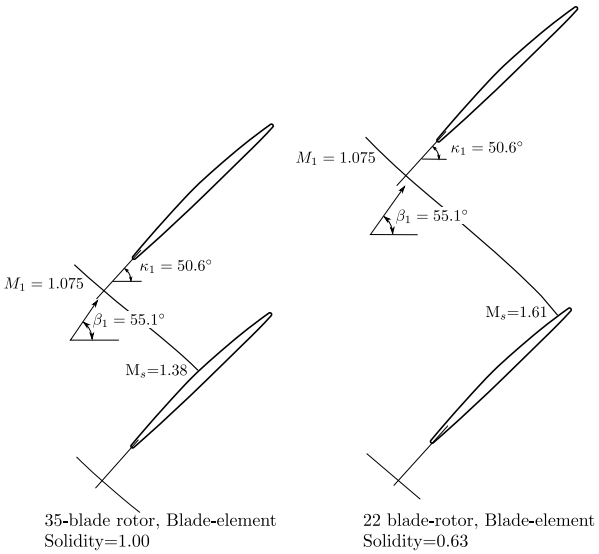


Figure 2.47: *Supersonic flow pattern through a cascade for two different solidities[27]*

Schwenk and Lewis ([26] and [27]) also noticed different stall patterns depending on the solidity. By performing hot-wire measurements (at low speed only), large non-periodic fluctuations were observed for the low solidity rotors. The high-solidity rotor displayed low amplitude periodic fluctuations which can be associated to a typical rotating stall phenomenon. Moreover, these low amplitude oscillations were observed at lower mass-flow than with the low-solidity compressors which illustrates the stability enhancement provided by high solidity rotors.

In 1960, Turner and Burrows [37] performed compressor tests at low speed where the difference between three solidity levels clearly appears. Results are shown in Fig. 2.48. The efficiency and the pressure ratio evolutions with solidity are predictable from cascade correlations: the higher the solidity, the higher the pressure ratio and the lower the efficiency. Nonetheless, the choking behavior of the high solidity rotor does not follow this trend. At choke, the high solidity rotor delivers a bad pressure rise and reaches low efficiency level compared to the other rotors. At high mass flow, the efficiency of the low solidity rotor starts to fall and it enters into surge before the others.

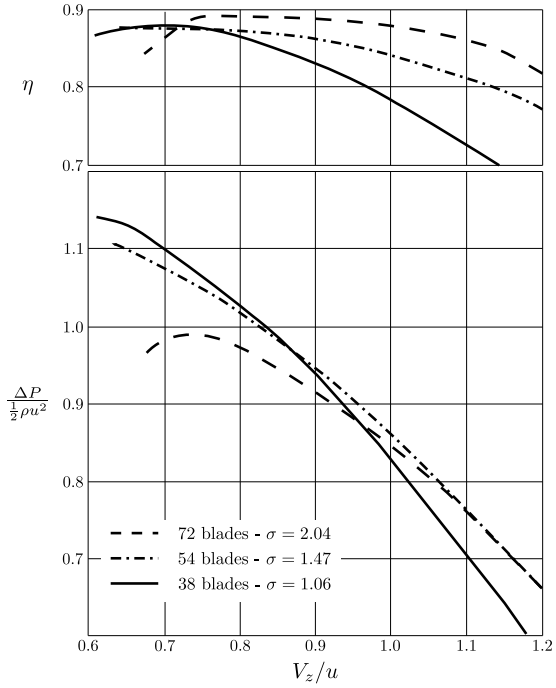
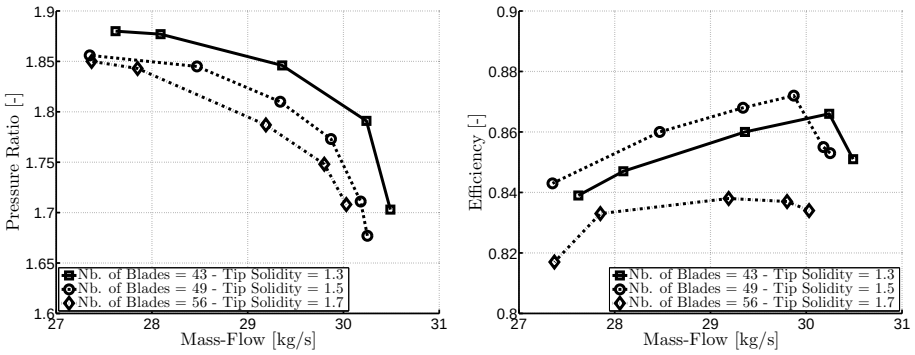


Figure 2.48: *Performance and comparison of three rotors with different pitches[37]*

Moore et al. studied at NASA the effect of the solidity on three different compressors ([38], [39] and [40]). They represent a typical fan stage with high mass-flow, high pressure ratio of 1.8 (uniform) and rotor-tip inlet relative Mach number of 1.4. Based on the same design target, rotors having tip solidities of 1.3, 1.5 and 1.7 were tested. Results were reported respectively in [38], [39] and [40] and are gathered in Fig. 2.49 to allow a convenient comparison. The results are quite surprising since the high solidity rotor demonstrates the worst performance in terms of efficiency, pressure ratio and also stall margin. The authors commented in [40] that these bad results mainly came from a bad design and underestimated stator losses.



(a) **(b)**

Figure 2.49: *Effect of solidity on rotor performance (results from NASA experimental investigations [38], [39] and [40]):(a) Pressure ratio and (b) adiabatic efficiency as a function of mass-flow*

In 1979, a NASA report from Britsch et al. [41] summarized the results performed on 14 different compressors. The solidity influence was examined as well as the aspect ratio and design diffusion factor. Focusing on the solidity effect, some of their results are shown in Fig. 2.50 (a) and (b) for two different diffusion levels and three aspect ratios. It is observed that reducing the solidity (by removing blades) at constant aspect ratio mainly shifts the performance curves to higher mass-flows, increases the maximum efficiency and decreases the pressure ratio. It is also interesting to mention that the performance at choke was significantly deteriorated for the high solidity rotors. At the end, the increase of solidity contributes to decrease the stall margin since the gain in the low mass-flow region is not big enough to compensate the reduction of operating range in the high mass-flow region.

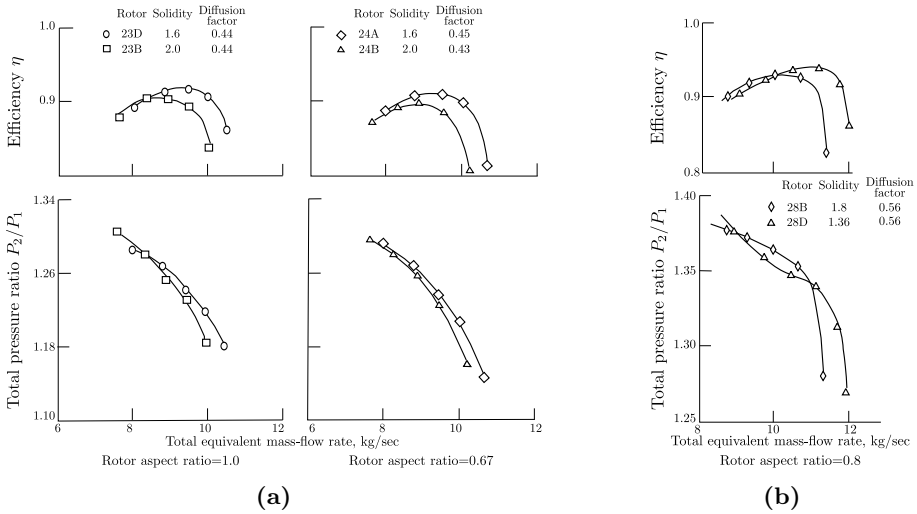


Figure 2.50: *Effect of solidity on rotor performance (Britsch and al. [41]):(a) Diffusion factor ≈ 0.44 , rotor aspect ratio of 1 and 0.67; (b) Diffusion factor of 0.56 , rotor aspect ratio of 0.8*

Although no exhaustive study of the influence of solidity on compressor performance and stability has been found, some rules can be highlighted (admitting some exceptions and making a distinction between rotors and stators):

1. the higher the solidity, the higher the rotor pressure ratio (improved guidance);

2. the higher the solidity, the lower the rotor efficiency (increased friction);

3. the higher the solidity, the higher the stator total pressure losses (increased friction);

4. the higher the solidity, the higher the stall margin (as the loading decreases).

Somewhere between very high solidities that induce high friction losses and very low solidities that lead to poor guidance, stability margins and also sometimes very high losses due to high diffusion, an optimum most probably exists. It is the trade-off between efficiency and stability that makes the choice of the solidity very difficult for a compressor. To maximize both efficiency and stability margin, new solutions must be considered. A very good example is the work of Houghton and Day [42] which shows that the use of casing treatment can help to delay the inception of stall caused by a solidity decrease for a tip critical rotor. Although the losses usually increase when casing treatments are implemented, the efficiency loss was compensated by the blade count reduction.

To conclude this section, it must be emphasized that most of the correlations that are reported in this thesis were established between 1950 and 1965. Since then, similar experimental investigations have been most probably carried out by engine manufacturers in order to improve those empirical models but, it is strongly believed that, due to confidentiality reasons, the results of such studies remained unpublished.

2.3 The optimum solidity

As mentioned in the previous section, between a high number of blades inducing high friction and a low number of blades inducing high diffusion and separation, an optimum solidity should exist. This section is dedicated to the definition and selection of an optimum solidity for a given compressor design. The choice must be done very early in the design process, at the level of the meridional design, which makes the choice of solidity very crucial and difficult.

Two methods are presented in this section. The first one addresses theoretical and empirical methods that do not rely on any external optimization tool. Those methods will be called *Direct Methods*. It means that from a given velocity triangle, the designer can directly obtain an optimum solidity. This is a fast and very practical solution for the designer and, before the introduction of computer aided design, this technique was used by all engine manufacturers. The second method is based on the use of optimization tools coupled with meridional design programs in order to get the best solidity in terms of pressure ratio, efficiency and, if off-design correlations are implemented, stability margin. Nowadays, the use of optimization tools has become very common as it is fast and robust but, in order to understand the results of a solidity optimization, it is essential to summarize the methods developed by Howell, Zweifel or McKenzie and highlight the main factors that affect the selection of the optimum solidity.

2.3.1 Direct methods

The upstream and downstream conditions are known from an isentropic radial equilibrium calculation. Based on that first guess, the designer tries to select the best solidity to achieve the desired turning and pressure ratio while keeping a low level of losses. After choosing a solidity, the designer refines the meridional calculation by taking loss correlations into account (non-isentropic radial equilibrium) and adapts the design. During this iterative process, the solidity is still a free parameter that can be modified to match the design requirements. To help the designer in this task, different methods exist in the literature. Unfortunately, none of those are consistent with each other and, most of the time, they all lead to different results.

The methods of Howell [2] and Zweifel [3] were previously presented in Eq. (2.3) and Eq. (2.10) respectively. Imposing the diffusion factor can also

give a first guess of the solidity using Eq. (2.13) but, contrary to Zweifel, no optimum diffusion factor was highlighted by Lieblein.

Another possibility is to use the Lieblein or Koch and Smith loss correlations to find the optimum solidity corresponding to the minimum losses. This was done in Fig. 2.25 and Fig. 2.26. It showed that the resulting optima usually sit at very high diffusion factors that are not realistic for design applications. Another example comes from Hearsey [43]. The same method is used relying on the loss parameter of Eq. (2.31).

$$\frac{\omega \cos(\beta_2)}{2\sigma} \left(\frac{\cos(\beta_2)}{\cos(\beta_1)} \right)^2 \tag{2.31}$$

From the comparison of Fig. 2.18 and Fig. 2.20, Hearsey considered this loss parameter to be a better estimate of the wake momentum thickness since it captures the growth of the momentum thickness at high diffusion factor. Hearsey then expressed the loss parameter as a function of the diffusion factor:

$$\frac{\omega \cos(\beta_2)}{2\sigma} \left(\frac{\cos(\beta_2)}{\cos(\beta_1)} \right)^2 = 0.004 \; e^{6.16773 \; D^{1.436794}} \tag{2.32}$$

The optimum solidity is defined as the solidity for which the losses are minimum. Mathematically, it corresponds to:

$$\sigma_{opt} =: \{\sigma \text{ such as } \frac{\partial \omega}{\partial \sigma} = 0\} \tag{2.33}$$

In the case of a rotor, and considering a possible change of radius, Hearsey gives the solution of the optimization problem of Eq. (2.33) by the following implicit equation[4]:

$$\sigma_{opt} = \frac{8.861805 \; \Delta(rW_\theta)}{r_m \; W_1} \; D_{opt}^{0.436794} \tag{2.34}$$

where D_{opt} is the diffusion factor calculated with σ_{opt} and the standard definition of the diffusion factor recalled in Eq. (2.35).

$$D = (1 - \frac{V_2}{V_1}) + \frac{\Delta V_\theta}{2V_1\sigma} \tag{2.35}$$

The optimum solidity can then be easily calculated knowing the flow angle β_1 and β_2. This is plotted in Fig. 2.51. Unlike the resuts of Fig. 2.25 or Fig. 2.26, the optima sit at acceptable diffusion factors. The drawback of this method is that it only takes into account viscous losses. It can give a good first guess of solidity as long as no shock develops in the blade passage. This approach is also used by Liu [44] but is based on the equivalent diffusion ratio.

[4]The derivation of this implicit expression is not detailed by Hearsey in [43] and remains questionable to the author. However, the method and its results seem valuable.

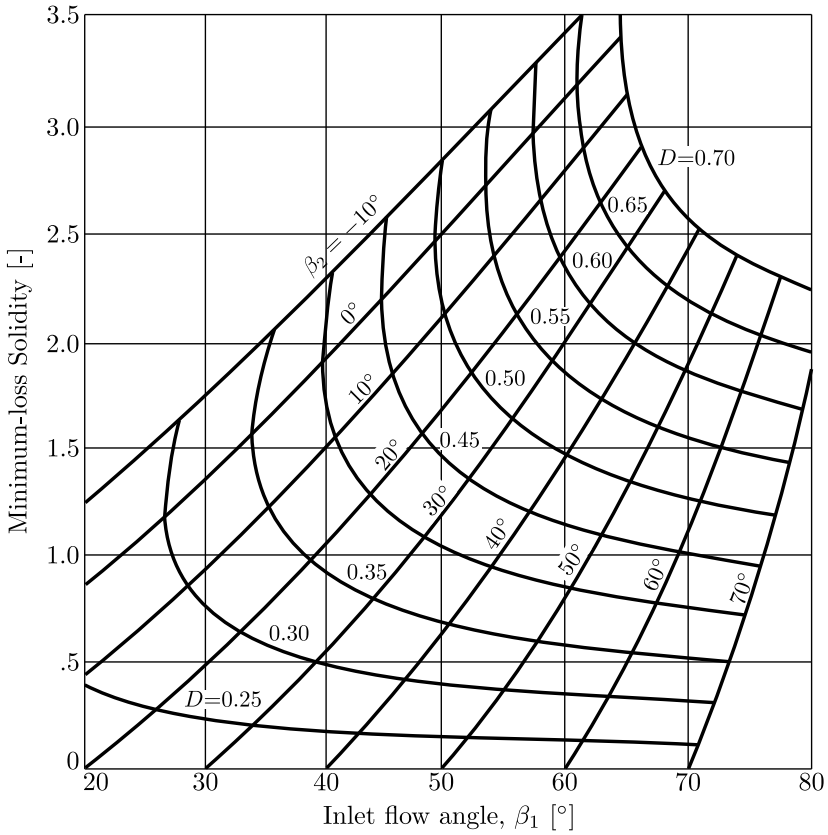


Figure 2.51: *Optimum solidity for minimum losses as a function of inlet and outlet flow angles [43]*

Another method is presented by McKenzie [45] to select the optimum solidity for fan blades. Analyzing previous fan test results, he indicated that the efficiency is linked to the ideal static pressure rise and to the pitch-chord ratio. The ideal static pressure rise is defined as:

$$C_{p_i} = \frac{p_{s_2} - p_{s_1}}{1/2\ \rho_1 W_1^2} = 1 - \frac{\rho_2}{\rho_1}\left(\frac{W_2}{W_1}\right)^2 \tag{2.36}$$

The results are presented in Fig. 2.52 where the optimum pitch-chord ratio (in terms of maximum efficiency) appears to be a linear function of the ideal static pressure rise given by:

$$s/c = 9(0.567 - C_{p_i}) \tag{2.37}$$

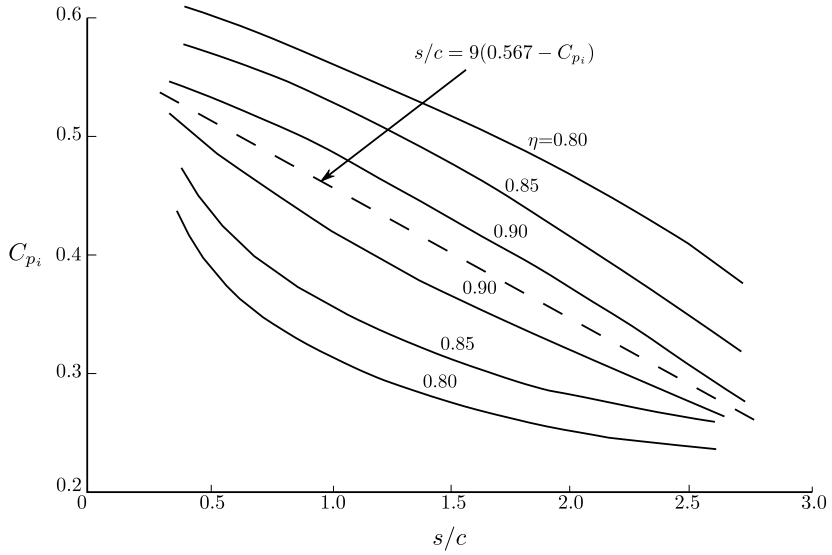


Figure 2.52: *Efficiency contours as a function of the pitch-chord ratio s/c $(= 1/\sigma)$ and the ideal static pressure rise C_{p_i} [45]*

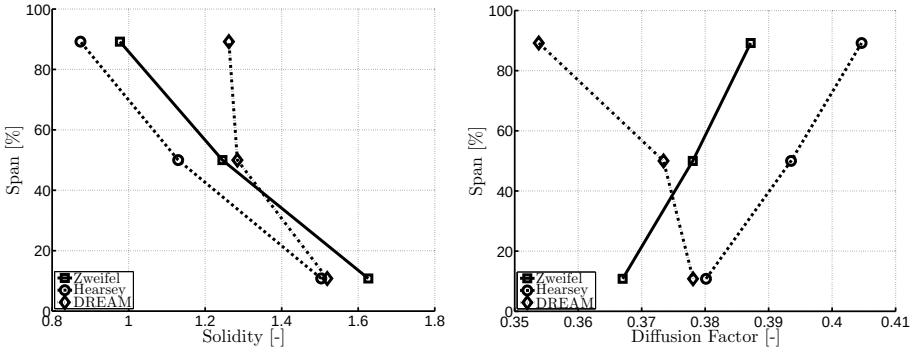
As an example, different optimum solidities have been calculated with the methods presented above. Howell's (Eq. (2.3)), Zweifel's (Eq. (2.10)), Hearsey's (Eq. (2.34)) and McKenzie's (Eq. (2.37)) optimum solidities are compared in Table 2.5 for given inlet and outlet rotor velocity triangles coming from the DREAM project compressor (cf. Appendix A). Results are compared with the actual rotor solidity of the DREAM compressor.

	OPTIMUM SOLIDITIES					
	SPAN	HOWELL	ZWEIFEL ($\psi = 0.9$)	HEARSEY	MCKENZIE	DREAM BOOSTER
σ	HUB	1.76	1.63	1.50	0.54	1.52
	MID	0.90	1.25	1.13	0.61	1.28
	TIP	0.49	0.98	0.87	0.59	1.26

Table 2.5: *Solidity recommendations from Howell's, Zweifel's, Lieblein's, Hearsey's and McKenzie's methods*

In Table 2.5, all the methods give different results. McKenzie's solidity seems to lie far from the state-of-the-art. According to McKenzie [45], this method

is more to be applied for design of highly staggered fan blades. Howell is also giving unrealistically low values at the tip. Zweifel and Hearsey show better agreement with the state-of-the-art. In that prospect, it is interesting to compare the resulting solidities and diffusion factors of Hearsey and Zweifel methods with the distributions of the DREAM project booster. In Fig. 2.53, the optimum solidities at the three span locations are shown in Fig. 2.53 (a) and the corresponding diffusion factors in Fig. 2.53 (b).



(a) **(b)**

Figure 2.53: *Zweifel and Hearsey optimum σ and diffusion distributions compared with the distributions of the DREAM project booster: (a) Optimum solidity and (b) Diffusion factor (at optimum solidity)*

At the hub, both methods give reasonable values of solidity and an acceptable level of diffusion. The high solidity at mid span may be reduced by allowing higher loading ($\psi > 1$). By following Hearsey's method, the designer may overload the blade at certain span locations. The loading cannot be controlled because Hearsey's method optimizes the solidity for minimum losses, disregarding the level of diffusion. By imposing the Zweifel coefficient or the diffusion level, the loading can be adjusted depending on the experience of the designer but it may not sit at minimum loss conditions.

The analysis of Fig. 2.53 reveals that the solidity can neither be dissociated from the loading nor the losses. Both considerations must be taken into account and be coupled by allowing to decrease the level of losses while keeping loading constraints in terms of diffusion factor or Zweifel factor. This can be done through an optimization process that is exposed in the following section.

2.3.2 Meridional optimization

Coupling any meridional design program or any throughflow solver to an optimization tool, one can find the optimum compressor geometry in terms of pressure ratio and/or efficiency and/or stall margin under given constraints. Good examples are given by Massardo et al. [46], Joly et al. [47] or Teichel et al. [48]. They illustrate that any geometrical (e.g. solidity, channel height) or mechanical (e.g. RPM) parameters of the compressor can be optimized at the level of the meridional design. More particularly, Joly et al. [47] and Teichel et al. [48] used the VKI meridional calculation tool and the VKI optimizer CADO (Verstraete [49]). The latter relies on an Evolutionary Algorithm. Such a method firstly requires the evaluation of the performance of a population and is then based on Darwinian evolution. From the first population, the best individuals are chosen and, through mechanisms such as cross-over or mutation, the population evolves and the optimization process takes place.

A very good example of a meridional solver is described by Creveling and Carmody in [50] and [51]. This code has been rewritten and improved at VKI. It is based on the Non-Isentropic Radial Equilibrium equation. Some recent uses and validations of this program are described by Hurlbrink [52]. Currently, this tool referred to as *ACPreDesign*, does not provide off-design predictions. A specific chapter (Chapter 5) is dedicated to the use of this tool in the framework of the optimization of the solidity. Examples of meridional optimizations using ACPreDesign can be found in [47] or [48].

Although meridional optimization is very appealing, any radial-equilibrium solver relies on empirical correlations to provide an estimate of the total pressure losses generated by a blade row. It is thus essential to ensure the correlations are trustworthy. Another possibility is to include typical uncertainty within the design process by introducing uncertainty quantification methods. The specific theoretical background for those techniques are very well exposed by Iaccarino [53] but will be summarized in Chapter 5. Coupling the CADO optimizer with uncertainty quantification, it is possible to perform optimization under uncertainty in order to converge to a *robust* design. It has been applied on the optimization of the solidity of the DREAM project booster (cf. Appendix A) in Chapter 5.

Chapter 3

Numerical Investigation

3.1 Motivation

In order to get an estimate of the losses or of the flow turning, empirical inputs are still required in every mean-line or throughflow design tool. The selection and optimization of solidity will rely on those correlations. It is then very important to ensure that the empirical data can be applied to the design problem of interest. In particular, it is must be checked that the correlations are still up-to-date considering the state-of-the-art controlled diffusion blade designs and remain applicable at subsonic compressible Mach numbers (from 0.40 to 0.70). Moreover, as the CFD capabilities are constantly improving and will remain the current practice in compressor design, it seems essential to compare the CFD results with the correlation data.

Focusing on solidity variations, both numerical and experimental investigations were carried out in this thesis. The research aims at validating and updating the low-speed correlations both with numerical simulations and high-speed cascade tests in the VKI-C3 facility.

In that framework, the current chapter is focused on the numerical investigation of the impact of solidity on linear compressor cascade performance. The software used is FINE/Turbo from Numeca International. As the purpose is to update loss and deviation correlations for current blade designs, the study is performed on a state-of-the-art controlled diffusion blade (CDB) representative of a low-pressure compressor stator profile. But, besides the CDB, a standard double circular arc (DCA) profile has also been considered. The choice of the latter is explained by the extensive amount of literature about this geometry that enables to validate the CFD predictions.

The geometry and numerical model are presented. To build a numerical database to be compared with the correlations, the calculations were performed for both the controlled diffusion airfoil and the DCA blade at 3 solidities, 13 incidences (from choke to stall) and 4 inlet Mach numbers. From the results of the simulations, the issues of optimum incidence, deviation, losses and diffusion factor are discussed and compared with the literature. The blade isentropic Mach number distributions are also given. Finally, the issue of the operating range is approached.

3.2 Geometrical model

Two blade profiles have been set-up into a linear cascade configuration. The first geometry comes from Techspace Aero. It is a controlled diffusion blade that is representative of a state-of-the-art low pressure compressor stator profile while the second is a standard DCA blade. Both profiles are displayed in Fig. 3.1.

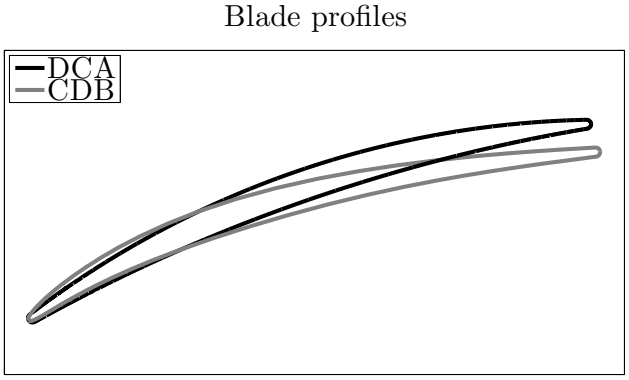


Figure 3.1: *Investigated CDB and DCA profiles (not to scale)*

The CDB thickness and camber distributions are the results of an optimization process. Since the camberline is not a circular arc like DCA blades or the NACA 65 series referenced in the literature, an easy definition of the camber angle as $\phi = \kappa_1 - \kappa_2$ for a DCA (cf. Fig. 2.1) is not possible. The blade parameters that have been kept constant are the aerodynamic chord c, the maximum thickness-to-chord ratio t_{max}/c and both inlet and outlet blade metal angles, i.e. the metal turning $(\kappa_1 - \kappa_2)$. As a consequence of this choice, the stagger angles γ are different as well as the achieved flow turning. The blade parameters are summarized in Table 3.1.

	CDB	DCA
Chord	33.09 mm	
t_{max}/c	5%	
$\kappa_1 - \kappa_2$	28.3°	
γ	16.5°	19.3°
σ	1.38, 1.24, 1.10	
Leading edge geometry	Elliptical	Circular

Table 3.1: *CDB and DCA geometrical parameters*

A big difference between the two profiles also lies at the leading edge as the CDB has an elliptical nose and the DCA has been kept circular to match the

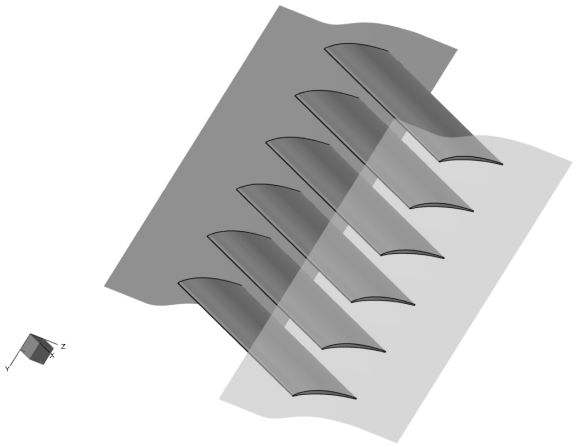


Figure 3.2: *Picture of the linear cascade model*

correlations. The strong impact of the nose geometry is very well described by Wheeler et al. [54] and Goodhand and Miller [55]. Circular noses may induce velocity spikes that deteriorate the performance while elliptical or optimized nose shapes smooth the velocity profiles and improve the performance of the profile, in particular at off-design conditions.

Finally, both blades have a span of 100 mm to match the dimensions of the high-speed cascade facility at VKI. A picture of the controlled diffusion profile within its cascade configuration is displayed in Fig. 3.2. Given that the chord and the blade height are not changing, the aspect ratio ($h/c = 3.02$) is kept constant as well as the chord-based Reynolds number at a given Mach number.

3.3 Numerical Model

The FINE/Turbo software package (Numeca International) has been used both for meshing the domain and solving the flowfield by means of the Navier-Stokes equations. Within this investigation, only fully-turbulent steady RANS computations are considered.

Total pressure and temperature conditions and flow angle are imposed at the inlet and static pressure at the outlet (set to the standard atmospheric pressure level of 101325 Pa). The solidity is only varied by changing the pitch in order to keep the chord-based Reynolds number constant at a given inlet Mach number (Re$\approx$ 320.000 at $M_1 = 0.4$ and Re$\approx$ 540.000 at $M_1 = 0.7$). In the pitchwise direction, periodic boundary conditions are applied corresponding to the assumption of an infinite number of blades.

The cascade configuration has been considered in view of the measurement campaign. Therefore, as it can be seen in Fig. 3.2, the end-walls have not been

removed. As a consequence, secondary flows and corner separation are growing as the incidence increases.

The low Reynolds $k-\varepsilon$ Yang-Shih turbulence model has been used. A turbulence intensity of 1% is set at the inlet of the computational domain to match the inlet conditions of the experimental facility C3 of the VKI (Mesbah et al., 2009, [56]). For the spatial discretization, the Jameson central scheme has been selected and a 4-stage Runga-Kutta method combined with an implicit residual smoothing phase (Zhu et al. [57]) has been used for the time discretization. To fasten the convergence, a local time stepping approach and a multigrid strategy are by default considered. The choice of numerical scheme and turbulence model has mainly been driven by the current practices of Techspace Aero and previous work performed at VKI.

However, before entering the core of the subject, the mesh sensitivity analysis, the choice of the turbulence model and the numerical scheme must be addressed. Although the turbulence model and numerical scheme are fixed, it is essential to quantify and assess the variability of the results with respect to those parameters. The originality of the work also resides in the comparison of the observed variability of the results with typical experimental uncertainties. This study has been extensively addressed by Resmini [58] as well as Sans et al. [59] and the main results are summarized in the following sections.

3.3.1 Expected experimental uncertainty

In order to determine if some numerical effects are significant and measurable, a preliminary quantification of the experimental uncertainty has been carried out (at an average Mach number of 0.5).

Typical uncertainty values (given within a 95% confidence level) taken from many experimental campaigns conducted at VKI with similar probes and measurement chains are indicated in Table 3.2. However, the uncertainty values of Table 3.2 do not represent the best practice but should be considered as guidelines to assess the quality and the variability of the numerical results. The expected uncertainties on the derived values, such as Mach number, total pressure losses and diffusion factor are obtained by a typical uncertainty propagation method ([14], [60]).

Measurements	P_0, P_s	$\pm$ 0.5	[mbar]
	α	$\pm$ 0.3	[deg]
Derived quantities	M_2	$\pm$ 0.001	[-]
	ω	$\pm$ 0.004	[-]
	DF	$\pm$ 0.003	[-]

Table 3.2: *Reference values for typical measurement uncertainties* - $M_1 = 0.5$

3.3.2 Mesh sensitivity

Great care has been dedicated to the mesh generation with Autogrid5 [61] in order to reach a grid-independent solution. The mesh domain extends from one chord upstream of the leading edge to one chord downstream of the trailing edge and includes the whole blade passage. The structured mesh is composed of hexahedral cells, organized in an O4H-topology (Fig. 3.3).

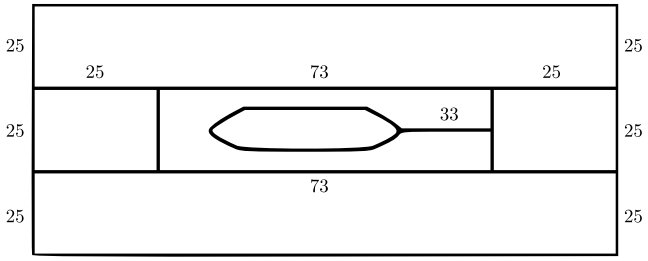


Figure 3.3: *Blade-to-blade O4H grid topology*

The impact of the mesh characteristics on the cascade performance has been assessed considering the expected uncertainty quantification presented in Table 3.2. The cell size at the wall of $1\mu m$ has been set to ensure a y^+ around 1. The grid independence has been verified for different turbulence models (considering $i = 0°$, $M_1 = 0.5$, $Tu = 1\%$) on 4 different grids. The turbulence models are: Balwin-Lomax, Spalart-Allmaras, low Re $k-\varepsilon$ Yang-Shih and the $k-\omega$ SST. The main features of the 4 meshes are given in Table 3.3, together with some synthetic quality information such as the minimum skewness angle or maximum expansion ratio (ER). The skewness angle or the orthogonality measures the angular variation between two adjacent cells. Values as close as possible to 90° (meaning that the cells have orthogonal faces) are preferred not to amplify some discretization errors and to ensure a good convergence. The expansion ratio characterizes the variation of the size of two neighboring cells and should be as close as possible to 1.0 (i.e. constant cell size). High values of expansion ratio may lead to large errors in presence of strong gradients as it may be encountered in the vicinity of the walls.

	Nbr. of grid points	Nbr. of grid levels	Min. Skewness	Max. ER
A	$0.33\,10^6$	4	44.0°	2.7
B	$\mathbf{0.78\,10^6}$	**3**	**48.2°**	**1.6**
C	$1.24\,10^6$	3	48.5°	1.5
D	$1.75\,10^6$	3	47.9°	1.5

Table 3.3: *Grid characteristics*

Typical convergence curves are shown in Fig. 3.4 for the mesh B with the $k-\varepsilon$ turbulence model. The convergence may be assessed in terms of residuals, inlet and outlet mass-flows or total pressure recovery ratio. In Fig. 3.4, the mass-flow and the total pressure ratio convergence curves are shown at $M_1 = 0.5$ for $i = 0°$ and $i = 10°$.

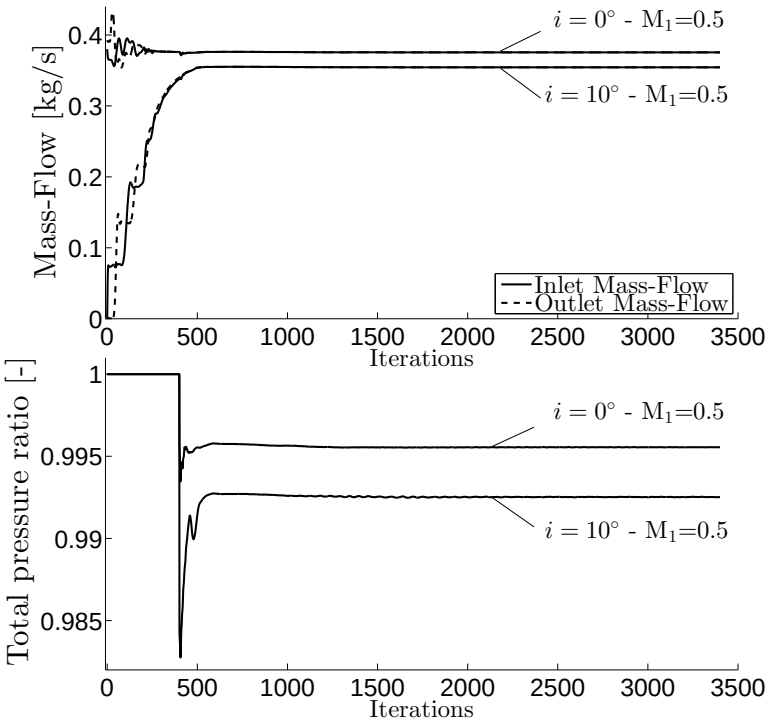


Figure 3.4: *Mass-flow and total pressure ratio convergence curves for mesh B at* $M_1 = 0.5$ *for* $i = 0°$ *and* $i = 10°$

Fig. 3.5 shows the dependence of the loss parameter, the outlet flow angle and the outlet Mach number on the mesh resolution. The expected uncertainty band is also indicated for each parameter. An asymptotic behavior is clearly noticeable and it is possible to remark that the variations of every quantity for meshes B, C, D are always below the uncertainty band considered.

Regarding the choice of the minimum cell size, the y^+ distributions shown in Fig. 3.6 for the mesh B and at $i = 0°$ and $M_1 = 0.5$ confirm that a first cell size of $1\mu m$ satisfies the requirement of having a y^+ around 1 along the blade profile. Similar distributions are obtained for all the meshes since they all have the same first cell size and that the mesh clustering of Autogrid5 is optimized to keep a low expansion ratio (≈ 1.1) at the walls rather than in the middle of the blade passage.

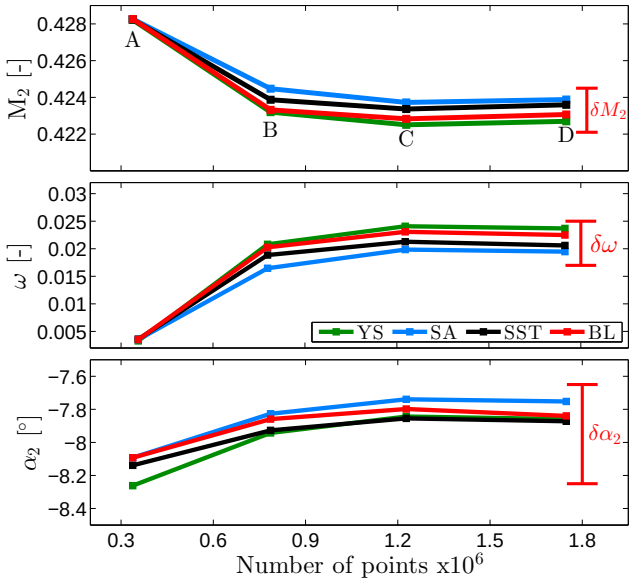


Figure 3.5: *Outlet Mach number, outlet flow angle and losses grid independence at* $i = 0°$ *and* $M_1 = 0.5$

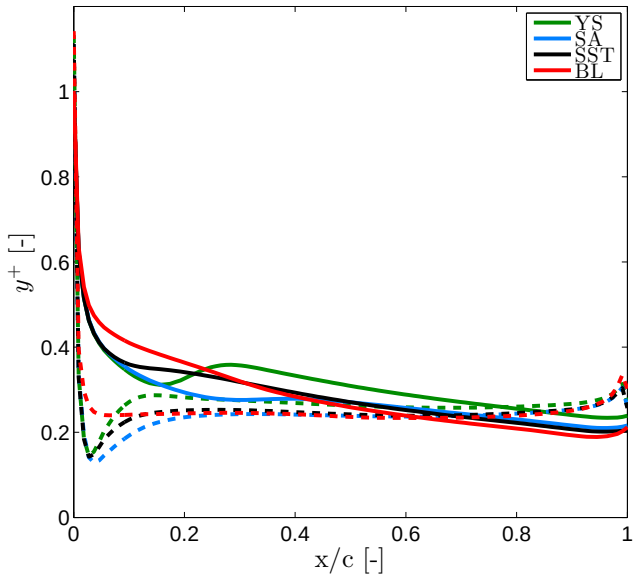


Figure 3.6: y^+ *distributions for various turbulence models at mid-span on the blade suction (plain line) and pressure (dashed line) sides (mesh B -* $i = 0°$ *and* $M_1 = 0.5$*)*

As the investigation covers a wide incidence range, the considerable differences of flow topology can be diversely affected by the grid quality. Hence, as suggested by Biesinger et al. ([62], 2013), the mesh independence of the solution has been verified in off-design conditions with the $k-\varepsilon$ turbulence model. No substantial variation has been noticed in terms of losses, outlet flow angle or Mach number considering meshes B and D from Table 3.3 at $i = 10°$. The variation of the last converging incidence does not exceed 0.5°.

On the basis of these results, mesh B has been considered as the best candidate to perform the investigation since it permits to limit the grid error below the threshold value while requiring a reduced amount of resources. The latter argument is not negligible to the extent that, in order to build a correlation database, a very large amount of computations is expected (> 500).

It must also be mentioned that, in the framework of this mesh sensitivity analysis, 15 meshes have been studied in order to evaluate the effects of the minimum cell-size at the solid surfaces and the discretization in both blade-to-blade and spanwise directions. More details can be found in [58] (Resmini, 2013).

3.3.3 Turbulence model effects

To perform Reynolds-averaged Navier-Stokes (RANS) simulations, it is necessary to be able to compute the Reynolds stress tensor $\overline{u_i' u_j'}$ to close the Navier-Stokes system of equations. This problem also known as the *closure problem* requires the introduction of models in order to be solved. Among those models, a difference can be made between first order and second order closure models. First order models directly relate the Reynolds stresses $\overline{u_i' u_j'}$ to the mean flow velocities $\overline{u_i}$ while, in second order models, the unknown terms of the Reynolds stress transport equations are linked to the mean flow velocities as well as the Reynolds stresses. Second order closure models also known as Reynolds stress transport models have not been considered in this thesis but more details can be found in [63, 64].

All the turbulence models that have been used in this thesis are first order *eddy viscosity models*. They are based on the Boussinesq hypothesis which postulates that the momentum transfer due to turbulent eddies can be modeled by an eddy viscosity μ_t in analogy to the molecular viscosity μ from the Newtonian relationship between viscous stress and the strain rate. Those eddy viscosity models are isotropic and have the advantage to only model a single quantity, the eddy viscosity μ_t or the kinematic turbulent viscosity $\nu_t (= \mu_t/\rho)$.

A distinction can be made between algebraic, one-equation or two-equation models depending on the number of equations that are added to close the Navier-Stokes equations system.

In algebraic model, the eddy viscosity depends only on local average flow quantities. Different versions exist (cf. [63, 64]) but one of the most famous is the Baldwin-Lomax algebraic model [65]. Such models are not supposed to

be used in presence of strong adverse pressure gradient because, physically, the turbulent viscosity do not only depend on local quantities but rather on the whole history of the flow development. In order to overcome this issue, one- and two-equation models were developed.

In one-equation models, the eddy viscosity is computed either after solving a turbulent kinetic energy equation or by directly solving a transport equation for the kinematic eddy viscosity ν_t. This latter approach is the one developed by Spalart and Allmaras [66] which has become quite popular over the last years because of its robustness and its ability of dealing with complex flows.

Finally, in two-equation models, two closure equations are solved respectively for the turbulent kinetic energy k and either the turbulent kinetic energy dissipation rate ε or the specific dissipation rate ω. The eddy viscosity is then calculated with Eq. (3.1) where $C_\mu = 0.09$.

$$\nu_t = C_\mu \frac{k^2}{\varepsilon} = \frac{k}{\omega} \tag{3.1}$$

Five different turbulence models have been investigated in this section: the Balwin-Lomax [65] algebraic model, the Spalart-Allmaras [66] one-equation model, the low Re $k-\varepsilon$ Yang-Shih [67], the low Re $k-\varepsilon$ Launder-Sharma [68] and the $k-\omega$ SST [69, 70]. For all those models, no wall function has been considered and the viscous sublayer has been resolved ($y^+ \approx 1$ - cf. Fig. 3.6). While the $k-\varepsilon$ model are supposed to be used only in presence of small adverse pressure gradients, the $k-\omega$ SST is advised when strong pressure gradients or even flow separation are expected. Additional information about those models may be found in [58, 63, 64, 71].

In the framework of the whole numerical investigation, the low Re $k-\varepsilon$ Yang-Shih was chosen based on the current practices of Techspace Aero as well as previous experimental work performed at VKI. The selection of the turbulence model is very crucial and depends on the application. For turbomachinery design problems, each company may follow different recommendations based on the experimental database through which their code and turbulence model have been calibrated. It must be pointed out that the objective of this section is not to determine the best or the worse turbulence model but rather to investigate the variability in the results due to turbulence modeling from an user perspective. In particular, two specific issues have been investigated within this section:

- the impact of the turbulence model boundary conditions imposed at an incidence of 0° and an inlet Mach number of 0.5;
- the effect of turbulence model over the complete incidence range, considering an inlet turbulence intensity of 1% and inlet Mach number of 0.4 and 0.6.

According to the common practice in compressor design simulations and to prevent unexpected interaction between the transition model and the other features studied in this numerical investigation, the flow has been always considered fully turbulent. However, at the lowest inlet Mach number (=0.4), the

chord-based Reynolds number is around 320.000 and is very close to conditions where a boundary layer transition could still be observed.

3.3.3.1 Turbulence setting effects

Before looking at the effects of the turbulence model on the whole incidence range, it is important to analyze the effects of the turbulence boundary conditions that must be imposed for each model.

Using the Spalart-Allmaras model, the inlet turbulent viscosity ν_t must be given at the inlet boundary. The manual of FINE/Turbo [71] provides an indication for the ratio $\frac{\nu_t}{\nu}$ which should lay between 1 and 5 for internal flows. Similarly, Menter[72] suggests to use *small values* of $\frac{\nu_t}{\nu}$. The manual from another commercial software [73] recommends a more physical expression:

$$\nu_t = \sqrt{\frac{3}{2}} V_{ref} Tu\, \ell \tag{3.2}$$

which in fact relates the kinematic eddy viscosity to the turbulence intensity and the turbulence length scale.

Various definitions of the turbulence length scale can be found in the literature coming from both numerical and experimental research. The manual suggests to set it equal to one tenth of the hydraulic diameter, which is given in Eq. (3.3) for a rectangular inlet section with a height h and a width s.

$$D_h = \frac{4\, Area}{Perimeter} = \frac{2\, s\, h}{s + h} \tag{3.3}$$

Other commercial software [73] suggests $\ell = 0.07\, D_h$ but, in the scope of the present investigation, the value recommended by the manual of FINE/Turbo has been preferred.

Considering either Eq. (3.2) or FINE/Turbo recommendations, different orders of magnitude are obtained: $\nu_t \approx 10^{-3}$ m^2/s using Eq. (3.2) while $\nu_t \approx 10^{-5}$ m^2/s following the manual of FINE/Turbo. Therefore, to stress out the sensitivity of the results with respect to the choice of ν_t, 8 different values (cf. Table 3.4) have been tested, inside and outside the suggested range of FINE/-Turbo.

VALUES FROM SOFTWARE MANUAL					
ν_t	[m^2/s]	1.5 10^{-5}	3.5 10^{-5}	5.5 10^{-5}	7.5 10^{-5}
VALUES SET TO STRESS EDDY VISCOSITY EFFECT					
ν_t	[m^2/s]	1.0 10^{-4}	1.0 10^{-3}	1.0 10^{-2}	1.0 10^{-1}

Table 3.4: *Values of turbulent eddy viscosity imposed for the Spalart-Allmaras model - i=0° and $M_1 = 0.5$*

In Fig. 3.7 some pitchwise averaged quantities at mid-span are presented with respect to the eddy viscosity. The red interval represents the uncertainty band expected from the measurements. The dotted red line is the result obtained with the Balwin-Lomax algebraic model. Two different zones, separated by a dotted black line, are marked on the plots. It represents the threshold between values recommended by the manual and values arbitrarily imposed to stress the effect of the inlet turbulence. While the outlet flow angle is not significantly affected, the loss parameter and the outlet Mach show a possible effect considering a high value of the eddy viscosity (for $\nu_t > 0.001\ m^2/s$).

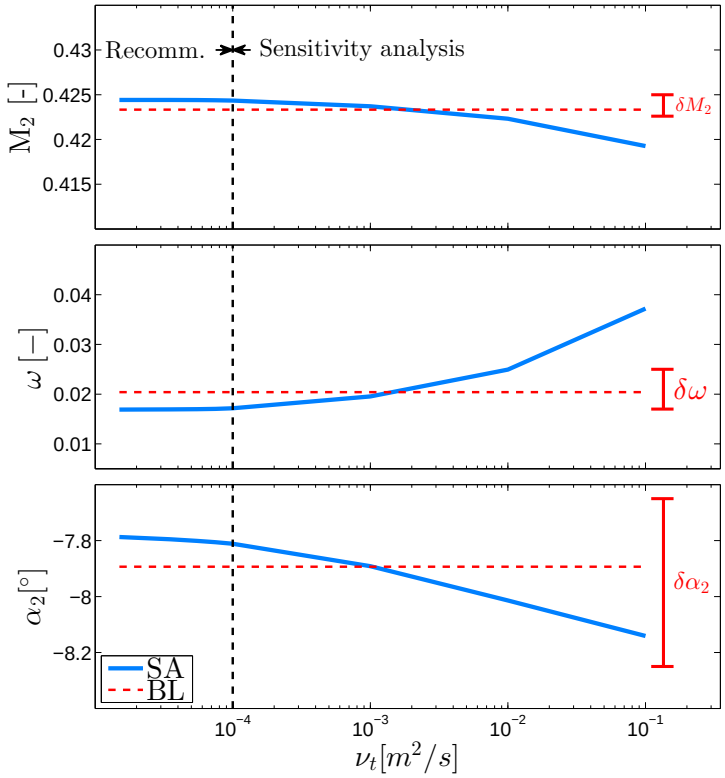


Figure 3.7: *Influence of the turbulent eddy viscosity on the outlet Mach number, the outlet flow angle and the total pressure losses - i=0° and $M_1 = 0.5$*

The two-equation models ($k-\varepsilon$ and $k-\omega$) require to impose k and ε at the inlet. By definition, the turbulent kinetic energy can be derived from the turbulence intensity:

$$k = \frac{3}{2}\left(V_{ref} Tu\right)^2 \tag{3.4}$$

To estimate the turbulent dissipation rate ε, two possibilities from the manual of FINE/Turbo [71] have been considered:

- specify the ratio of the turbulent viscosity to the laminar viscosity $\frac{\mu_t}{\mu}$ in Eq. (3.5) (equivalent to Eq. (3.1));

$$\varepsilon_I = C_\mu \frac{\rho_{ref} k^2}{\mu_t} = C_\mu \frac{\mu}{\mu_t} \frac{\rho_{ref} k^2}{\mu} \tag{3.5}$$

- specify the turbulence length scale ℓ in Eq. (3.6).

$$\varepsilon_\ell = \frac{C_\mu^{\frac{3}{4}} k^{\frac{3}{2}}}{\ell} \tag{3.6}$$

Two different procedures have then been used to calculate ε: one considering Eq. (3.5) and another, suggested by the common practice at VKI, averaging the results of Eq. (3.5) and Eq. (3.6) ($\varepsilon_{II} = \frac{\varepsilon_I + \varepsilon_\ell}{2}$). The reason of this average is that Eq. (3.6) usually leads to very low values. It must be mentioned that, according to the manual of FINE/Turbo, the ratio $\frac{\mu_t}{\mu}$ ($= \frac{\nu_t}{\nu}$) should be around 50 for turbomachinery applications. This is different than the values that are advised when using the Spalart-Allmaras turbulence model (i.e., $1 < \frac{\nu_t}{\nu} < 5$). Finally, the imposed values for k and ε are summarized in Table 3.5.

	Tu	**1%**	**2%**	**5%**	**10%**
k	$[m^2/s^2]$	4.1	16.5	103.3	413.3
ε_I	$[m^2/s^3]$	1.5 10^3	2.5 10^4	9.6 10^5	1.5 10^6
ε_{II}	$[m^2/s^3]$	0.9 10^3	1.4 10^4	5.0 10^5	7.9 10^6

Table 3.5: *Turbulence boundary conditions for two-equation models ($i = 0°$ and $M_1 = 0.5$)*

The effects on the losses, the outlet Mach number and the outlet flow angle of both the turbulence intensity and the dissipation rate are given in Fig. 3.8. The dashed green and black lines are respectively the results with the Yang-Shih and SST models using ε_{II}, while the solid lines are computed with ε_I.

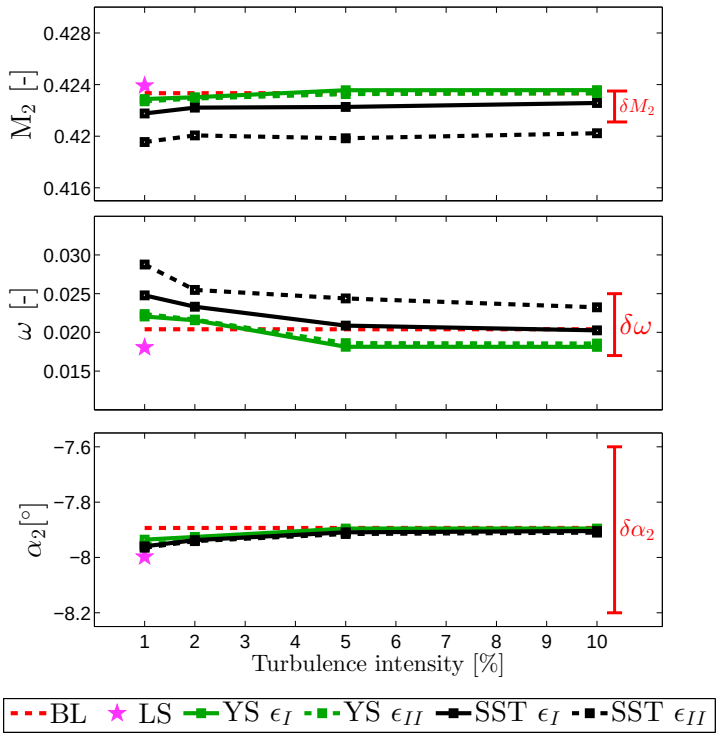


Figure 3.8: *Turbulence intensity and dissipation rate effects on the outlet Mach number, the exit flow angle and the losses for two-equation models ($i = 0°$ and $M_1 = 0.5$)*

Considering the exit flow angle, the computed differences are always below the least measurable value. The losses present an asymptotic behavior with respect to turbulence intensity as they decrease until $Tu = 5\%$, remaining almost constant afterwards. This trend is in agreement with experimental observations which showed that, at constant Reynolds number (and above 250.000), when the turbulence intensity was increased, the losses decreased (cf. [6, 74]). However, since the loss reduction remains very small, specific efforts must be dedicated to reduce the measurement uncertainties if variations must be measured and validated between 1% and 5% of turbulence intensity.

The sensitivity of the outlet Mach number regarding the variation of the turbulence intensity is always within the uncertainty band. The turbulence dissipation rate has a different impact for the Yang-Shih and SST simulations: while for the $k - \varepsilon$ model the effect is always negligible, for the $k - \omega$ model, both the losses and the outlet Mach number appear to be shifted to a different level. It should also be noticed that convergence was only reached for $Tu = 1\%$

with the $k-\varepsilon$ Launder-Sharma model for which the result is indicated by a pink star in Fig. 3.8.

The results obtained with the Baldwin-Lomax model are also presented in Fig. 3.8. Although such an algebraic model is not advised for compressor applications where adverse pressure gradients are encountered, Fig. 3.8 shows that this basic model can offer satisfactory results over the whole turbulence intensity range with respect to the one-equation or two-equation models. In [75], the Baldwin-Lomax also showed interesting results as it was too optimistic in terms of pressure ratio and efficiency predictions but it was the best turbulence model (compared with a $k-\varepsilon$ and a $k-\ell$ turbulence model) in terms of stall margin. Those evidences are not sufficient to be generalized but, when the experimental inlet turbulence conditions are not known, this basic algebraic model still represents an attractive solution in order to obtain a first guess.

3.3.3.2 Turbulence model effects

Once the boundary conditions have been fixed, the variability of the results regarding the turbulence models can be analyzed. The first important effect of the turbulence model concerns the incidence range and in Fig. 3.9, the different convergence limits of the cascade are shown.

While the $k-\omega$ SST model presents the most limited extension, the $k-\varepsilon$ model allows to reach the widest range, specially on the highly negative incidences. The values of incidence below $i=-13.4°$ have not been investigated since they are not relevant for design applications. At high positive incidence, the Baldwin-Lomax and Spalart-Allmaras models converged until $i=11°$.

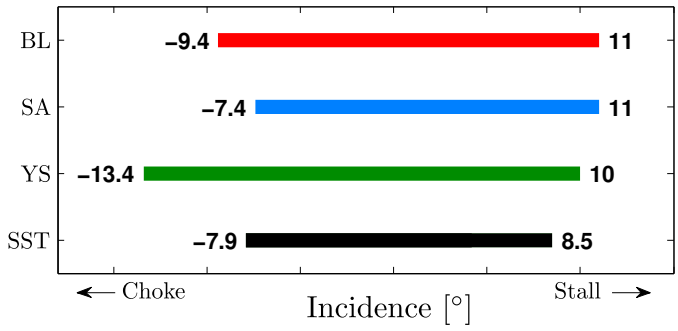


Figure 3.9: *Turbulence model effect on operating range*

The total pressure losses at mid-span are presented in Fig. 3.10 at M_1=0.40 and M_1=0.60 for the four turbulence models.

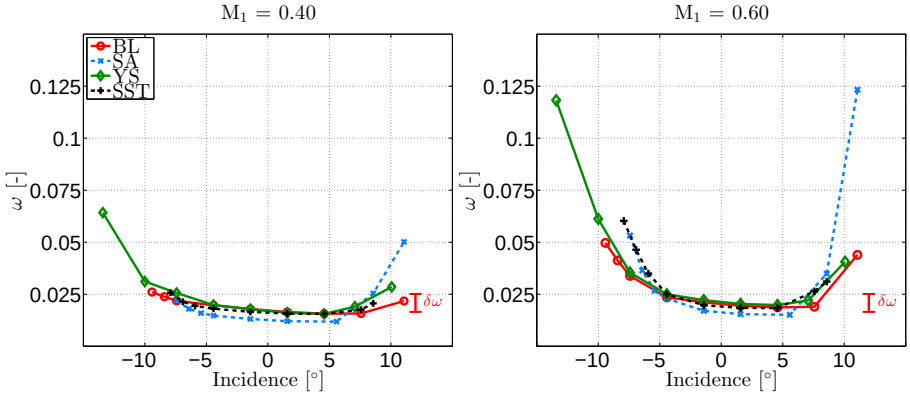


Figure 3.10: *Turbulence model effects on total pressure losses*

Considering an interval from $i = -3°$ to $i = 6.5°$, the predictions of all the models are in good agreement. The Spalart-Allmaras model shows slightly lower values but, comparing the results with typical uncertainties, none of the models can be easily validated within that range. The one-equation model predictions abruptly increase towards stall condition, where the losses reach twice the value of the other models which all provide similar losses. With respect to measurement uncertainties, none of them can be discarded.

Regarding this specific cascade geometry and as far as global performance are concerned, the effect of the turbulence modeling is limited and no firm conclusion can be drawn. A deeper analysis of the flow at mid-span as well as at the end-walls would probably help to discard the use of some turbulence models but it falls out of the scope of the current analysis. At this stage, if the designer must choose a turbulence model, it is probably more recommended to use a two-equation model that is supposed to handle better an adverse pressure gradient as it is experienced by the flow on a compressor blade suction side. However, in the present case, the poor numerical stability limit of the SST model (considered as the best choice in the case of adverse pressure gradients and slight flow separations) may be very constraining for the designer which may then opt for the Spalart-Allmaras one-equation model or the $k-\varepsilon$ model. To conclude this section, it should be emphasized, that the choice of the best turbulence model is very case-sensitive and the purpose of the current investigation was not to select the most appropriate turbulence model but rather to highlight the variability of the results related to the turbulence modeling.

3.3.4 Numerical scheme effects

Two different numerical schemes are considered in the present comparison: a central and an upwind scheme. The first is a standard scheme based on the formulation of Jameson et al. [76] using a scalar dissipation model with the 2^{nd} and 4^{th} order derivatives of the conservative variables. The second scheme is a second order upwind scheme characterized by a symmetric total variation diminishing property (STVD) as proposed by Yee [77]. The two schemes present similar convergence quality. Both numerical schemes have been used for both the $k-\varepsilon$ and Spalart-Allmaras turbulence models in order to investigate the coupled effects of both numerical scheme and turbulence model.

As displayed in Fig. 3.11, the numerical scheme appears to play a crucial role on the numerical stability limit. The use of an upwind scheme causes a reduction in the last stable incidence between 2.5° and 3°. Considering highly negative incidences, Spalart-Allmaras model reaches $i = -10.5°$ that is a lower limit than using the central scheme. The $k-\varepsilon$ model achieves a similar behavior towards choke conditions until $-13.4°$. However, as mentioned earlier, incidences below $-13.4°$ have not been investigated since it has been considered outside of the range of interest for design applications. Therefore, no firm conclusion can be drawn and differences may be expected below that value.

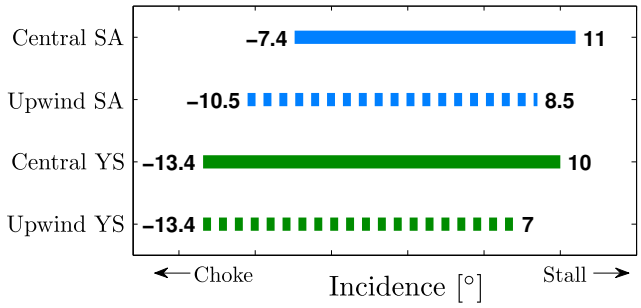


Figure 3.11: *Numerical scheme effects on incidence limits*

Contrary to the turbulence model comparison, considerable differences appear in the prediction of losses, as shown in Fig. 3.12. Within the Mach number range considered as well as in a wide range of incidence (from $i = -7°$ to the last incidence), the upwind scheme shows higher losses.

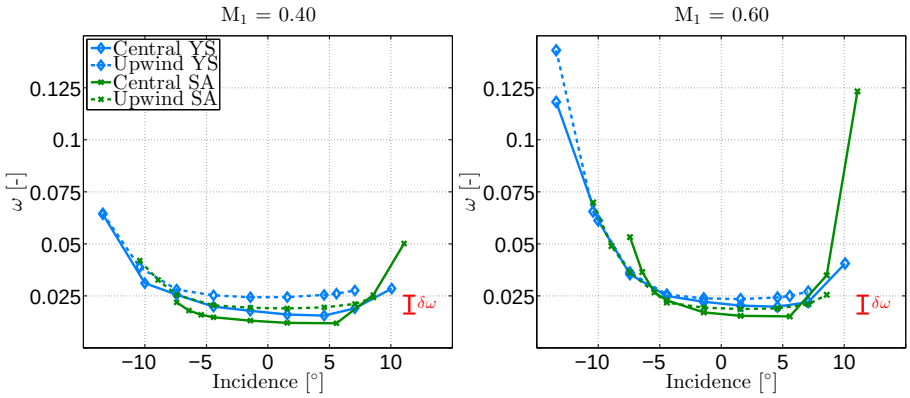


Figure 3.12: *Numerical scheme effects on total pressure losses at mid-span*

The higher losses observed with the upwind scheme may be explained by looking at the total pressure wakes in the outlet plane. It can be seen in Fig. 3.13 that the use of a central spatial discretization gives overshoots and undershoots of losses at both sides of the wake.

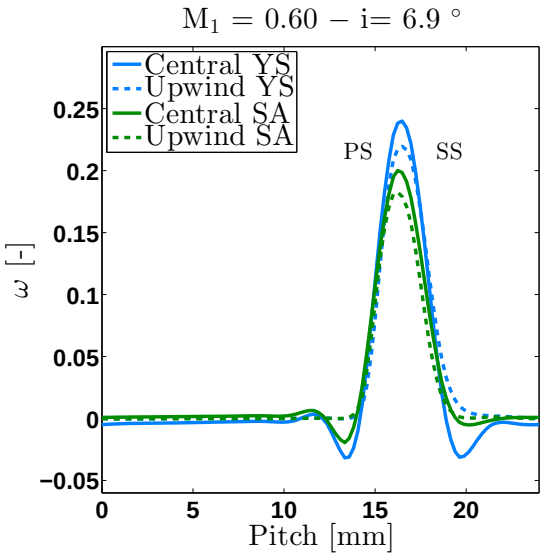


Figure 3.13: *Numerical scheme effects on total pressure loss wakes*

Those negative losses are not physical and decrease the mean loss level. It also depends on the turbulence model and the undershoots appear more intense with the Spalart-Allmaras model. This is especially true on the suction side.

This behavior is directly explained by the dispersive nature of the central scheme which is very robust and poorly dissipative but may show some oscillations when the solution presents some discontinuities such as a shock or a blade wake. This problem may be solved by the use of an upwind scheme which is able to capture flow discontinuities but it requires the introduction of limiters or entropy fix (which can be seen as a numerical dissipation) to avoid a non-physical solution which would violate the second law of thermodynamics. The issue is widely developed by Yee in [77].

In order to obtain a better perspective of the numerical scheme effects, the total pressure loss maps at the last common incidence (i.e at $i = 7°$ using the $k - \varepsilon$ Yang Shih model and $i = 8.5°$ using the Spalart-Allmaras model) are displayed in Fig. 3.14 and Fig. 3.15 respectively for the $k - \varepsilon$ and Spalart-Allmaras turbulence models. The comparison of Fig. 3.14 and Fig. 3.15 reveals strong discrepancies between both numerical schemes and a good agreement between both turbulence models. The biggest differences are visible in the corner separation patterns and the wake shapes. White contour lines have been added to indicate the presence of negative losses. Regions of negative losses are also visible in the upwind outlet maps but they are two orders of magnitude smaller than the one observed using the central scheme. Those negative losses may be attributed to numerical errors and are not affecting significantly the mean loss level. A relevant assessment of these differences will be possible with the corresponding experimental data but it already shows that the results depend much more on the numerical scheme rather than on the turbulence model.

As mentioned earlier, regarding the solidity variation study, the Yang-Shih $k-\varepsilon$ has been chosen together with a Jameson central scheme. Those choices are motivated by the years of experience in the design of low-pressure compressors at Techspace Aero and the validated high accuracy in predicting global performance of real compressor geometries (cf. [75, 78]). However, the previous observations suggest that some numerical aspects must always be monitored.

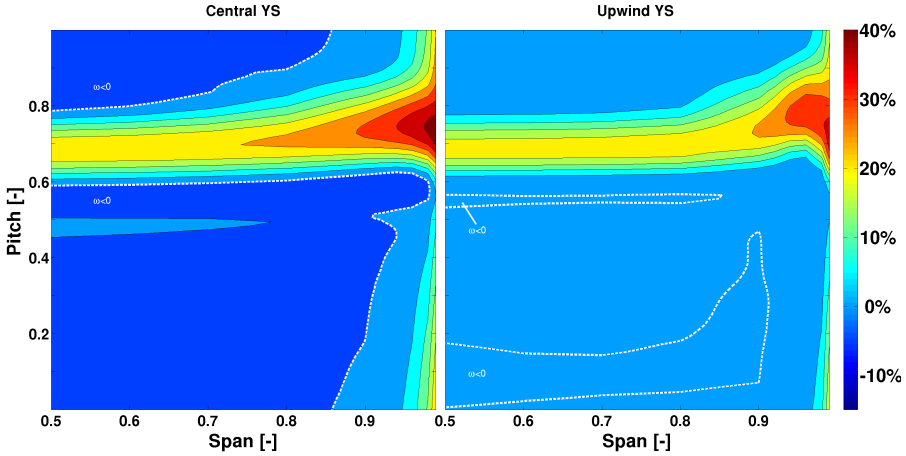


Figure 3.14: *Numerical scheme effects on the loss distribution at* $M_1 = 0.6$ *-* $k - \varepsilon$ *Yang Shih -* $i = 7°$

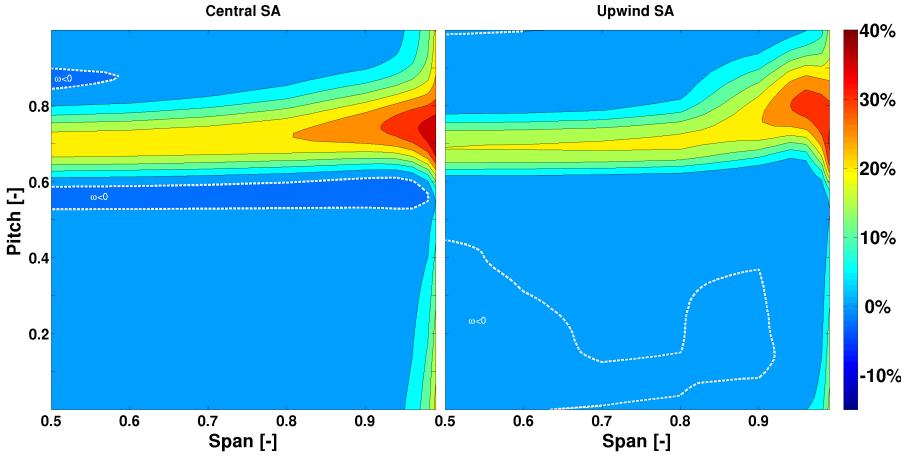


Figure 3.15: *Numerical scheme effects on the loss distribution at* $M_1 = 0.6$ *- Spalart Allmaras -* $i = 8.5°$

3.4 Results and discussion

To extract the performance of the 2 cascades and compare with the correlations, computations have been performed at 3 solidities, 4 inlet Mach numbers of 0.4, 0.5, 0.6 and 0.7 and the incidence range has been discretized from choke to stall into 12 different inlet angles. An iterative refinement has been applied to find the minimum loss incidence that is not the result of any interpolation.

The performance is presented in terms of total pressure losses, deviation and diffusion factor. Firstly, the evolution of those quantities is analyzed against incidence. Secondly, the results at optimum incidence are compared with the correlations. Finally, the issues of the incidence range and the stability are addressed.

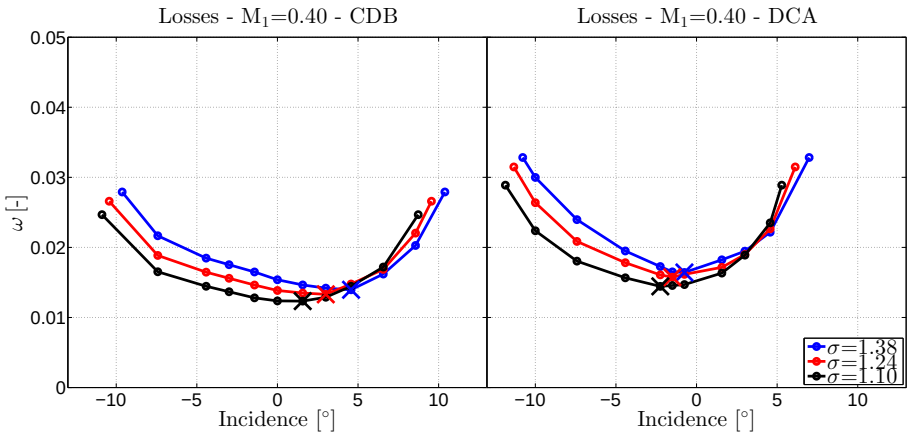
The emphasis is set on the analysis of the mid-span performance and no analysis of the secondary flows is presented. All the data have been extracted one chord downstream the trailing edge of the blade and averaged over one pitch. An arithmetic average has been used rather than a mass average. Contrary to an arithmetic average that weights similarly every single data point, a mass average is supposed to lead to the most accurate value of the absolute performance as every point is weighted by the local mass-flow. However, because it requires the knowledge of the local mass-flow (i.e. ρV_z), a mass average requires additional measurements and leads to higher uncertainties than an arithmetic average. The use of the most appropriate averaging technique remains an open issue. General guidelines are given in [79] but they depends on the quantity (pressure or temperature, static or stagnation conditions,...) and the situation (compressor, turbine, combustor,...). The absolute performance presented in this thesis may not be completely correct because arithmetic averages were considered for every quantity but, since the exact same processing methods have always been applied to all numerical data (as well as to all the measurements in Chapter 4), all the comparisons remain valid.

3.4.1 Performance

The total pressure losses for the CDB and DCA blades are given as a function of incidence in Fig. 3.16 at inlet Mach numbers of 0.4, 0.5, 0.6 and 0.7. The minimum losses ω_{min} are indicated by a cross. The first and last incidences correspond to incidences yielding $2\omega_{min}$ and to match exactly this loss level, both first and last incidences have been interpolated. In the case of the controlled diffusion blade, at M_1=0.6 and M_1=0.7, the two lowest solidity blades stalled before reaching $2\omega_{min}$. Except those specific cases, the last incidence is not the last converged incidence. It has been chosen to present the results in a limited incidence range as the emphasis is set the performance at optimum incidence and the comparison with the correlations. It must also be mentioned that in the whole incidence range, the AVDR was always between 1.00 and 1.04 and the flow conditions may be considered as two-dimensional.

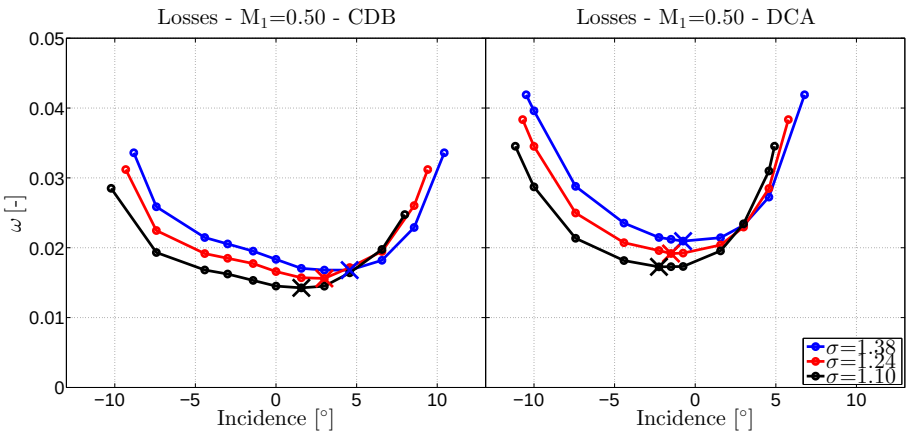
Comparing the performance of both blades, the CDB produces lower total pressure losses since it has been optimized. Regarding the effect of solidity, both blades present the same behavior. From choke to the minimum loss incidence, the total pressure losses increase with solidity. This can be explained by an enlarged wetted area when the solidity is increased. Beyond the minimum loss incidence, the trend reverses. The loading and the diffusion increase and the losses grow faster for lower solidities.

As predicted by correlations [6], the minimum loss incidence varies with solidity and moves towards higher incidences when the solidity is increased. No influence of Mach number is noticed and the minimum loss incidence remains the same as the inlet Mach number increases. This is not true for the low solidity DCA for which the minimum loss incidence is changing at M_1=0.7 that is an inlet Mach number very close to typical critical Mach numbers. It must be pointed out that the influence of Mach number on the optimum incidence may also be affected by the discretization of the incidence range and the impossibility of having a continuous incidence evolution.

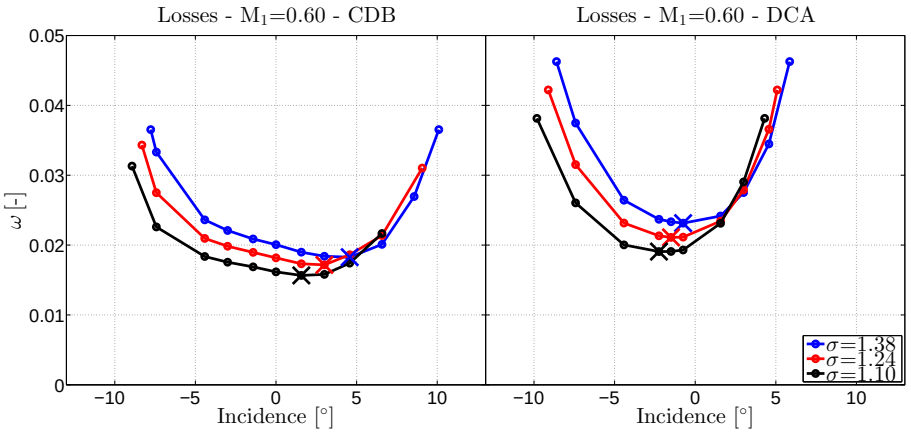


(a)

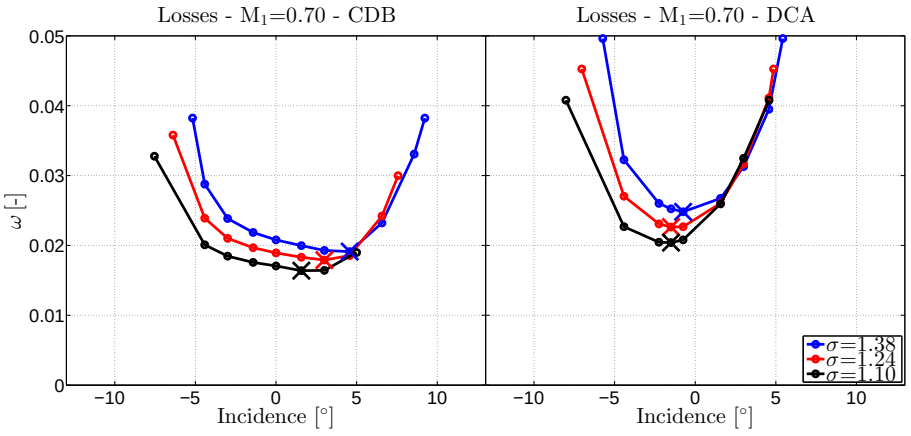
Figure 3.16: *Total pressure losses versus incidence at M_1=0.4, 0.5, 0.6 and 0.7*



(b)



(c)

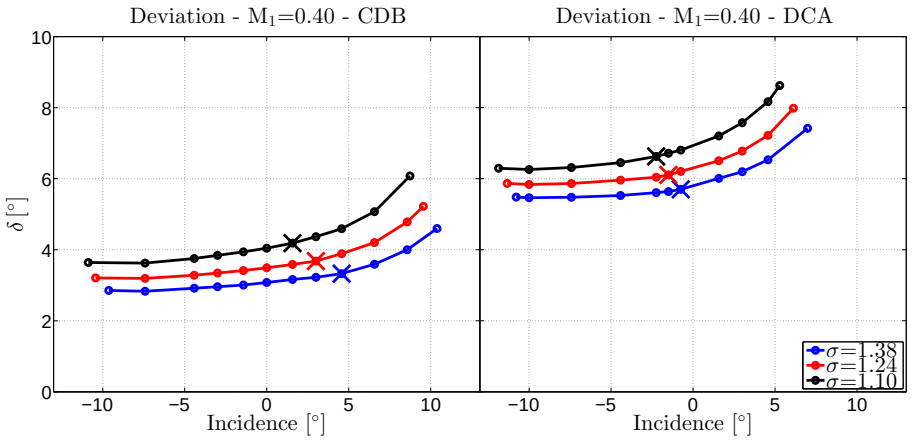


(d)

Figure 3.16: *Total pressure losses versus incidence at M_1=0.4, 0.5, 0.6 and 0.7 (continued)*

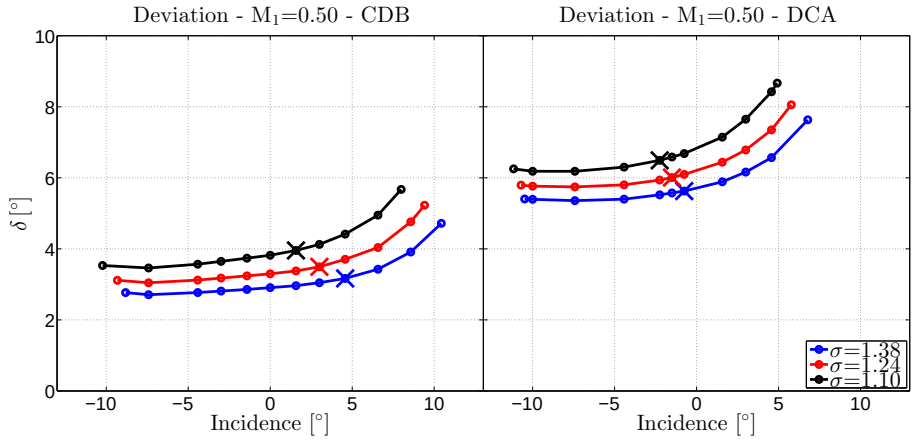
The deviation is displayed in Fig. 3.17. It clearly appears that the deviation decreases with increasing solidity. This illustrates the enhancement of the flow guidance and consequently, the turning, when the number of blades is increased. If a rotor is considered, the higher turning will result in an increase of the total pressure ratio.

At each Mach number level, the CDB deviation appears to be 3° lower than the DCA. Going to stall, as the flow starts to separate at the rear suction side of the blade, the flow cannot properly follow the blade anymore and the deviation increases. The influence of Mach number is very limited but a small decrease of less than 1° in deviation is observed as the Mach number increases. No correlation data includes this effect for inlet Mach numbers below 0.75 or critical Mach numbers. Some evidences exist showing a similar trend as in Fig. 2.29 and Fig. 2.30 but, since the decrease in deviation appears very small, it seems reasonable to neglect the influence of Mach number below critical Mach number.

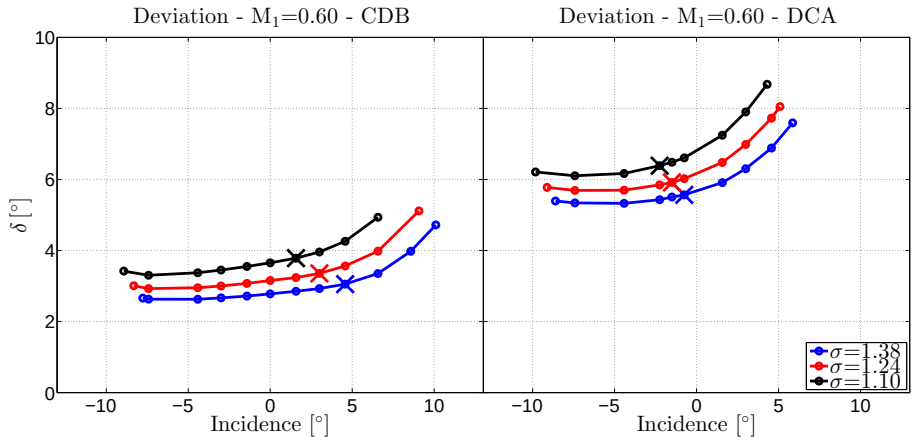


(a)

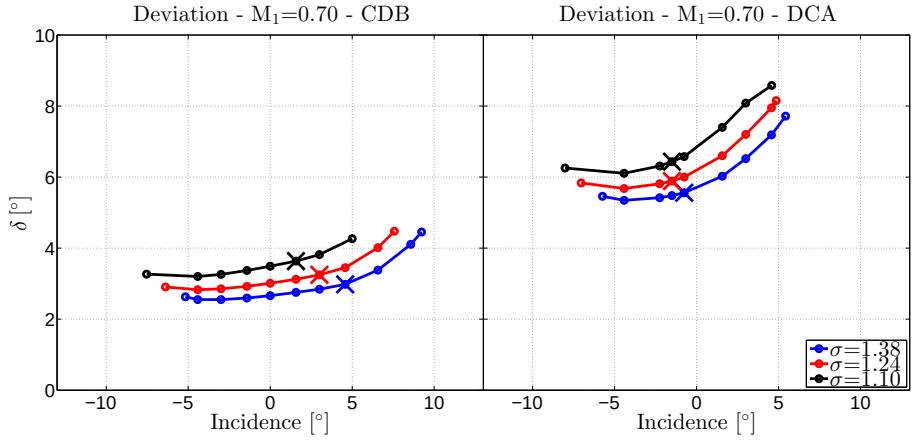
Figure 3.17: *Deviation versus incidence at M_1=0.4, 0.5, 0.6 and 0.7*



(b)



(c)

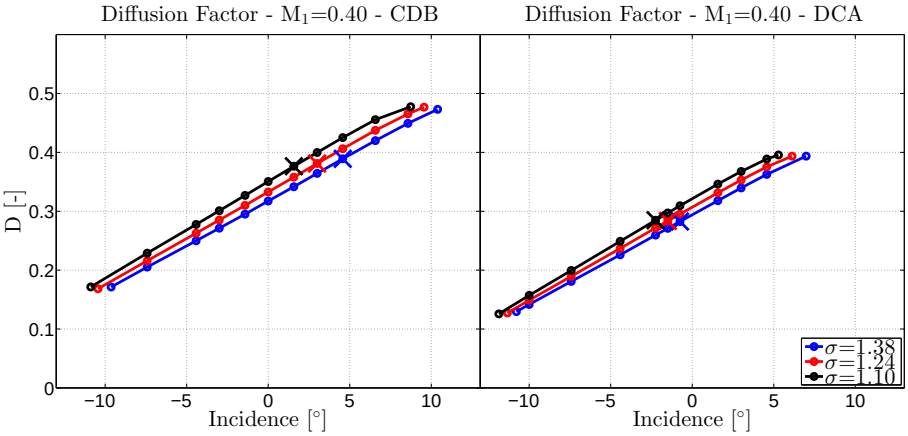


(d)

Figure 3.17: *Deviation versus incidence at M_1=0.4, 0.5, 0.6 and 0.7 (continued)*

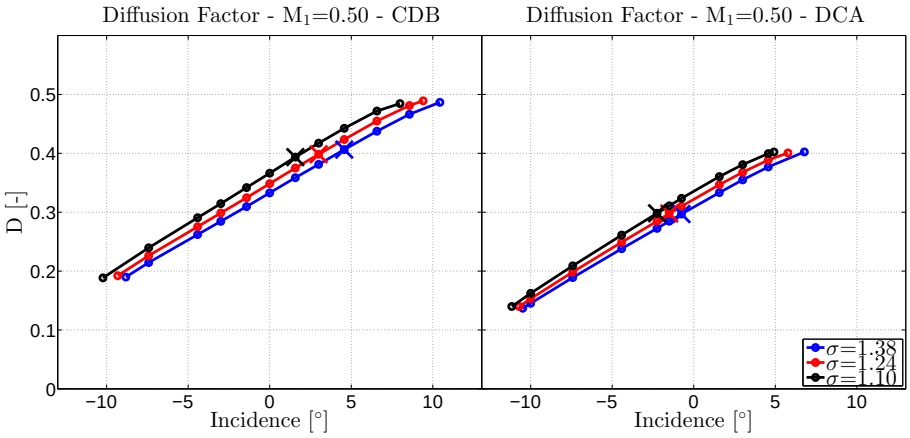
The diffusion factor is given in Fig. 3.18. By definition (Eq. (2.13)), for the same inlet flow angle, the lower the solidity, the higher the diffusion. The evolution with incidence is linear for all solidities and Mach numbers.

It appears that, except for the DCA at $M_1 = 0.7$, the minimum losses are always achieved at the same diffusion factor for a given type of blade and inlet Mach number. This is a very interesting observation that is not addressed in the literature. It underlines that an optimum diffusion factor can be selected apart from the optimum incidence and the solidity. As an example, in the case of the DCA, at $M_1 = 0.5$, the minimum losses are observed at a diffusion factor of 0.3 for all solidities and, for the CDB, the minimum loss conditions are sitting around D=0.4 for the same inlet Mach number. However, the available data are not sufficient to drawn any general conclusion since the optimum diffusion factor still depends on the flow turning, the camber, the thickness distribution as well as the stagger. Regarding the last positive incidence, corresponding to $2\omega_{min}$, a similar observation can be made and approximately the same diffusion level is reached for each solidity.

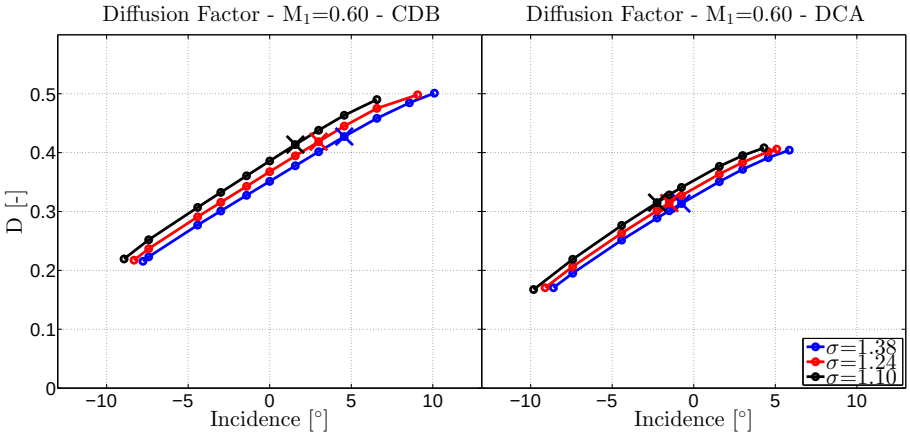


(a)

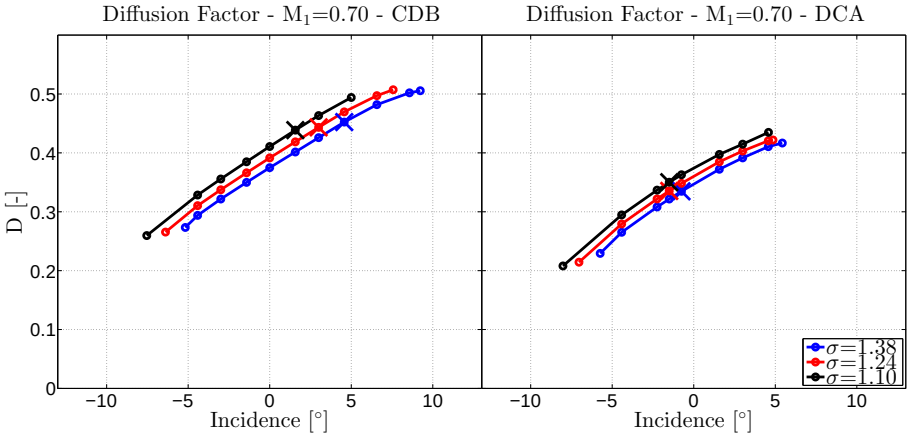
Figure 3.18: *Diffusion factor versus incidence at M_1=0.4, 0.5, 0.6 and 0.7*



(b)



(c)



(d)

Figure 3.18: *Diffusion factor versus incidence at M_1=0.4, 0.5, 0.6 and 0.7 (continued)*

3.4.2 Comparison with correlations

Most of the correlations (e.g., [4], [6], [18]) mainly focus on the minimum loss incidence performance. This section presents the optimum incidence, deviation, diffusion factor and losses versus solidity and Mach number as well as the comparison with the existing correlations.

The optimum incidences for both CDB and DCA are given in Fig. 3.19. As no influence of the Mach number has been noticed (except for the low solidity DCA), all the results are gathered in the same plot. The CFD results are compared with the NASA prediction available for the DCA and NACA 65 (cf. Eq. (2.5)). The NASA rule for DCA is giving higher optimum incidences and the best agreement is achieved at high solidity where it predicts an optimum incidence 0.5° too high. For both blades, the calculated trend is definitely linear and the optimum incidence increases with solidity. Linear polynomials seem to fit the CDB and DCA quite well and are indicated by dashed lines in Fig. 3.19.

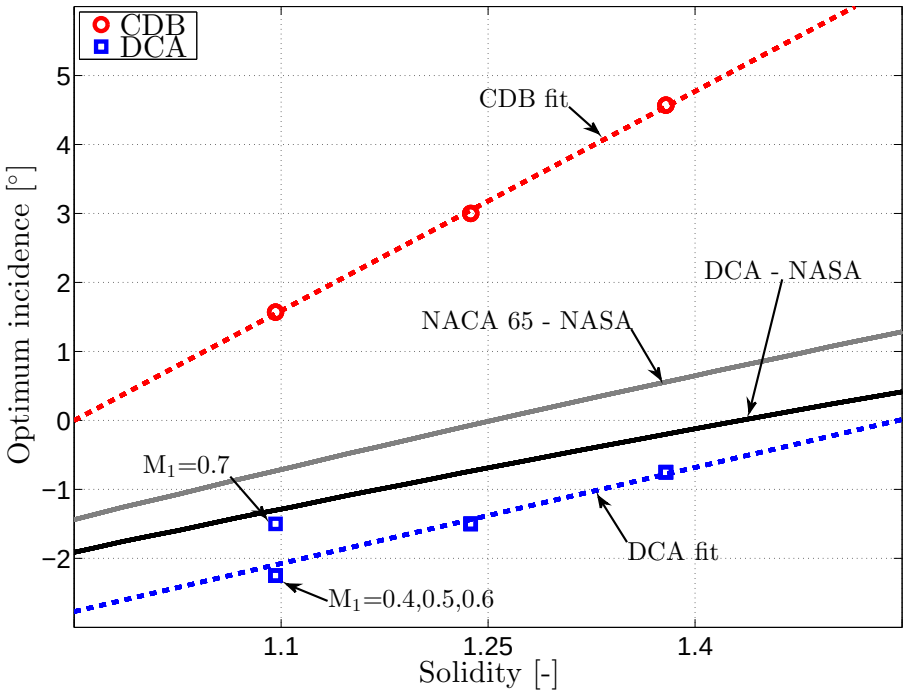


Figure 3.19: *Minimum loss incidence versus solidity*

The deviation at optimum incidence is plotted versus solidity in Fig. 3.20. Carter's DCA rule (cf. Eq. (2.4)) as well as both the DCA and NACA 65 NASA rules (cf. Eq. (2.7)) are also plotted. Carter's DCA predictions are in good agreement with the DCA results for all Mach numbers. At high solidity, it gives slightly higher values but the highest discrepancy is around 0.4°. It

proves that, although the correlations are from low speed data, they are valid up to the critical Mach number. The NASA rule is very close to Carter's predictions but only at high solidity. Towards the low solidities, the NASA rule diverges from Carter's one. Regarding the CDB, none of the correlations match the CFD results. A curve fit matching the data at all Mach numbers can be obtained by applying an offset of $-1.3°$ to the NASA rule for the NACA 65 series. The compressibility effect is very limited for the DCA and slightly stronger for the CDB. For the latter, the Mach number influence is higher at low solidity where a decrease of $0.6°$ is observed between M_1=0.4 and M_1=0.7. The typical measurement uncertainty on flow angle measured with a standard three-hole probe sits around $0.3°$ and those effects may not be validated during the measurement campaign. It must also be mentioned that those compressibility effects have the same order of magnitudes as those of Fig. 2.29 and Fig. 2.30 but, for design purposes, they were considered as negligible in the NASA manual [6].

Both Fig. 3.19 and Fig. 3.20 indicate that changing the blade count of an existing compressor design may have strong consequences. Indeed, in such a case, the blades have to be restaggered to keep working at optimum conditions and ensuring the same stall margin. The camber must also be adapted as the outlet flow angle is affected.

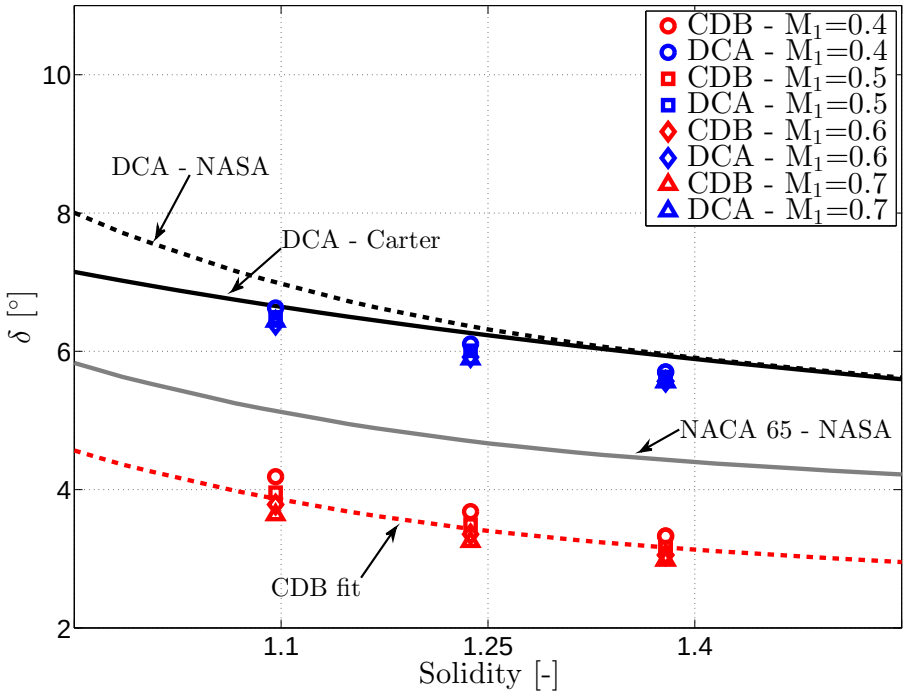


Figure 3.20: *Deviation at minimum loss incidence versus solidity*

The diffusion factor at optimum incidence and at stall are displayed in Fig. 3.21 in function of Mach number. As mentioned earlier, the diffusion factor at minimum loss incidence remains approximately constant with solidity for both CDB and DCA. At stall, the diffusion factor corresponding to $2\omega_{min}$ is also independent of the solidity choice. Merging those data in one plot, Fig. 3.21 directly shows that the diffusion factor range from optimum conditions to stall is decreasing when increasing the inlet Mach number and is not related to the solidity. Although the optimum diffusion factor (i.e at optimum incidence) changes with the type of blade and Mach number, it is a very relevant information for the designer. For a given Mach number and blading, the minimum loss conditions are encountered for a given value of the diffusion factor that is independent of the solidity. The same conclusion can be drawn at stall, for the conditions yielding $2\omega_{min}$. It is thus possible to design for a given optimum diffusion factor before selecting an optimum incidence and a solidity. Unfortunately, it is not as straightforward to determine the optimum diffusion factor given that it still depends on the flow turning, the camber, the thickness distribution as well as the stagger. Nonetheless, it suggests another design approach by choosing an optimum loading before choosing the solidity.

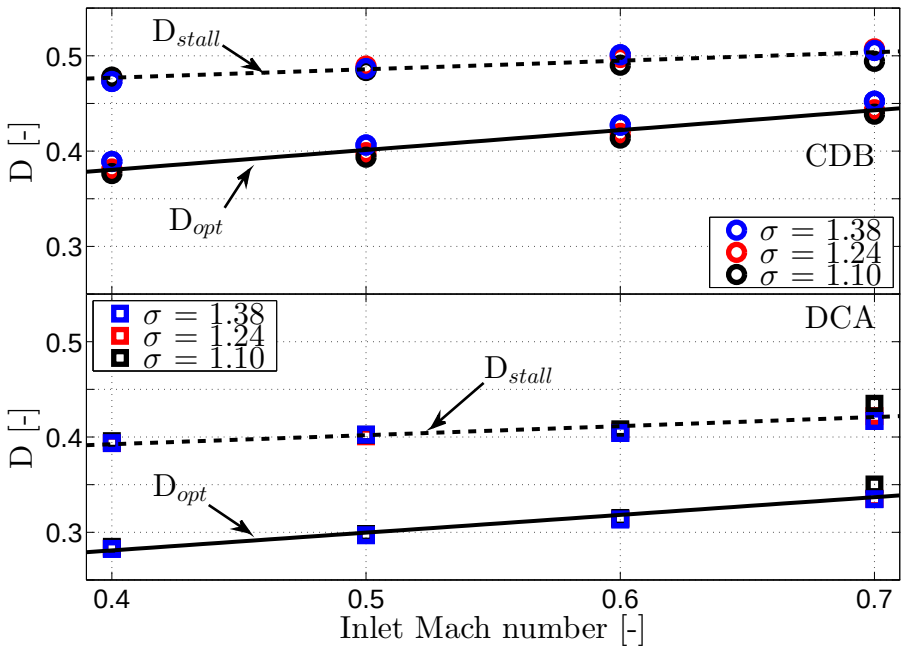


Figure 3.21: *Diffusion factor at minimum loss incidence and at stall versus Mach number*

As explained in the previous section, the loss parameters ζ_1 and ζ_2 (respectively Eq. (2.17) and Eq. (2.18)) are supposed to provide an approximation of the wake momentum thickness. To assess the quality of this approximation, the wake momentum thickness has been calculated as exposed by Lieblein [15]. The definition of θ has been recalled in Eq. (2.15). The profile of the outlet velocity V_2 normalized by the free-stream outlet velocity $V_{2,fs}$ required for the momentum thickness calculation is displayed for M_1=0.4 to M_1=0.7 over one pitch in Fig. 3.22 for the high solidity CDB. For the definition of $V_{2,fs}$, that is not unambiguous, a mean velocity averaged over 5% of the points in the middle of the passage has been considered.

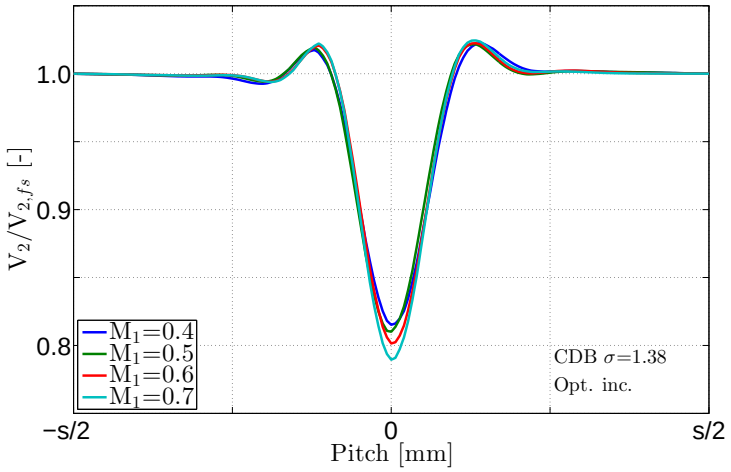


Figure 3.22: *Normalized outlet velocity wake of the high solidity CDB for the momentum thickness calculation (cf. Eq. (2.15))*

The calculated momentum thickness is shown at minimum loss incidence in Fig. 3.23 and Fig. 3.24 together with the loss parameter ζ_1 and ζ_2[1]. In both figures, the black line represents the NASA correlations of [6] (cf. Fig. 2.20). Two dashed lines surround the NASA curve to give an image of the scatter of the data points in Fig. 2.20. The dotted lines that pass through the minimum loss data represent the neighboring incidences, i.e. the off-design incidences.

Although small effects of the Mach number can be noticed for the DCA, the calculated ζ_1 are in satisfactory agreement with the NASA correlation for both blades. Comparing both the correlation and the ζ_1 from the simulations with the computed wake momentum thickness to chord ratio, it appears that they are 0.5% too low. It indicates that ζ_1 may not be a good estimate of the wake momentum thickness and that some terms of Eq. (2.16) may not be negligible.

[1] Since the wake momentum thickness is an integral quantity, to provide a fair comparison, pitchwise mass average quantities have been considered for the calculation of ζ_1 and ζ_2.

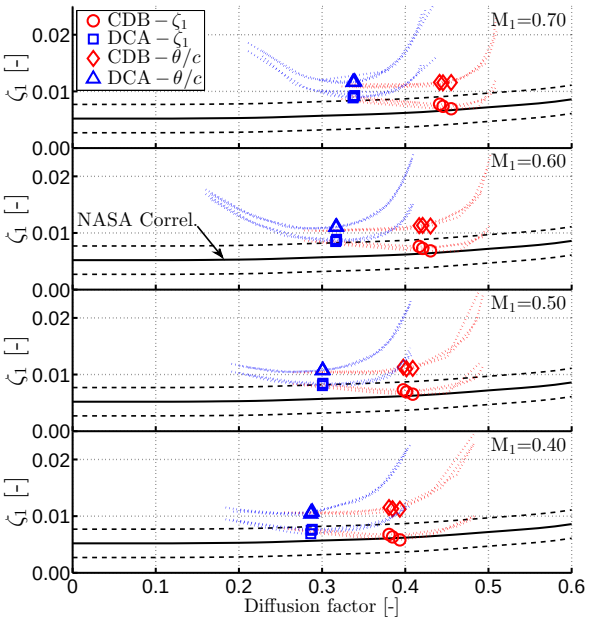


Figure 3.23: *Loss parameter ζ_1 and wake momentum thickness to chord ratio versus diffusion factor compared with NASA correlation line of Fig. 2.20 (b)*

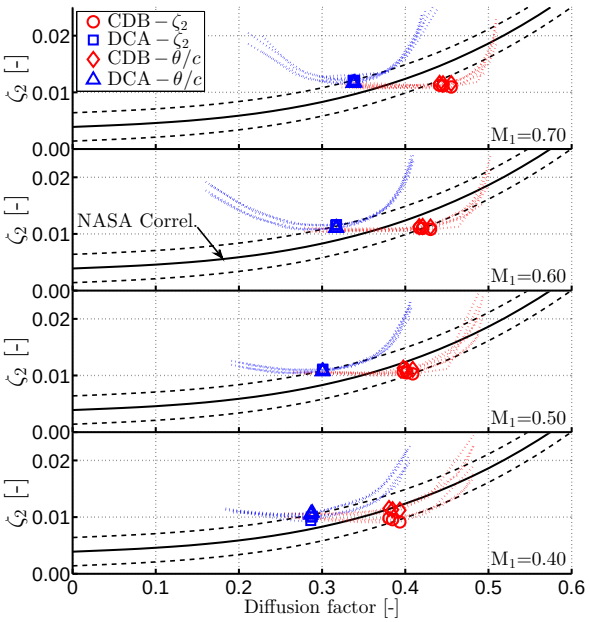


Figure 3.24: *Loss parameter ζ_2 and wake momentum thickness to chord ratio versus diffusion factor compared with NASA correlation line of Fig. 2.20 (a)*

Looking at Fig. 3.24, the use of ζ_2 to approximate θ/c appears satisfactory. Nonetheless, the CDB sits at the lower limit of the correlation uncertainty band. It points out that, for a state-of-the-art CDB, the use of the correlation remains conservative but is overestimating the total pressure losses. On the other hand, for the DCA, the correlation curve is always lower and may give an optimistic loss prediction.

Focusing on the CDB, new correlations can be established and are shown in Fig. 3.25. The dashed lines represent the new correlations that have simply been translated from the original NASA curves. The modifications are very small when ζ_1 is used but are more significant if ζ_2 is considered.

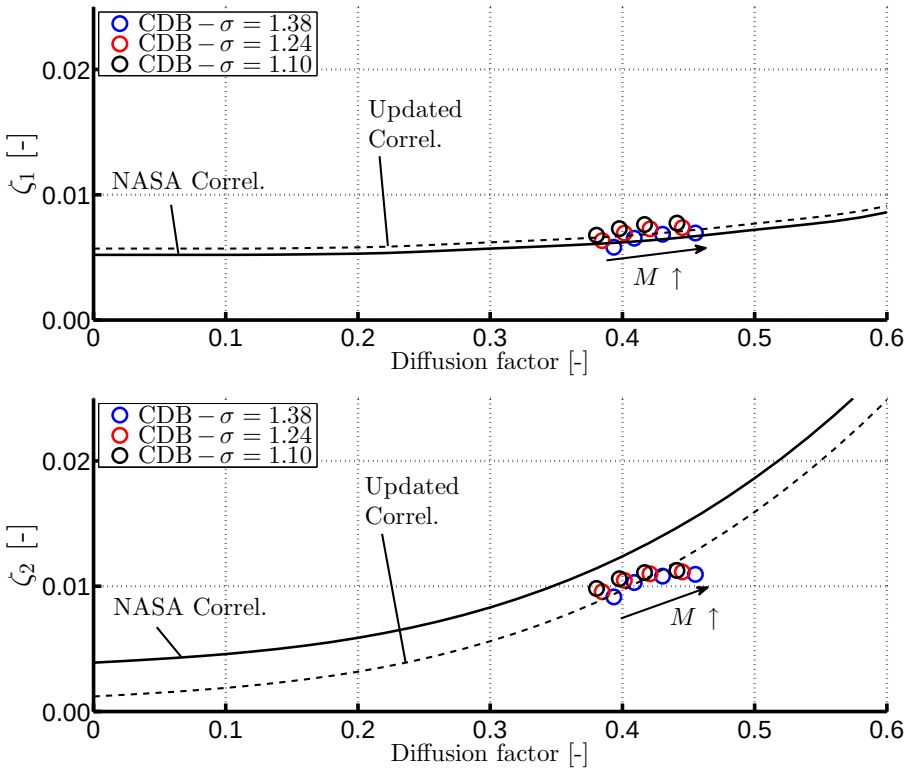


Figure 3.25: *Updated loss correlation curve for the CDB (including compressibity effects)*

Typically, compressible correlations are always based on the low-speed incompressible predictions which are then corrected by a factor depending on the operating Mach number. This is the approach presented in [22, 23]. Another method, presented in [20], is to provide a family of correlation curves that depend on the Mach number. However, as the diffusion factor increases with the Mach number, it seems, as shown in Fig. 3.25, that, for a typical

state-of-the-art controlled diffusion blade, a single correlation curve may already include compressibility effects. It means that, although they should be validated experimentally, the correlation curves of Fig. 3.25 could be easily implemented into any throughflow solver and would then be valid as long as sonic conditions do not appear on the blade suction side. Unfortunately, to be complete, the correlation curve should also firstly be validated and generalized for various blade profiles achieving different flow turnings.

Finally, from a designer point of view, it must be pointed out that the quantity that must be predicted is the total pressure deficit ω and not the wake momentum thickness θ. In that sense, the correlation of ζ_1 appears very useful. Indeed, looking back at Fig. 3.23, it is a simple parameter that offers satisfactory predictions, especially for the CDB. At the level of the meridional design, it can provide a very good estimate of the total pressure losses in function of the diffusion factor for various types of bladings and solidities.

3.4.3 Isentropic Mach number

The distributions of isentropic Mach number around the blades are shown in this section. The analysis of such plots can help to determine if the blades are well designed and operate below the critical conditions. The isentropic Mach number distributions at optimum incidence are given in Fig. 3.26, Fig. 3.27, Fig. 3.28 and Fig. 3.29 respectively for inlet Mach numbers of 0.4, 0.5, 0.6 and 0.7.

The analysis of the plots shows that the optimum incidence of the CDB is not perfectly resolved. At an inlet Mach number of 0.4 and 0.5, the presence of a small velocity peak on the suction side before the smooth diffusion indicates that the blade is operating slightly above the optimum incidence. At an inlet Mach number of 0.6, the diffusion on the suction side appears smoother and very close to the optimum incidence but a slight velocity peak is still present close to the leading edge for the highest solidity.

At M_1=0.7, a slightly supersonic isentropic Mach number is reached on the blade suction side, meaning that the critical Mach number is already exceeded. Regarding the DCA, the presence of a velocity peak on the suction side had already been observed for such an airfoil by Breugelmans [80]. It is due to the circular shape of the leading edge which can be smoothed by applying a thickness and camber optimization or using an elliptical nose. This specific topic has been addressed by Goodhand and Miller [55]. Apart from the velocity peak at the leading edge, sonic conditions are not reached.

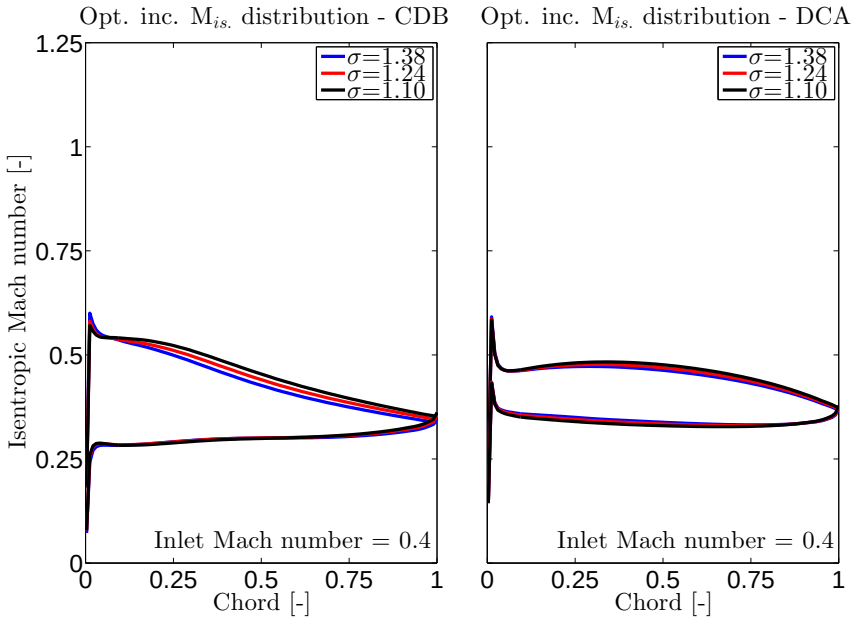


Figure 3.26: *Isentropic Mach number distributions at optimum incidence ($M_1 = 0.40$)*

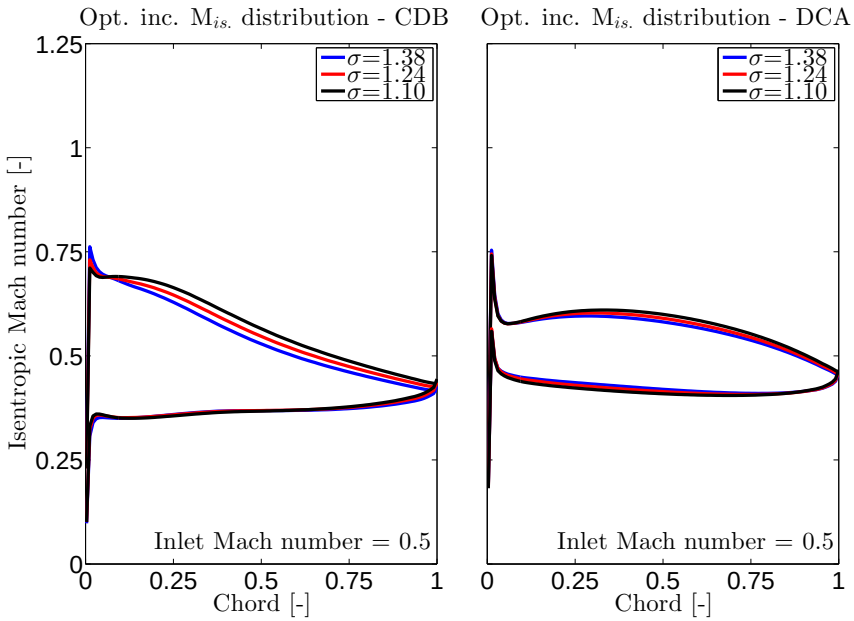


Figure 3.27: *Isentropic Mach number distributions at optimum incidence ($M_1 = 0.50$)*

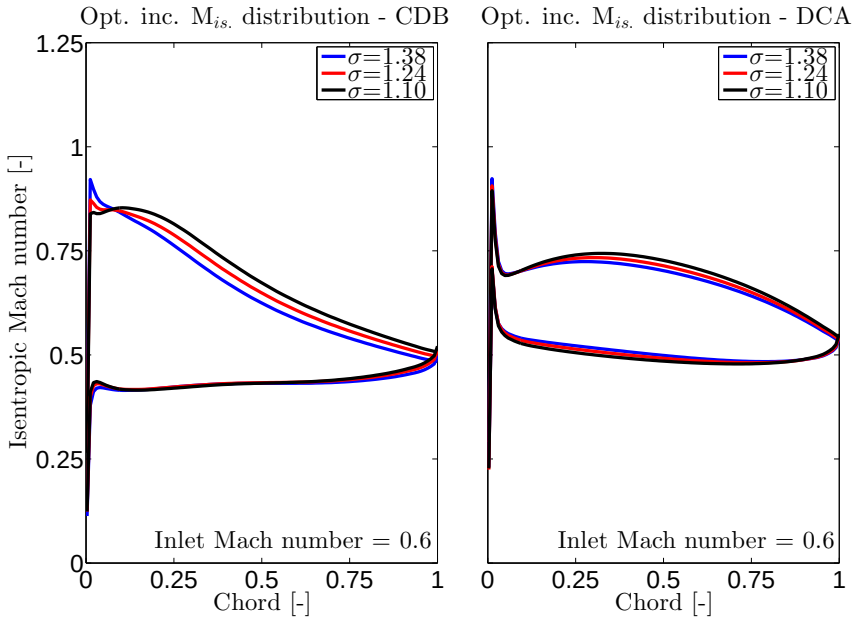


Figure 3.28: *Isentropic Mach number distributions at optimum incidence ($M_1 = 0.60$)*

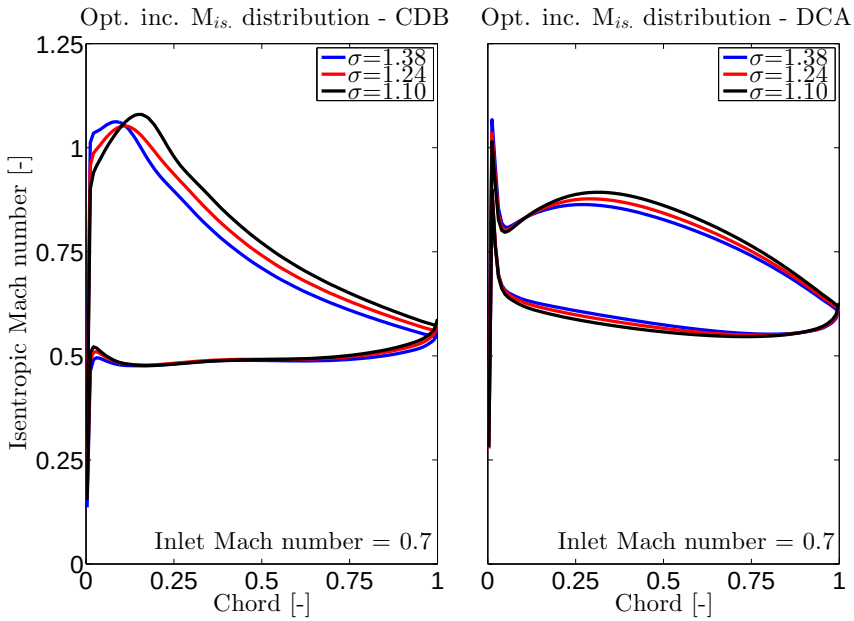


Figure 3.29: *Isentropic Mach number distributions at optimum incidence ($M_1 = 0.70$)*

According to theoretical prediction of Eq. (2.26), the critical Mach number can be predicted with the minimum pressure coefficient of the suction side defined by Eq. (2.24). Using the $C_{p,min}$ at both M_1=0.4 and M_1=0.6, Fig. 3.30 and Fig. 3.31 suggest that critical conditions should be met between M_1=0.6 and M_1=0.7. This is in agreement with Fig. 3.28 and Fig. 3.29 where slightly supersonic Mach numbers are observed for M_1=0.7 and not for M_1=0.6. Both figures 3.30 and 3.31 also show that the predictions remain reasonably similar using data at M_1=0.4 or M_1=0.6 ($\Delta M_{cr} \approx 0.03$). It indicates that $C_{p,min}$ remains approximately constant and that incompressible data may be used to predict critical conditions if only a first guess is required.

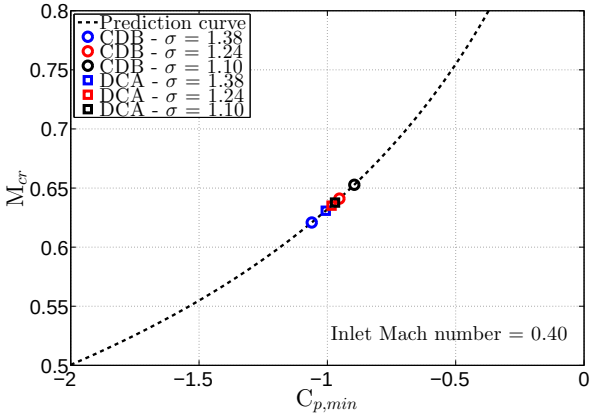


Figure 3.30: *Critical Mach number prediction of Eq. (2.26) using data at M_1=0.4*

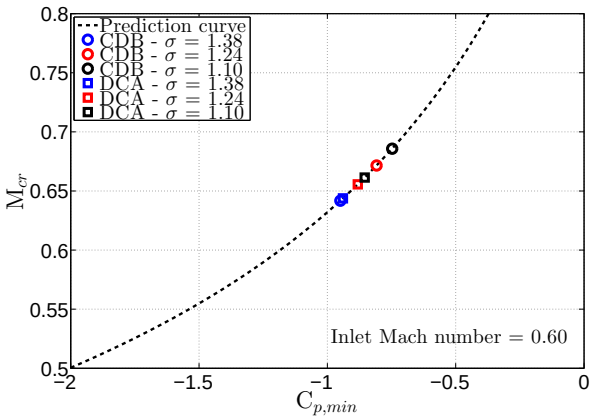


Figure 3.31: *Critical Mach number prediction of Eq. (2.26) using data at M_1=0.6*

3.4.4 Stall margin

The solidity plays an important role on the maximum loading that can be reached and the stall limit of the blade. The stall is a phenomenon widely commented and discussed in the literature and it is commonly agreed that CFD still fails at capturing the stall. Some examples can be found in [75] (Brouckaert et al.) or [78] (Sans et al.) from previous work at VKI. The works of Horlock and Denton [81, 82] constitute excellent references that summarize the last advancements and the remaining hurdles of CFD for turbomachinery applications.

To analyze the impact of the solidity on the stability limit, it is firstly essential to define the stall incidence. To remain consistent with the correlations, it has been decided to define the operating range like it is done in Fig. 2.2(b), i.e. by taking the difference Δi between the negative and positive incidence that both yield $2\omega_{min}$. As already mentioned, in the case of the CDB, the two lowest solidity cascades could not reach $2\omega_{min}$ above M_1=0.6. The operating range in function of Mach number is displayed in Fig. 3.32.

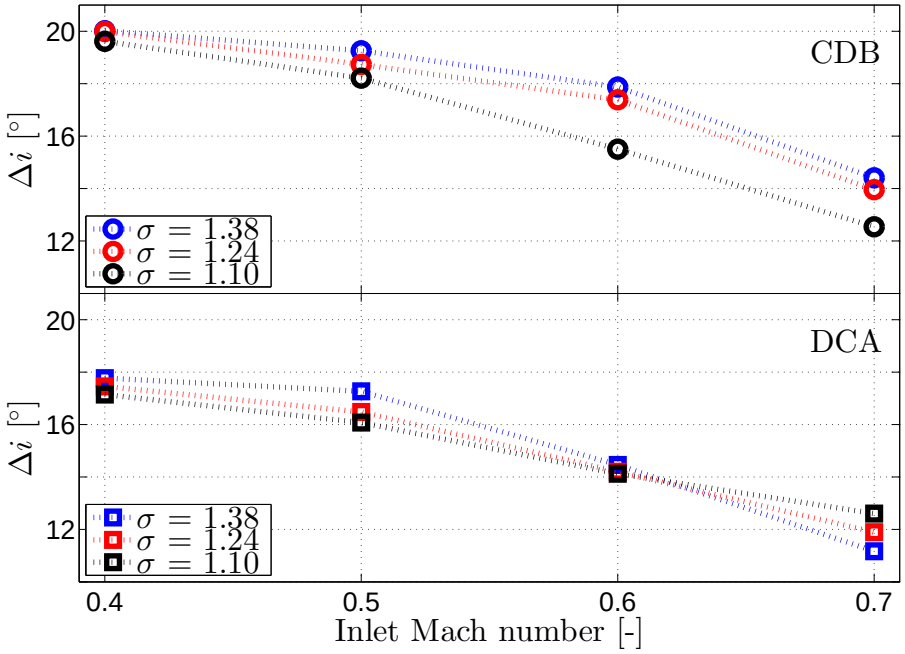


Figure 3.32: *Operating range versus Mach number*

As already pointed out in Fig. 3.21 looking at the diffusion factors, the higher the Mach number the lower the working range. For the CDB, the incidence range also decreases when the solidity decreases. It confirms that, although some efficiency improvements can be achieved, the stability cannot be main-

tained if the solidity is reduced. A compromise must be found. In a real compressor configuration, another solution must be implemented in order to compensate the decrease of stability due to a blade count reduction. For rotors, a solution is for instance presented by Houghton and Day [42] where casing treatment helps to delay the inception of stall caused by a solidity decrease. It can also be seen that for all solidities and Mach numbers, the optimized profile has a greater range than the DCA. Regarding the latter, it can be observed that, until M_1=0.6, increasing the solidity helps to improve the operating range. At M_1=0.7, the trend reverses and the low solidity DCA experiences the highest incidence range. This may be due to the appearance of supersonic pockets and shocks at off-design incidences that induce a steeper and faster rise of losses. The $2\omega_{min}$ limit is then reached faster than expected. Some previous works of Heilmann et al. [25] or Schwenk and Lewis [26] done at high subsonic and low supersonic Mach numbers confirm that such an unexpected result should not be discarded. More specifically, Schwenk and Lewis [26] observed that the solidity effects on three DCA compressor rotors were reversed compared to the subsonic solidity trend as the rotational speed was increased to its design value. They concluded that, at high inlet relative Mach numbers, the stall margin was slightly extended and the losses increased when the number of blades was decreased.

To illustrate the compromise that has to be done when choosing the solidity, the quantity $1 - \omega$, that can be seen as an efficiency, and the operating range have been plotted for the CDB against solidity in Fig. 3.33. It clearly shows that for every Mach number, the highest solidity always shows the best stall margin but the poorest efficiency. After selecting an optimum diffusion factor from Fig. 3.21 depending on the operating Mach number, a chart like Fig. 3.33 brings out quantitative information about the compromise that must be done by the designer between low losses and a high operating range when choosing the solidity.

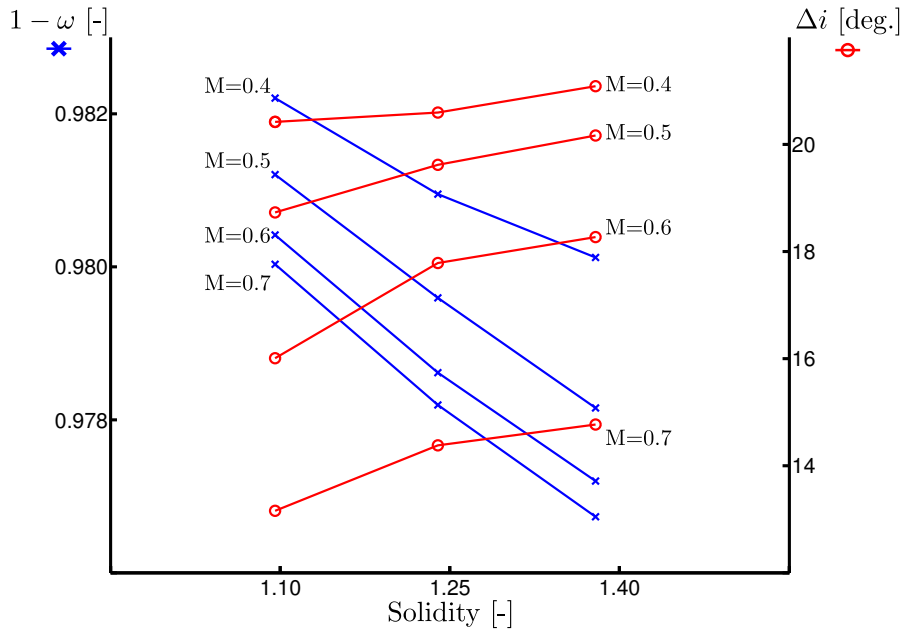


Figure 3.33: *Losses (presented as $1-\omega$) and operating range versus solidity (CDB data)*

3.5 Conclusion

In the current chapter, the effect of solidity has been studied numerically on two linear compressor cascades. The first geometry involves a controlled diffusion blade, representative of a state-of-the-art low pressure compressor stator while the second cascade uses a standard double circular arc profile.

Before varying the solidity, various numerical aspects such as the spatial discretization scheme and the turbulence model have been investigated on the baseline geometry. The scatter obtained has been analyzed and compared with typical measurement uncertainties. While most of the turbulence models effects remain within the expected uncertainties, the numerical scheme effects show tremendous differences in terms of outlet loss topologies. Finally, although an upwind scheme gave more physical total pressure loss wakes, the model used to perform the solidity analysis was the $k-\varepsilon$ turbulence model with a central scheme to match the design practices of Techspace Aero.

The solidity has then been varied on both blade geometries. From the analysis of the results, it emerges that the losses decrease when solidity decreases. This underlines possible efficiency enhancements. However, this is only true at optimum incidence. At high positive incidence, the low solidity cascade generates more losses than the high solidity. This is explained by the higher loading endured for the low solidity profile that also decreases the stability range of the cascade. A compromise should be found between high efficiency and high

stability margin.

It also appears that decreasing the solidity increases the deviation. Considering a rotor, the flow turning is directly linked to the pressure ratio which would then be reduced if the blade number is decreased. But, more generally, considering a real engine, changing the solidity has a direct impact on the incidences to the following blade row. It is therefore not straightforward to reduce the blade count of an existing engine without redesigning the next blade rows, or even to adapt the flowpath contraction to match velocity triangles and mass-flow distributions.

Both the CDB and DCA performance at optimum incidence have also been presented against existing correlations. The optimum incidence is increasing with solidity. The predictions of NASA gave higher optimum incidences. The famous Carter rule offered really good deviation prediction for the DCA blade. Regarding the CDB, it appears that the form of the NASA deviation rule is still valid but with empirical coefficients adapted for the CDB. Compressibility effects have been depicted but they are very limited. It demonstrates that, although they rely on low-speed data, the correlations can still be trusted as long as the critical Mach number is not reached. The trends of optimum incidence and deviation versus solidity prove that reducing the blade count in a compressor can not be done without restaggering and recambering the blades.

Regarding the total pressure losses, they can be predicted using Lieblein's simple ζ_1 loss parameter. However, coming back to the original work of Lieblein, the definition of the loss parameters as an approximation of the wake momentum thickness are only valid considering ζ_2. Analyzing the results from M_1=0.4 to M_1=0.7, compressibility effects have also been highlighted but they appeared very limited. New loss prediction curves have been derived and, contrary to standard compressible correlations, it appears a single correlation curve may already include compressibility effects. They can be implemented in a meridional design tool and may be used as long as critical conditions are not reached on the blade suction side.

It has also been highlighted that the minimum loss diffusion factor does not depend on the solidity. This issue is not addressed in the literature and reveals that the whole compressor design could be based on the choice of an optimum diffusion factor independent of the optimum incidence and the solidity. The design procedure is summarized in a flow chart given in Fig. 3.34. From a specified mass-flow and inlet Mach number, the designer chooses an optimum diffusion factor. The choice of the solidity follows and relies on a compromise between high efficiency (low losses) and high stability. Finally, depending on the solidity selection, both optimum incidence and deviation (together with the losses and the operating range) are computed. It is unfortunately not as simple since the the optimum diffusion factor is not straightforward and depends on the flow turning, the camber and thickness distributions as well as the stagger. Nonetheless, it suggests another design approach where it would be possible to choose an optimum loading before choosing the solidity.

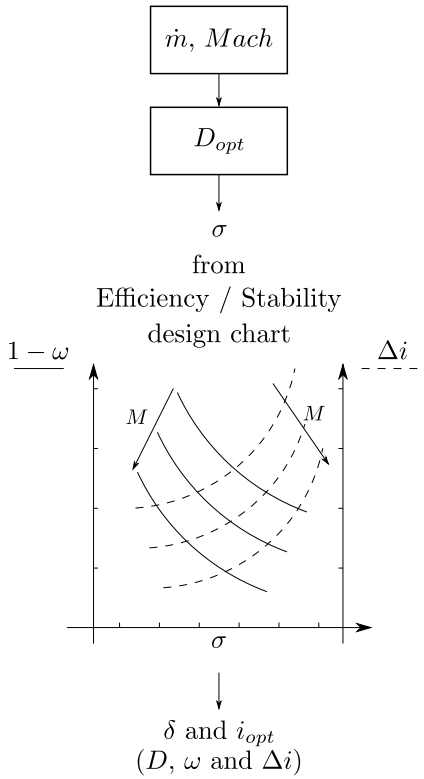


Figure 3.34: *Flow chart of a design process based on the choice of an optimum diffusion factor*

To support the CFD data presented in the current chapter, an experimental investigation has been carried out in the VKI-C3 high-speed facility. Since the current pre-test analysis has been performed before the experimental campaign, the numerical domain does not match perfectly the experimental configuration. Moreover, the inlet boundary conditions must be set according to the measurements. To obtain more faithful predictions, post-test CFD computations have also been performed.

Because of the very low differences to be measured, specific care has been dedicated in the experimental set-up to the uncertainty assessment and reduction. The conclusions previously presented in this chapter remain valid for a pre-test investigation but some numerical effects must still be monitored within the post-test analysis. In that prospect, the Yang-Shih $k-\varepsilon$ and Spalart-Allmaras turbulence models have been selected and more comparisons will be done varying the numerical parameters as the turbulence length scale or the spatial discretization.

Chapter 4

Experimental Investigation

4.1 Introduction

The previous chapter focused on the numerical investigation of the effect of solidity on both a DCA blade and a controlled diffusion airfoil. The study on the DCA blade was motivated by the amount of available empirical data that enables to evaluate the capabilities of the CFD. However, such a profile is not representative of state-of-the-art axial compressor bladings.

In Chapter 3, some trends emerged for the CDB that could be used in any meridional design solver. In order to validate the CFD results, an experimental campaign was set-up for the CDB in the high-speed VKI-C3 facility. This is the focus of the current chapter.

The solidity effects were only studied by changing the pitch to keep the chord-based Reynolds number constant (at a given inlet Mach number) as well as the aspect ratio. Any modification of the aspect ratio is changing the secondary flow patterns which will affect the performance of the whole blade. Aspect ratio variations have been considered within the same measurement campaign by varying the blade chord at constant solidity and the Reynolds number is thus not kept constant. The results have been reported in [83].

A description of the facility, the instrumentation and the test section is firstly presented. The results of the measurements are then analyzed on their own. Finally, they are compared with both the correlations and the numerical predictions. Due to a change of inlet conditions, some calculations have been repeated at the specific tested incidences and inlet Mach numbers on a different numerical domain which exactly matches the experimental configuration. Post-test numerical data have therefore been established and will also be analyzed next to the results of Chapter 3. The establishment of new correlation rules is also addressed.

4.2 Facility and test section

A sketch of the high-speed cascade tunnel C3 facility is given in Fig. 4.1. It is a blow-down facility discharging to atmosphere mainly used for turbine or compressor linear cascade test sections. Typical dimensions of the inlet section

are 100mm x 200mm. As it can be seen in Fig. 4.1, the air enters the settling

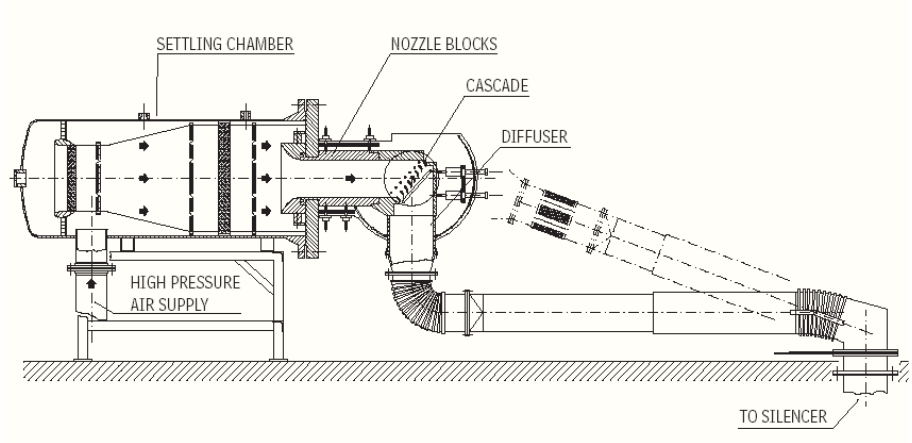


Figure 4.1: *Sketch of the high-speed cascade tunnel C3 facility*

chamber at its bottom left from the VKI high pressure air circuit (40 bar line). It is then admitted to the test section after passing through several grids and a final honeycomb just before the test section.

The inlet air angle is varied by rotating the test section. The lower and upper walls can be moved in order to close the cascade in every configuration. Depending on the studied solidity, the cascade has 10 or 11 blades. The blade profile corresponds to the controlled diffusion airfoil provided by Techspace Aero and studied in Chapter 3.

Inlet and outlet grooves have been manufactured to allow the passage of the probes and enable the measurement of both inlet and outlet flow conditions at several blade heights and along several pitches. Two motors allow the movements of the probes in both span and pitch directions. However, inlet or outlet traverses cannot be performed simultaneously. Finally, four static pressure taps are located 3.5 chords upstream the blade leading edge and two rows of 50 static pressure taps are set up respectively 0.5 chord and 1.5 chords downstream the blade trailing edge in the flow direction.

Views of the test section CAD model are given in Fig. 4.2 while a photograph of the real cascade is given in Fig. 4.3. Note that in Fig. 4.3, the inlet groove was not yet manufactured. Another picture (Fig. 4.4) shows the section with the probes mounted in the inlet groove.

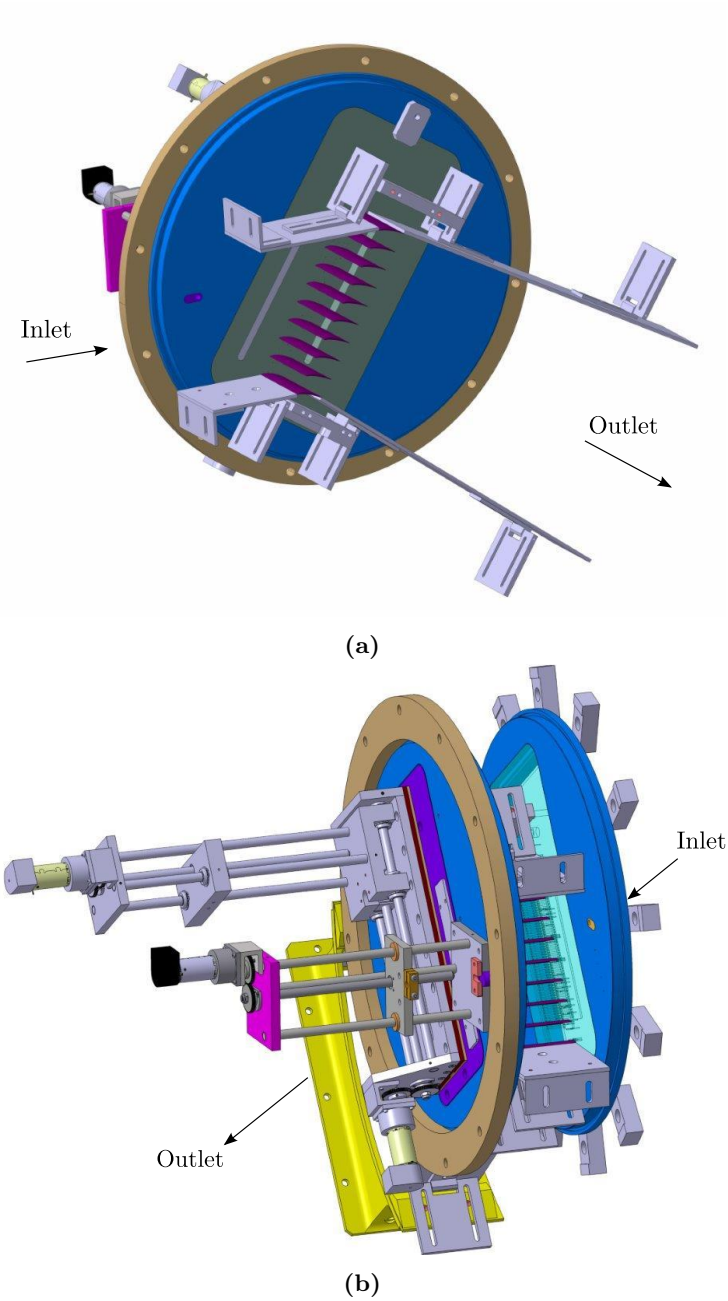


Figure 4.2: *Views of the CAD model*

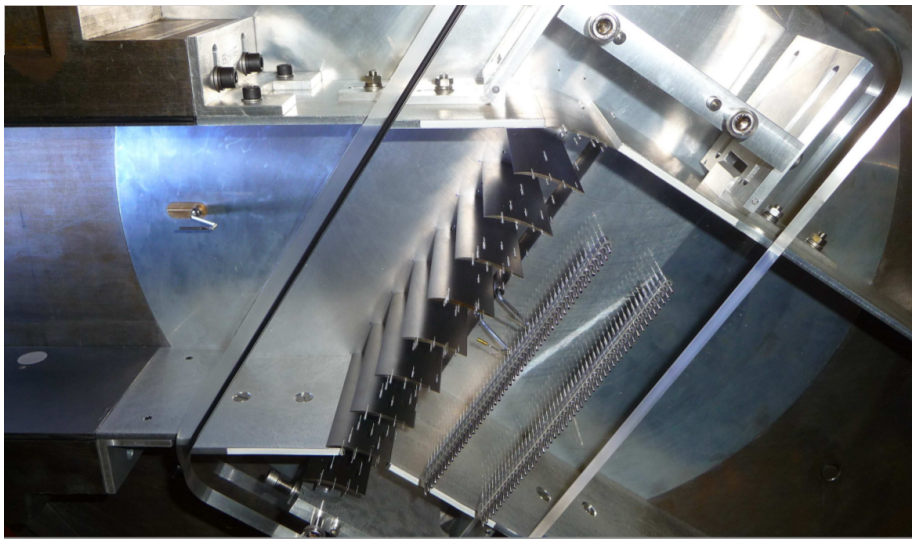


Figure 4.3: *Picture of the test section*

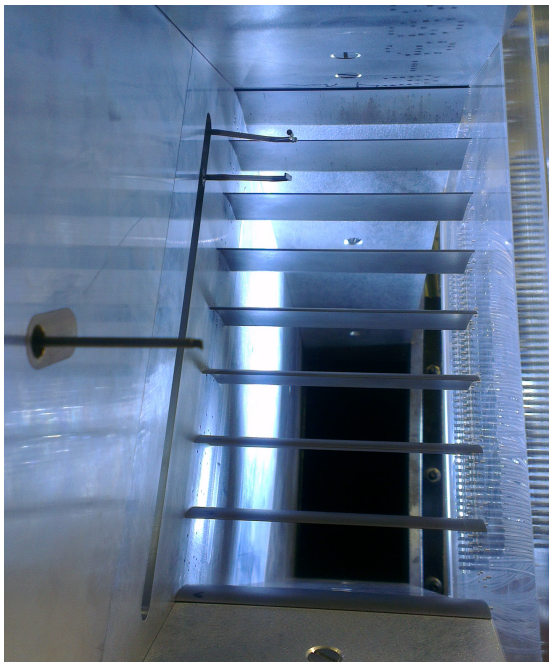


Figure 4.4: *Picture of the probes when mounted in the inlet groove (inlet view)*

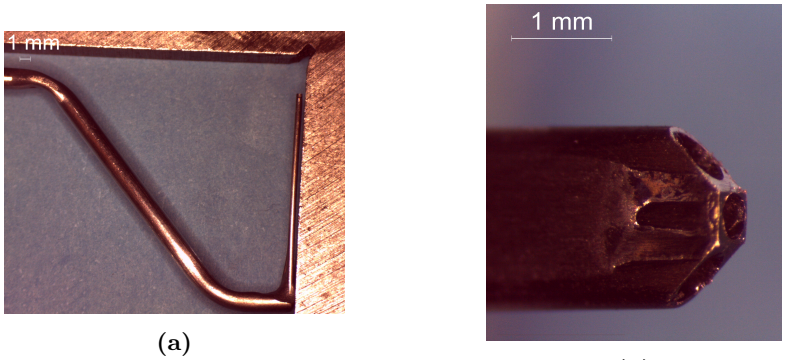
4.3 Instrumentation and probes

All pressures are acquired through two scanners with a range of 1034 mbar (15 psi) for the outlet static pressures and one scanner with a range of 345 mbar (5 psi) for all inlet and probe measurements. Measurements are acquired at 312.5 Hz and stored in the temporary memory of the scanners. Every 5 points, an average is computed, sent to the computer and recorded. This allows to limit the amount of data without losing any valuable information. The data are thus saved at a frequency of 62.5 Hz and each data point recorded in the output file represents an average of 5 points acquired at 312.5 Hz.

The motor displacement is controlled by the user and its speed has been set to 1mm/s. Hence, during a traverse, the spatial density of data is 62.5 points/mm. The position of the motors can not be recorded while moving. To get the motor positions, the acquisitions should have be taken at discrete positions when the motors are not moving. This procedure has been rejected as it tremendously increases the test duration. To preserve a high density of points and a reasonable test time ($\sim$2 minutes per traverse), it has thus been preferred not to record the motor positions.

All the traverses started and finished at the same absolute positions. However, to fit various values of pitches in the same test section, all the blades must be moved when the solidity is varied. Consequently, the absolute motor positions do not correspond to equivalent relative positions of the blades when the solidity is varied.

Traverse measurements were performed with a three-hole probe and a kiel probe which are displayed in Fig. 4.5 and Fig. 4.6. The inlet total pressure is measured with a standard kiel probe (cf. Fig. 4.7) used at VKI within the DREAM booster measurement campaign [78].



(a) **(b)**

Figure 4.5: *Picture of the three-hole probe used for traverse measurements*

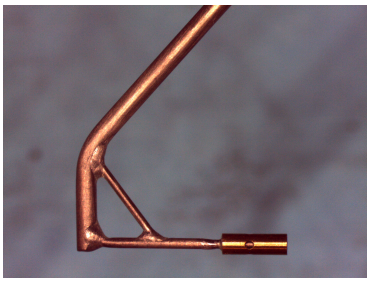


Figure 4.6: *Picture of the kiel probe used for traverse measurements*



Figure 4.7: *Inlet kiel probe for inlet total pressure measurement*

A prior calibration of the three-hole probe allows to retrieve the flow angle as well as both total and static pressures. Because of the angular calibration, the three-hole total pressure always presents a slightly higher uncertainty than the kiel probe measurement and, in the calculation of total pressure losses, only the kiel probe is used. The uncertainties (within a 95% confidence interval) of the measured and the derived quantities are respectively summarized in Table 4.1 and Table 4.2. Calibration details together with the uncertainty derivation of the performance quantities are given in Appendix B.

Table 4.1: *Uncertainties of all measured quantities (given at 95%)*

Total pressure (kiel probe)	± 0.23 [mbar]
Total pressure (3-hole probe)	± 0.3 [mbar]
Wall static pressure	± 0.13 [mbar]
Flow angle	± 0.3 [°]

Table 4.2: *Uncertainties of derived quantities (given at 95%)*

Total pressure losses	± 0.0025 [-]
Turning	± 0.4 [°]
Inlet Mach number	± 0.6 10^{-3} [-]
Diffusion factor	± 0.003 [-]
AVDR	± 0.004 [-]

4.4 Test matrix

Three solidities have been studied: 1.38, 1.24 and 1.10 respectively σ_1, σ_2 and σ_3 in Table 4.3. Measurements have been done at inlet Mach numbers of 0.45 and 0.60. Five common incidences i of 0°, 3°, 6°, 9° and 10.5° have been selected. A sixth incidence has been chosen depending on the solidity. For each incidence, probe traverses have been performed at 4 span positions h (5%, 20%, 30% and 50%). However, for each solidity, for $M_1 = 0.45$, and for both $i = 3°$ and $i = 9°$, a more complete outlet flow map has been acquired by measuring at every 5% of the span. Finally, it represents approximately 170 traverse tests without including repeat tests and periodicity checks. The test matrix is summarized in Table 4.3.

h \ i	0°	3°	6°	7.5°	8°	9°	10.5°	12°
5%	$\sigma_{1,2,3}$	$\sigma_{1,2,3}$	$\sigma_{1,2,3}$	σ_3	σ_2	$\sigma_{1,2,3}$	$\sigma_{1,2,3}$	σ_1
10%	-	$\sigma_{1,2,3}$	-	-	-	$\sigma_{1,2,3}$	-	-
15%	-	$\sigma_{1,2,3}$	-	-	-	$\sigma_{1,2,3}$	-	-
20%	$\sigma_{1,2,3}$	$\sigma_{1,2,3}$	$\sigma_{1,2,3}$	σ_3	σ_2	$\sigma_{1,2,3}$	$\sigma_{1,2,3}$	σ_1
25%	-	$\sigma_{1,2,3}$	-	-	-	$\sigma_{1,2,3}$	-	-
30%	$\sigma_{1,2,3}$	$\sigma_{1,2,3}$	$\sigma_{1,2,3}$	σ_3	σ_2	$\sigma_{1,2,3}$	$\sigma_{1,2,3}$	σ_1
35%	-	$\sigma_{1,2,3}$	-	-	-	$\sigma_{1,2,3}$	-	-
40%	-	$\sigma_{1,2,3}$	-	-	-	$\sigma_{1,2,3}$	-	-
45%	-	$\sigma_{1,2,3}$	-	-	-	$\sigma_{1,2,3}$	-	-
50%	$\sigma_{1,2,3}$	$\sigma_{1,2,3}$	$\sigma_{1,2,3}$	σ_3	σ_2	$\sigma_{1,2,3}$	$\sigma_{1,2,3}$	σ_1

Table 4.3: *Test matrix in span, incidence and solidity*

4.5 Periodicity and inlet conditions

Before presenting the results of the measurements, a very essential issue when performing cascade measurements is the flow periodicity in the pitchwise direction. Gostelow [9] mentions that the flow is periodic if every measured quantity is periodic. To achieve such conditions, between 5 and 7 blades (depending on the reference) are required. Once the flow periodicity is assessed, the measurements are usually concentrated on the passage in the middle of the cascade.

If the flow is directly ejected to the atmosphere, the periodicity of the flow is usually not an issue if enough blades are considered in the cascade. In the VKI-C3 facility, the exit flow discharges through an exhaust pipe that must be as much as possible aligned with the flow to minimize the appearance of flow

stagnation regions. Those are characterized by higher static pressure and create a pressure gradient between the upper and lower walls. The static pressure gradient is checked by two rows of 50 pressure taps downstream the blade trailing edges. They are displayed in Fig. 4.3. The flow is considered as periodic when there is no static pressure gradient between the lower and upper walls.

As the outlet flow direction is a priori not known, two flat tailboards must be adjusted in the right angular position. If the tailboards are not correctly set, a static pressure gradient is observed. Once they are aligned with the flow, the static pressure gradient vanishes. This is illustrated in Fig. 4.8. The pressure distribution at a tailboard angle of 8.3° is considered as periodic. This procedure must be repeated for each solidity and incidence angle.

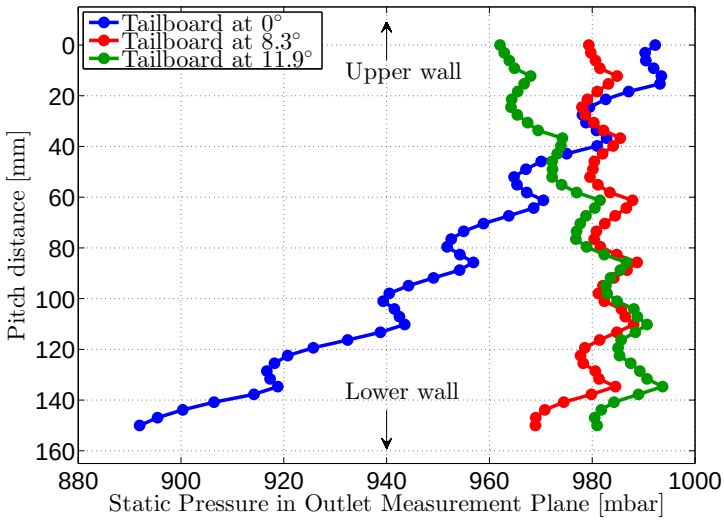


Figure 4.8: *Effect of tailboard setting angle on outlet static pressure distribution*

The periodicity of the outlet flow is obviously strongly depending on the upstream conditions that must be as much uniform as possible. Unfortunately large non-uniformities have been identified in the inlet plane. This phenomenon prevents the flow to be fully periodic. To check the inlet flow uniformity, total pressure and flow angle measurements were obtained by inlet traverses in front of the blades as displayed in Fig. 4.4. The inlet total pressure map is given in Fig. 4.9 where the inlet total pressure has been normalized by the pressure in the settling chamber and then mapped along the span and pitch directions.

Analyzing the inlet measurements, pressure deficits are observed at mid-height on the side walls as well as on the upper and lower walls[1]. They represent

[1]The pressure deficit on the lower wall is not visible in Fig. 4.9 but has been observed during other measurements.

a pressure loss between 5% and 8% of the settling chamber stagnation pressure. In Fig. 4.9, on the right hand side, two pressure deficits are depicted. At around 20% of the channel height, on the right hand side, the pressure drop is the wake of the inlet probe used to measure the inlet conditions. The pressure deficit at mid-height is not expected. It is more intense than the one of the probe wake and is coming from further upstream. The inlet flow non-uniformity is believed to be due to a wrong design of the air intake inside the settling chamber. To improve the flow uniformity, various honeycomb grids having different sizes have been placed right before the test section inside the settling chamber but none of the attempts gave satisfactory results.

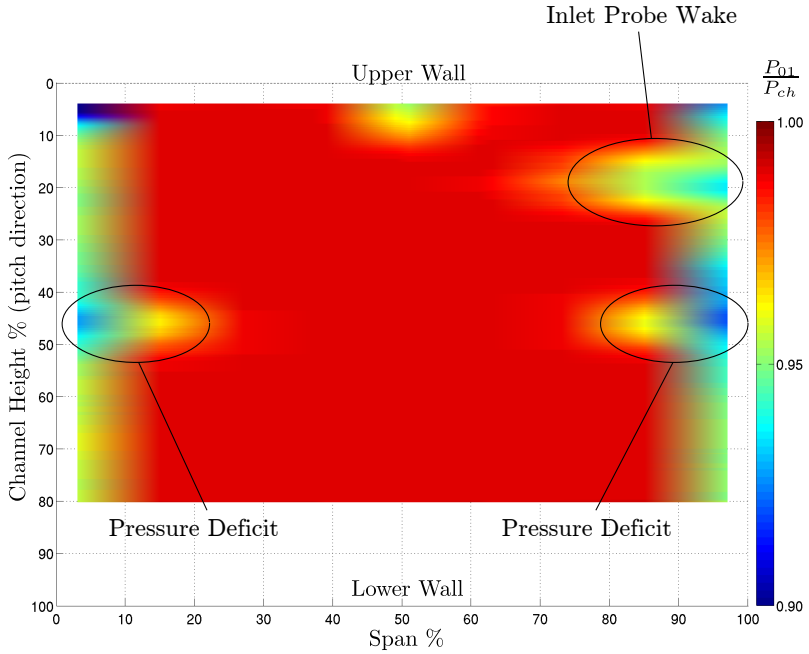


Figure 4.9: *Inlet pressure distribution normalized by the settling chamber pressure*

In practice, the flow remains periodic at mid-span but from 30% of the span to the wall, the flow is not fully periodic anymore. Taking those non-uniform flow conditions into account, the whole experimental campaign has finally been focused on the upper blades before the appearance of the pressure deficit in order to be able to measure the performance from 5% to 50%. It is believed that it does not affect the following conclusions for the mid-span sections. Unfortunately, the development of the secondary flow is most probably affected by the inlet flow non-uniformity.

Finally, after averaging the total pressure and the inlet air angle in the upper region of the map (before the pressure drop), the measured inlet profiles are

displayed in Fig. 4.10 and Fig. 4.11, respectively for the inlet total pressure and the inlet incidence. The wall static pressure measurements have been indicated to complete the pressure profile. While the pressure profile is typical, the incidence profile is rather unexpected and a 3° difference is measured between mid-span and 5% of the wall. It means that the 5% section sees a flow 3° of incidence lower than the mid-span section. This may have a big influence on the corner separation development.

It must also be mentioned that the same inlet profiles have been measured at two different setting angles (0° and 10.5°) of the whole cascade. It is thus assumed that the inlet profiles do not depend on the incidence angle.

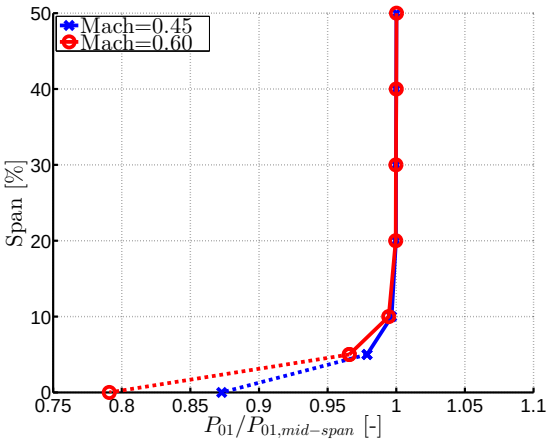


Figure 4.10: *Inlet total pressure profile*

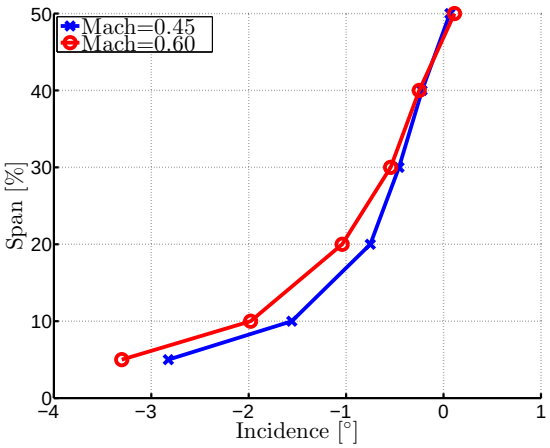


Figure 4.11: *Inlet incidence profile*

4.6 Experimental results

Before comparing the results with the correlations and the CFD predictions, the experimental data are analyzed on their own. One of the objectives of the work is the validation of CFD and correlations and those data most of the time focus on the mid-span section. Therefore, the performance of the three cascades are firstly compared in terms of losses, deviation, diffusion factor and AVDR versus incidence at 50% for both inlet Mach numbers of 0.45 and 0.60. As mentioned in Chapter 3, all those performance parameters have been computed based on pitchwise arithmetic averages (over one pitch) of the outlet total and static pressures and the outlet flow angle. Secondly, for the incidences of 0°, 6° and 9°, spanwise distributions are compared based on the measurements at 50%, 30%, 20% and 5%. The spanwise distributions of losses, turning and AVDR give a better representation of the three-dimensional nature of the flow. Finally, the evolution of total pressure loss wakes is shown for various incidences.

4.6.1 Mid-span performance

In Fig. 4.12, the averaged total pressure losses are displayed as a function of incidence. At 0° and 3°, the losses are very similar for all solidities. The lowest losses are achieved by the mid solidity. However, the measured differences are very small and sit below the uncertainty bands so that it is difficult to draw any conclusion. From 6° to the last incidence, the lower the solidity, the higher the losses. This is explained by the appearance of a stronger separation that induces larger wakes and bigger losses.

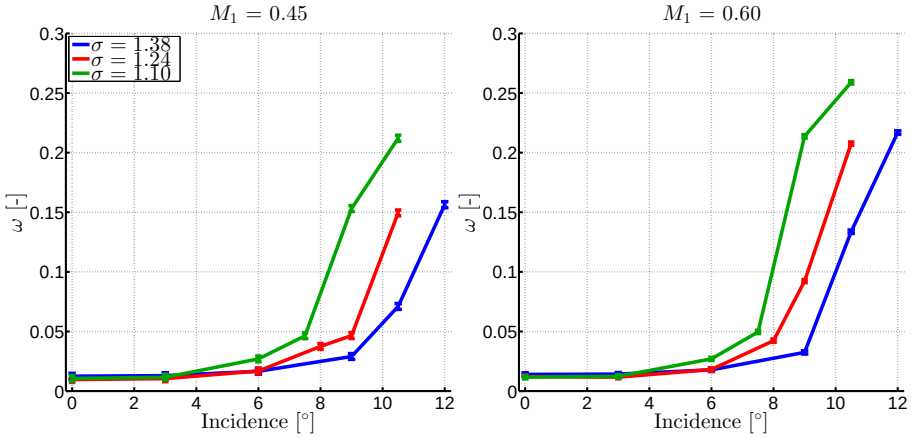


Figure 4.12: *Total pressure losses versus incidence*

The same data are plotted in Fig. 4.13 but the losses have been normalized by the losses at 0°, noted ω_0, which is approximately identical for each solidity. It is then easier to highlight that towards high incidences the losses grow faster when the solidity decreases. Two arbitrary levels of $2\omega_0$ and $5\omega_0$ have been indicated

in Fig. 4.13 in order to make the comparison easier. As an example, the lowest solidity reaches $2\omega_0$ and $5\omega_0$ approximately 3° earlier than the highest solidity. It must also be pointed out that ω_0 is a priori not the minimum loss incidence and from Fig. 4.12 and Fig. 4.13 it appears that the optimum incidence most probably sits between 0° and 3°. This issue is addressed in a following section.

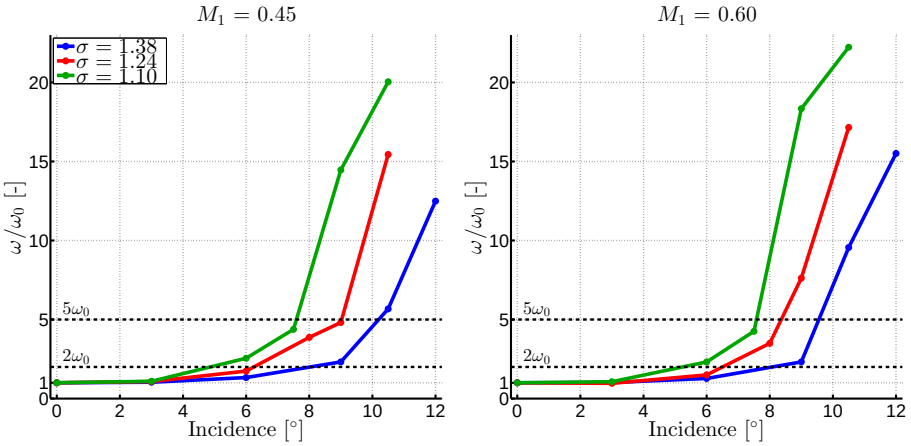


Figure 4.13: *Normalized total pressure losses versus incidence*

The turning is displayed in Fig. 4.14. It is very clear that the higher the solidity, the higher the turning. This demonstrates the guidance role of the solidity that helps the flow to follow the blade. It must be said that, at M_1=0.45 and 3°, it is believed that either the high-solidity or the mid-solidity point should most probably be considered as an outlier. Unfortunately, within the timeframe of the current experimental campaign, this measurement could not be repeated.

At low incidence, the turning rises with incidence but towards stall, the trend is not as obvious. This is especially true for the lowest solidities as the high solidity keeps a relatively linear evolution over the whole incidence range. Going to high incidence, the blade is subjected to strong separation that induces a decrease of the turning. This situation depicts a typical behavior of the lift coefficient of an airfoil in function of the angle of attack that is sketched in Fig. 4.15. Reaching high angles of attack, the flow separates and the lift decreases. Those operating conditions are usually known to be associated to separated flow and high unsteadiness and it suggests that the flow field at high incidences is most probably separated and highly unsteady.

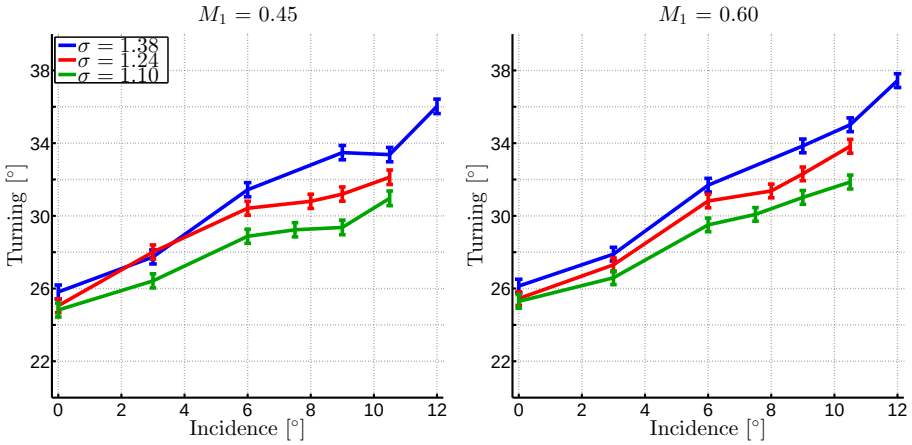


Figure 4.14: *Turning versus incidence*

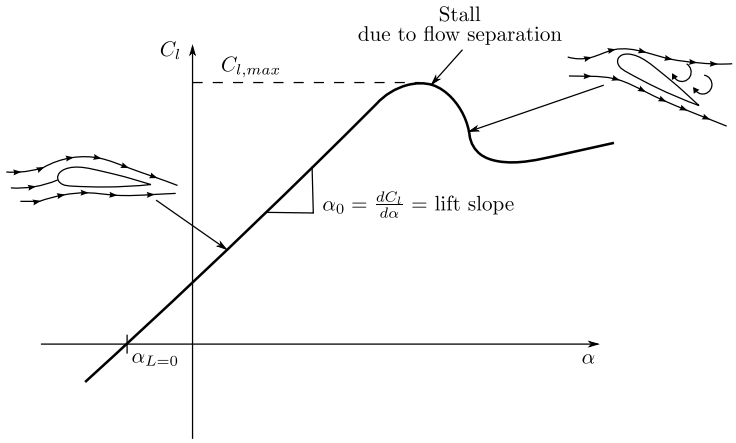


Figure 4.15: *Sketch of a typical evolution of the lift coefficient against the angle of attack [84]*

The diffusion factor as defined by Eq. (2.13) and recalled in Eq. (4.1) is shown in Fig. 4.16 against incidence.

$$D = 1 - \frac{V_2}{V_1} + \frac{\Delta V_\theta}{2\sigma V_1} \tag{4.1}$$

By definition, the lower the solidity, the higher the diffusion, and decreasing the number of blades tends to increase the loading of the blade. The evolution with incidence is not as linear as CFD results suggested in Chapter 3 (cf. Fig. 3.18). Moreover, the level of diffusion at stall is relatively low compared to typical values that usually sit between 0.5 and 0.6. This observation can be very misleading for the designer. These results suggest that more conservative

values of the maximum diffusion factor are between 0.45 and 0.50 and are depending on the inlet Mach number.

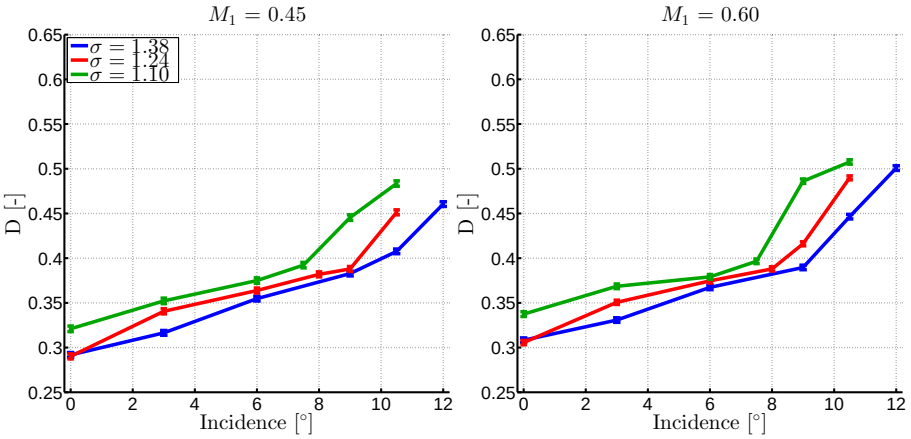


Figure 4.16: *Diffusion factor versus incidence*

The behavior of the diffusion factor is directly related to the AVDR, recalled in Eq. (4.2). The AVDR is given in Fig. 4.17 at all incidences.

$$AVDR = \frac{\rho_2 V_{ax,2}}{\rho_1 V_{ax,1}} \tag{4.2}$$

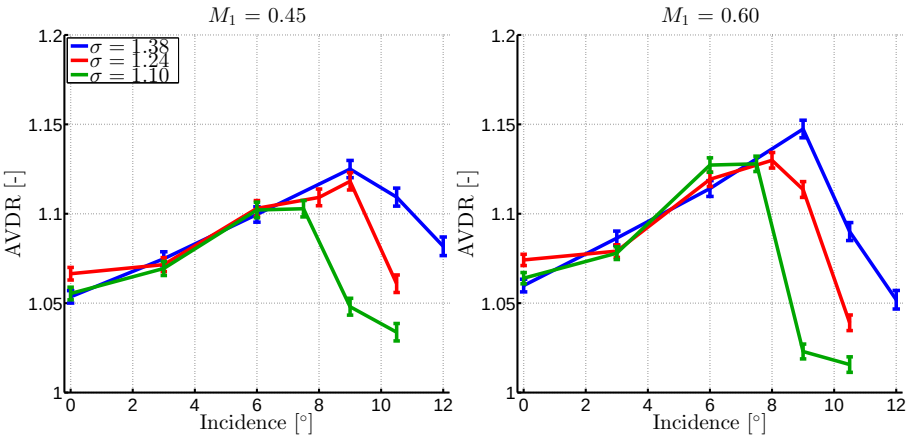


Figure 4.17: *AVDR versus incidence*

Due to presence of corner separation, most of the mass-flow goes through the mid-sections. This induces an increase of the AVDR. Going to stall, as all the blade sections begin to separate, the mass-flow is redistributed and the AVDR

decreases. The definitions of the diffusion factor (Eq. (2.13)) and of the AVDR (Eq. (2.30)) are intimately linked and when the AVDR decreases, the diffusion factor increases. The level of diffusion at optimum incidence or at stall is thus strongly dependent on the AVDR and will vary between cascade tests (with or without suction) and real compressor tests.

To remove this dependence, it may be interesting to look back at a two-dimensional diffusion factor, defined in Eq. (4.3). It is based on the assumption that the axial velocity ratio is equal to 1 (i.e. $AVDR \approx 1$) although this is not the case as it was depicted in Fig. 4.17.

$$D_{2D} = 1 - \frac{\cos(\beta_1)}{\cos(\beta_2)} + \frac{\tan(\beta_1) - \tan(\beta_2)}{2\sigma} \cos(\beta_1) \tag{4.3}$$

The two-dimensional diffusion factor is displayed in Fig. 4.18 where it can be seen that a linear trend is retrieved. The diffusion levels increased but the commonly accepted stall limit around a diffusion level of 0.6 still looks too optimistic and a more sound stall limit would be at a diffusion of 0.5. It must be mentioned that the two-dimensional diffusion factor of Eq. (4.3) may not be representative of the actual deceleration taking place on the blade suction side but, because of its linear trend, the two-dimensional diffusion factor may be more appropriate for the designer to set up design and stall criteria.

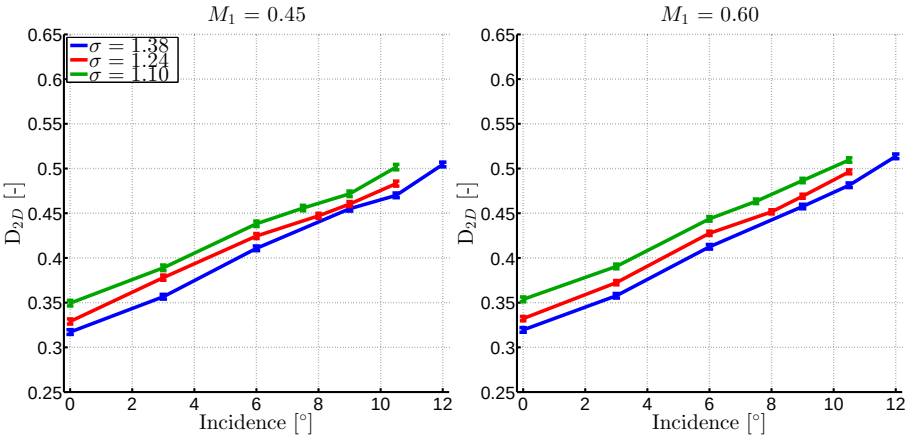


Figure 4.18: *Two-dimensional diffusion factor versus incidence*

4.6.2 Spanwise distributions

The spanwise distributions of losses are available in Fig. 4.19 at 0°, 6° and 9° for an inlet Mach number of 0.45.

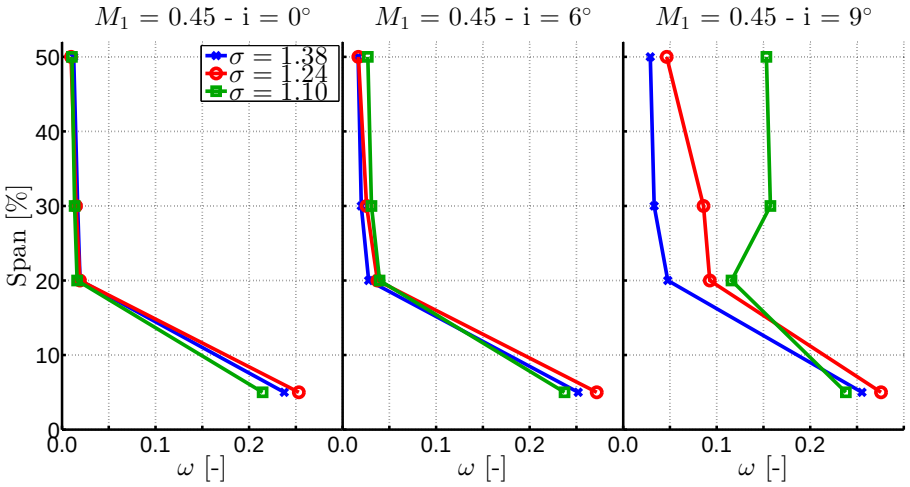


Figure 4.19: *Spanwise total pressure losses distributions at i=0°, 6° and 9° for M_1=0.45*

At 0° and 6°, the losses at 50%, 30% and 20% are very similar and the highest losses are located at 5% span. In that location, the losses do not significantly change with incidence. It indicates that this region is always separated. At 9°, the 30% and 20% sections present higher losses than at mid-span. At high incidence, the corner separation starts to influence a bigger portion of the blade and induces higher losses. However, for the lowest solidity, an unexpected pattern is observed and the 20% section shows lower losses than at 30% and 50% span. This can be explained by the incoming incidence profile. Indeed, it can be seen in Fig. 4.11, that the incidence is decreasing towards the wall. Furthermore, at 9°, the sensitivity of losses with respect to incidence is high (especially for low solidity) and a small variation of incidence of 0.5° can have substantial consequences on the losses. Some previous (proprietary) reports available at VKI indicate the same spanwise topology at high incidences [85]. Unfortunately, the inlet non-uniformity presented in Fig. 4.9 is most probably the one of the cause of the measured incidence profile.

The spanwise turning evolution is given in Fig. 4.20. The turning is always decreasing towards the wall. The trend with respect to solidity remains the same as pointed in the previous section, i.e. the higher the solidity, the higher the turning. Towards high incidences, the turning evolution of the low solidity cascade tends to be more complex and the turning at 30% and 20% is much closer to the turning at the wall. It suggests that the flow is presumably separated and consequently highly three-dimensional. Although the three-hole

probe offers a small range of insensitivity to pitch angle variations (cf. Appendix B), in such a three-dimensional flow environment, a five-hole probe would be more appropriate and would additionally provide both yaw and pitch angles.

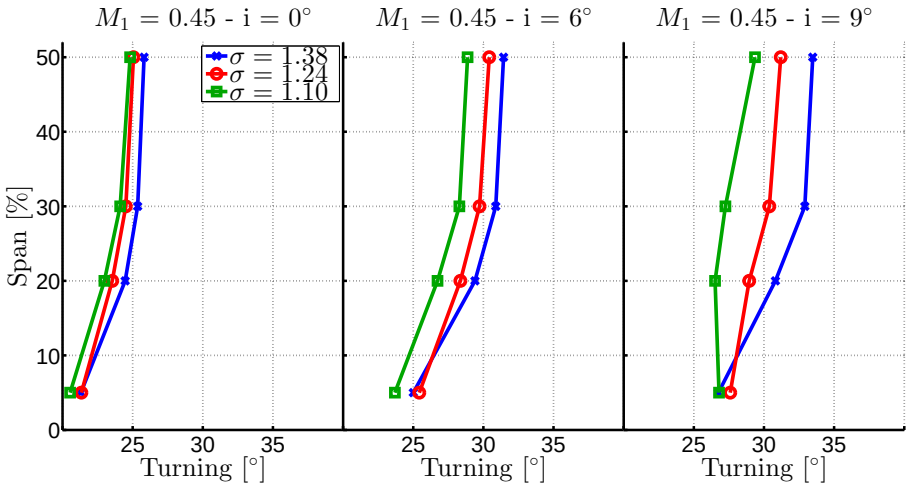


Figure 4.20: *Spanwise turning distributions at i=0°, 6° and 9° for M_1=0.45*

The diffusion factor (Eq. (4.1)) is shown in Fig. 4.21. At 0° and 6°, the diffusion is not significantly changing until 5% span. The trend observed for the low solidity at 9° is closely related to the AVDR evolution given in Fig. 4.22 which is lower at at 30% than at mid-span and 20% span.

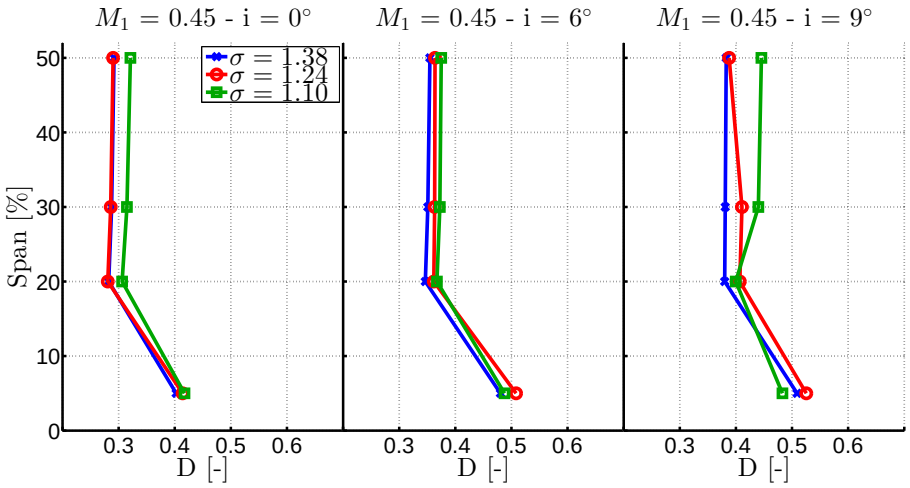


Figure 4.21: *Spanwise diffusion factor distributions at i=0°, 6° and 9° for M_1=0.45*

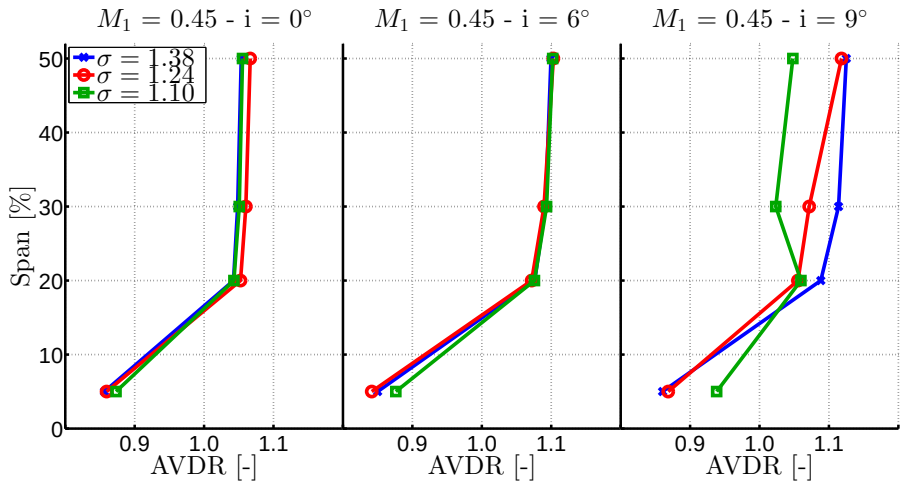


Figure 4.22: *Spanwise AVDR distributions at i=0°, 6° and 9° for M_1=0.45*

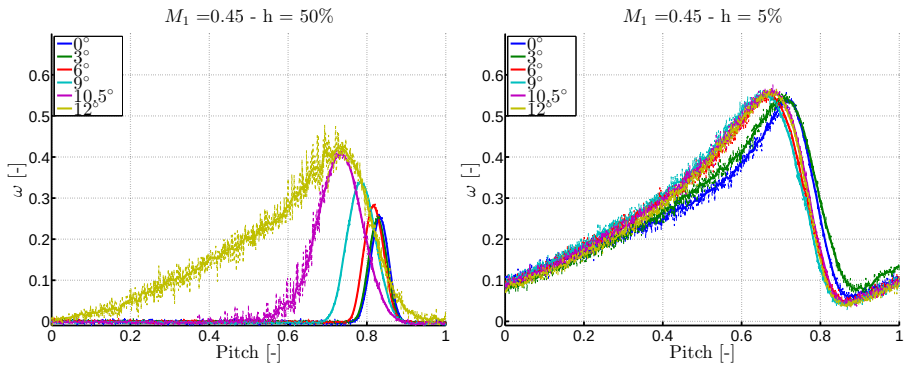
The evolution of the AVDR of Fig. 4.22 is an image of the mass-flow distribution along the span. The low AVDR at 5% is due to the corner separation inducing a high blockage and a low mass-flow. Because of the high blockage of the corner stall, the AVDR increases at mid-span. Towards high incidence, the mass-flow is redistributed along the span since the whole blade starts to be stalled and the AVDR at mid-span decreases as shown in Fig. 4.17.

Similar trends have been obtained at M_1=0.60 for all quantities and are reported in Appendix C.

4.6.3 Wakes

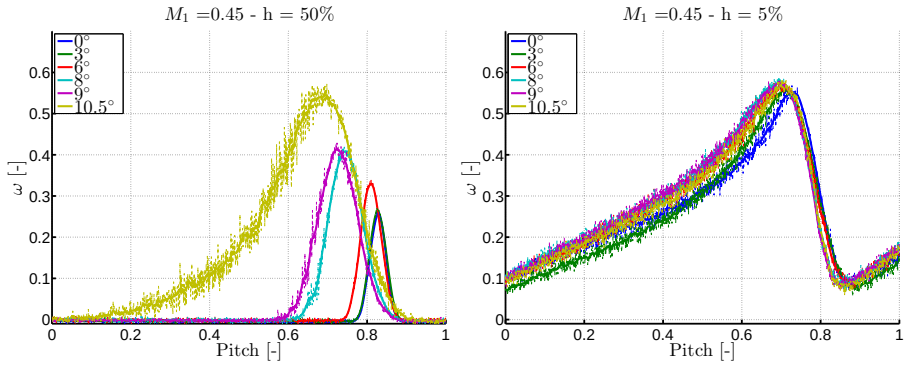
Total pressure wakes at mid-span are given in Fig. 4.23a, Fig. 4.24a and Fig. 4.25a respectively for σ=1.38, 1.24 and 1.10. Wakes at 5% are displayed in Fig. 4.23b, Fig. 4.24b and Fig. 4.25b. The plain line displayed through the data scatter is the smoothed solution obtained by applying a non-causal moving average filter [86]. A distinctive feature of such a low-pass filter is that it does alter neither the average nor the phase of the signal.

At 0°, the wakes of the three solidities are very similar but from 6°, the lowest solidity shows the most intense wakes. With such plots, the intensification and the thickening of the wakes as the incidence increases is very well depicted. At high incidence, only 10% to 20% of the pitch show a zero-loss level, meaning that 80% to 90% of the passage is affected by the suction side separation. The displacement of the loss peak is also a qualitative information about the deflection of the flow but it is difficult to extract quantitative deviation rule from such analysis. Close to the walls, the incidence has a very little impact on the wake. It shows that, initially at 0°, the flow already presents a big corner separation. Total pressure wakes at M_1 = 0.60 as well as outlet flow angles at both M_1=0.45 and M_1 = 0.60 are available in Appendix C.



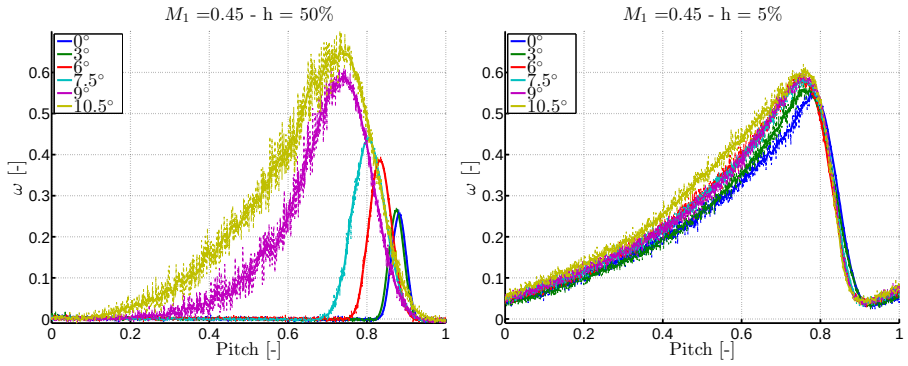
(a) *h=50%* **(b)** *h=5%*

Figure 4.23: *Total pressure loss wakes at* $\sigma = 1.38$ *and* $M_1 = 0.45$



(a) *h=50%* **(b)** *h=5%*

Figure 4.24: *Total pressure loss wakes at* $\sigma = 1.24$ *and* $M_1 = 0.45$



(a) *h=50%* **(b)** *h=5%*

Figure 4.25: *Total pressure loss wakes at* $\sigma = 1.10$ *and* $M_1 = 0.45$

4.7 Comparison with CFD and correlations

Within this section, the measurements are compared to the CFD predictions and the existing empirical correlations exposed in Chapter 2. The emphasis is set on the comparison of the minimum loss incidence data at mid-span since the correlations usually focus on those specific operating conditions. However, the off-design performance are also commented. The establishment of updated correlations is approached for the various performance parameters.

As mentioned in Chapter 3, regarding the CFD data, post-test calculations have been performed. The geometrical model is slightly different than the configuration of Chapter 3. The main difference resides in the position of both inlet and outlet measurement planes that have been moved to the same position as in the test section. A picture of the model is shown in Fig. 4.26.

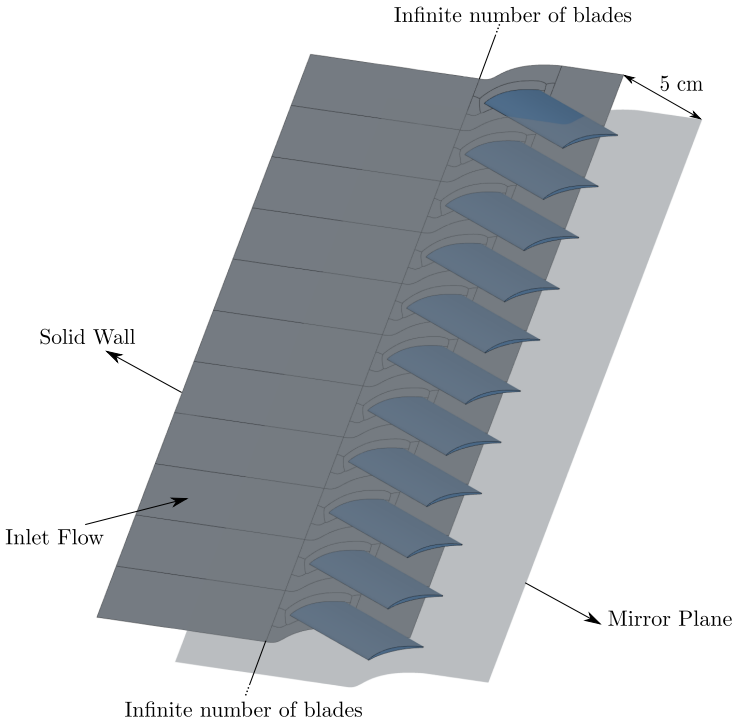


Figure 4.26: *Geometrical model used for the post-test CFD computations*

While the inlet of the pre-test CFD model was located one chord upstream, the experimental inlet measurement plane is positioned approximately three chords upstream. Likewise, the position of the outlet was set according to the location of the downstream static pressure taps. Only half of the span has been meshed and mirror boundary conditions have been set at mid-span. The final grid counts 2.500.000 cells and ensures a $y^+ < 1$ at the walls. For the boundary

conditions, the measured total pressure and flow angle inlet profiles have been used (cf. Fig. 4.10 and Fig. 4.11). Since the turbulence intensity and length scale have not been measured, a constant turbulence intensity profile of 1% has therefore been considered as well as a turbulence length scale equal to a tenth of the hydraulic diameter [71] ($\ell = 0.1 \times D_H \approx 4mm$). In the following, the experimental data are analyzed against results of both CFD models referred to as *pre-test* and *post-test* CFD. This enables to assess the importance of realistic boundary conditions in the CFD predictions.

Unlike the numerical investigation of Chapter 3, the computations have only been done at the measurement points and no specific refinement has been applied in incidence in order to identify the optimum incidence as well as the last numerically stable incidence. The prediction of the optimum incidence is more specifically addressed in the next section.

4.7.1 Optimum incidence prediction

4.7.1.1 Loss curve analysis

The total pressure losses for the three solidities are displayed in Fig. 4.27 against both initial and updated CFD models. Firstly it appears that, above 9° of incidence, the measured losses rise up to 15% or 20% while the CFD never exceeds 5% over the whole incidence range.

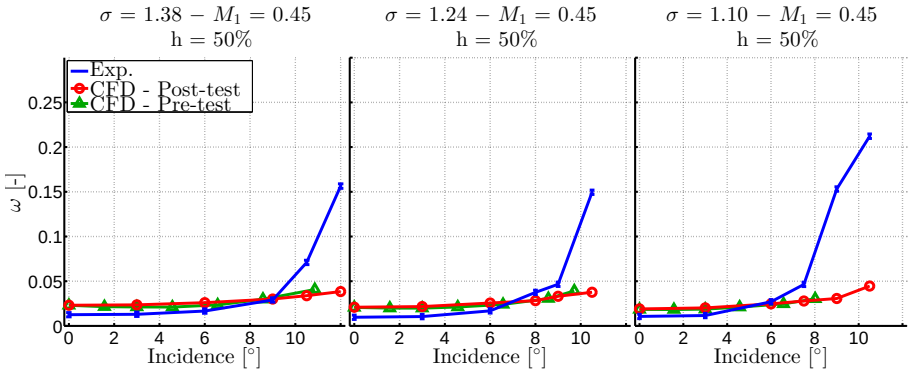


Figure 4.27: *Total pressure losses versus incidence for experimental data and both pre-test and post-test CFD models*

In Fig. 4.28, the loss scale is cut at 5% in order to get a closer look at the behavior of the loss curve at low incidence. It appears that the CFD predictions always overestimate the losses at 0° by about 1% (absolute). Increasing the incidence, the measured data quickly overtake the CFD results that fail in capturing the loss rise.

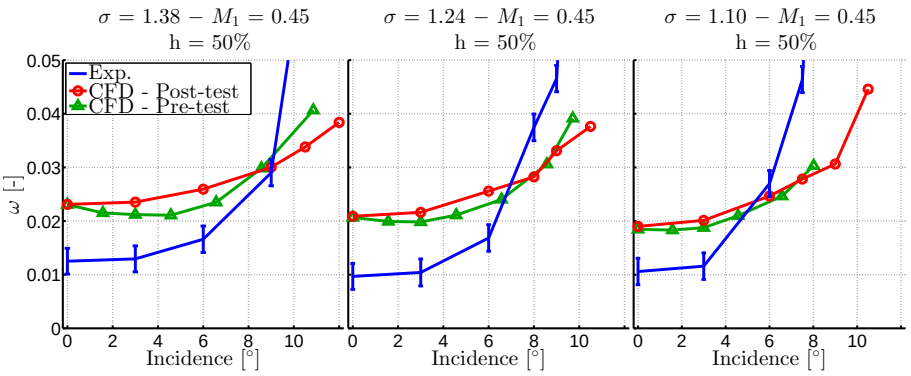


Figure 4.28: *Total pressure losses versus incidence for experimental data and both pre-test and post-test CFD models - Limited scale*

The disagreement at low incidence may also be attributed to the inlet turbulence intensity that is not accurately known and to the state of the blade boundary layer. Although it is assumed that the boundary layer is fully turbulent similarly to engine applications, the Reynolds number ($\approx$ 340.000 at M_1=0.45) is very close to the transitional zone (cf. Kiock [74]). It is even more true considering the very small turbulence level of such cascade wind tunnels. The turbulence level has not been measured during the current experimental investigation but is around 0.95% according to previous measurements performed within the TATMo European project in 2009 (Mesbah et al., [56]). At similar Reynolds and turbulence conditions, Ma [87] observed very transitional boundary layers during compressor cascade tests. Ma [87] recommends to apply trips (i.e. sandpaper) close to the leading edge to force the blade boundary layer to be turbulent. This has not been done in order to maintain a representative blade profile and, in particular, the blade surface roughness (Ra$\approx$0.8). Furthermore, measurements performed at higher Reynolds number (up to 900.000) indicate similar differences between numerical and experimental data at low incidences for various values of the Reynolds number. Results are given in a further section (cf. Sec. 4.7.1.2) together with isentropic Mach number measurements. In the end, it is not possible to draw any conclusion on the blade boundary layer features without properly measuring the blade boundary layer development by optical measurements (LDV or PIV) or blade surface measurements (static pressure taps or hot films).

The discrepancy between the numerical and the experimental results at low incidence may also be explained by examining the evolution of AVDR that is presented in Sec. 4.7.3. Since the secondary flows are not well computed, the blockage is different as well as the mass-flow distribution. This results in a different AVDR at mid-span between the measurements and the numerical calculations and this difference may then have an effect on the total pressure losses as suggested experimentally in [31, 32] or numerically in [33]. More de-

tails will be given in Sec. 4.7.3 when comparing the measured and computed AVDR.

Very small differences are noticed between the two CFD predictions (pre- and post-). It shows that the inlet boundary layer has very little consequences on the performance at mid-span. Nonetheless, with the updated configuration, the losses at 3° are always slightly higher than at 0°. It indicates that the minimum loss incidence moved to lower incidences. The same behavior is observed in the experimental data and the optimum incidence may be affected by the presence of the inlet boundary layer and stronger secondary flows.

Regarding the stability range, it seems that the post-test CFD model is more stable because it reaches higher incidences (especially for $\sigma = 1.10$). It is believed that this due to the experimental inlet incidence profile as well as to the position of the outlet plane that is further down the trailing edge compared with the pre-test configuration. No attempt has been dedicated to reach the stability limit of the post-test CFD model and higher incidences may be reached.

In Fig. 4.29, the losses are normalized by the losses at 0° and the loss scale is limited to $5\omega_0$. The CFD data barely reach $2\omega_0$ while the experimental results go above $5\omega_0$. Both CFD computations predict similar trends and do not predict the loss rise at high incidence. An important observation is that, at a given incidence, the lower the solidity, the bigger the discrepancy between both CFD and experimental data. This is explained the growth of the loading and the diffusion as the solidity decreases. The adverse pressure gradient encountered on the blade suction side becomes then stronger and the CFD predictions seems then less accurate. In other words, the higher the diffusion, the more the CFD is failing.

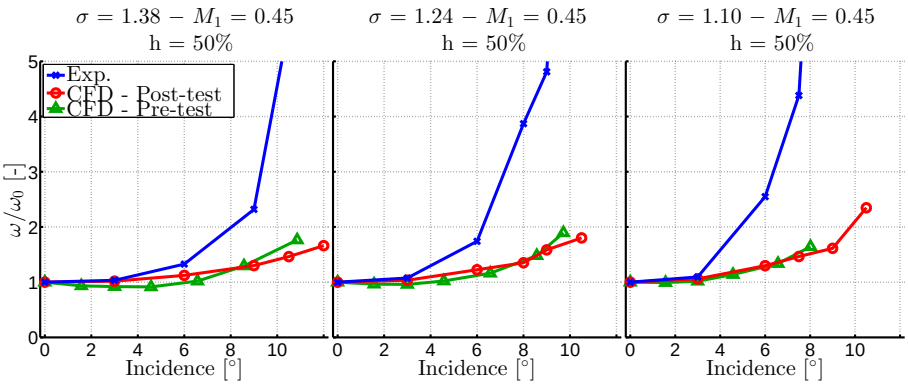


Figure 4.29: *Normalized total pressure losses versus incidence for experimental data and both pre-test and post-test CFD models*

In order to predict the optimum incidence, some curve fitting methods must be applied because of the discrete resolution of incidence. The influence of the inlet Mach number has been neglected and the optimum incidence is supposed to be independent from the Mach number. If a typical loss bucket is guessed, some assumptions can be done on the order of the curve fit. For instance, based on Fig. 2.2, it can be assumed that the loss curve should have only one single minimum (i.e. the minimum loss incidence) and have a strictly positive curvature over the whole incidence range. This leads to even degree polynomials which are symmetric with respect to the minimum loss incidence.

Although typical off-design predictions suggest to use parabolas (e.g. [23, 88, 89]) that would satisfy the above-mentioned constrains, a fast analysis of the scatter of the data reveals that the fit order should be higher than 2. The next possibility is the following 4^{th} order polynomial:

$$\omega = (a\,i + b)^4 + c \tag{4.4}$$

Finding the coefficients a, b, c such as Eq. (4.4) minimizes the distance of the data points to the fit enters the field of non-linear least square curve fitting. Some methods exist in advanced processing tools such as MATLAB® and results are given in Fig. 4.30.

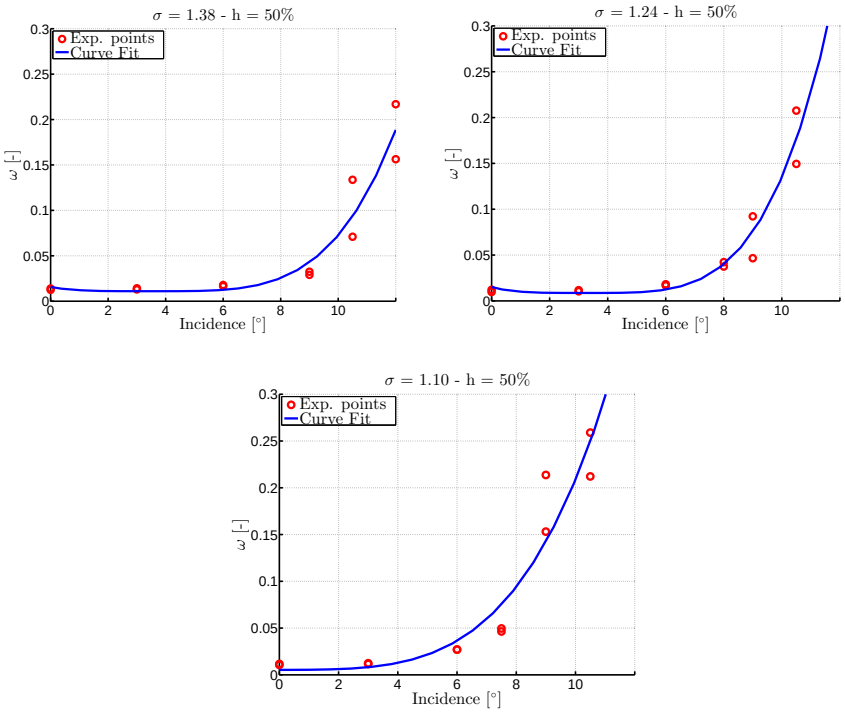


Figure 4.30: *Total pressure loss 4^{th} order curve fit for σ =1.38, 1.24 and 1.10 - Experimental data*

A standard 4^{th} order linear least square regression was also considered (i.e. $\omega = \kappa_4\, i^4 + \kappa_3\, i^3 + \kappa_2\, i^2 + \kappa_1\, i + \kappa_0$) but the resulting polynomial was not satisfactory and only a non-linear least square approach such as Eq. (4.4) did offer a physical loss evolution against incidence.

However, using such a high order fit, the prediction of optimum incidence is very much affected by the data at high incidence. For this reason, a standard second order fit like Eq. (4.5) has also been considered using only the 4 lowest incidences.

$$\omega = a\, i^2 + b\, i + c \tag{4.5}$$

The resulting curve fits are shown in Fig. 4.31 together with the experimental data points at all incidences. It must be emphasized that above the fourth incidence, the polynomials are not valid and they have only been used to get an estimate of the optimum incidence. Because the post-test computations did not present a minimum in the loss curve like the pre-test results, the same quadratic fit has been applied to the post-test CFD data. Curve fits of the numerical post-test results are shown in Fig. 4.32 where it can be seen all incidences have been used to establish the polynomial and that parabolas do match nearly perfectly the numerical loss evolution.

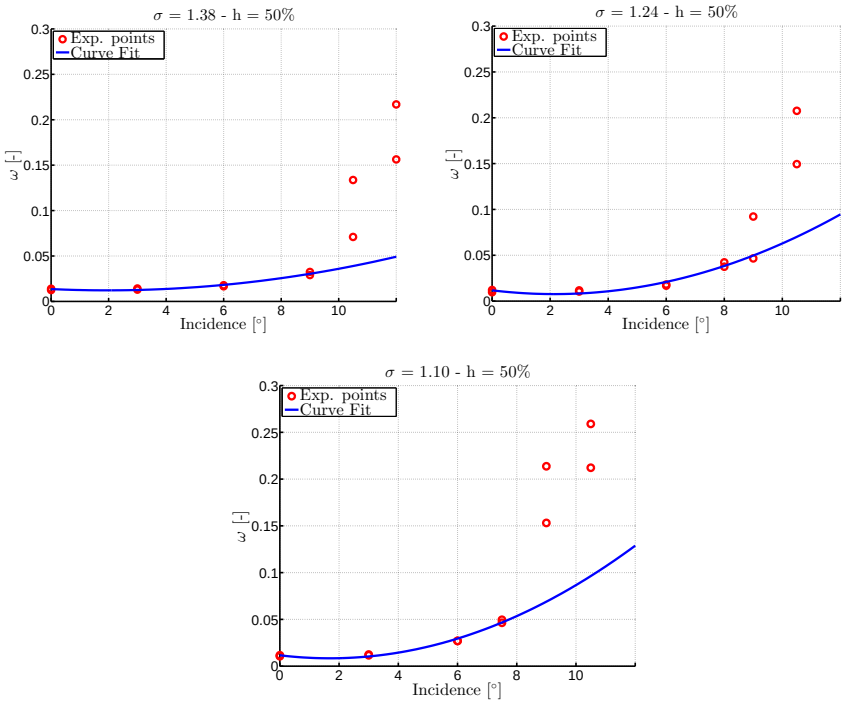


Figure 4.31: *Total pressure loss 2^{nd} order curve fits for σ =1.38, 1.24 and 1.10 - Experimental data*

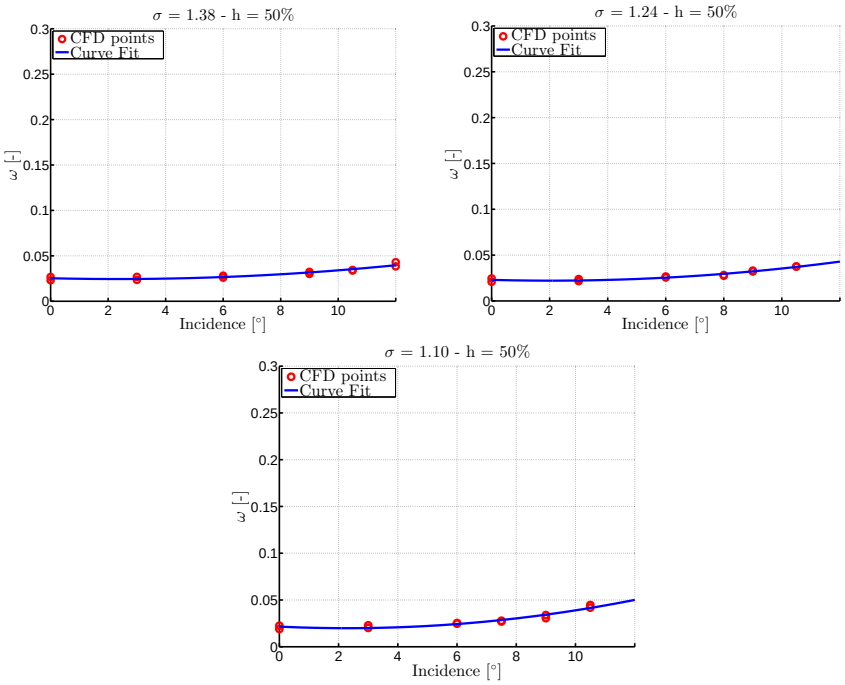


Figure 4.32: *Total pressure loss 2^{nd} order curve fits for σ =1.38, 1.24 and 1.10 - Post-test CFD data*

The experimental optimum incidences are plotted in Fig. 4.33 in function of solidity for both the 4^{th} and 2^{nd} order polynomials. Both pre- and post-test CFD optimum incidences have been added as well as the NASA correlations. Linear trends have been assumed (dashed lines) since the correlations suggested a linear behavior of the optimum incidence versus solidity. As shown in Fig. 4.33, the experimental trends do not agree with each other. The same observation can be done for both CFD models. The post-test results offer satisfactory agreement with the 2^{nd} order fit of the experimental data. This was expected since at low incidence the updated CFD geometry presented a similar loss evolution.

The analysis of Fig. 4.33 clearly shows that the prediction of optimum incidence is not unambiguous. Particularly, the lack of information on the negative incidence side of the loss curves prevents to draw any definitive conclusion. Unfortunately, the exploration of the negative incidence was not included in the industrial scope of the work. Considering the very flat loss evolution at low incidences, an error of 1° or 1.5° will not have tremendous consequences on the minimum loss prediction. However, in terms of operating range, 1° becomes significant and the missing information on the negative incidence side of the loss bucket may also have an important impact. In the following sections, the

experimental optimum incidences have been considered to be given by the 2^{nd} order fit. This choice is simply driven by the need of extrapolation at negative incidence if the 4^{th} order polynomial is selected.

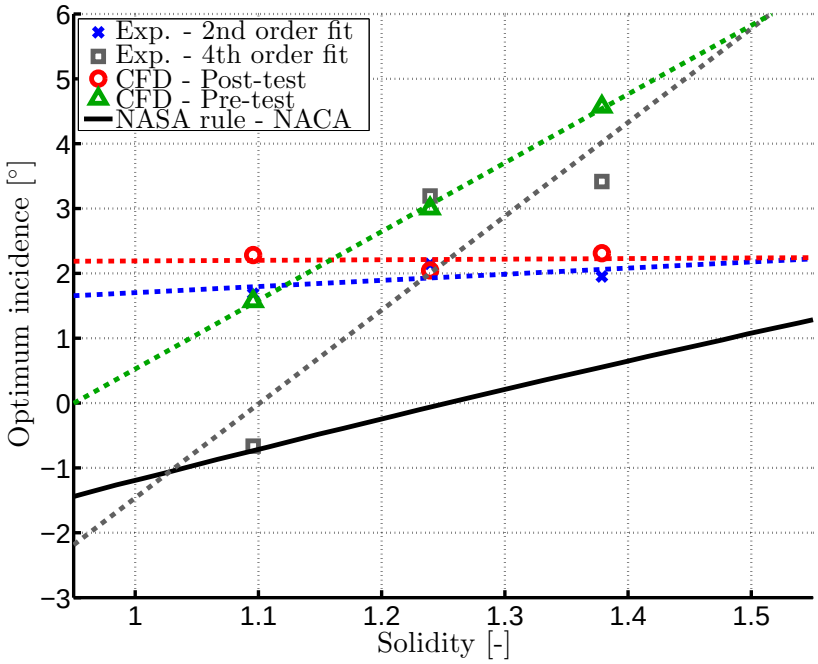


Figure 4.33: *Comparison of optimum incidence predictions*

4.7.1.2 Blade isentropic Mach number distribution analysis

Blade isentropic Mach number distributions can also support, in a qualitative way, the determination of the optimum incidence. Because of the small chord (33.09mm) and its very small thickness (max. 1.6mm), the baseline blade could not be instrumented. Within the work of [83], a scale-2 cascade model having the same solidity (i.e, c=66.18mm, s=48mm, $\sigma = 1.38$) was tested in order to highlight some Reynolds and aspect ratio effects for the same solidity. On this model, suction side static pressure measurements were also perform. A picture of the instrumented blade is given in Fig. 4.34 where the 22 suction side static pressure taps can be seen. A spanwise translation mechanism attached to the blade enabled automated measurements at different span heights. The pressure side is not instrumented.

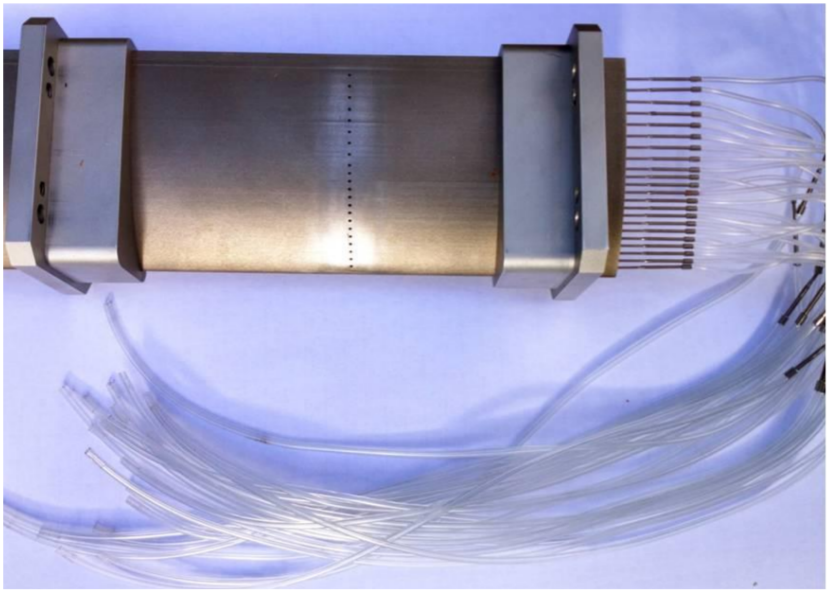


Figure 4.34: *Picture of the instrumented blade*

Inserting the scale-2 blade profile in the same numerical model as sketched in Fig. 4.26, computations have been run at same incidences and inlet Mach numbers. The suction side static pressure distributions have been extracted and the blade isentropic Mach number distributions have been computed. The same turbulence model and numerical scheme have used. It should not be forgotten that, since the chord has been scaled up, the chord-based Reynolds number increased to 680.000 compared to the baseline.

A wider study of the effect of aspect ratio was also considered by decreasing the chord (and decreasing the pitch to keep the same solidity). This is reported in [83]. Big discrepancies in terms of total pressure losses emerged from 20% of the span to the wall and over the whole incidence range (from 0° to 12°) but the work demonstrated no total pressure loss difference at mid span.

Both experimental and numerical loss buckets at mid-span are given in Fig. 4.35 and Fig. 4.36 for the baseline and the low aspect ratio cascades at M_1=0.45 and M_1=0.60. Some discrepancies emerge at high incidence due to very different secondary flow development but at low incidence, very small differences are depicted between both aspect ratios. The predictions of CFD are also very similar at low incidence. It is therefore assumed for the following discussion that the effect of aspect ratio can be disregarded as far as the mid-section performance are concerned.

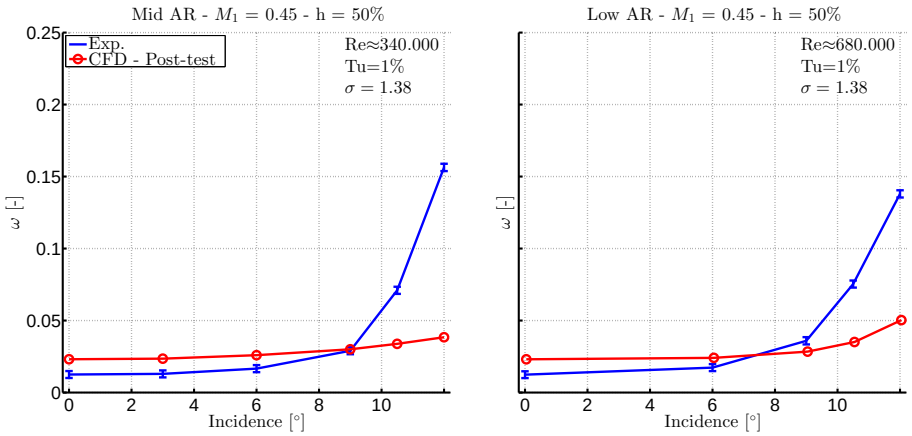


Figure 4.35: *Total pressure losses versus incidence for the baseline and the low AR cascades - M_1=0.45*

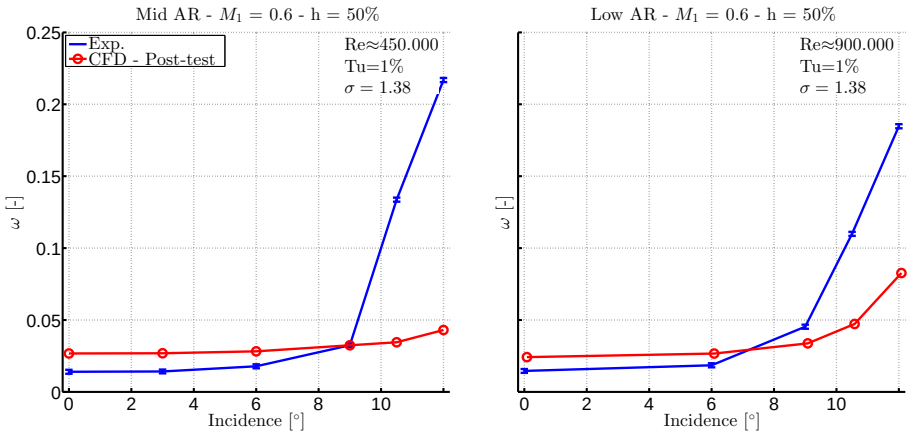


Figure 4.36: *Total pressure losses versus incidence for the baseline and the low AR cascades - M_1=0.60*

The measured isentropic Mach number distributions are shown next to the CFD results in Fig. 4.37 for $M_1 = 0.45$. The agreement between both experimental and CFD data is extremely good until 9°. At higher incidence, the measurements show a constant isentropic Mach number from 50% of the chord to the trailing edge, indicating flow separation. On the other hand, the CFD distributions still show deceleration on the rear part of the suction side. It illustrates that the rear separation and the growth of losses occurring at high diffusion is not properly simulated.

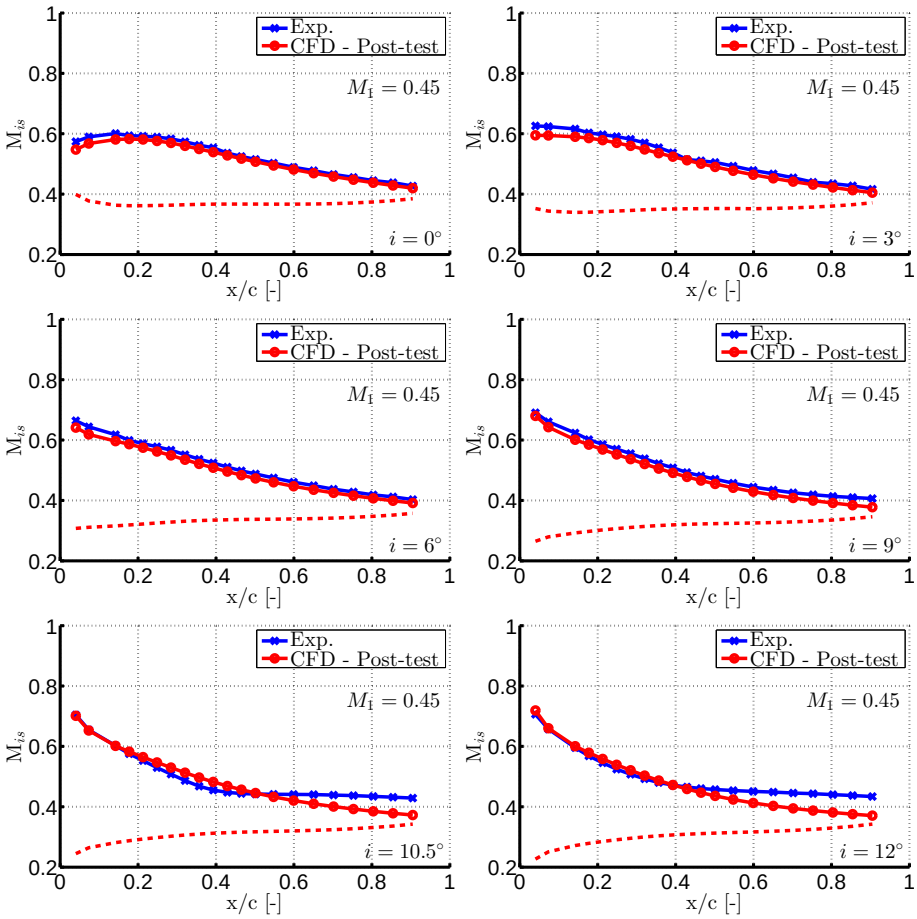


Figure 4.37: *Experimental and numerical isentropic Mach number distributions ($M_1 = 0.45$ - scale-2 model)*

Regarding the determination of the optimum incidence, the analysis must be focused on the first 10% of the blade chord. The Mach number distributions at 0° still reflect the presence of an acceleration at the pressure side leading edge and the suction peak velocity is relatively far from the leading edge, around 20% of the blade chord. Going to 3°, the peak velocity moves towards the leading edge. Such a distribution resembles to a state-of-the-art controlled diffusion distribution. At 6° and higher incidences, the peak velocity is at the very front of the blade. Assuming that the optimum incidence at mid-span is not affected by the aspect ratio and the Reynolds number, the qualitative analysis of Fig. 4.39 confirms that the optimum incidence of the baseline solidity profile is between 0° and 3°. Similar conclusions can be drawn at $M_1 = 0.60$ as displayed in Fig. 4.38. Moreover, for low incidences (i.e. close to optimum conditions), Fig. 4.38 also shows that the profile operates under critical conditions.

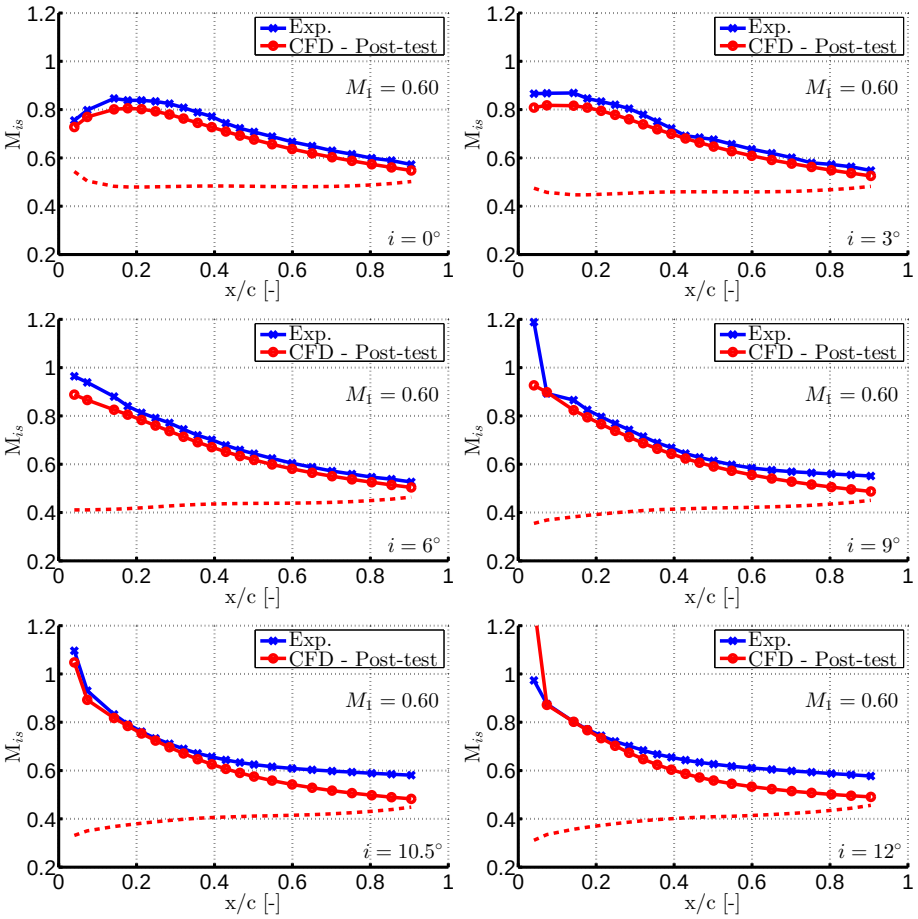


Figure 4.38: *Experimental and numerical isentropic Mach number distributions ($M_1 = 0.60$ - scale-2 model)*

The rear suction separation can also be directly related to the total pressure loss wakes that are compared at 9° and 12° in Fig. 4.39. It proves that the growth of the wake due to a rear suction side separation as the incidence increases is not accurately computed. For the baseline solidity, further comparisons of the complete outlet flow topology are given in Appendix C at 3° and 9°.

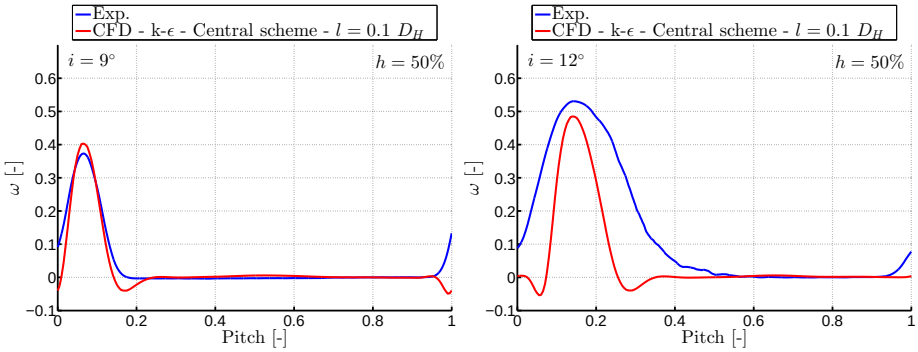


Figure 4.39: *Comparison of experimental and numerical total pressure loss wakes at 9° and 12° for the scale-2 model ($M_1 = 0.45$)*

4.7.2 Deviation rule

Before comparing the deviation at optimum incidence, the results are given over the whole incidence range in Fig. 4.40.

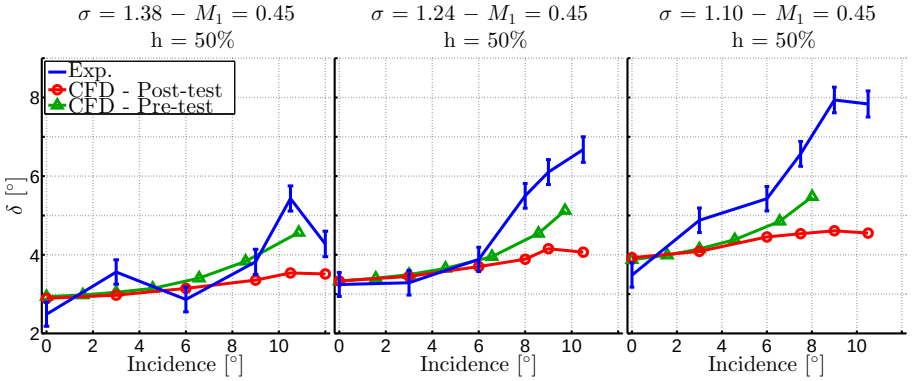


Figure 4.40: *Deviation versus incidence for experimental data and both pre-test and post-test CFD models*

The agreement between both CFD models is very good until 6°. Above that value, the influence of secondary flows arises and the deviation from the post-test calculations is lower than the pre-test results. The agreement with the experiments is satisfactory taking the uncertainties into account. Nonetheless, from the comparison between the experimental data and both CFD models, it appears that the predictions become worse as the solidity decreases. It must also be pointed out that, once separation occurs, the measured deviation is approximately 1.5 times higher than the CFD.

Interpolating the deviation at the optimum incidence obtained in the previous section, the data can be plotted versus solidity together with the CFD

data. By analogy with the NASA correlations (cf. Eq. (2.7)), a 2-parameter curve fit is defined in Eq. (4.6).

$$\delta = \frac{m\phi}{\sigma^b} \tag{4.6}$$

The only difference with Eq. (2.7) is the absence of a zero-camber deviation. However, having only 3 points for the curve fit (i.e. 3 solidities), only a two-parameter fit may be derived. Both parameters m and b of Eq. (4.6) are found by a linear least-square regression after rewriting Eq. (4.6) under the form of Eq. (4.7).

$$\log\left(\frac{\delta}{\phi}\right) = -b\log\sigma + \log m \tag{4.7}$$

In Fig. 4.41 and Fig. 4.42, the agreement between both CFD and experimental rules is very satisfactory and they all corroborate the fact that the NASA rule needs to be updated for such a profile. The discrepancy between CFD and experimental results is lower than 0.5°. It can also be observed that the deviation at optimum incidence slightly decreases for M_1=0.60. The decrease is lower than 0.5° but has been measured and predicted by CFD. This compressibility effect had already been identified for some profiles (cf. Fig. 2.29 and Fig. 2.30) and, most of the time, it was considered as negligible. If accurate predictions are required, compressibility corrections should be included. Given that the effect of Mach number is very small, it appears reasonable to neglect it.

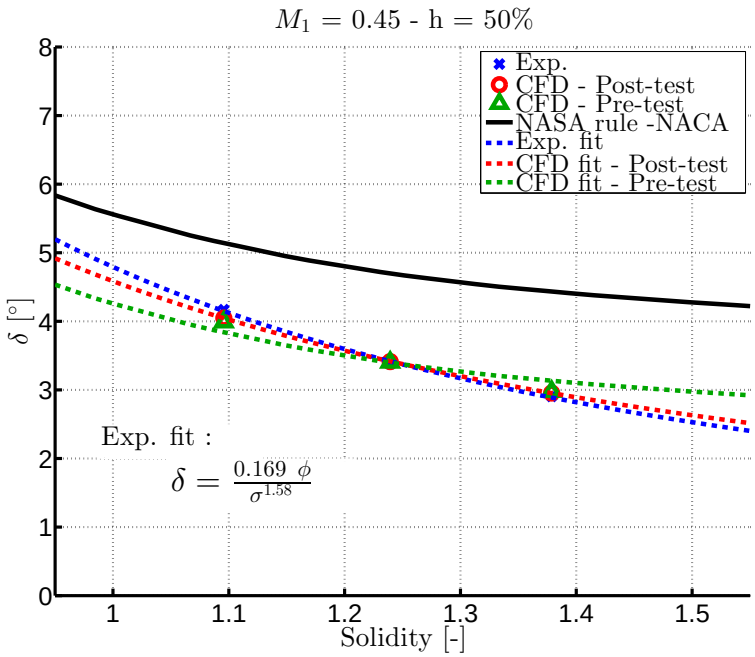


Figure 4.41: *Deviation at optimum incidence for M_1=0.45*

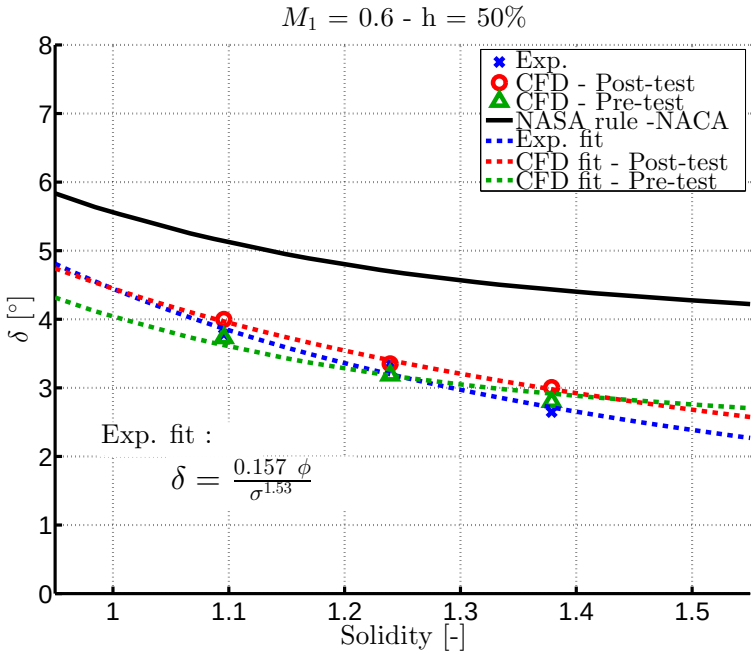


Figure 4.42: *Deviation at optimum incidence for M_1=0.60*

4.7.3 Diffusion factor, AVDR and loss parameters

The diffusion factor versus incidence is given in Fig. 4.43. As mentioned earlier, the calculation of the diffusion factor is very sensitive to the AVDR. The latter is given in Fig. 4.44. As the experimental data and both CFD results operate at different axial velocity ratios (which indicates they all have different secondary flow topologies), they all lead to a different diffusion factor at mid-span. The highest diffusion factor appears in the pre-test CFD results. The presence of an inlet boundary layer generates more secondary flows and more blockage at the wall. Most of the flow passes through the mid-sections and the AVDR increases. However, an AVDR different from 1 may also occur when the flowpath presents a contraction or an opening. Finally, depending on the AVDR, very different diffusion levels may be obtained at design or at stall and this may compromise some design choices.

The use of the two-dimensional diffusion factor of Eq. (4.3) may help to remove this dependence because it only relies on flow direction rather than on velocities. It is shown in Fig. 4.45. All the curves collapse. It confirms that the velocity triangles are well captured in terms of flow angles and that the axial velocity ratios are responsible for the disagreement in diffusion factors. For the pre-test CFD data, the comparison of Fig. 4.43 and Fig. 4.45 does not show big differences since the AVDR was already close to 1 but big discrepancies are observed between the experimental data and the post-test CFD results. In Fig. 4.45, the level of diffusion at high incidence is close to 0.5. This level of diffusion sits below the commonly accepted stall limit of Lieblein which is around 0.6.

The two-dimensional diffusion factor is just an approximation and may not represent the diffusion at which the blade operates but it definitely looks very useful to establish design or stall criteria since it is not affected by the AVDR. Moreover, because it presents a very good agreement with the numerical data, a recommendation for design purposes would be to use both definitions of diffusion factors (Eq. (4.1) and 4.3) with a stall criterion relying on the two-dimensional diffusion factor (for example, $D_{2D} = 0.5$).

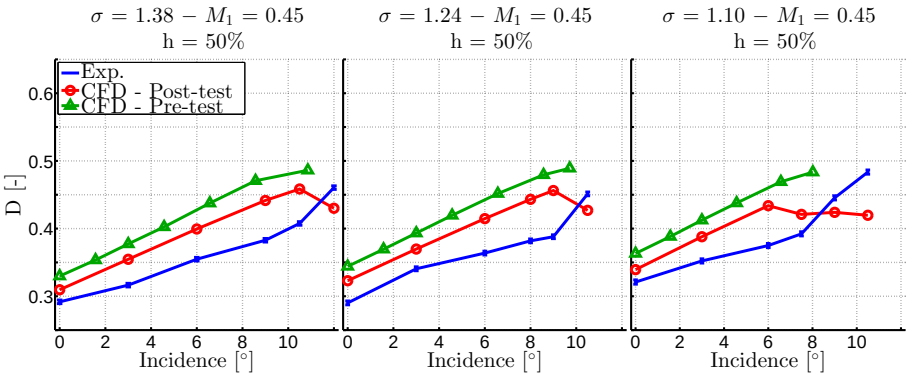


Figure 4.43: *Diffusion factor versus incidence for experimental data and both pre-test and post-test CFD models*

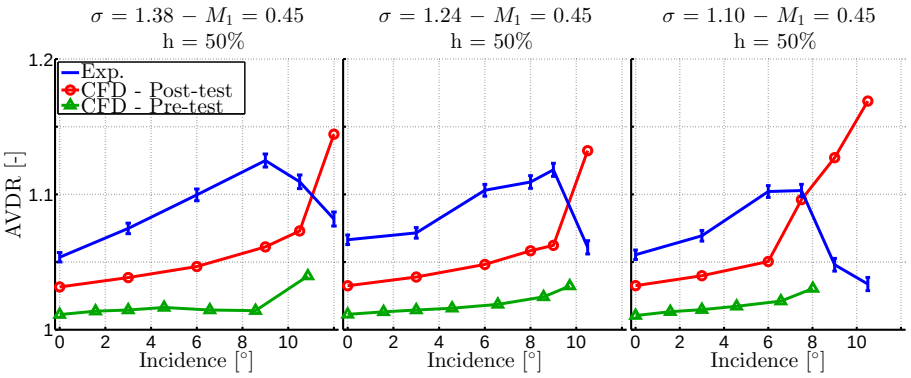


Figure 4.44: *AVDR versus incidence for experimental data and both pre-test and post-test CFD models*

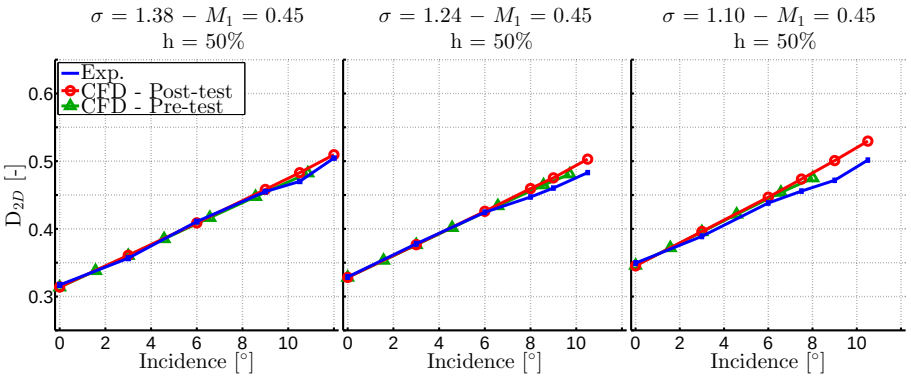


Figure 4.45: *Two-dimensional diffusion factor versus incidence for experimental data and both pre-test and post-test CFD models*

Before analyzing the loss parameters, specific attention must be dedicated to the analysis of Fig. 4.44 and the discrepancy between the experimental and the numerical AVDR at low incidence. Since the secondary flows are not well captured by CFD (already at low incidence), the resulting blockage and the AVDR vary between the measurements and the computations. This can directly affect the prediction of losses and, as exposed in [31, 32, 33], when the AVDR increases, the losses tend to decrease. Comparing Fig. 4.27 and Fig. 4.44, it can indeed be observed that as the experimental conditions present a higher AVDR, lower losses are achieved. This is explained by an increased outlet total pressure at mid-span as the exit velocity is increased when the AVDR grows. To improve the prediction of losses at mid-span, it was attempted to simulate properly the flow at mid-span with a quasi-3D blade model presenting a streamline contraction such that an AVDR equal to the experimental level is generated. Without reaching the measured losses, a better prediction of the mid-span losses could then be obtained but the study revealed that the AVDR is not a sufficient parameter to characterize the operating conditions of the blade. Ideally, it is the whole static pressure distribution all along the pressure and suction sides (i.e. the actual blade loading) that should be maintained constant between the measurements and the calculations. Only in those conditions, the development of the blade boundary layer and the generated wake momentum thickness could be fairly compared between the experimental and numerical results. This is a very complex problem and more efforts should be devoted to this specific task before drawing any firm conclusion. Nonetheless, this issue demonstrates that the influence of the secondary flows should never be disregarded.

In Fig. 4.46, the loss parameter ζ_1 of Eq. (2.17) is given versus diffusion factor (Eq. (4.1)) for both Mach numbers. The scatter of the original data of Lieblein available in Fig. 2.20 is represented by an uncertainty band marked by two dashed lines. Instead of interpolating the performance at optimum incidence, data at 0°, 3° and 6° are plotted for both experimental and CFD results. At those three incidences, nearly all the data points fall within the uncertainty band of the original cloud of points of Fig. 2.20. One experimental data point falls out the band and corresponds to the low solidity data at 6°. At low solidity, this incidence is most probably already too far from optimum conditions. The compressibility effects are very limited and it seems that such a correlation curve may be used for both Mach numbers. This is true until M_1=0.60 but higher Mach numbers may lead to different conclusions.

The second loss parameter ζ_2 (cf. Eq. (2.18)) is given in Fig. 4.47 for both M_1=0.45 and M_1=0.60. The agreement is as satisfactory as with ζ_1 in Fig. 4.46. As mentioned in Chapter 3, this loss parameter is most probably a better estimate of the wake momentum thickness but regarding the prediction of total pressure losses and the effect of solidity, both loss parameters offer similar quantitative predictions. From an experimental point of view, ζ_1 is easier to measure and will always present lower uncertainties than ζ_2 since less quantities are considered for the determination of ζ_2.

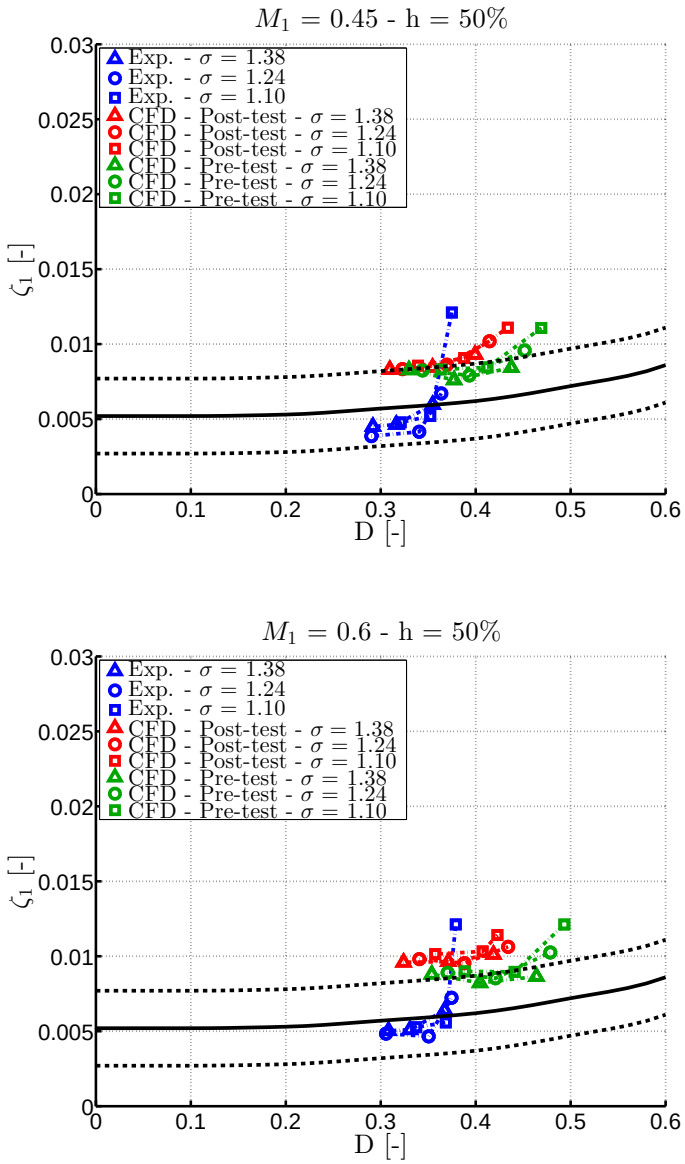


Figure 4.46: *Loss parameter ζ_1 versus diffusion factor at M_1=0.45 and M_1=0.60*

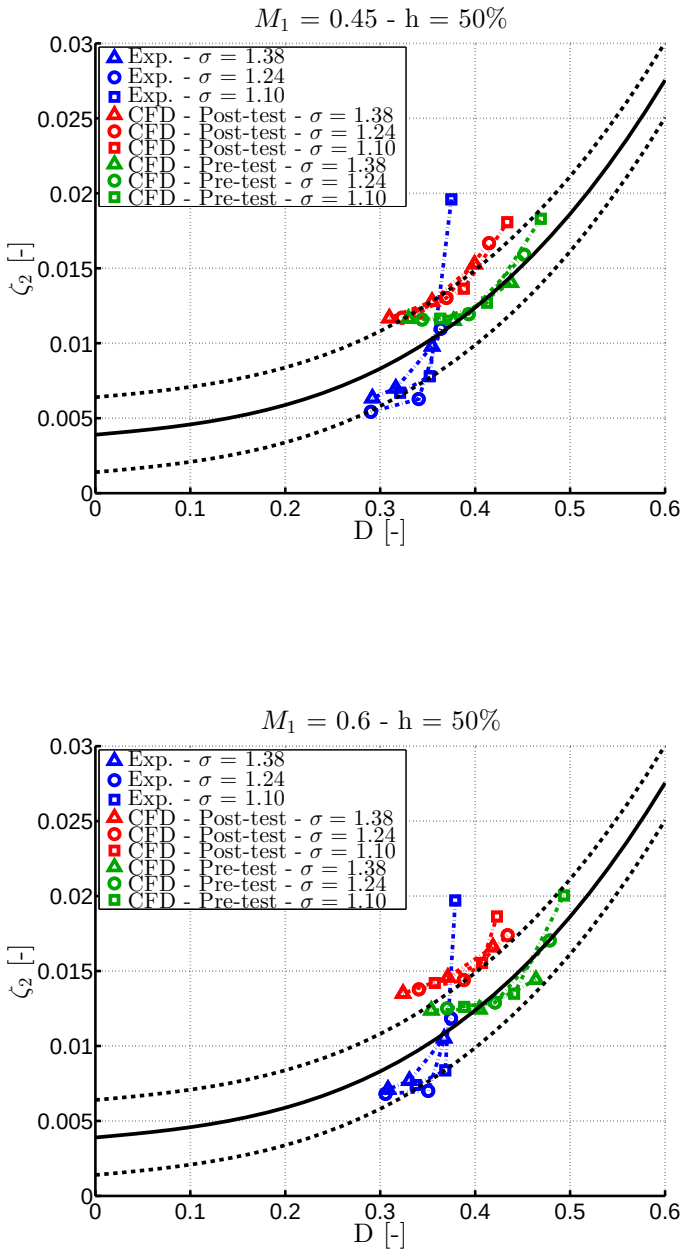


Figure 4.47: *Loss parameter ζ_2 versus diffusion factor at M_1=0.45 and M_1=0.60*

The same can be done using the two-dimensional diffusion factor in Fig. 4.48 and Fig. 4.49 for ζ_1 and ζ_2. Similar observations can be done as when using the standard definition of the diffusion factor and it looks like the two-dimensional diffusion factor may serve for loss prediction purposes.

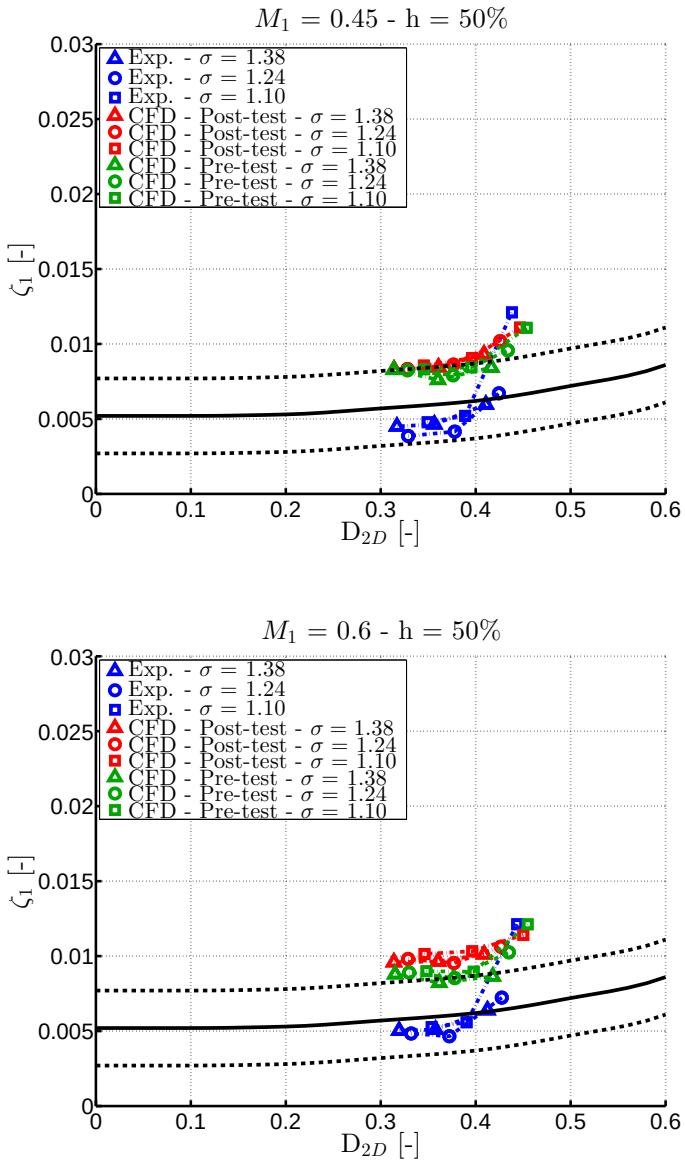


Figure 4.48: *Loss parameter ζ_1 versus 2D diffusion factor at (a) M_1=0.45 and (b) M_1=0.60*

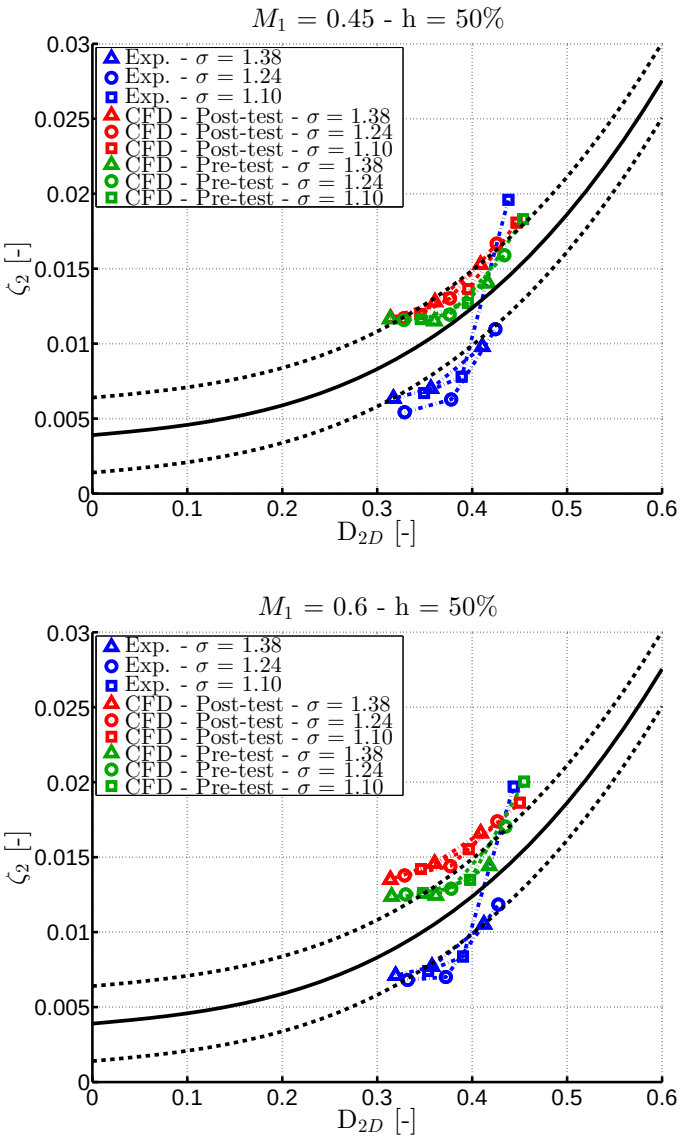


Figure 4.49: *Loss parameter ζ_2 versus 2D diffusion factor at (a) M_1=0.45 and (b) M_1=0.60*

From the analysis of Fig. 4.46 to Fig. 4.49, both experimental ζ_1 and ζ_2 are always slightly below the correlation curve. This is due to the fact that the CDB profile is an optimized blade shape. The compressor airfoils studied by Lieblein are not representative of the state-of-the-art in compressor blade design. With the appearance of computer-aided design methods and optimization techniques, the profiles considerably evolved and lead to lower total pressure losses than

a standard NACA65 airfoil or a DCA. It makes no doubt that if an extensive measurement campaign was conducted such as the one of Herrig et al. on which Lieblein based his conclusions, the correlation curves would be shifted to lower loss levels.

4.7.4 Off-design correlations

The previous sections dealt with the performance predictions at design condition, i.e. at optimum incidence. For design purposes, it is also essential to predict the deviation and the losses away from the optimum incidence, at off-design conditions. In cascade correlations, off-design conditions are usually referred to as the incidence conditions leading to two times the minimum losses $i_{2\omega_{min}}$ (cf. Fig. 2.2). The off-design performance of various profiles are thus compared at equivalent relative loss levels. However, as shown in Fig. 4.29, during the current investigation, the experimental results reached a much higher level of losses. On the opposite, CFD results barely reached $2\omega_{min}$. For that reason, off-design performance are analyzed at constant incidence rather than at equivalent loss level. Moreover, only the updated CFD model has been considered. By presenting the data in such a way, the off-design discrepancies between experimental results and CFD clearly emerged.

The deviation at constant incidence is given in Fig. 4.50 for both M_1=0.45 and M_1=0.60. Deviation laws like Eq. (4.6) have been drawn at constant incidence to make the comparison easier. It clearly highlights that the lower the solidity the worse the CFD predictions. Focusing on the experimental results, it can also be seen that the off-design corrections are bigger at low solidity. In other words, the higher the solidity, the less sensitive is the deviation to incidence variations. This underlines again the guidance role of the solidity.

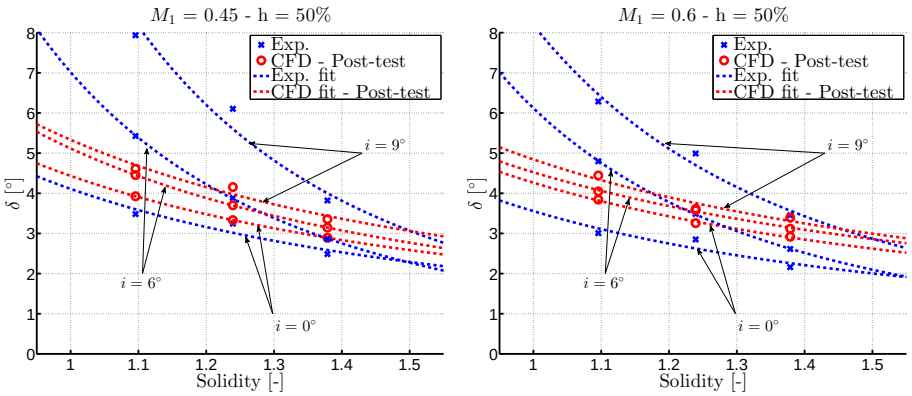


Figure 4.50: *Deviation at constant incidence for M_1=0.45 and M_1=0.60*

The same exercise can be done with the two-dimensional diffusion factor plotted at constant incidence in Fig. 4.51. The agreement is very good at 0° for all solidities. At 6°, the low solidity starts to show some discrepancies. At 9°, only the results of the high solidity are still satisfactory. For design applications, a confidence region can be drawn. Outside this region, the CFD should not be trusted. This may be simply defined as a limit based on the last diffusion factor where both CFD and experimental data are in agreement. In the present situation, this would be $D_{2D} < 0.45$. The confidence region can also be more complex by considering the good quality of the high solidity predictions. Both situations are illustrated in Fig. 4.52 which also clearly indicates that the incidence range decreases as the solidity decreases. However, such confidence regions can only be established with the two-dimensional diffusion factor that is very linear in function of incidence and solidity and is not affected by the AVDR.

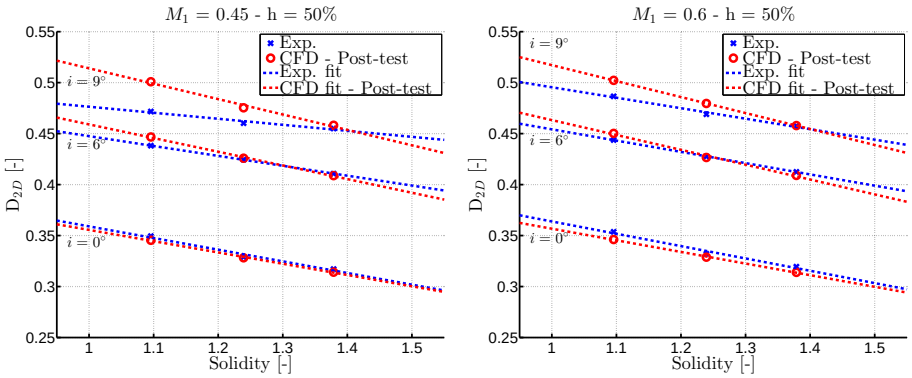


Figure 4.51: *Two-dimensional diffusion factor at constant incidence for M_1=0.45 and M_1=0.60*

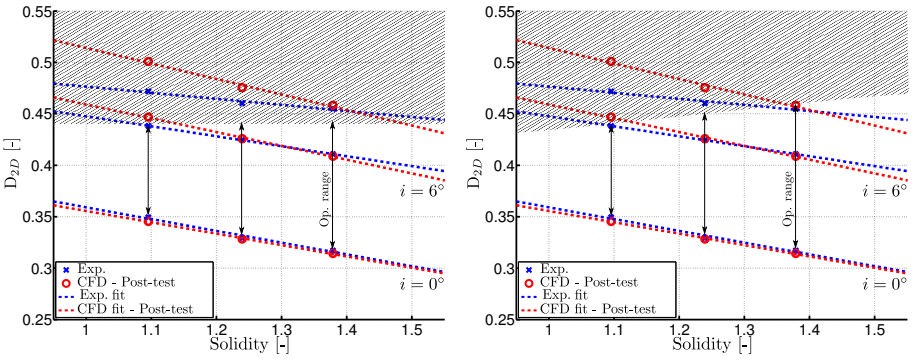


Figure 4.52: *Examples of design confidence regions based on the two-dimensional diffusion factor (M_1=0.45)*

Regarding the off-design loss prediction, in Fig. 4.53, it seems that all the experimental results collapse using ζ_1 or ζ_2. Moreover, the compressibility effects were very limited and it is thus possible to define an off-design prediction rule which would be valid for such CDB profiles in both incompressible and compressible regimes. The data of the 5 common incidences (cf. Table 4.3) at both Mach and including all solidities have been gathered in order to fit a 4^{th} order polynomial. The post-test CFD data are also available. A 4^{th} order polynomial captures the sharp rise of losses and could be used for off-design prediction. Regarding the CFD data, a quadratic polynomial brings a sufficient representation of the off-design trend and predict much lower losses over the whole off-design range.

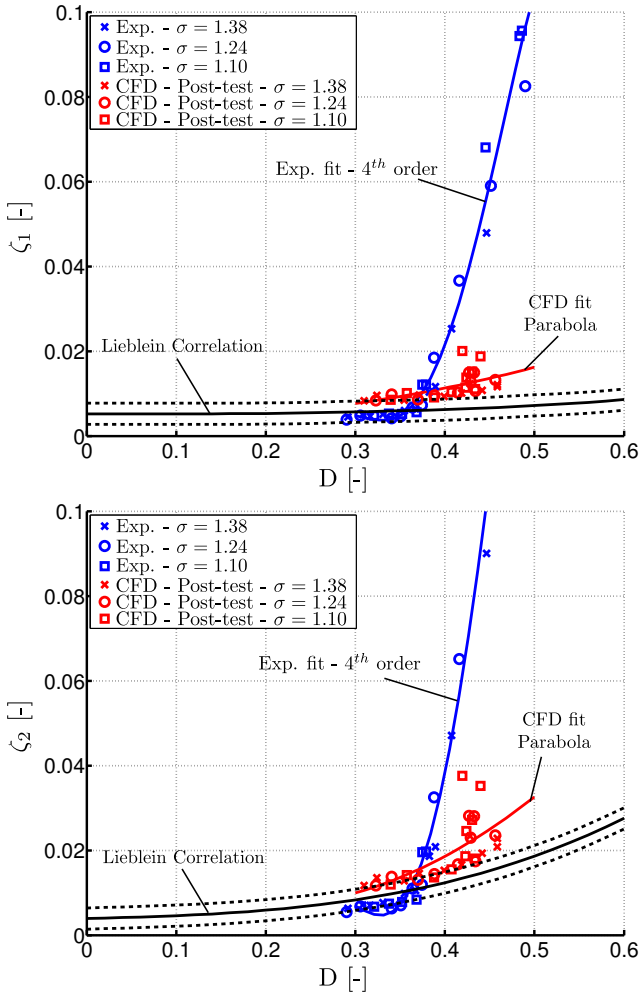


Figure 4.53: *Off-design incidence correlations based on ζ_1 (top) or ζ_2 (bottom) and the diffusion factor at both Mach numbers.*

In Fig. 4.54, similar comparisons are done based on the two-dimensional diffusion factor. Because the diffusion levels are very similar when two-dimensional conditions are assumed, it is possible to clearly indicate the corresponding optimum and off-design incidence conditions. It can then be seen that the losses start to rise for $i > 3°$ or, in terms of diffusion factor, for $D_{2D} > 0.40$.

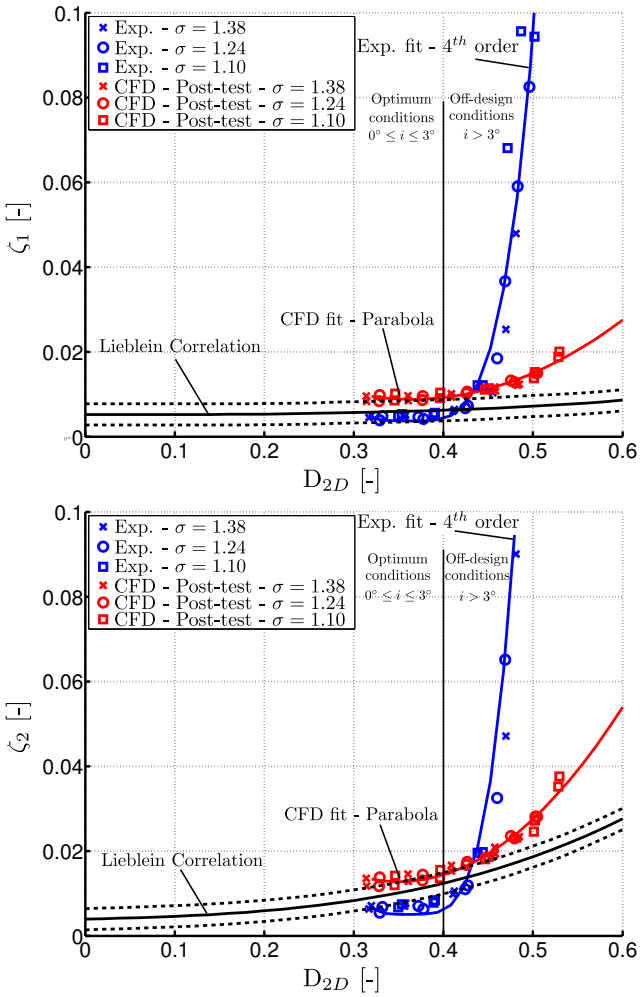


Figure 4.54: *Off-design incidence correlations based on ζ_1 (top) and ζ_2 (bottom) and the two-dimensional diffusion factor at both Mach numbers.*

The experimental curve fits for both diffusion factors and both loss parameters are given from Eq. (4.8) to Eq. (4.11).

$$\zeta_1 = (\,1.84093\,D - 0.34460\,)^4 - 0.00109 \tag{4.8}$$

$$\zeta_2 = (\,2.14172\,D - 0.39962\,)^4 - 0.00385 \tag{4.9}$$

$$\zeta_1 = (\,3.95541\,D_{2D} - 1.42862\,)^4 + 0.00370 \tag{4.10}$$

$$\zeta_2 = (\,4.63572\,D_{2D} - 1.67718\,)^4 + 0.00504 \tag{4.11}$$

They may be implemented in a meridional solver for both design and off-design loss predictions. They all remain valid as long as the diffusion factor at minimum losses is between 0.3 and 0.35 (0.4 if the D_{2D} is used). This depends on the nature of the profile, the application (fan, low-pressure or high-pressure compressors) as well as the design requirements.

4.7.5 Stability margin

In the literature, the stability limit is often considered as the incidence difference between the optimum incidence and $i_{2\omega_{min}}$. In Fig. 4.55, since the experimental losses reached levels as high as $5\omega_{min}$, the stability margin has been defined by $i_{2\omega_{min}} - i_{opt}$ as well as $i_{5\omega_{min}} - i_{opt}$. No significant influence of the inlet Mach number could be noticed and the results indicated in Fig. 4.55 are an average of the results at M_1=0.45 and M_1=0.60. Nearly no difference appears between σ=1.24 and σ=1.10 but a decrease between 2° and 4° is observed going from σ=1.38 to σ=1.24. It illustrates the big drawback of a blade count reduction which may dramatically affect the stall margin. In the current case, decreasing the solidity by 10% reduces by approximately 60% the baseline stall margin.

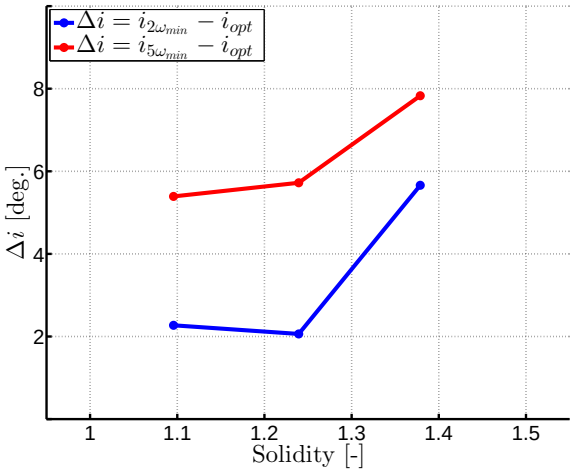


Figure 4.55: *Incidence range versus solidity*

Unfortunately, the effect of solidity on the working range and the stability is compromised by the lack of information on the choking side of the loss curve, i.e. at negative incidence. As the pitch is decreased, the passage may be choked earlier at higher mass-flow. If the stability range was defined as $i_{stall} - i_{choke}$, where both i_{stall} and i_{choke} yield similar amount of losses, the better performance of the high solidity cascade on the stall side may in fact be compensated by an early choke and the increase in stability range may not be as important as foreseen.

4.8 Outlet flow topology

At i=3° and i=9°, the total pressure losses have been measured every 5% of the span at an inlet Mach of 0.45. This allows the comparison of the flow topology in function of incidence and solidity. Firstly, only the experimental results are compared to highlight the effects of incidence and solidity. At i=9°, the comparison with the CFD is done for the 3 solidities. The numerical data presented in this section have been obtained with the $k-\varepsilon$ turbulence model and with a central scheme. For the baseline solidity, the influence of the turbulence length scale ($\ell = 0.1\,D_H$ or $\ell = 0.0001\,D_H$), of the turbulence model ($k-\varepsilon$ and Spalart-Allmaras) and of the numerical scheme (central or upwind) have also been studied. The analysis of those numerical parameters is discussed in Appendix C.

4.8.1 Effects of incidence and solidity

The experimental outlet total pressure maps are given from the figures 4.56 to 4.61. A threshold has been set to -1% and represents the lowest loss level in the following figures. This has been applied to prevent the appearance of uncolored regions due to local negative losses (from the measurement uncertainties) and wrong interpolations. When the comparison with the numerical data will be addressed, this threshold will be essential to shed light on the non-physical negative losses predicted by CFD.

The analysis of Fig. 4.56 to Fig. 4.61 exposes the wake and corner stall development while moving towards high incidence or changing solidity. By increasing the incidence, the wakes thicken and become more intense. By changing solidity, nearly no effect can be depicted at i=3° but strong discrepancies emerge at i=9°. In particular, close to the walls where the corner separation becomes more and more intense as the solidity decreases. However, for the lowest solidity, the loss distribution was not expected. The wakes are deeper and thicker at 30% than at 20% while, in theory, the wake intensity and width should decrease towards mid-span. A similar flow topology was already observed at comparable conditions (in terms of Reynolds number and incidence angle) on a different cascade during a previous measurement campaign in C3 [85]. Additional measurements, preferably unsteady techniques, would be advised to definitely assess the corner stall development.

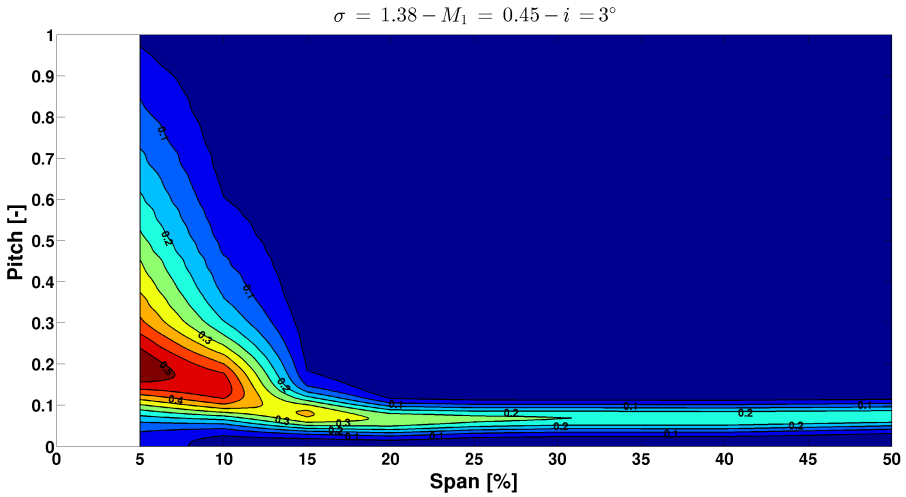


Figure 4.56: *Total pressure loss map for* $\sigma = 1.38$ *at i=3° and* $M_1 = 0.45$

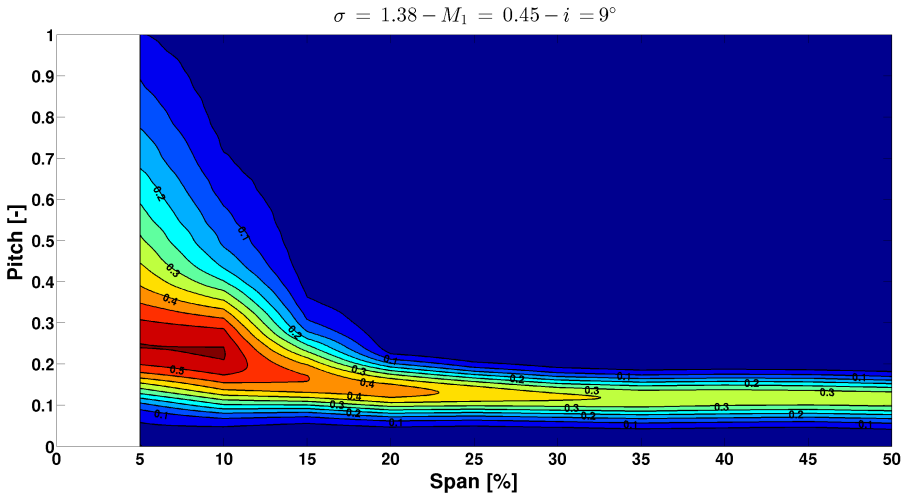


Figure 4.57: *Total pressure loss map for* $\sigma = 1.38$ *at i=9° and* $M_1 = 0.45$

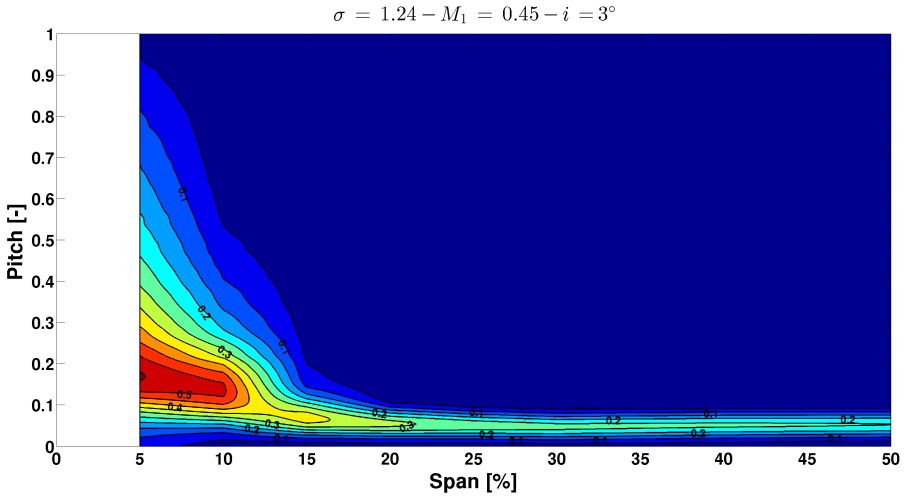


Figure 4.58: *Total pressure loss map for* $\sigma = 1.24$ *at i=3° and* $M_1 = 0.45$

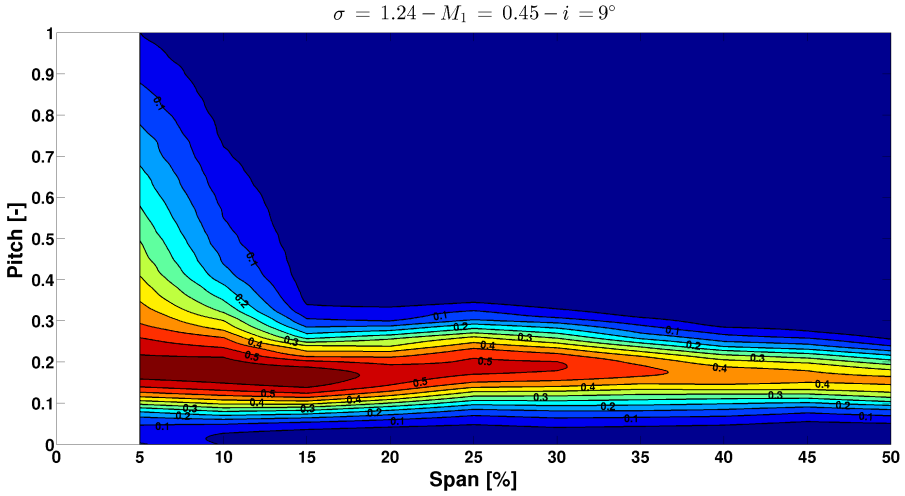


Figure 4.59: *Total pressure loss map for* $\sigma = 1.24$ *at i=9° and* $M_1 = 0.45$

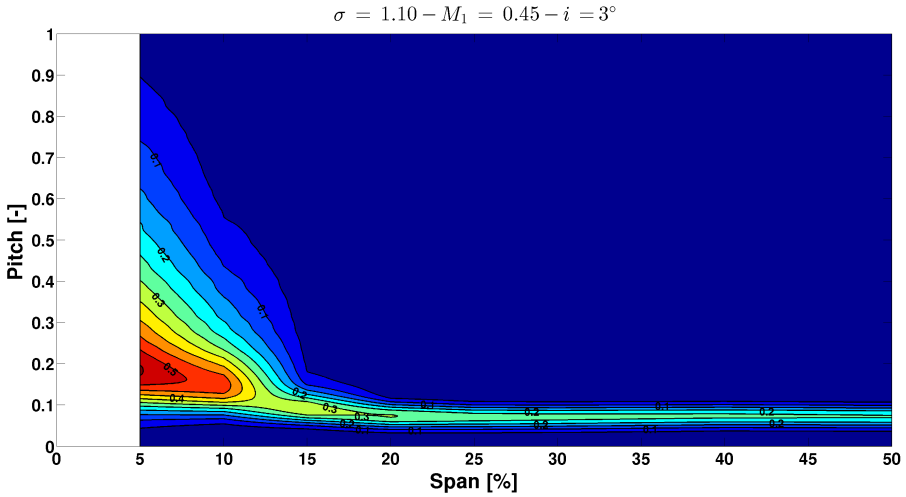


Figure 4.60: *Total pressure loss map for* $\sigma = 1.10$ *at* i=3° *and* $M_1 = 0.45$

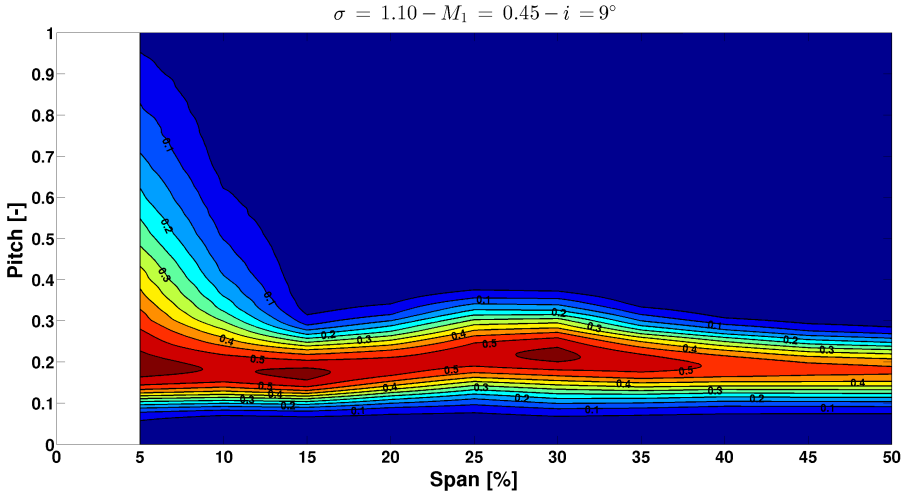


Figure 4.61: *Total pressure loss map for* $\sigma = 1.10$ *at* i=9° *and* $M_1 = 0.45$

4.8.2 Comparison with CFD

The numerical outlet total pressure maps are given at 9° for the three solidities in Fig. 4.63, Fig. 4.65 and Fig. 4.67. To make the comparison easier, the experimental results have been repeated in Fig. 4.62, Fig. 4.64 and Fig. 4.66. The same threshold is set at -1%. It means that all the white zones in Fig. 4.63, Fig. 4.65 and Fig. 4.67 are below this level. It must be noted that, during the experiments, when changing the pitch of the cascade, the relative position of the blade trailing edges is varying with respect to the probes. And, as mentioned in Sec. 4.3, since the exact position of the probes is not recorded during the motor displacement, it is difficult to extract the absolute positions of the wakes. Therefore, they have been shifted in the pitch direction to match the corresponding experimental loss maxima at mid-span. Consequently, no firm conclusion can be drawn concerning the circumferential position of the wakes.

The best agreement is found at high solidity. This was already visible in the performance curve (cf. Fig. 4.28) and, for $\sigma = 1.38$, experimental and post-test CFD data collapsed on each other at 9°. For $\sigma = 1.10$, the discrepancy is obvious and the CFD completely fails in the corner stall prediction. For the same inlet profiles as the experiments, the CFD results of Fig. 4.67 show very divergent flow topology.

As pointed out in Chapter 3, the central scheme also systematically presents loss overshoots and undershoots on both side of the wakes. Therefore, a couple of numerical parameters have been varied such as the numerical scheme or the turbulence model. More comparisons are available in Appendix C for the high solidity cascade using various numerical parameters but also at i=3°. Within the framework of the current study, apart from the loss undershoots, the central scheme $k-\varepsilon$ results still offer very satisfactory agreement with the experiments. Advanced parameters exist and may be tuned in the solver to decrease the intensity of the negatives losses but they have not yet been investigated. The use of an upwind scheme may help to remove them completely. Unfortunately, this dispersive non-physical phenomenon is then replaced by more diffusive features and the upwind scheme fails at capturing the right wake intensity. Currently, the better numerical stability, the years of experience in low-pressure compressor design and the validated high accuracy in predicting global performance of real compressor geometries ([75, 78]) are important points playing in favor of the central scheme.

However, more recently, in 2014, numerical investigations were performed by Gao [90] on a linear cascade configuration at similar Reynolds conditions and at a solidity that is equivalent to the low solidity cascade of the current study (i.e. $\sigma \approx 1.10$). Gao did show that RANS and even URANS calculations completely failed to predict the flow topology and only Large Eddy Simulations (LES) were able to provide a more accurate representation of the corner stall. Such simulations require a much bigger computational cost and have not been

considered in the current investigation but the work of Gao suggests that LES is an interesting approach if a better flow representation is required. In the prospect of a further validation of advanced CFD methods, it is undeniable that all the measurements presented in this section constitute a very useful and extensive database.

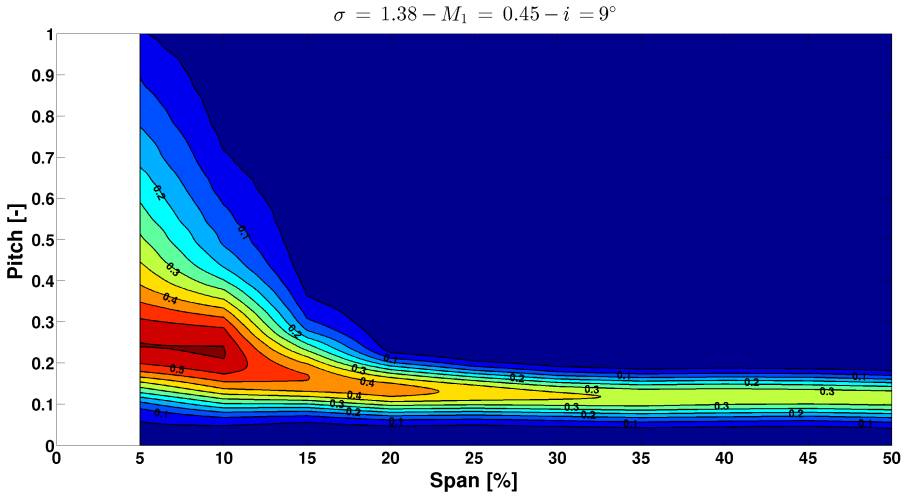


Figure 4.62: *Experimental total pressure loss map for* $\sigma = 1.38$ *at i=9° and* $M_1 = 0.45$

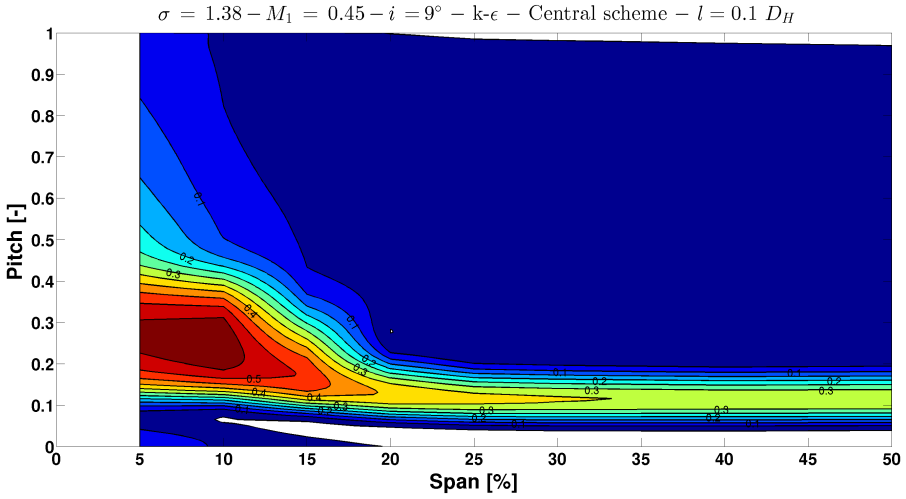


Figure 4.63: *Numerical total pressure loss map for* $\sigma = 1.38$ *at i=9° and* $M_1 = 0.45$

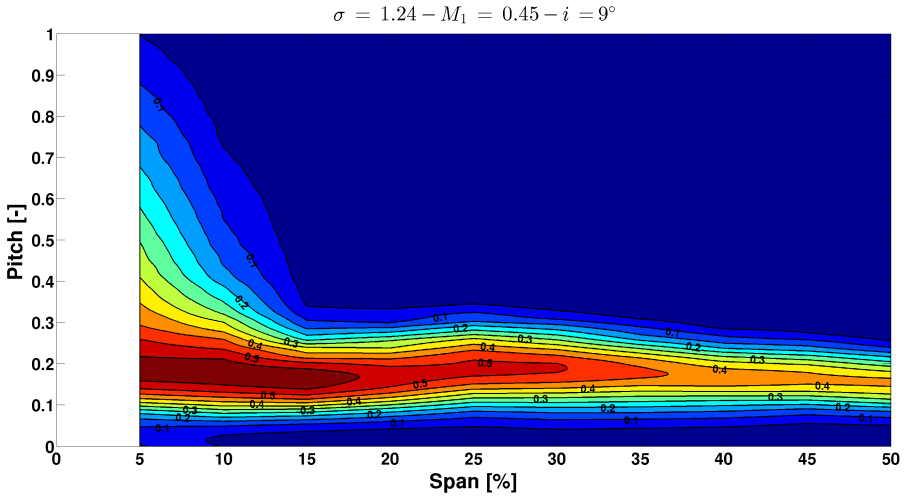


Figure 4.64: *Experimental total pressure loss map for* $\sigma = 1.24$ *at i=9° and* $M_1 = 0.45$

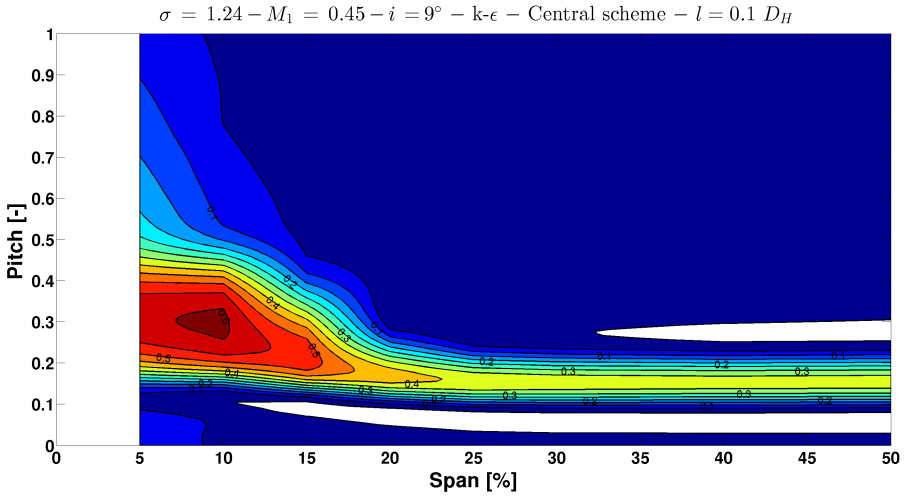


Figure 4.65: *Numerical total pressure loss map for* $\sigma = 1.24$ *at i=9° and* $M_1 = 0.45$

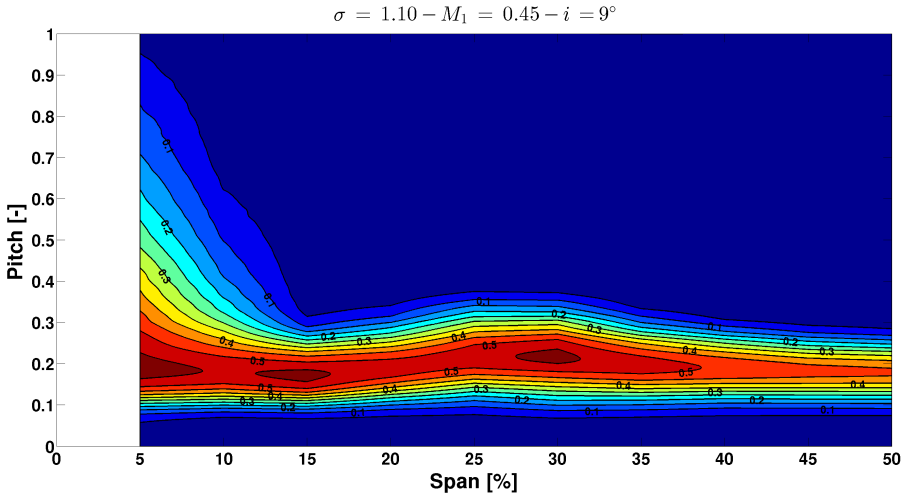


Figure 4.66: *Experimental total pressure loss map for* $\sigma = 1.10$ *at i=9° and* $M_1 = 0.45$

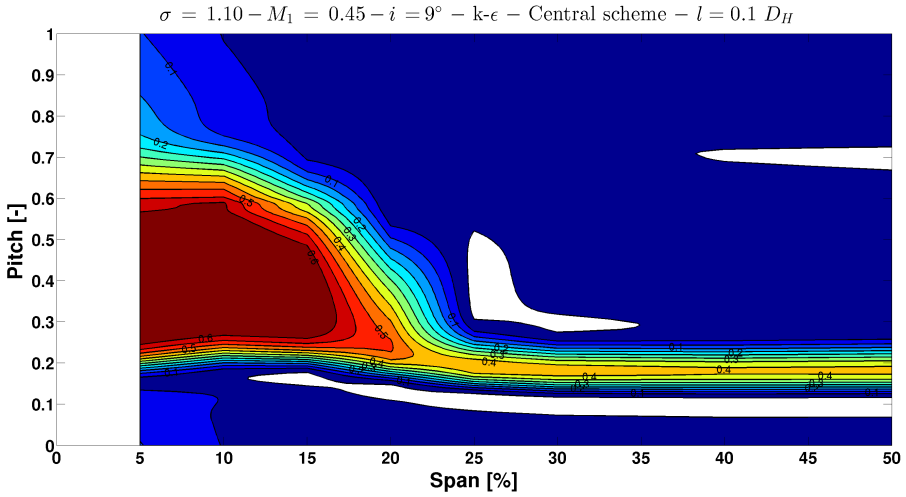


Figure 4.67: *Numerical total pressure loss map for* $\sigma = 1.10$ *at i=9° and* $M_1 = 0.45$

4.9 Conclusion

The effect of solidity has been studied in the high-speed VKI C3 facility on a controlled diffusion airfoil. Three values of solidity have been considered by varying the pitch. Measurements have been performed at 6 incidences, 2 inlet Mach numbers and at various span locations. To exactly match the experimental domain and to provide a fair comparison with the CFD predictions, a different numerical model than the configuration of Chapter 3 has been studied. Both pre-test and post-test CFD data have been examined against the measurements.

The influence of solidity on the total pressure losses appeared very small at low incidence and no clear trend emerged. However, from 6°, the loss growth is faster and steeper as the solidity decreases. The guidance role of the solidity has been confirmed and the turning decreases when the solidity is reduced. Until an inlet Mach number of 0.60, very small compressibility effects have been observed on both total pressure losses and turning which corroborates the conclusions of Chapter 3. Both total pressure losses and turning increase as the Mach number increases but the variations are very small and may be reasonably neglected.

Emphasis has also been set on the calculation of the diffusion factor that is strongly related to the AVDR. By definition, the diffusion factor decreases as the AVDR increases. In a cascade, an AVDR higher or lower than 1 is induced by the three-dimensional nature of the flow and the development of secondary flows. More generally, in a three-dimensional compressor geometry, the AVDR is also influenced by the curvature of the flowpath. This may be very misleading for the designer since different diffusion levels may be reached if the AVDR varies and it is then difficult to establish coherent design or stall criteria. The use of a two-dimensional diffusion factor, assuming a constant axial velocity ratio, removed this dependence and offered an alternative loading coefficient increasing linearly with incidence. It seems that it may be used in addition to the traditional diffusion factor of Lieblein in order to set up limits at design or stall conditions. Nonetheless, both definitions of diffusion factor indicate that considering a stall limit at a diffusion level of 0.6 as suggested by Lieblein's work is too optimistic and a more realistic limit would be around 0.5.

Comparing the results to the pre- and post-test CFD calculations, at low incidence, very little difference appears at low incidence but, as secondary flows develop, more differences emerge at high incidence. It recalls the importance of having a model as faithful as possible in terms of spatial extension and boundary conditions. Regarding the total pressure losses, it turned out that the numerical results overestimate the losses by approximately 1% (absolute) at low incidence. At high incidence, both CFD models fail to capture the steep loss rise of the measurements and predict much lower losses. This is especially true for the low solidity cascade.

The definition of an optimum incidence is not trivial and, because of the discrete resolution in incidences, many fitting methods have been tried in order to predict the optimum incidence. It does not have tremendous consequences on the loss predictions given that the loss curves are very flat at low incidence. Nonetheless it must be underlined that, compared with Chapter 3, the optimum conditions look like they have been shifted towards more negative incidences. The absence of experimental data on the negative side of the curve prevents drawing final conclusions on this issue. However, isentropic Mach number measurements performed on a scale-2 blade model having the same solidity as the baseline configuration confirm the optimum incidence of the highest solidity is very close to 3°.

The analysis of the deviations showed satisfactory agreement between the experiments and the CFD at low incidence and the establishment of CDB updated deviation rules for both Mach numbers has been performed. Towards off-design incidence, strong discrepancies arise and especially as the solidity decreases. It underlines one of the most important conclusions of the current investigation: the lower the solidity, the worse the CFD predictions in terms of either losses or flow angles.

The comparison of the loss parameters with the correlation curve of Lieblein suggested that the correlations should be updated but could seemingly still be used under the same form. The off-design analysis reveals that standard quadratic prediction models are obsolete for such controlled diffusion profiles and higher order polynomials are required to match the steep rise of losses at off-design incidences. While parabolas always have a linear slope and constant curvature, higher order polynomials have more complex derivatives. This may lead to a loss evolution that is very flat for a wide range of incidences yielding very low losses and followed by a steep rise. The nature and the shape of the loss bucket are directly linked to the working range of a compressor. A very flat curve followed by a steep rise of losses may result in a compressor that operates at high efficiency for a wide range of mass-flow, ending on an abrupt stall. Adding negative incidences to the test matrix would definitely provide complementary information at choke conditions and would complete the assessment of the effects of solidity on the working range and the stability of a compressor.

Regarding the use of the diffusion factor, it seems that new design and off-design correlations could be easily derived using both definitions of diffusion factor. The fact that the numerical two-dimensional diffusion factor offers much better agreement with the experiments makes it a powerful design parameter.

Finally, although the current chapter focused on the mid-span performance, the total pressure outlet maps were compared and revealed the weakness of CFD in providing an accurate and physical flow topology over the whole span. This is especially true regarding the low solidity cascade. Outside the frame-

work of the effect of solidity, the experimental database established during this investigation constitutes an excellent basis to validate and improve current numerical models, particularly regarding the secondary flow topology and the corner separation.

The derived deviation and loss prediction rules that emerged at both optimum and off-design incidences can now be implemented in a meridional solver. This may yield possible enhancements in the compressor design already at the level of the meridional design. The issue of the solidity effect and optimization within a throughflow solver is treated in the next chapter.

Chapter 5

Meridional optimization

5.1 Introduction

The meridional design is an essential step in the elaboration of any turbomachinery component. Many choices, such as the channel geometry or the solidity, are done at the level of the meridional design and may influence the rest of the whole design process.

However, any radial equilibrium solver relies on empirical correlations. Those correlations provide an estimate of the total pressure losses of a blade row depending on the loading and the number of blades. For compressors, such correlations originally come from the work of Lieblein et al. (1953) already presented in Chapter 2. They have been completed to provide spanwise corrections like in the work of Robbins et al. (1965). Nevertheless, it must not be forgotten that all empirical correlation data have been obtained within given measurement uncertainty bands. Similarly, many correlations often present a big scatter in the data due to the wide variety of tested profiles and a polynomial curve fit is usually drawn through the measurement points to allow for an implementation in a throughflow solver. The uncertainties or the data scatter is then neglected.

Since nowadays meridional calculations are very cheap in terms of computational time, it is very appealing to combine throughflow solvers with optimizer tools and/or with uncertainty quantification (UQ) techniques which both require many evaluations such as evolutionary algorithms [49] or Monte-Carlo sampling and stochastic collocation techniques [53].

The main purpose of UQ methods is to improve the confidence in any numerical prediction by considering a probabilistic framework and epistemic uncertainties. These are defined as a potential defect or deficiency due to a lack of knowledge. They may be considered as model uncertainties. The use of correlations is a good example of an epistemic uncertainty source such as turbulence modeling in any CFD computation.

To illustrate meridional design optimization as well as the use of UQ methods, the emphasis is set on the solidity optimization of a particular compressor geometry. After briefly presenting the compressor geometry and the solver, the results of solidity optimization without UQ are firstly given. Based on those optimum designs, UQ is introduced by using both sampling or quadrature

methods. Different loss parametrizations are studied to analyze their impact on the results. The last issue addressed in the chapter is the problem of optimization under uncertainty commonly referred to as *robust design*. The results are discussed with and without the use of UQ.

5.2 Axial Compressor Pre-design tool

The meridional solver that is used is *ACPreDesign*. This multi-stage axial compressor design program originally comes from Creveling and Carmody (1968, [50, 51]) and has been recently implemented at VKI. It solves the non-isentropic radial equilibrium equations for given design input parameters. Currently, the program does not provide off-design predictions. Examples of meridional optimization using ACPreDesign can be found in the work of Joly et al. [47] or Teichel et al. [48].

5.2.1 Input

The compressor flowpath geometry must be imposed and divided into a number of axial stations where the radial equilibrium equations will be solved. The mass flow, the inlet total pressure and temperature, the desired global mass-averaged pressure ratio and the rotating speed of every stage must be provided. If the flow does not enter the rotor axially, the rotor inlet tangential velocity distribution can be modeled by an IGV row. For each stage, outlet tangential velocity distributions (at both rotor and stator outlets) as well as both rotor and stator solidity distributions are also required.

The channel coordinates are coming from the DREAM project booster (cf. Appendix A) geometry. An IGV has been set in front of the rotor in order to match the desired inlet tangential velocity distribution. For this investigation, the IGV has been considered as ideal and does not generate any pressure loss. The channel geometry and the axial stations are available in Fig. 5.1. All tangential velocity profiles have been imposed following the original design specifications.

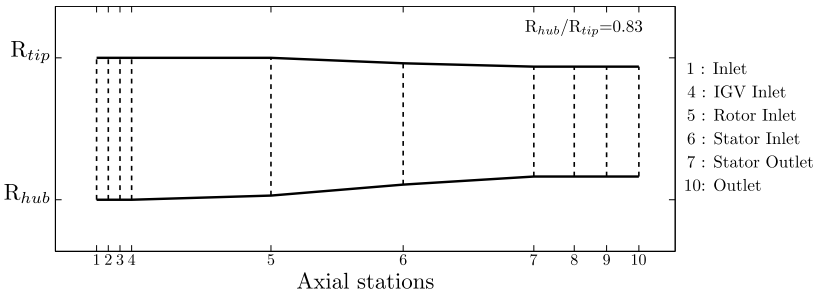


Figure 5.1: *Channel and axial station repartition*

5.2.2 Loss correlations

Similar to any meridional flow solver, in order to compute the total pressure losses of each row, ACPreDesign relies on loss correlations originally coming from the work of Lieblein et al. ([5]), presented in Fig. 2.20. The correlations implemented by Creveling and Carmody are based on the work of Robbins et al. ([35]) and include three-dimensional corrections to have a realistic spanwise loss evolution. Different correlations are available for the stator. Rotor and stator correlation curves are respectively available in Fig. 5.2 and Fig. 5.3. They are given in terms of a loss parameter (cf. Eq. (2.17)) ζ_R or ζ_S, respectively for rotor and stator, versus diffusion factor. Hub, mid-span and tip sections correspond to 10%, 50% and 90% of the span.

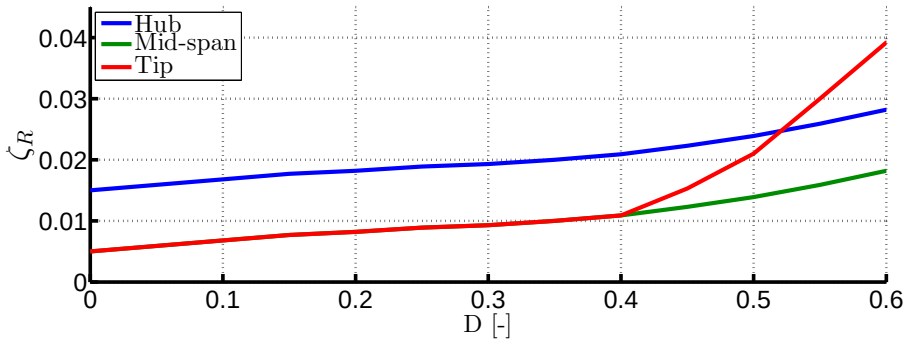


Figure 5.2: *Rotor loss correlations of ACPreDesign*

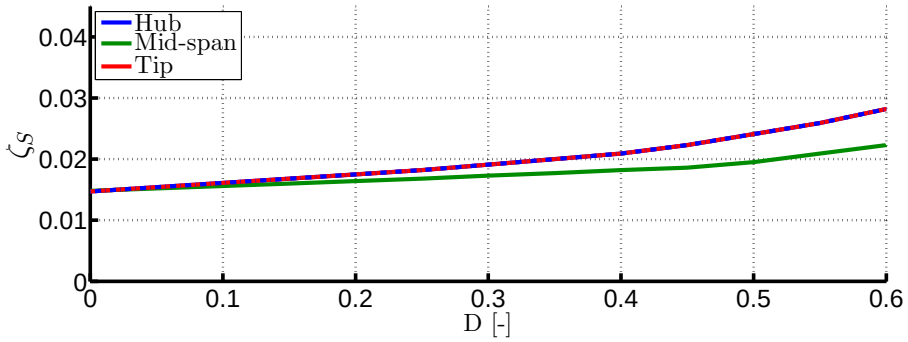


Figure 5.3: *Stator loss correlations of ACPreDesign*

The mid-span rotor loss evolution is the lowest as it only contains profile losses. The hub curve is shifted to a higher loss level to account for secondary flows and potentially corner vortex separation. The tip losses are equal to the mid-span losses until a diffusion factor of 0.40 which triggers the growth of losses due to the tip gap vortex. For the stator, the spanwise evolution is symmetric and hub and tip losses are exactly equal. They are slightly higher than

the mid-span losses over the whole diffusion range.

From the comparison of Fig. 2.20 with Fig. 5.2 or Fig. 5.3, it clearly emerges that the scatter of Fig. 2.20 has not been implemented in the correlations of ACPreDesign. This is a typical example of an epistemic uncertainty.

5.3 Optimization

5.3.1 Method and constraints

ACPreDesign has been coupled to the VKI optimizer CADO [91] to find the best solidity distributions in terms of stage efficiency for a given pressure ratio distribution. The solidity is controlled at three span locations (10%, 50% and 90%) and a 2^{nd} order Bezier interpolation is used to compute the solidity distribution. The pressure ratio distribution is imposed through a rotor outlet tangential velocity distribution which is thus also optimized in order to converge to the desired pressure ratio distribution.

To impose the pressure ratio profile, the tangential velocity distribution must be controlled by several parameters (ideally 4 or 5) and more constraints must be implemented. In the present situation, a tangential velocity profile that was known to provide the required pressure ratio distribution (based on the DREAM project booster design) was considered. To maintain a limited number of optimized parameters, a single parameter allows the profile to be translated. The influence of this choice on the pressure ratio distribution is presented in a further section. Finally, if the whole stage is considered, it consists of 6 parameters, i.e. 3 for the rotor solidity distribution and 3 for the stator solidity distribution. Adding the tangential velocity parameter, 7 variables have to be optimized.

The VKI optimization code (CADO) is based on a Differential Evolution (DE) algorithm. This evolutionary method has been developed by Price and Storn (1997, [92]). Originally developed by Pierret [93] for axial turbomachinery blade optimization, CADO has since then been improved and extended to multidisciplinary optimizations by Verstraete (2008, [49]). The algorithm can easily be coupled to any other solver as in the present case to ACPreDesign. As mentioned previously, examples of ACPreDesign optimization using CADO can be found in [48, 47]. The major drawback of DE is that it requires a large number of evaluations which, in some situations, may become unrealistic. The use of metamodels may help to reduce the total computational cost but, in the case of ACPreDesign, the number of evaluations does not represent an issue.

An evolutionary algorithm may be explained by analogy to the Darwinian evolution theory through which a population of individuals evolves in a given environment by various mechanisms such as cross-over reproduction, mutation and selection. During this process, the individual features that are best fitted

for their survival have more chance to be preserved and to remain in the following generation of individuals.

For the specific case of solidity optimization with ACPreDesign, the evolutionary algorithm can be easily explained. Firstly, random solidity distributions are computed. This constitutes the first generation of individuals. For each solidity distribution, ACPreDesign solves the NISRE equations. The efficiency and pressure ratio are computed as well as the loading distributions of all rows. Among all the individuals, only those respecting all the specified constraints (for instance, minimum or maximum diffusion, minimum or maximum pressure ratio etc...) are kept and considered as successful. Priority is given to the individuals with the fewest amount of constraint violations rather than on the best objective function. By mutation and cross-over mechanisms, the successful cases give birth to a new generation. According to the evolution theory, the individuals of this new population have more chance to present no or less constraint violations and a better efficiency and/or pressure ratio. For the current optimizations, convergence was reached very quickly after 150 to 200 generations of 200 individuals.

Various constraints may be imposed by the designer. They may be set on aerodynamic performance parameters (maximum turning of the airfoil, diffusion factor etc...) or involve mechanical considerations (maximum RPM). In the current situation, two constraints are set on the pressure ratio, fixed to 1.25, and the pressure ratio distribution shown in Fig. 5.4. This total pressure ratio profile is typical for a booster which is more always more loaded at the hub in order to compensate for the very skewed total pressure distribution of the fan outlet.

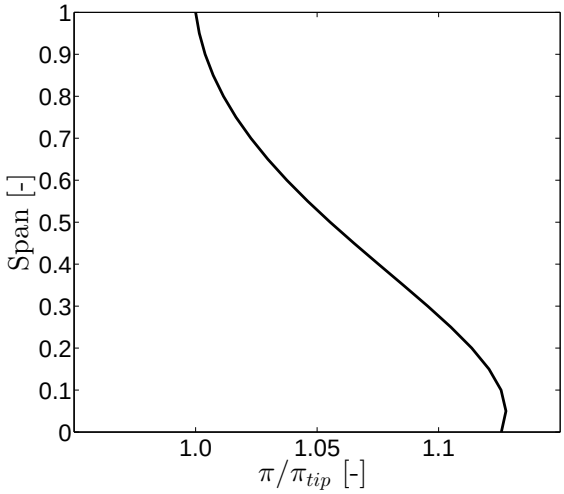


Figure 5.4: *Target normalized pressure ratio distribution*

However, the most important constraint is the maximum diffusion factor which is imposed by the designer over the whole span and for both rotor and stator. As it will be presented in the next section, this parameter has a big influence on the results of the optimization. Since the pressure ratio is imposed, the problem is a single-objective optimization and only the efficiency is maximized. The objective function and the constraints can be summarized as follows:

$$\begin{aligned} &\text{Objective function:} \\ &\qquad \text{Maximize } \eta(\sigma, V_\theta) \\ &\text{Constraints:} \\ &\qquad \pi = 1.25 \\ &\qquad \frac{\pi(h)}{\pi_{tip}} \, \forall h \\ &\qquad D(h) \leq D_{max} \, \forall h \end{aligned} \tag{5.1}$$

To conclude this section, it must be emphasized that the solidity is also directly linked to the spanwise distribution of the chord length which may be subjected to various mechanical additional constraints. Consequently, the solidity profile is not completely arbitrary. Although no chord length limitation has been considered in the current section, it must be mentioned that it is also possible to add specific constraints on the slope or the curvature of the solidity or the chord. In some situations, this can fasten the whole design process by taking into account some mechanical requirements of the latest design phase at the early stage of the throughflow design. Examples of such limitations are given in Appendix D.

5.3.2 Results

The constraint on the diffusion factor has quickly been identified as a crucial parameter. Optimizations have been run varying the maximum diffusion factor D_{max} of both rotor and stator from 0.375 to 0.45 by steps of 0.025 as well as for $D_{max} = 0.50$. Optimizations have been run on the whole stage and on a single rotor configuration. This section focuses on the whole stage analysis and single rotor optimization results are summarized in Appendix D.

First the results of multi-objective (i.e. pressure ratio and efficiency) and single-objective (efficiency only) stage optimizations are compared. The pareto fronts obtained by varying the maximum diffusion factor are displayed in Fig. 5.5 together with the optimization results obtained for a pressure ratio fixed to 1.25. It directly appears that they are consistent with each other. Efficiencies about 0.1% higher are observed when the pressure ratio is fixed but the pareto fronts tends to converge towards the same direction. For post-processing concerns, it is faster and more convenient to perform single-objective optimizations. The higher pressure ratios and efficiencies are achieved with the highest diffusion factor as can be expected.

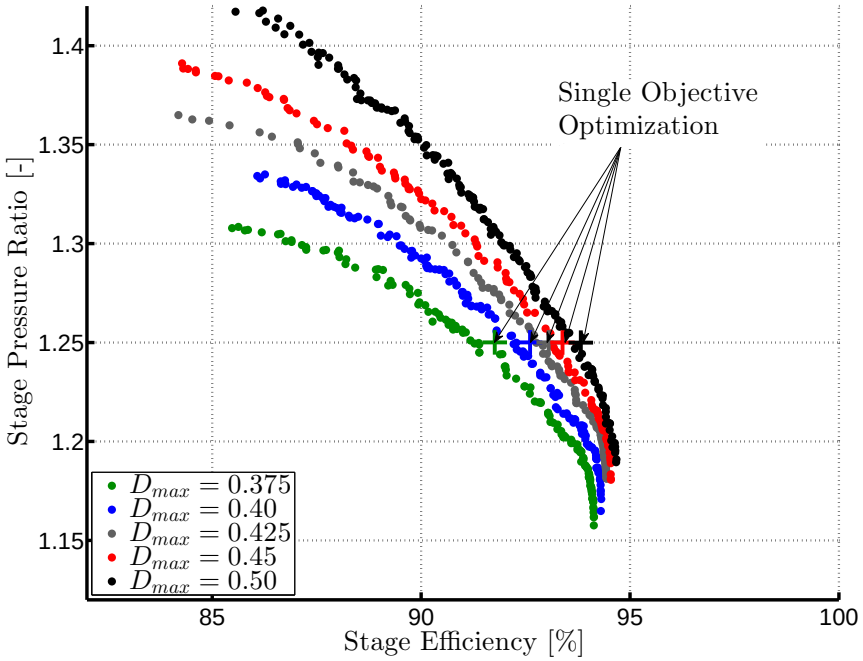


Figure 5.5: *Comparison of pareto fronts and best efficiencies at* $\pi = 1.25$ *for various values of diffusion factors*

The rotor optimum solidity distributions are displayed in Fig. 5.6 next to the corresponding diffusion factor distribution in Fig. 5.7. The optimum so-

lidity distribution obtained when $D_{max} = 0.375$ sits in the same range as the distribution of DREAM but presents a different curvature. Increasing D_{max}, the mean solidity decreases. The trend of solidity versus span becomes linear for $D_{max} = 0.425$ and then changes curvature for higher diffusion. For $D_{max} > 0.425$, the tip solidity remains around 0.9. Looking at the corresponding diffusion factors, it seems that, for $D_{max} \leq 0.425$, the diffusion factor is higher at the hub than at the tip. More precisely, the diffusion level remains around 0.40 in the tip section. It underlines that an optimum diffusion lies around 0.40 at the tip but does not remain optimal towards the hub sections. This conclusion is mainly depending on the correlations and the velocity triangles of the DREAM booster.

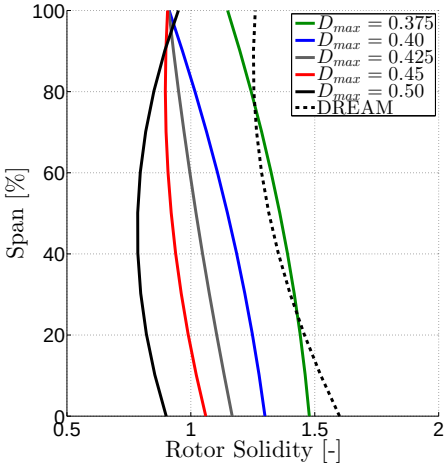


Figure 5.6: *Optimum rotor solidity distributions for different values of D_{max} and for the DREAM rotor*

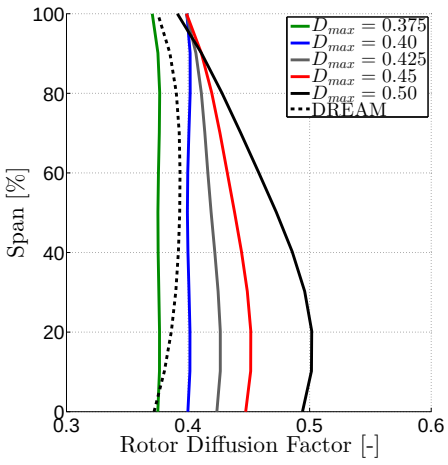


Figure 5.7: *Rotor diffusion factor distributions for different values of D_{max} and for the DREAM rotor*

The same can be done for the stator distributions in Fig. 5.8 and in Fig. 5.9. The optimum solidity distributions are far from the distribution of the DREAM stator. It comes from a design choice of Techspace Aero to unload the stator which works with a very low diffusion. This ensured to bring the stall inception to the rotor which was of interest for Techspace Aero within the DREAM project. Apart from that, it can be seen that the higher D_{max}, the lower the mean solidity. It means that in order to minimize the losses, the optimization tends to achieve the highest diffusion allowed.

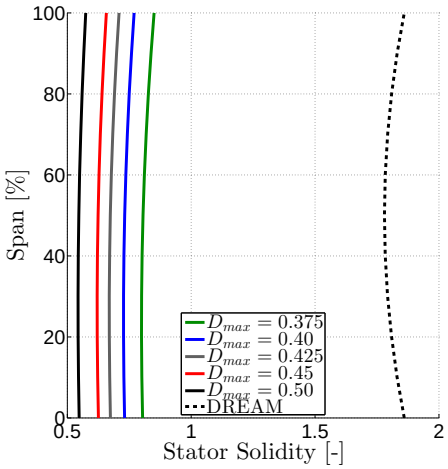


Figure 5.8: *Optimum stator solidity distributions for different values of D_{max} and for the DREAM stator*

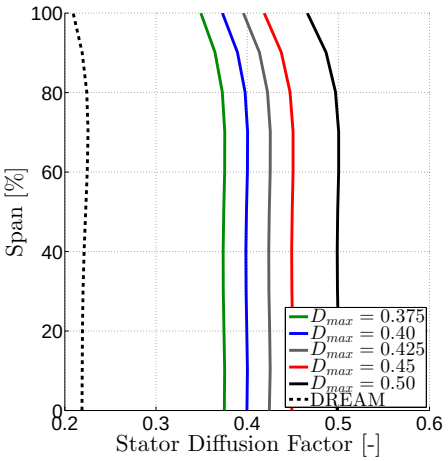


Figure 5.9: *Stator diffusion factor distributions for different values of D_{max} and for the DREAM stator*

The stage pressure ratio and efficiency are respectively given in Fig. 5.10 and Fig. 5.11. The pressure ratio profiles are all similar since this is imposed as a constraint in the optimization process. The small discrepancies comes from the fact that it is the tangential velocity that is imposed rather than the pressure ratio. This could easily be improved by adding constraints and optimization parameters.

The stage efficiency distributions show that a higher efficiency is obtained when increasing D_{max}. While the hub and mid-span efficiencies always increase for higher D_{max}, at the tip, the efficiency remains constant for $D_{max} > 0.40$. It can also be noticed that for each value of D_{max}, the highest efficiency is achieved at mid-span since the correlation curves of Fig. 5.2 or Fig. 5.3 always give the lowest amount of losses at mid-span. The highest efficiency is achieved with $D_{max} = 0.50$ which is obviously a very theoretical result since a rotor enduring a diffusion factor of 0.50 at design would most probably have no stall margin. As mentioned earlier, off-design predictions are not yet available in ACPreDesign but the current study can already highlight the importance of the loss correlations in the choice of the solidity.

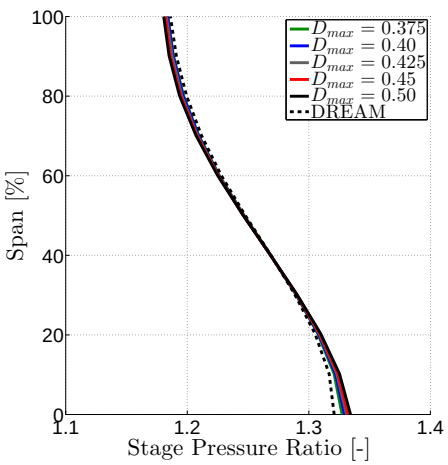


Figure 5.10: *Stage pressure ratio distributions for different values of D_{max} and for the DREAM stage*

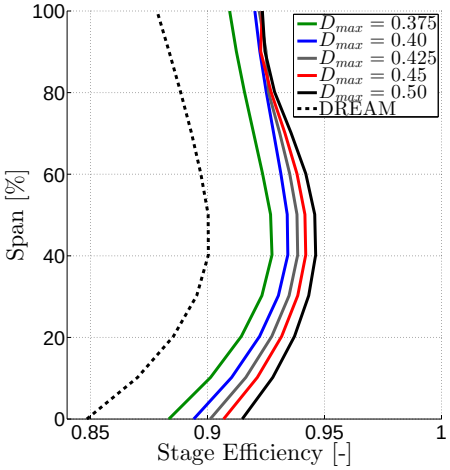


Figure 5.11: *Stage efficiency distributions for different values of D_{max} and for the DREAM stage*

Making an assumption of two-dimensional flow (i.e., $V_{ax} = cst$ across the rotor) and considering the rotor velocity triangle of the DREAM project booster (cf. Appendix A), it is possible, based on the ACPreDesign loss correlations, to find the solidity resulting in minimum losses. This method had already been exposed in Chapter 2. For given inlet and outlet flow angles, the losses only depend on the solidity and are plotted in Fig. 5.12. Lines of constant diffusion factor are also indicated.

At hub, no optimum exists for $D < 0.6$. At mid-span, an optimum solidity exists for $D < 0.6$ if a low turning of 15° is considered. However, it still lies at $D > 0.4$. At tip, it is possible to find an optimum solidity for various values of turning. In particular, for a turning of 15°, an optimum diffusion factor can be found very close to 0.4. The latter case is representative of the rotor tip conditions of the DREAM project booster. This is in agreement with the optimum that has been observed in Fig. 5.6.

The analysis of Fig. 5.12 underlines that seeking for the optimum solidity in terms of minimum loss most of the time lead to very low solidities. Without off-design considerations, this approach will rarely yield a realistic design.

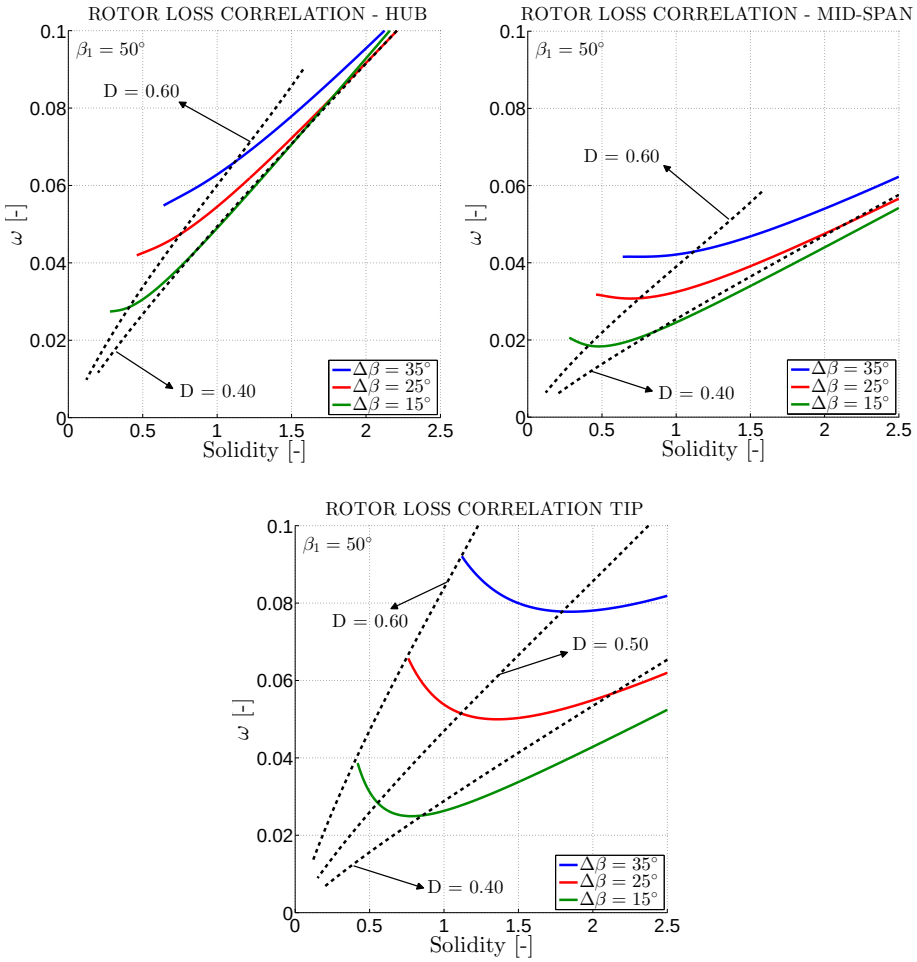


Figure 5.12: *Losses versus solidity for different inlet and outlet flow angles based on ACPreDesign rotor loss correlation curves*

The same optimization study has been performed removing the stator row. Solidity profiles are slightly lower since the stator losses must not be compensated but the main conclusions remain unchanged. Optimal solidity distributions as well as diffusion factors and efficiencies of the single rotor configuration are summarized in Appendix D.

5.4 Uncertainty quantification

The previous section revealed that the loss correlations play an important role in the determination of an optimum solidity. The correlations affect the prediction of efficiency and the existence of an optimum diffusion (and solidity). In that prospect, looking back at the correlation data of Lieblein et al. in Fig. 2.20, a scatter is observed in the data points. This source of uncertainty can be taken into account by the use of uncertainty quantification techniques.

The main idea of such methods is to improve the confidence in the predictions of ACPreDesign by adopting a non-deterministic approach. Within that probabilistic framework, an input vector $X = (x_1, x_2, ..., x_D)$ and an output $y = g(X)$ are considered. The input vector X is an independent random variable corresponding to a given sample space and the output variable y is a stochastic quantity. The function g is the solver ACPreDesign in the current investigation but could possibly be any complex fluid dynamics model or CFD tool. The objective is to compute the probability density function (PDF) f_y of the output in order to compute its statistics, such as the expected value $\mathbb{E}[y]$ and the variance $Var[y]$ given in Eq. (5.2) and Eq. (5.3).

$$\mathbb{E}[y] = \int_{-\infty}^{+\infty} z\, f_y(z)\, dz \tag{5.2}$$

$$Var[y] = \int_{-\infty}^{+\infty} (z - \mathbb{E}[y])^2 f_y(z)\, dz = \mathbb{E}[y^2] - (\mathbb{E}[y])^2 \tag{5.3}$$

Different methods exist in order to include uncertainties within the numerical predictions. They are characterized by their *intrusive* or *non-intrusive* nature. The method is considered as intrusive if the deterministic mathematical formulation (i.e. the source code) of the problem must be modified. Those methods have not been considered. On the opposite, sampling and quadrature methods are non-intrusive. Both are briefly presented below but more details about UQ methods in general are given by Iaccarino [53].

5.4.1 Sampling techniques

Sampling techniques are the simplest approaches to propagate uncertainties. They rely on repeated simulations with different values of the input variables to generate the statistics of the output population. The input variables are generated randomly corresponding to their PDF's (e.g. Gaussian, uniform,...). The most famous sampling approach is the Monte-Carlo method. As mentioned by Iaccarino, the strength of sampling resides in the fact that it is universally applicable and will always converge to the exact stochastic solution if the number of samples tends to infinity. The main drawback of Monte-Carlo sampling is that the convergence is very slow as, to build the statistics, it requires a large number of realizations.

5.4.2 Stochastic collocation

Stochastic collocation refers to as quadrature methods used to directly compute the statistics of random variables. Such methods enable to calculate the integrals (such as Eq. (5.2) and Eq. (5.3)) from a discrete (preferably low) number of realizations. Gaussian quadratures are mostly used in the field of uncertainty quantification. The general formulation is for a n-points quadrature:

$$\int_b^a y(\xi)\, f(\xi)\, d\xi \approx \sum_{i=0}^{n} w_i y(\xi_i) \tag{5.4}$$

where ξ_i are the roots of orthogonal polynomials, w_i are weights and f is a weight function which, in the current context, represents a PDF. Depending on the nature of the function $f(x)$, different quadrature methods exist. For random variables described by a normal distribution, the Gauss-Hermite quadrature is used. It is employed for an integral of the form:

$$\int_{-\infty}^{+\infty} y(\xi)\, e^{-\xi^2}\, d\xi \tag{5.5}$$

The complete formulation of the quadrature is:

$$\int_{-\infty}^{+\infty} y(\xi)\, e^{-\xi^2}\, d\xi \approx \sum_{i=0}^{n} w_i y(\xi_i) \tag{5.6}$$

The weight w_i are defined using the Hermite polynomials $H_n(x)$:

$$w_i = \frac{2^{n-1} n! \sqrt{\pi}}{n^2 \left[H_{n-1}(\xi_i)\right]}. \tag{5.7}$$

More generally, the weights depend on the nature of the orthogonal polynomials and directly ensue from the mathematical properties of such polynomials. The mathematical derivation of those weights is given in [94] (Hildebrand, 1974) while both the weights and the roots of the Hermite polynomials are tabulated in [95] (Abramowitz and Stegun, 1964). The first 5 Hermite polynomials are defined as follows:

$$\begin{aligned} H_0(x) &= 1 \\ H_1(x) &= 2x \\ H_2(x) &= 4x^2 - 2 \\ H_3(x) &= 8x^3 - 12x \\ H_4(x) &= 16x^4 - 48x^2 + 12. \end{aligned} \tag{5.8}$$

They are linked through the following recurrence relation:

$$H_{n+1} = 2xH_n(x) - H_n'(x) \tag{5.9}$$

or, observing that $H_n'(x) = 2nH_{n-1}(x)$,

$$H_{n+1} = 2xH_n(x) - 2nH_{n-1}(x). \tag{5.10}$$

For the case of a normally distributed variable x of mean μ and variance σ, the computation of the expectation of a function $y(x)$ is given by the following integral:

$$\mathbb{E}[y(x)] = \int_{-\infty}^{+\infty} \frac{1}{\sigma\sqrt{2\pi}} e^{-\frac{(x-\mu)^2}{2\sigma^2}} y(x)\, dx \tag{5.11}$$

Changing the variable such as,

$$\xi = \frac{(x-\mu)}{\sqrt{2}\sigma} \Leftrightarrow x = \sqrt{2}\sigma\,\xi + \mu \tag{5.12}$$

the quadrature becomes

$$\begin{aligned} \mathbb{E}[y(x)] &= \int_{-\infty}^{+\infty} \frac{1}{\sqrt{\pi}} e^{-\xi^2} y(\sqrt{2}\sigma\xi + \mu)\, d\xi \\ &\approx \frac{1}{\sqrt{\pi}} \sum_{i=1}^{n} w_i\, y(\sqrt{2}\sigma\xi_i + \mu). \end{aligned} \tag{5.13}$$

Similarly, the calculation of the variance is then given by:

$$Var[y(x)] \approx \frac{1}{\sqrt{\pi}} \sum_{i=1}^{n} w_i\, y(\sqrt{2}\sigma\xi_i + \mu)^2 - \mathbb{E}[y(x)]^2. \tag{5.14}$$

5.4.3 Parametrization

Different inputs may be subjected to uncertainties and may impact the results of ACPreDesign. For the present case, it appears natural to consider the uncertainty linked to the loss correlations. Two different loss parametrizations have been implemented in order to include uncertainties, one involving the whole stage and another dealing with an isolated rotor configuration.

5.4.3.1 Full stage loss parametrization

The first parametrization is very basic. It considers two uncertain parameters U_R and U_S, one for the rotor and one for the stator. For a given value of diffusion factor D, both rotor and stator loss parameters are independent, normally distributed random variables of mean μ and variance σ. The mean μ is given by the default evolution of ACPreDesign of the loss parameter versus diffusion factor, i.e. $\mu_R = \zeta_R(D)$ and $\mu_S = \zeta_S(D)$ respectively for rotor and stator means. The variance is constant over the whole span and the diffusion range and results from the analysis of Fig. 2.20. Assuming that the data observed in Fig. 2.20 correspond to 95% of the individuals, it can be stated that the full uncertainty band is equal to $2 * 1.96 * \sigma = 3.92\,\sigma$. Finally, observing that the scatter is about 0.005 at constant diffusion, the variance σ is equal to $1.275\,10^{-3}$. The parameters U_R and U_S uniformly shift the loss curves to higher or lower levels. The situation is depicted in Fig. 5.13 for the rotor loss curves. The mean and variance of U_R and U_S are summarized in Table 5.1.

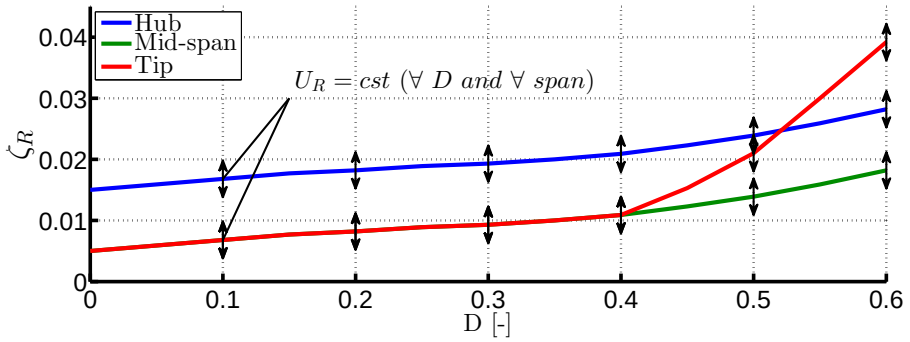


Figure 5.13: *Sketch of the rotor loss parametrization with constant uncertain variable U_R*

	μ [-]	σ [-]
U_R	$\zeta_R(D)$	$1.275\,10^{-}3$
U_S	$\zeta_S(D)$	$1.275\,10^{-}3$

Table 5.1: *Mean and variance of U_R and U_S*

5.4.3.2 Single-rotor loss parametrization

For the second loss parametrization, the rotor losses have been parametrized with three uncertain parameters. The first parameter U_{mean} shifts the mean loss level of hub, mid-span and tip correlation curves, exactly as with U_R. For the hub and mid-span loss curves, U_{mean} is the only variable parameter and both curves are just translated. For the tip correlation curve, another parameter, noted U_D, controls the value of the diffusion factor where the losses start to rise. Finally, the parameter U_{stall} introduces an additional uncertainty on the losses at stall, i.e. at $D = 0.6$. By changing U_{stall} independently from U_{mean} and U_D, the slope of the tip loss curve between the diffusion factor given by U_D and $D = 0.6$ is varying. The situation is illustrated in Fig. 5.14 showing the three uncertain parameters U_{mean}, U_D and U_{stall}.

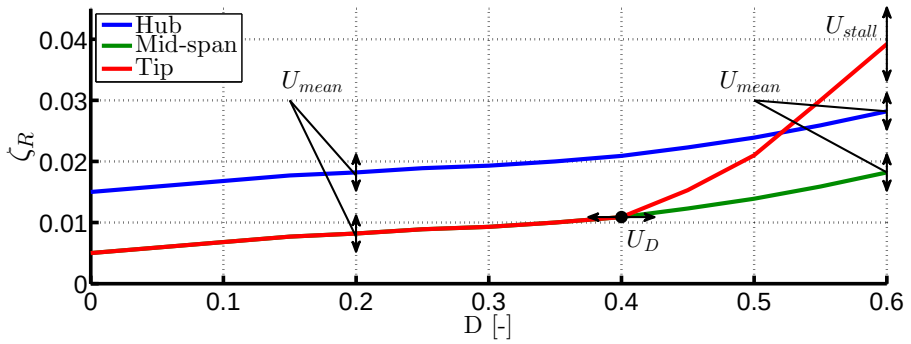


Figure 5.14: *Sketch of the rotor loss parametrization with three uncertain variables U_{mean}, U_D and U_{stall}*

The choice of the mean and variance of U_D and U_{stall} is more arbitrary. The variance of U_{stall} has been set to two times the variance of U_{mean} (i.e., $\sigma_{U_{stall}} = 2 * 1.275\,10^{-}3$). For U_D, a mean diffusion factor of 0.4 and a variance of 0.01 have been considered. Those values are summarized in Table 5.2.

	μ [-]	σ [-]
U_{mean}	$\zeta_R(D)$	$1.275\,10^{-}3$
U_D	0.40	0.01
U_{stall}	$\zeta_R(D = 0.6)$	$2.55\,10^{-}3$

Table 5.2: *Mean and variance of U_{mean}, U_D and U_{stall}*

5.5 Uncertainty quantification results

5.5.1 Full stage

Based on the optimum solidity distributions of the previous section at $D_{max} = 0.40$ and $D_{max} = 0.45$, both U_R and U_S have been randomly sampled 35.000 times although a minimum of 10.000 samples is usually sufficient. After 35.000 computations of ACPreDesign, the statistics of this population have been analyzed in terms of pressure ratio and efficiency. Both Fig. 5.15 and Fig. 5.16 illustrate the convergence of the efficiency mean and standard deviation when $D_{max} = 0.40$. The minimum amount of samples is very case sensitive and depends on the order of statistics that is required. In the current case, 20.000 appeared sufficient since the variations of both the mean and the standard deviation are below 0.005% of efficiency above 20.000 samples.

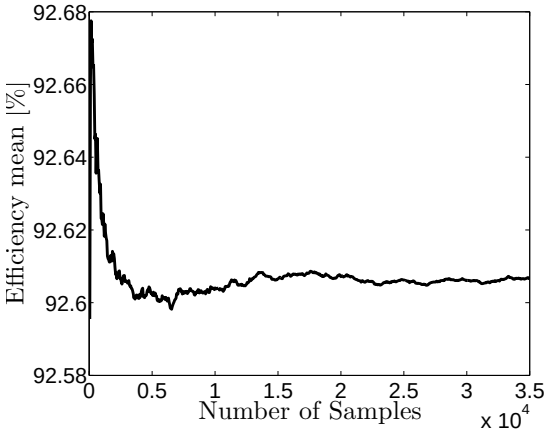


Figure 5.15: *Evolution of the efficiency mean with the number of samples ($D_{max} = 0.40$)*

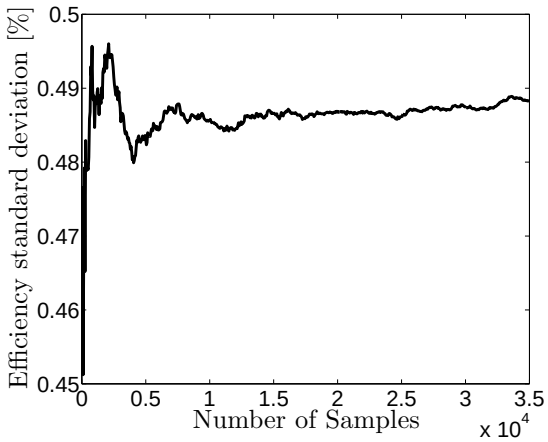


Figure 5.16: *Evolution of the efficiency standard deviation with the number of samples($D_{max} = 0.40$)*

Before stochastic collocations may be applied, the user must know the nature of the output PDF. Indeed, depending on the kind of the output PDF, different quadrature methods exist. Although Monte-Carlo sampling is very time and resource consuming, it remains the only way to characterize almost continuously the output PDF. To ensure a PDF is following a normal distribution, the population is presented in a histogram as well as in a probability plot. To build such a plot, based on the resulting mean μ and standard deviation σ, a theoretical normal distribution $N(\mu, \sigma)$ is plotted against the obtained population that has been formerly sorted in ascending order. If the population is normally distributed, the plot must be a straight line.

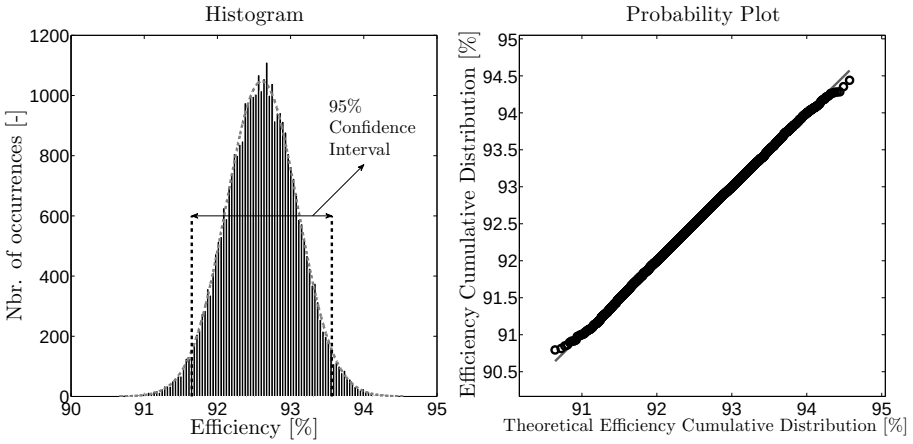


Figure 5.17: *Histogram and probability of the efficiency ($D_{max} = 0.40$)*

The histogram and the probability plot are shown in Fig. 5.17 which clearly proves that the efficiency is normally distributed. The histogram in Fig. 5.17 also gives a very good image of the scatter induced by non-deterministic loss correlations on the efficiency. For a 95% confidence interval, the width approaches 2.0%.

Given that the output PDF is Gaussian, the Hermite's quadrature may be used to perform stochastic collocation. Quadratures using 2, 3 and 4 points (per uncertain parameters) have been applied. With two uncertain parameters, ACPreDesign must be run 4, 9 or 16 times in order to generate the output statistics. Results of stochastic collocations are compared to Monte-Carlo sampling in Fig. 5.18 for both efficiency mean and standard deviation.

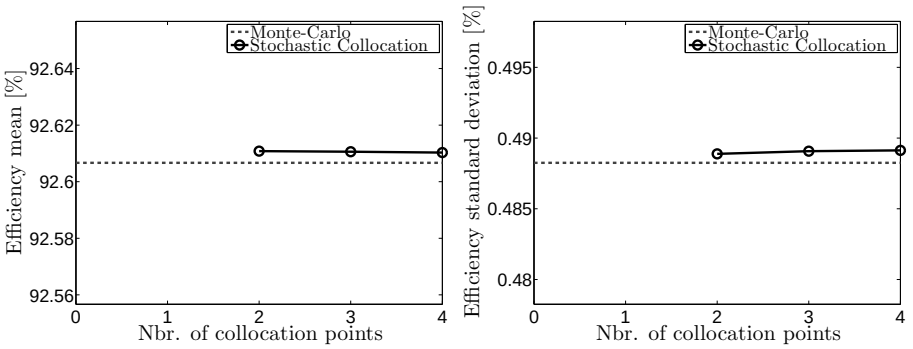


Figure 5.18: *Efficiency mean and standard deviation in function of the number of collocation points ($D_{max} = 0.40$)*

Both efficiency mean and standard deviation are not significantly changing with the number of collocation points. It depends on the system that is studied and the order of the statistics that is required. In the present case, 2 collocation points are sufficient to calculate the mean and standard deviation. Small differences are observed between the results of the Monte-Carlo sampling and the stochastic collocation method but this is not surprising since neither the Monte-Carlo nor the collocation technique are perfect. The first would require an infinite number of samples and the second is based on the approximation of an integral quantity. As the difference is around $4\,.\,10^{-3}\%$, it can be considered as negligible.

The choice of the method will depend on the application. If an accurate representation of the population statistics is required, the Monte-Carlo sampling remains the most appropriate option. Considering the use of an optimization problem under uncertainty, only quadrature methods that requires a few number of evaluations can be considered.

The same procedure has been applied to the optimum candidate at $D_{max} = 0.45$. Results are summarized in Table 5.3 and Table 5.4 for both optima at $D_{max} = 0.40$ and $D_{max} = 0.45$ respectively using Monte-Carlo sampling and stochastic collocation. The mean, the standard deviation and the 95% confidence interval $[\mu \pm 1.96\sigma]$ are indicated.

		MONTE-CARLO SAMPLING		
		μ	σ	$[\mu \pm 1.96\sigma]$
$D_{max} = 0.40$	π [-]	1.2510	0.0014	[1.2510 ± 0.0027]
	η [%]	92.61	0.49	[92.61 ± 0.96]
$D_{max} = 0.45$	π [-]	1.2510	0.0012	[1.2510 ± 0.0024]
	η [%]	93.41	0.41	[93.4 ± 0.80]

Table 5.3: *Monte-Carlo sampling results using two uncertain parameters (full stage configuration)*

		STOCHASTIC COLLOCATION		
		μ	σ	$[\mu \pm 1.96\sigma]$
$D_{max} = 0.40$	π [-]	1.2510	0.0014	[1.2510 ± 0.0027]
	η [%]	92.61	0.49	[92.61 ± 0.96]
$D_{max} = 0.45$	π [-]	1.2508	0.0012	[1.2508 ± 0.0024]
	η [%]	93.35	0.41	[93.35 ± 0.80]

Table 5.4: *Stochastic collocations results using two uncertain parameters (full stage configuration)*

The analysis of Table 5.3 and Table 5.4 reveals the importance of accurate and trustworthy correlations. The minimum standard deviation of the stage efficiency reaches 0.41%. Nowadays, compressor designers seek for 0.1% efficiency increase using three-dimensional blade design. Moreover, as seen in Fig. 5.17, it represents a 95% confidence interval that covers close to 2%. This study demonstrates that the meridional design already brings a non-negligible amount of uncertainty due to the correlations. This may have heavy consequences on the design targets. They may require to be increased to guarantee that the minimum efficiency still satisfies the performance specifications.

For $D_{max} = 0.45$, it is also interesting to observe in Table 5.3 and Table 5.4 that a difference of 0.06% appears between the mean efficiencies respectively computed with the Monte-Carlo sampling and the stochastic collocation. In such context, if 0.1% of efficiency improvement is forecasted by optimization, the difference between Monte-Carlo sampling and stochastic collocation becomes significant. It may be due to the mass-flow tolerance used inside ACPreDesign to assess the convergence. It may also be linked to the precision and rounding errors in ACPreDesign. It is thus recommended to monitor this difference and to compute the statistics by sampling techniques when possible.

The standard deviations of U_R and U_S, σ_R and σ_S have then be varied to evaluate their effects on the efficiency mean and standard deviation. Dividing and multiplying by 2 the baseline standard deviation σ_R ($=\sigma_S$) of Table 5.1 and running stochastic collocations (with 2 collocation points), the efficiency mean and standard deviation are given in Fig. 5.19 and Fig. 5.20. While, as expected, the efficiency mean does not change, the standard deviation shows a clear linear trend and as the standard deviation of U_R (and U_S) doubles, the efficiency standard deviation is multiplied by 2 to reach close to 1%. This illustrates that ACPreDesign acts as a very linear system.

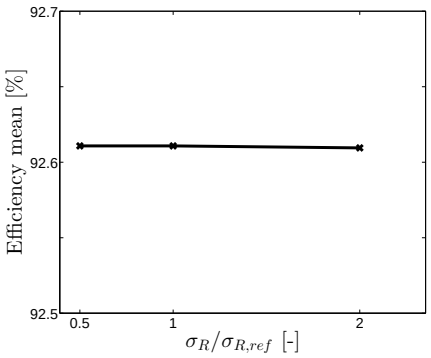


Figure 5.19: *Evolution of the efficiency mean with σ_R (=σ_S) - $D_{max} = 0.40$ - 2 collocation points*

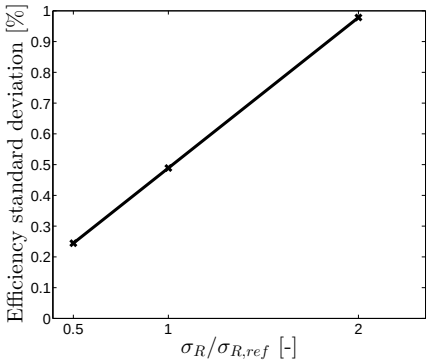


Figure 5.20: *Evolution of the efficiency standard deviation with σ_R (=σ_S) - $D_{max} = 0.40$ - 2 collocation points*

5.5.2 Single rotor

The same study as the full stage has been performed on a single rotor configuration and considering 3 uncertain parameters as displayed in Fig. 5.14. The optimum solidity distributions presented in Appendix D at both $D_{max} = 0.40$ and $D_{max} = 0.45$ have been considered. The results of both Monte-Carlo sampling and stochastic collocation are summarized in Table 5.5 and Table 5.6. Convergence plots and histrograms are also reported in Appendix D. The confidence intervals (at 95%) given both Tables 5.5 and 5.6 cover from 1.5% to 1.6%.

The mean efficiencies are higher than in Table 5.3 and Table 5.4 since no stator row is considered. Regarding the standard deviation, despite the fact that the second parametrization seems more accurate by taking into account various sources of uncertainties, it does not bring any additional information compared with the full stage results. It indicates that, in the present case, a single uncertain variable (per row) is already enough to highlight the weakness of deterministic computations and to obtain representative statistics.

		MONTE-CARLO SAMPLING		
		μ	σ	$[\mu \pm 1.96\sigma]$
$D_{max} = 0.40$	π [-]	1.2509	0.0012	[1.2509 ± 0.0024]
	η [%]	95.56	0.44	[95.56 ± 0.86]
$D_{max} = 0.45$	π [-]	1.2509	0.0011	[1.2509 ± 0.0022]
	η [%]	95.98	0.37	[95.98 ± 0.73]

Table 5.5: *Monte-Carlo sampling results using three uncertain parameters (single rotor configuration)*

		STOCHASTIC COLLOCATION		
		μ	σ	$[\mu \pm 1.96\sigma]$
$D_{max} = 0.40$	π [-]	1.2509	0.0012	[1.2509 ± 0.0024]
	η [%]	95.55	0.43	[95.55 ± 0.84]
$D_{max} = 0.45$	π [-]	1.2509	0.0011	[1.2509 ± 0.0022]
	η [%]	95.98	0.37	[95.98 ± 0.73]

Table 5.6: *Stochastic collocations results using three uncertain parameters (single rotor configuration)*

5.6 Optimization under uncertainty

In the previous section, it has been exposed how uncertainty quantification techniques allow to take into account the uncertainties inherently present in any correlation. The study highlighted very important efficiency uncertainty bands close to 2%. Furthermore, the stochastic collocation method offers very good estimates of the mean and the standard deviation of the output performance at affordable computational cost. For n uncertain variables and p collocation points, p^n computations are necessary. In the case of ACPreDesign and because only the mean and the standard deviation were required, the previous section demonstrated that 2 collocation points were sufficient. For the single rotor case with 3 uncertain parameters, it makes 8 computations. Since it does not represent an important computational cost, in order to decrease the efficiency uncertainty bands, it is then realistic to perform a solidity distribution optimization where the pressure ratio, the average efficiency as well as its standard deviation are optimized.

Optimization under uncertainty is most of the time mentioned as the problem of *robust design*. This approach is not very common in compressor or turbine blade design, mainly due to high computational costs of CFD computations. Ideally, the aim is to look at a solution that is less sensitive to the uncertain-

ties. In the case of Fig. 5.21, while a standard optimization, disregarding any fluctuation, would tend to the extremum in X_1, a robust design may lead to an extremum in X_2 since it shows a lower standard deviation. However, the existence of such a robust optimum obviously depends on the system that is studied and the situation of Fig. 5.21 may not always occur. The main problems encountered in engineering when dealing with robust designs are exposed by Poloni et al. (2011, [96]).

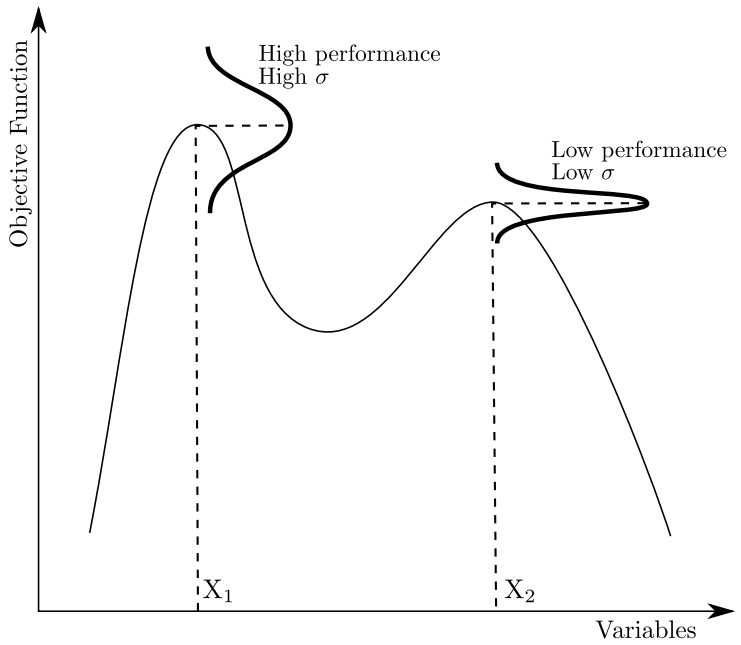


Figure 5.21: *Illustration of the* robust design *problem on an arbitrary function presenting two extrema*

Robust optimization has been performed involving 3 uncertain variables. The maximum diffusion factor has been set to 0.40 and 0.45. The pressure ratio, the efficiency and the efficiency standard deviation must be optimized. It is thus not anymore a single objective optimization. Since there are 3 uncertain parameters and 2 collocations points, each individual generated according to the DE algorithm requires 8 computations of ACPreDesign to obtain a mean and a variance. The rest of the optimization process remains unchanged. The pareto fronts are given in Fig. 5.22 in terms of pressure ratio versus efficiency. No difference appears between the standard optimization and the robust optimization. Such results are very dependent on the solver that is studied, the chosen parametrization and the optimized parameters but the situation depicted in Fig. 5.21 does not exist for the current test case. In other words, for the given problem of solidity optimization, the optimum solutions of Fig. 5.6 are also robust designs. It also means that a robust optimization cannot help to decrease the uncertainty bands highlighted in the previous section. The

only remaining option for the designer is then to rely on more trustworthy correlations presenting lower discrepancies than in Fig. 2.20 and that are more representative of state-of-the-art compressor designs.

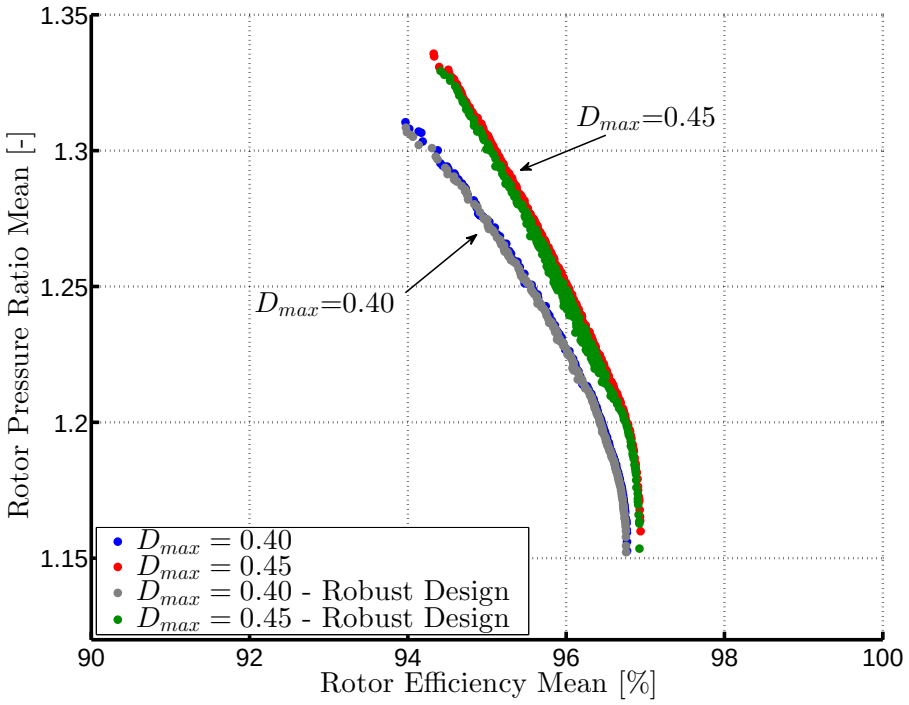


Figure 5.22: *Comparison of pareto fronts with or without considering uncertainties*

5.7 Conclusion

A meridional solver relies on empirical correlations to obtain an estimate of the total pressure losses of a blade row. In the present investigation, the NISRE solver *ACPreDesign* is based on typical correlations originally established by Lieblein et al. However, empirical data often come with uncertainties that are usually neglected at the level of the meridional design.

The current chapter presented the implementation of uncertainty quantification methods in the specific case of solidity optimization of a single rotor compressor. The study shows that both Monte-Carlo sampling as well as quadrature methods compute uncertainty bands that cover 1.5% in efficiency. While, nowadays, 3D blade design optimization chases 0.1% improvements that are very difficult to validate experimentally, it represents a non-negligible amount of uncertainty that is disregarded by a standard deterministic approach. Such

additional information may imply to increase the target efficiency according to the uncertainty band to guarantee a minimum efficiency above the design requirements.

Outside the framework of solidity optimizations, uncertainty quantification could be implemented at the level of meridional design to take into account various sources of epistemic uncertainties. For example, the use of UQ techniques may compensate the lack of knowledge related to the influence of the inlet boundary layer profile, the Reynolds number or the inlet turbulence intensity which can cause big variation in the meridional design performance in terms of pressure ratio, efficiency and mass-flow. Off-design correlations also represents a tremendous source of uncertainty that can radically affect the whole design. Regarding stability, the correlation curve of Fig. 2.35 from Koch [29] could easily be added in ACPreDesign. It would give stability capabilities at the level of meridional design without performing off-design calculations. The correlation of Koch provides a maximum static pressure rise $C_{p,max}$ depending on solidity and stagger angle. The opposite evolution of efficiency and stability with respect to solidity would definitely lead to very interesting results in the framework of solidity optimization. Finally, beyond the meridional design, non-deterministic CFD calculations may also play a crucial role in the management of turbulence modeling uncertainties.

The issue of the robust design was also addressed and, in the present case, the standard optimum designs were already robust. The existence of a robust optimum strongly depends on the nature of the problem that is studied and, in many situations, an optimization under uncertainty may lead to the same solution as a standard optimization. It means that, for the current problem, a robust optimization cannot help to reduce the sensitivities of the performance parameters and better correlations are required to improve the accuracy of the prediction. Nevertheless, the study reveals the capability of performing meridional robust optimizations which may represent a breakthrough in turbomachinery design.

Chapter 6

Conclusions and perspectives

6.1 Conclusions

The present investigation covered the effect of solidity on compressor performance and stability. The research was carried out to improve the current design practices in compressor design, most particularly in view of reducing the solidity and consequently the weight of the engine. After reviewing the literature, both numerical and experimental investigations were considered on linear compressor cascades. Solidity effects have been studied by varying the pitch at constant aspect ratio (i.e. constant chord-based Reynolds number). The last part of the work focused on solidity optimization at the level of meridional design.

The experimental campaign took place in the high-speed VKI-C3 cascade facility. The blade profile under investigation was a CDB provided by Techspace Aero that is is representative of a state-of-the-art low pressure compressor stator mid-span section. Total pressure and flow angle measurements have been performed at two inlet Mach numbers, 6 incidences and 4 span heights. Performance parameters such as total pressure losses, deviation and diffusion factor have been calculated at all Mach and incidence conditions.

Numerical simulations were performed with FINE/Turbo from Numeca International. Although a specific turbulence model and numerical discretization scheme were imposed by the common design practices of Techspace Aero, different numerical parameters were varied to consider their influence on the performance predictions. Two numerical domains were also considered and investigated with FINE/Turbo. The first configuration was only considered before the test campaign in order to demonstrate the capabilities of CFD regarding cascade performance predictions. To support this investigation, two compressor profiles were examined, the CDB of interest as well as a standard DCA. The choice of the latter was motivated by the extensive amount of data available in the literature that enables to assess the quality of the CFD predictions against the existing correlations. The study showed very good agreement for the DCA but shed light on the need for new correlations for the CDB. The second configuration that has been studied only involved the CDB. It was established after the measurements to exactly match the experimental domain in terms of distance between inlet and outlet planes. Moreover, the measured boundary conditions were set at the inlet.

Globally, both pre-test and post-test CFD results are in fair agreement at low incidences. As the incidence increases, the influence of the inlet boundary layer on the secondary flow generation becomes more important and bigger discrepancies are observed. It recalls the importance of having realistic inlet boundary layer information to obtain accurate predictions. In that prospect, it must also be underlined that the inlet turbulent kinetic energy and its dissipation rate have not been measured during the experimental campaign but a representative inlet turbulence intensity of 1% has been used based on previous work at VKI and standard practices have been followed regarding the calculation of the turbulence length scale.

Effect of solidity on compressor performance At low incidence, decreasing the solidity slightly decreases the minimum losses. This loss reduction was observed both numerically and experimentally but could not be validated as it was within the measurement uncertainty bands. Going to off-design incidences, the losses grow faster and steeper as the solidity decreases. Removing blades (or reducing their chord) increases the loading and suction side separation occurs at lower incidence. This leads to wider and more intense wakes which induce the total pressure losses to grow faster when the solidity is reduced. Consequently, there is a compromise to be found to keep low losses at both optimum and off-design conditions. Numerical predictions are very unsatisfactory in terms of total pressure losses as they overestimate the losses at low incidence and fail at capturing the steep loss rise at high incidence. This is especially true for low solidity.

The prediction of optimum incidence is also of great importance in compressor design. Existing correlations already highlighted that the optimum incidence decreases as the solidity decreases. Due to the experimental discrete resolution in incidence, various optimum incidence rules have been derived from the measurements. Together with the CFD results, they all agree to show that the existing rules are not satisfactory. However, the determination of the optimum incidence is not unambiguous. In particular, the absence of data at negative incidence prevents establishing an ultimate updated rule.

High solidity also helps to deflect the flow in the required direction. This is usually assessed by quantities such as deviation and turning. Previous research showed that the deviation decreased as the solidity increased but the existing empirical rules appeared obsolete for the controlled diffusion blade. The experimental campaign yielded new deviation laws at design and off-design conditions. Particularly at off-design conditions, the guidance role of the solidity was clearly identified. While for high solidities the deviation remains quasi-constant for various incidences, the deviation rises quickly as the solidity is reduced. At optimum incidence, very good agreement was found with the numerical predictions. Going to stalling incidences, big discrepancies emerged. The agreement with the CFD results declines as the solidity is reduced. This underlines an

important conclusion of the whole research: current computational techniques do not manage to simulate properly the solidity effects, in particular because of the appearance of separated flow and secondary flows.

The assessment of the loading usually relies on a diffusion factor which characterizes the deceleration of the flow on the blade suction side. This quantity, originally defined by Lieblein, is inherently linked to the AVDR. This parameter characterizes the two-dimensional behavior of the flow and as it increases, the diffusion factor decreases. Considering a cascade geometry, an AVDR higher or lower than 1 reflects the three-dimensional nature of the flow and the development of secondary flows. More generally, in a three-dimensional compressor environment, the AVDR is also influenced by the curvature of the flowpath. The fact that the calculation of the diffusion factor is affected by the AVDR may thus be very misleading for the designer who must adapt his design or stall loading criteria depending on the AVDR. The use of a two-dimensional diffusion factor (obtained if an AVDR equal to 1 is assumed) removes this dependence and linearizes the loading evolution with incidence. It then appeared that considering a stall limit at a diffusion factor of 0.6 (as it is commonly suggested in the literature) is too optimistic and lowering this limit to 0.5 would lead to more realistic designs. Furthermore, because it presented an extremely good agreement with the numerical predictions, the two-dimensional diffusion factor can become a complementary loading parameter that may be used in compressor design in addition to the standard diffusion factor of Lieblein in order to set up design and stall criteria.

Loss correlations were compared against both definitions of diffusion factors. In both cases, the correlations should be slightly updated. Nowadays, compressor profiles are the results of an optimization process. It seems thus natural that those optimized controlled diffusion blades generate less total pressure losses than original NACA or DCA airfoils. Regarding off-design loss predictions, the experimental investigation also revealed that standard parabolas mentioned in the literature for NACA or DCA profiles are obsolete and higher order polynomials are recommended for a state-of-the-art CDB.

Another important conclusion also resides in the very small compressibility effects that were observed on both total pressure losses and deviation as the Mach number was increased up to M=0.6 during both the numerical and experimental investigations. Most of the correlation data were obtained at low speed ($M \leq 0.3$) and very few evidences were found suggesting to apply any correction as long as sonic conditions (i.e. critical conditions) are not reached on the blade suction side. For the high solidity, isentropic Mach number distribution measurements support that no sonic point is observed at low incidence. Assuming that sonic conditions are also not reached for low solidities, it would confirm that, for such a profile, low-speed correlations are still reliable as far as critical conditions do not occur.

Solidity optimization and uncertainty quantification Between a high number of blades inducing high stability but high friction and a low number of blades yielding high diffusion but high efficiency, a compromise must be found. The definition and selection of an optimum solidity remains a critical step in the whole design process. Theoretical methods have been proposed very early by Howell or Zweifel but remain unsatisfactory for recent applications.

By coupling a meridional solver to an optimization code, it is possible to perform a solidity optimization for a given pressure ratio distribution. The results obtained with the NISRE solver ACPreDesign coupled to the VKI optimization code CADO showed the influence of the maximum diffusion that is allowed by the designer on the determination of an optimum solidity distribution. Depending on the span and on the required velocity triangle, an optimum diffusion factor and consequently an optimum solidity may exist. Currently ACPreDesign does not provide off-design predictions but simple off-design considerations can be implemented to enhance the definition of an optimum solidity. The importance of loss correlations has also been highlighted.

The implementation of uncertainty quantification methods can help to consider the epistemic uncertainties related to the correlations at the level of meridional design. Both sampling and quadrature methods shed lights on uncertainty bands that cover 2.0% in efficiency. While, nowadays, 3D blade design optimization seeks 0.1% or even less efficiency improvements (that are additionally very difficult to validate experimentally), those uncertainty bands represent a non-negligible amount of uncertainty that are disregarded by a standard deterministic approach. Those complementary information may have strong consequences on the target efficiency that will have to be increased to guarantee a minimum efficiency always sitting above the design requirements.

6.2 Perspectives

The consequences of the new correlation rules that have been derived during this investigation must now be analyzed and implemented in a throughflow solver like ACPreDesign. Design and off-design meridional solidity optimizations must be performed and results must be compared with the previous design practices. The validation should also be supported by 3DNS computations. Together with the implementation of the new correlation laws, the use of the two-dimensional diffusion factor must be monitored. Because of the better agreement obtained between the numerical and experimental data considering a two-dimensional assumption, this loading parameter seems to be a very promising design parameter that should be used in addition to the standard diffusion factor of Lieblein.

To fully characterize the effect of solidity on the compressor stability, it seems essential to consider the exploration of the negative incidence side of the loss

curves for all solidities. This would firstly bring very interesting information regarding the optimum incidence determination but would especially shed light on the choke behavior of the cascade as the solidity is varied. This would then enable to assess the effect of solidity over the whole operating range, from choke to stall conditions.

Although the compressibility effects appeared very small up to an inlet Mach number of 0.6, a similar study should be conducted for transonic and supersonic profiles typically for fans or high-speed compressors. Many evidences already showed that the appearance of strong shock patterns may modify the conclusions of the current investigation.

The study also uncovered the non-physical and dispersive nature of a centered spatial discretization even though it still remains the common practice in turbomachinery. The use of a second order upwind scheme does partially solve this issue but introduces more dissipation. Aiming at improving the current numerical prediction in compressor design, the present investigation truly constitutes an extensive database to develop high-fidelity CFD tools.

To complete the current database and provide all the required data to validate the CFD, inlet hot-wire traverses should be repeated at both Mach number conditions to measure both the inlet turbulence intensity and the length scale. Similarly, hot-film measurements would bring a lot of valuable information about the blade boundary layer status that could be compared to the CFD predictions.

Finally, although compressor design methods still rely on cascade correlations, it is undeniable that it remains very different than a full compressor stage where three-dimensional and unsteady features such as the tip leakage vortex or the rotor-stator interactions cannot be ignored. In that prospect, new technology effects can only be validated by performing single- or multi-stage compressor tests. In particular, the three-dimensional annular blade row may have a very different stall inception than the two-dimensional cascade and the stall criteria will certainly have to be adapted.

The emphasis must also be set on the use of uncertainty quantification in compressor design far beyond the framework of solidity optimizations. Compressor design still relies on various empirical or theoretical models that are huge sources of epistemic uncertainties. As an example, the influence of the inlet boundary layer profile or the inlet turbulence intensity could be considered in throughflow computations but, besides the meridional design, nondeterministic CFD calculations may also play a crucial role in the management of the various discrepancies related to the turbulence modeling. With the improvements of the computational resources, the implementation of uncertainty quantification techniques such as sampling or quadrature methods becomes more realistic and it may represent a breakthrough in turbomachinery design.

Appendix A

The DREAM project booster

The DREAM project booster is a LP compressor designed and manufactured by Techspace Aero within the European FP7 DREAM project (valiDation of Radical Engine Architecture systeMs) which aims to validate new architectures and advanced design concepts for more efficient turbomachinery components. The 1.5 DREAM compressor stage is representative of a current state-of-the-art booster. Both numerical and experimental investigations have been carried out in order to assess the performance of the stage. They have been reported in [78].
The 1.5 stage is composed of 100 inlet guide vanes, 76 rotor blades and 100 stator vanes. The compressor has been studied at VKI numerically with the commercial software FINE/Turbo of NUMECA International and experimentally in the high-speed R4 facility. A 3D view of the 1.5 stage is shown in Fig. A.1.

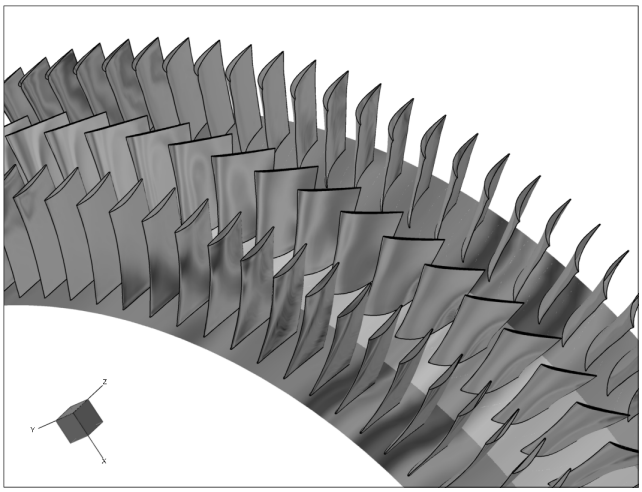


Figure A.1: *Three-dimensional view of the 1.5 DREAM booster stage*

A.1 Velocity triangles

In Table A.1, the rotor velocity triangles are given at three spanwise locations. Those data are used for various comparisons within Chapter 2 and Chapter 5.

	Span location	β_1	β_2	w_1	w_2
Velocity	Hub	49°	18°	263 m/s	207 m/s
Triangle	Mid	48°	28°	255 m/s	197 m/s
Data	Tip	49°	38°	252 m/s	192 m/s

Table A.1: *Rotor inlet and outlet velocity triangles of the DREAM project booster*

A.2 Preliminary study of the blade number effect

A preliminary solidity study had been done on this stage by removing and adding some rotor and stator blades. The whole 1.5 stage is considered but the rotor and stator blade numbers are varied independently. It must be mentioned that the booster has been designed such that the stall starts from the rotor hub (between 20% and 40% of the blade height from the hub). This may compromise the stability analysis of the compressor.

A.2.1 Influence of rotor blade number

The performance of three different rotors have been assessed from choke to stall. The corresponding blade numbers are indicated in the Table A.2. The

Tested rotor solidities				
	Blade number	σ_{hub}	σ_{tip}	Relative to design (%)
Design	66	1.32	1.09	-15%
	76	1.52	1.26	-
	86	1.72	1.43	+15%

Table A.2: *Tested rotor blade numbers and solidities*

rotor pressure ratio and efficiency are plotted in Fig. A.2 and Fig. A.3. In Fig. A.2, it appears that the high solidity rotor achieves the highest pressure ratio. This is in agreement with Carter's rule which predicts that the deviation is reduced when the solidity increased. As the deviation is lower, the flow turning increases and more pressure rise is achieved. In Fig. A.3, the effect on the maximum efficiency is clear and the lowest solidity shows the best efficiency. This is rather expected as cascade correlations predict less losses for low solidity. Nonetheless, the trend does not remain the same on the whole operating range. The low solidity rotor stalls first. No improvement appears between the mid and

the high solidity rotors. It is believed that the expected stability enhancement of the high solidity rotor is injured by the blade design between 20% and 40% of the span.

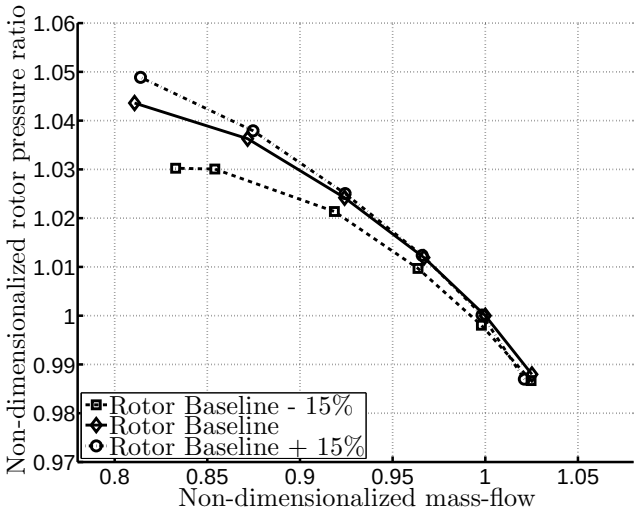


Figure A.2: *Rotor pressure ratio versus mass-flow for three values of the rotor blade number of the DREAM stage*

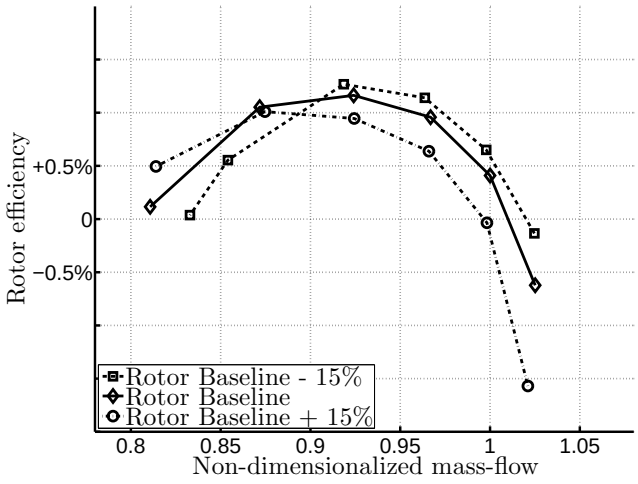


Figure A.3: *Rotor efficiency versus mass-flow for three values of the rotor blade number of the DREAM stage*

A.2.2 Influence of stator blade number

The influence of stator solidity has also been studied by changing the number of vanes. The tested stator solidities are available in the Table A.3.

Tested stator solidities				
	Blade number	σ_{hub}	σ_{tip}	Relative to design (%)
	80	1.47	1.46	-20%
Design	100	1.83	1.82	-
	120	2.20	2.19	+20%

Table A.3: *Tested stator blade numbers and solidities*

In terms of efficiency and pressure ratio, the effect of the stator solidity is more straightforward than for the rotor. Removing blades improve both pressure ratio (Fig. A.4) and efficiency (Fig. A.5). When there is no work addition, a blade row only represents a source of friction losses that decreases the total pressure and less pressure losses are encountered when less stator vanes are present. Therefore, decreasing the stator solidity results in a higher pressure ratio and a higher efficiency. The opposite situation happens when adding some blades.

Regarding the stability, no difference appears between the 100 and 120 blades stators. This is due to the rotor that has been designed to induce the stall. However, increasing the stator loading by lowering its solidity brings the stall to the stator. This can be seen by comparing the total pressure maps of the 80-blades and the 120-blades configurations in Fig. A.6 and Fig. A.7. The low solidity stator configuration reveals a total pressure deficit around the tip sections indicating the appearance of separation.

This preliminary study also highlights that the off-design analysis strongly depends on various design choices that usually takes place during the early stages of the design process. In the current case, it is believed that the design of the rotor avoids to notice any stability effect between the 100-blade and the 120-blade stator rows. The solidity is selected early in the design process and the whole meridional design relies on that choice. During the blade-to-blade and/or 3D optimization procedure(s), the solidity does not change anymore. Changing the solidity afterwards does not offer a fair comparison as the whole 3D blade design would have been different if a lower or higher solidity had been selected. From a designer point of view, the solidity effect must always be assessed with the same design targets.

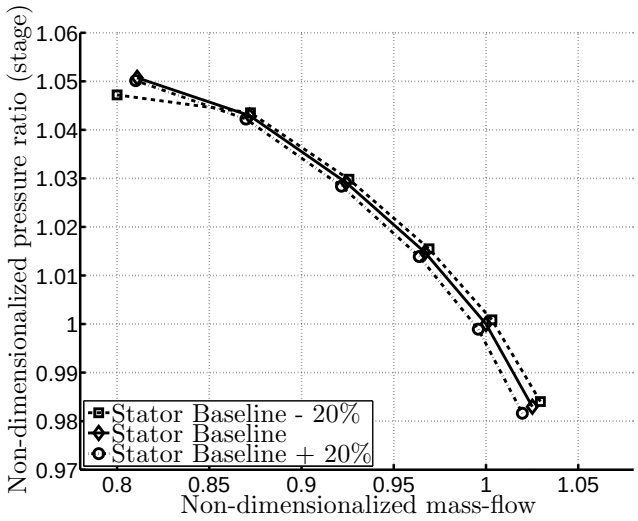


Figure A.4: *Stage pressure ratio versus mass-flow for three values of the stator blade number of the DREAM stage*

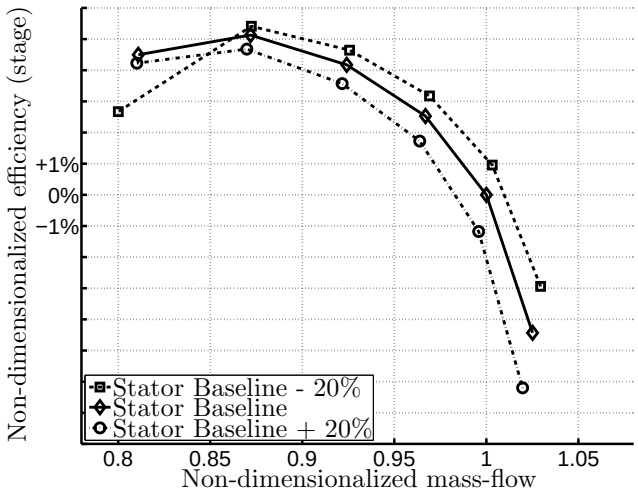


Figure A.5: *Stage efficiency versus mass-flow for for three values of the stator blade number of the DREAM stage*

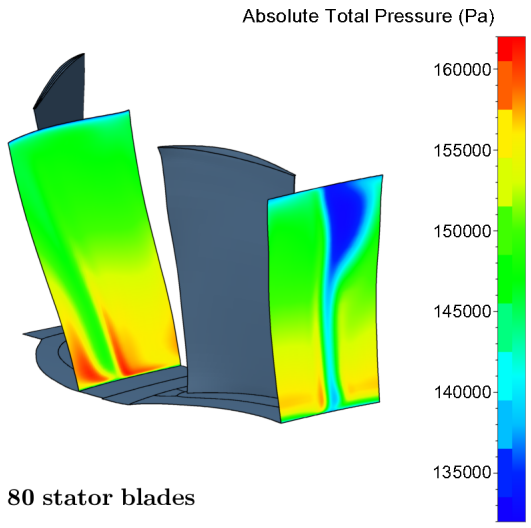


Figure A.6: *Stator outlet total pressure maps at near stall of the 80 stator blades configuration*

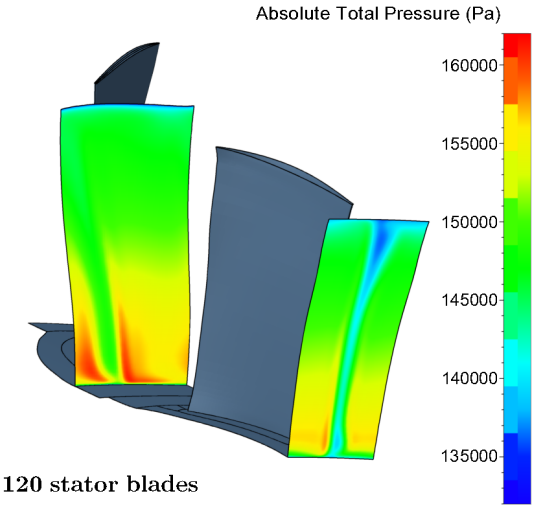


Figure A.7: *Stator outlet total pressure maps at near stall of the 120 stator blades configuration*

Appendix B

Probe calibration and uncertainty calculation

Two different types of probes have been used for the measurement campaign. The first one is a kiel probe that gives accurate total pressure measurements in a wide range of Mach number and flow angle. The second type is a three-hole probe that enables to measure the yaw angle, total pressure and static pressure after prior calibration. This appendix presents the calibration curves of both types of probes and approaches the uncertainty calculation.

B.1 Kiel probe calibration

A picture of the Kiel probe is given in Fig. 4.6. Such a probe offers a wide range of angular insensitivity for various Mach numbers. In Fig. B.1 and Fig. B.2, the ratios of the probe total pressure over the true value are shown at various Mach numbers for both yaw and pitch variations. A constant pressure ratio is reached from -30° to +30° in yaw and -16° to +16° in pitch. This ensures to measure the exact total pressure independently to the inlet flow angle.

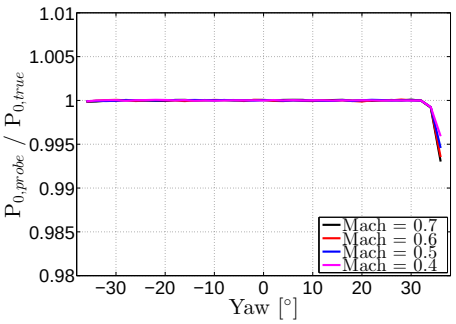


Figure B.1: *Kiel probe yaw calibration*

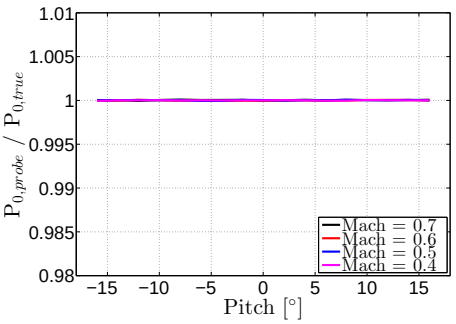


Figure B.2: *Kiel probe pitch calibration*

B.2 Three-hole probe calibration

The 3-hole probe (cf. Fig. 4.5) has been calibrated for yaw angle and Mach number in the C4 calibration facility of VKI. Calibration coefficients used in

order to retrieve the flow angle, the total pressure and the static pressure are recalled in Eq. (B.1), Eq. (B.2) and Eq. (B.3) where P_L, P_R, P_C, P_t and P_s stand for the left-hole, the right-hole, the center-hole, the true total and the true static pressures.

$$K_{yaw} = \frac{P_L - P_R}{P_C - \frac{P_L + P_R}{2}} \tag{B.1}$$

$$K_{tot} = \frac{P_t - P_C}{P_C} \tag{B.2}$$

$$K_{dyn} = \frac{\frac{P_L + P_R}{2} - P_s}{P_C} \tag{B.3}$$

The coefficients are plotted in Fig. B.3, Fig. B.4 and Fig. B.5. The coefficient K_{yaw} is nearly not affected by the Mach number between -20° and +20°. On the other hand, the coefficients K_{tot} and K_{dyn} are affected both by Mach number and inlet flow angle. Therefore, retrieving the total pressure (or the static pressure) with such a probe will always lead to higher uncertainties than a standard kiel probe that does not require any calibration.

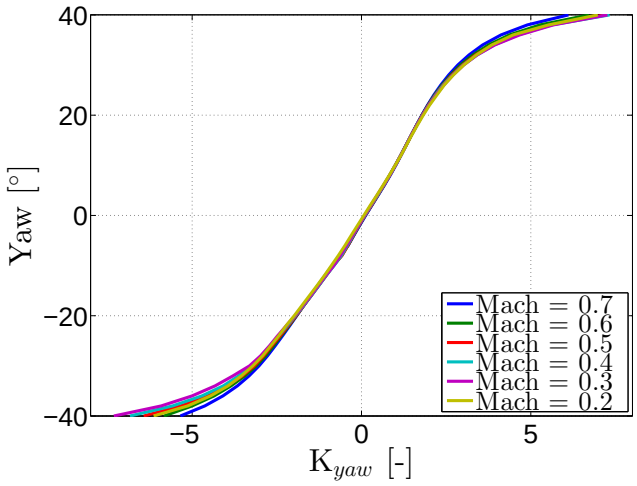


Figure B.3: *Yaw angle versus* K_{yaw}

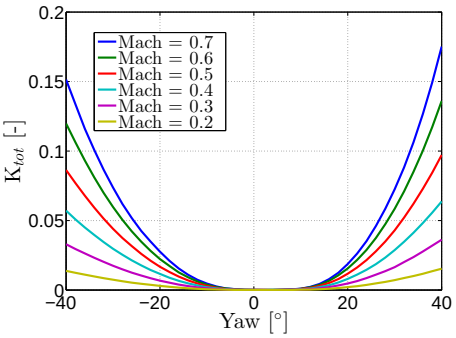


Figure B.4: *K_{tot} versus yaw angle*

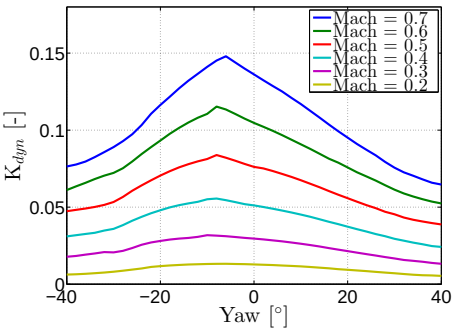


Figure B.5: *K_{dyn} versus yaw angle*

Although the pitch angle cannot be measured with a 3-hole probe, the same procedure has been applied at 5 different pitch angles to monitor its influence. The pitch angle effect is shown for the K_{yaw} coefficient at Mach numbers of 0.40 and 0.70 respectively in Fig. B.6 and Fig. B.7. The influence of the pitch appears very limited within the studied range, i.e. -16° to +16°.

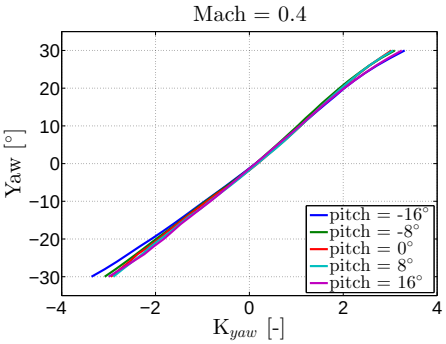


Figure B.6: *K_{yaw} versus yaw angle for various pitch angles*

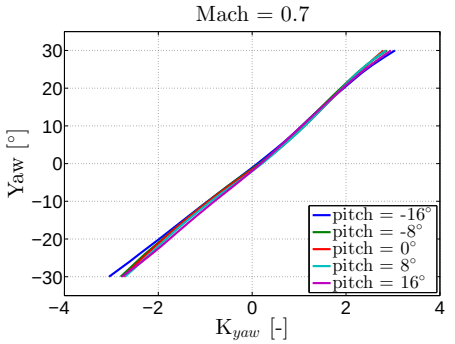


Figure B.7: *K_{yaw} versus yaw angle for various pitch angles*

B.3 Uncertainty analysis

B.3.1 Systematic and random uncertainties

The ASME method is used to assess the uncertainty of the measurements. The method is extensively presented by Dieck in [60]. An essential feature of this method is the distinction between systematic and random uncertainties. Systematic uncertainties are referred with b while σ is used for random uncertainties.

B.3.2 Pressure uncertainty

Scanners from Scannivalve company have been used for all pressure acquisitions. Those devices provide accurate relative pressure measurement with respect to a reference that can be the atmospheric ambient pressure or a given reference pressure. The scanners have been sent back for calibration before the measurement campaign. It is thus assumed that the specifications provided by Scannivalve can be trusted. The manufacturer assesses that the pressure scanners have an uncertainty (assumed to be given within a 95% confidence level) of 0.05% of the full scale. Three different pressure scanners have been used: two of 15-psi for the outlet static pressures and one of 5-psi range for the inlet pressures and the probes. Their uncertainty may then be calculated with Eq. (B.4) and Eq. (B.5) respetively for the 15- and 5-psi scanners.

$$b_{15psi} = 0.05/100 * 15 = 0.52 \text{ mbar (for the outlet static pressures)} \quad \text{(B.4)}$$

$$b_{5psi} = 0.05/100 * 5 = 0.17 \text{ mbar (for inlet and probe pressures)} \quad \text{(B.5)}$$

The scanner gives a relative measurement with respect to the atmospheric pressure. If an absolute pressure is desired, the atmospheric pressure must be added. The atmospheric pressure is obtained from the VKI pressure server connected in the S1 VKI-facility with an uncertainty of 0.15 mbar (within a 95% confidence level). To get the final uncertainty of any static pressure or kiel probe measurements, both values must be root-sum-square (cf. Eq. (B.6), Eq. (B.7) and Eq. (B.8)). The results are considered to be given at 95% confidence.

$$b_{s,1} = \sqrt{b_{5psi}^2 + b_{atm}^2} = 0.23 \text{ mbar} \quad \text{(B.6)}$$

$$b_{0,kiel} = \sqrt{b_{5psi}^2 + b_{atm}^2} = 0.23 \text{ mbar} \quad \text{(B.7)}$$

$$b_{s,2} = \sqrt{b_{15psi}^2 + b_{atm}^2} = 0.54 \text{ mbar} \quad \text{(B.8)}$$

According to the ASME method and its terminology recalled in [60], all the previous uncertainties are considered as systematic since they are present in all the following measurements. The 64 pressure taps of a scanner may also be considered to be correlated. In the case of pressure mean, ratio or difference, it can play an important role. As an example, for the total pressure difference $\Delta P_{0,1-2} = P_{0,1} - P_{0,2}$ with both $P_{0,1}$ and $P_{0,2}$ connected to the 5-psi scanner, the calculation of the systematic uncertainty taking the correlation into account

is given by Eq. (B.9).

$$\begin{aligned} b_{\Delta P_{0,1-2}} &= \left[\left(\frac{\partial \Delta P_{0,1-2}}{\partial P_{0,1}} b_{P_{0,1}} \right)^2 + \left(\frac{\partial \Delta P_{0,1-2}}{\partial P_{0,2}} b_{P_{0,2}} \right)^2 + ... \right. \\ &\quad \left. +2\ r\ \frac{\partial \Delta P_{0,1-2}}{\partial P_{0,1}} \frac{\partial \Delta P_{0,1-2}}{\partial P_{0,2}} b_{P_{0,1}} b_{P_{0,2}} \right]^{\frac{1}{2}} \\ &= \sqrt{\left(1 b_{P_{0,1}}\right)^2 + \left(-1 b_{P_{0,2}}\right)^2 + 2\ r\ (1)\ (-1)\ b_{P_{0,1}} b_{P_{0,2}}} \\ &= \sqrt{b_{P_{0,1}}^2 + b_{P_{0,2}}^2 - 2\ r\ b_{P_{0,1}} b_{P_{0,2}}} \\ &= \sqrt{b_{P_{5psi}}^2 + b_{P_{5psi}}^2 - 2\ r\ b_{P_{5psi}} b_{P_{5psi}}} \\ &= \sqrt{2 b_{P_{5psi}}^2 (1-r)} \end{aligned} \tag{B.9}$$

In the case of the pressure difference $P_{dyn,1} = P_{0,1} - P_{s,1}$, the same result as Eq. (B.9) may be obtained but, in the case of an average, as $P_{av,LR} = (P_L + P_R)/2$, the correlation may have a detrimental effect:

$$\begin{aligned} b_{P_{av,LR}} &= \left[\left(\frac{\partial P_{av,LR}}{\partial P_L} b_{P_L} \right)^2 + \left(\frac{\partial P_{av,LR}}{\partial P_R} b_{P_R} \right)^2 + ... \right. \\ &\quad \left. +2\ r\ \frac{\partial P_{av,LR}}{\partial P_L} \frac{\partial P_{av,LR}}{\partial P_R} b_{P_L} b_{P_R} \right]^{\frac{1}{2}} \\ &= \sqrt{\left(\frac{1}{2} b_{P_L}\right)^2 + \left(\frac{1}{2} b_{P_R}\right)^2 + 2\ r\ \frac{1}{2}\ \frac{1}{2}\ b_{P_L} b_{P_R}} \\ &= \sqrt{\frac{b_{P_L}^2}{4} + \frac{b_{P_R}^2}{4} + r\ \frac{1}{2} b_{P_L} b_{P_R}} \\ &= \sqrt{\frac{b_{P_{5psi}}^2}{4} + \frac{b_{P_{5psi}}^2}{4} + r\ \frac{1}{2} b_{P_{5psi}} b_{P_{5psi}}} \\ &= \sqrt{\frac{b_{P_{5psi}}^2}{2} (1+r)} \end{aligned} \tag{B.10}$$

Similarly, the systematic uncertainty on the wall static pressure that is the average of several measurements (4 at the inlet and 50 at the oulet) is given by Eq. (B.11) for the inlet and Eq. (B.12) for the outlet:

$$b_{P_{s,1}} = \sqrt{\frac{b_{P_{5psi}}^2}{4} (1+3r)} \tag{B.11}$$

$$b_{P_{s,2}} = \sqrt{\frac{b_{P_{15psi}}^2}{50} (1+49r)} \tag{B.12}$$

The correlation coefficient r may thus strongly influence the uncertainty calculation. When $r = 1$, measurements are fully correlated while when $r = 0$, measurements are fully independent. In the present case, both situations are not realistic. All the sensors of the same scanner are independent but are connected to the same reference and the same A/D converter. Moreover, they are subjected to the same temperature correction inside the scanner. A complete assessment of the correlation is unfortunately not mentioned by the manufacturer. Attempts have been tried to quantify the correlation factor but they remained unfruitful. As for most derived quantities, the worst case occurs when measurements are all considered independent, the correlation coefficient has been set to 0.

The random uncertainty is assessed by the standard deviation of the signal along time:

$$\sigma = \frac{s_X}{\sqrt{N}} = \frac{1}{\sqrt{N}} \sqrt{\frac{\sum_{i=1}^{N} X_i - \bar{X}}{N-1}} \tag{B.13}$$

where X_i and $\bar{X}$ are respectively an occurrence in the (total or static) pressure signal and the average over the whole signal and N is the number of points of the sample. For stationary measurements (i.e. inlet total and static pressures), this task is quite easy. For non-stationary measurements, as the downstream pressure traverses, the random uncertainty varies whether the probe is in a blade wake or not and it must be taken into account. The random uncertainty has therefore been calculated after setting the probe at various discrete pitch locations (inside and outside the wake) and computing the standard deviation of a 2-second signal at each pitch location. The whole procedure has been applied at two incidences, two span locations, two Mach numbers as well as in the absence of flow. The final standard deviation is a root-sum-square average of all the computed standard deviations. According to the terminology of [60], the final standard deviation corresponds to a *pooled* standard deviation. The random uncertainty is then obtained by dividing the pooled standard deviation by $\sqrt{N}$.

The correlation does not affect random uncertainties and thus, the random uncertainty of the average of many similar measurements is usually smaller than the uncertainty of a single measurement. Considering the inlet static pressure that is the average of 4 measurements, it becomes:

$$P_{s,1} = \frac{P_{s,1a} + P_{s,1b} + P_{s,1c} + P_{s,1d}}{4} \tag{B.14}$$

$$\begin{aligned} \sigma_{P_{s,1}} &= \sqrt{\frac{1}{16}\sigma^2_{P_{s,1a}} + \frac{1}{16}\sigma^2_{P_{s,1b}} + \frac{1}{16}\sigma^2_{P_{s,1c}} + \frac{1}{16}\sigma^2_{P_{s,1d}}} \\ &= \frac{1}{4}\sqrt{\sigma^2_{P_{s,1a}} + \sigma^2_{P_{s,1b}} + \sigma^2_{P_{s,1c}} + \sigma^2_{P_{s,1d}}} \end{aligned} \tag{B.15}$$

Uncertainty summary			
Quantity	b [mbar]	σ [mbar]	$U_{95} = 2\sqrt{b^2 + \sigma^2}$ [mbar]
$P_{0,1}$	0.115	0.010	0.231
$P_{s,1}$	0.058	0.030	0.130
$P_{0,2}$	0.115	0.070	0.269
$P_{s,2}$	0.038	0.090	0.269
P_C	0.115	0.030	0.238
P_L	0.115	0.020	0.233
P_R	0.115	0.030	0.238
$P_{dyn,1}$	0.163	0.032	0.332
$\Delta P_{0,1-2}$	0.163	0.071	0.355
ΔP_{L-R}	0.163	0.036	0.333
$P_{av,LR}$	0.081	0.018	0.167

Table B.1: *Systematic, random and total uncertainties of all measured pressures*

The systematic and random uncertainties of all measured pressures are summarized in Table B.1. As mentioned earlier, for the systematic uncertainties, a correlation coefficient $r = 0$ has been chosen. It can be seen that, for any quantity, it is always the systematic term that contributes the most.

B.3.3 Derived quantities

B.3.3.1 Total-to-static pressure ratios

The inlet total-to-static pressure ratio is also affected by correlations for the systematic terms. This is not true for the outlet total-to-static pressure ratio since outlet total pressure and outlet static pressure are not connected to the same scanner.

Inlet total-to-static pressure ratio

$$\begin{aligned} b_{P_{0,1}/Ps,1} &= \left[\left(\frac{\partial P_{0,1}/P_{s,1}}{\partial P_{0,1}} b_{P_{0,1}} \right)^2 + \left(\frac{\partial P_{0,1}/P_{s,1}}{\partial P_{s,1}} b_{P_{s,1}} \right)^2 + ... \right. \\ &\quad \left. +2\ r\ \frac{\partial P_{0,1}/P_{s,1}}{\partial P_{0,1}} \frac{\partial P_{0,1}/P_{s,1}}{\partial P_{s,1}} b_{P_{0,1}} b_{P_{s,1}} \right]^{\frac{1}{2}} \\ &= \sqrt{\left(\frac{b_{P_{5psi}}}{P_{s,1}} \right)^2 + \left(-\frac{P_{0,1}}{P_{s,1}^2} b_{P_{5psi}} \right)^2 - 2\ r \frac{1}{P_{s,1}} \frac{P_{0,1}}{P_{s,1}^2} b_{P_{5psi}}^2} \\ &= \sqrt{\frac{b_{P_{5psi}}^2}{P_{s,1}^2} \left(\frac{P_{0,1}^2}{P_{s,1}^2} - 2\ r \frac{P_{0,1}}{P_{s,1}} + 1 \right)} \end{aligned} \tag{B.16}$$

$$\sigma_{P_{0,1}/Ps,1} = \sqrt{\left(\frac{1}{P_{s,1}}\sigma_{P_{0,1}}\right)^2 + \left(-\frac{P_{0,1}}{P_{s,1}^2}\sigma_{P_{s,1}}\right)^2} \tag{B.17}$$

Outlet total-to-static pressure ratio

$$b_{P_{0,2}/Ps,2} = \sqrt{\left(\frac{1}{P_{s,2}}b_{P_{0,2}}\right)^2 + \left(-\frac{P_{0,2}}{P_{s,2}^2}b_{P_{s,2}}\right)^2} \tag{B.18}$$

$$\sigma_{P_{0,2}/Ps,2} = \sqrt{\left(\frac{1}{P_{s,2}}\sigma_{P_{0,2}}\right)^2 + \left(-\frac{P_{0,2}}{P_{s,2}^2}\sigma_{P_{s,2}}\right)^2} \tag{B.19}$$

B.3.3.2 Mach number

Inlet Mach number

$$M_1 = \sqrt{\left(\left(\frac{P_{0,1}}{P_{s,1}}\right)^{\frac{\gamma-1}{\gamma}} - 1\right)\frac{2}{\gamma-1}} \tag{B.20}$$

$$\begin{aligned} b_{M_1} &= \sqrt{\left(\frac{\partial M_1}{\partial\left(P_{0,1}/P_{s,1}\right)}b_{P_{0,1}/P_{s,1}}\right)^2} \\ &= \frac{1}{\gamma M_1}\left(\frac{P_{0,1}}{P_{s,1}}\right)^{\frac{-1}{\gamma}} b_{P_{0,1}/P_{s,1}} \end{aligned} \tag{B.21}$$

$$\begin{aligned} \sigma_{M_1} &= \sqrt{\left(\frac{\partial M_1}{\partial\left(P_{0,1}/P_{s,1}\right)}\sigma_{P_{0,1}/P_{s,1}}\right)^2} \\ &= \frac{1}{\gamma M_1}\left(\frac{P_{0,1}}{P_{s,1}}\right)^{\frac{-1}{\gamma}} \sigma_{P_{0,1}/P_{s,1}} \end{aligned} \tag{B.22}$$

$$\delta M_1 = 2.0\sqrt{b_{M_1} + \sigma_{M_1}} \tag{B.23}$$

Outlet Mach number

$$M_2 = \sqrt{\left(\left(\frac{P_{0,2}}{P_{s,2}}\right)^{\frac{\gamma-1}{\gamma}} - 1\right)\frac{2}{\gamma-1}} \tag{B.24}$$

$$\begin{aligned} b_{M_2} &= \sqrt{\left(\frac{\partial M_2}{\partial\left(P_{0,2}/P_{s,2}\right)}\sigma_{P_{0,2}/P_{s,2}}\right)^2} \\ &= \frac{1}{\gamma M_2}\left(\frac{P_{0,2}}{P_{s,2}}\right)^{\frac{-1}{\gamma}} b_{P_{0,2}/P_{s,2}} \end{aligned} \tag{B.25}$$

$$\begin{aligned}\sigma_{M_2} &= \sqrt{\left(\frac{\partial M_2}{\partial\left(P_{0,2}/P_{s,2}\right)}\sigma_{P_{0,2}/P_{s,2}}\right)^2} \\ &= \frac{1}{\gamma M_2}\left(\frac{P_{0,2}}{P_{s,2}}\right)^{\frac{-1}{\gamma}}\sigma_{P_{0,2}/P_{s,2}}\end{aligned} \tag{B.26}$$

$$\delta M_2 = 2.0\sqrt{b_{M_2}+\sigma_{M_2}} \tag{B.27}$$

B.3.3.3 Losses

$$\omega = \frac{P_{0,1}-P_{0,2}}{P_{0,1}-P_{s,1}} = \frac{\Delta P_{0,1-2}}{P_{dyn,1}} \tag{B.28}$$

$$\begin{aligned}b_\omega &= \sqrt{\left(\frac{\partial\omega}{\partial\Delta P_{0,1-2}}b_{\Delta P_{0,1-2}}\right)^2+\left(\frac{\partial\omega}{\partial P_{dyn,1}}b_{P_{dyn,1}}\right)^2} \\ &= \sqrt{\left(\frac{1}{P_{dyn,1}}b_{\Delta P_{0,1-2}}\right)^2+\left(\frac{-\Delta P_{0,1-2}}{P_{dyn,1}^2}b_{P_{dyn,1}}\right)^2}\end{aligned} \tag{B.29}$$

$$\begin{aligned}\sigma_\omega &= \sqrt{\left(\frac{\partial\omega}{\partial\Delta P_{0,1-2}}\sigma_{\Delta P_{0,1-2}}\right)^2+\left(\frac{\partial\omega}{\partial P_{dyn,1}}\sigma_{P_{dyn,1}}\right)^2} \\ &= \sqrt{\left(\frac{1}{P_{dyn,1}}\sigma_{\Delta P_{0,1-2}}\right)^2+\left(\frac{-\Delta P_{0,1-2}}{P_{dyn,1}^2}\sigma_{P_{dyn,1}}\right)^2}\end{aligned} \tag{B.30}$$

B.3.3.4 Yaw Angle

After calibration, the yaw angle is described by a function of the coefficient K_{yaw} and the Mach number. As it has been shown earlier, the dependence on the Mach number is very small and for the following calculation, it has been neglected.

$$\alpha = f(K_{yaw}, M) \approx f(K_{yaw}) \tag{B.31}$$

The uncertainty $\delta\alpha$ is given by the root-sum-square of the systematic and the random contributions.

$$\delta\alpha = 2\sqrt{b_\alpha^2+\sigma_\alpha^2} \tag{B.32}$$

Regarding the systematic uncertainty, it must be decomposed into a calibration and a test component. Indeed, any uncertainty accumulated during the calibration will systematically affect the test results. Both terms are combined by taking a root-sum-square.

$$b_\alpha = \sqrt{b_{\alpha,calib}^2+b_{\alpha,test}^2} \tag{B.33}$$

In Eq. (B.33), the first term comes from the calibration. It can be divided into many contributions. The most uncertainties are the accuracy of the engine

that provides the rotation of the probe and the curve fit that defines the relation between K_{yaw} and α. It is believed that the engine has an accuracy of 0.05° with an uniform distribution[1]. Likewise, the uncertainty associated to the alignment of the probe during the calibration is about 0.1°. The quality of the curve fit is given by the *Standard Error of the Estimate* or SEE:

$$SEE = \sqrt{\frac{\sum_{i=1}^{N}(Y_i - \tilde{Y}_i)^2}{N-1}} \tag{B.34}$$

where N is the number of points involved in the curve fit, Y_i is the measured data and $\tilde{Y}_i$ is the corresponding result obtained with curve fit. The SEE must then be divided by $\sqrt{N}$ to get an estimate of the standard deviation of the SEE. The final systematic uncertainty of the calibration is given by:

$$\begin{aligned} b_{\alpha,calib} &= \sqrt{b_{engine\ accuracy}^2 + b_{probe\ alignment}^2 + \left(\frac{SEE}{\sqrt{N}}\right)^2} \\ &= \sqrt{\left(\frac{2\ .\ 0.05^\circ}{\sqrt{12}}\right)^2 + \left(\frac{2\ .\ 0.10^\circ}{\sqrt{12}}\right)^2 + (0.10^\circ)^2} \\ &= 0.12^\circ \end{aligned} \tag{B.35}$$

Regarding the systematic uncertainty of the test as well as the random uncertainty, it can be developed as follows:

$$b_{\alpha,test} = \sqrt{b_{probe\ alignment}^2 + \left(\frac{\partial \alpha}{\partial K_{yaw}} b_{K_{yaw}}\right)^2} \tag{B.36}$$

$$\sigma_\alpha = \frac{\partial \alpha}{\partial K_{yaw}} \sigma_{K_{yaw}} \tag{B.37}$$

It is thus relying on both systematic and random uncertainties on K_{yaw}. The definition of K_{yaw} is given by Eq. (B.1). Using the notation $P_{dyn,3H}$ for the denominator of K_{yaw}, $b_{K_{yaw}}$ and $\sigma_{K_{yaw}}$ are given by:

$$b_{K_{yaw}} = \sqrt{\left(\frac{1}{P_{dyn,3H}} b_{\Delta P_{L-R}}\right)^2 + \left(\frac{-\Delta P_{L-R}}{P_{dyn,3H}^2} b_{P_{dyn,3H}}\right)^2} \tag{B.38}$$

$$\sigma_{K_{yaw}} = \sqrt{\left(\frac{1}{P_{dyn,3H}} \sigma_{\Delta P_{L-R}}\right)^2 + \left(\frac{-\Delta P_{L-R}}{P_{dyn,3H}^2} \sigma_{P_{dyn,3H}}\right)^2} \tag{B.39}$$

[1] For uniform distribution, the standard deviation is obtained by dividing the all span of the distribution by $\sqrt{12}$.

Through a similar process as in Eq. (B.9), it can be shown that b_D is equal to Eq. (B.40).

$$\begin{aligned} b_{P_{dyn,3H}} &= \Bigg[b_{P_C}^2 + \frac{b_{P_L}^2}{4} + \frac{b_{P_L}^2}{4} - r\ b_{P_C} b_{P_L} + ... \\ &\quad -r\ b_{P_C} b_{P_R} + r\ \frac{1}{2} b_{P_L} b_{P_R} \Bigg]^{\frac{1}{2}} \\ &= \sqrt{\frac{3}{2} b_{P_{5psi}}^2 (1-r)} \end{aligned} \tag{B.40}$$

The $\sigma_{\Delta P_{L-R}}$ and $\sigma_{P_{dyn,3H}}$ are given by:

$$\sigma_{\Delta P_{L-R}} = \sqrt{\sigma_{P_L}^2 + \sigma_{P_R}^2} \tag{B.41}$$

$$\sigma_{P_{dyn,3H}} = \sqrt{\sigma_{P_C}^2 + \frac{\sigma_{P_L}^2}{4} + \frac{\sigma_{P_L}^2}{4}} \tag{B.42}$$

In the case of the inlet air angle, no random contribution is considered but the whole cascade alignement accuracy must be taken into account. The uncertainty on the inlet air angle is thus:

$$\delta\alpha_1 = 2\ b_{cascade\ alignment} = 2\ .\ \frac{2\ .\ 0.1^\circ}{\sqrt{12}} = 0.11^\circ \tag{B.43}$$

B.3.3.5 Three-hole total and static pressures

If the total pressure is acquired by the kiel probe, no uncertainty should be added since no extra calibration is required. The total pressure can also be retrieved by the three-hole probe. It is then relying on the angular calibration through the coefficient K_{tot} defined in Eq. (B.2). From the definition of K_{tot}, the total pressure is obtained by:

$$P_{0,3H} = K_{tot} P_C + P_C \tag{B.44}$$

where P_C is the center-hole pressure. The systematic and random uncertainties are then given by:

$$\begin{aligned} b_{P_{0,3H}} &= \sqrt{\left(\frac{\partial P_{0,3H}}{\partial K_{tot}} b_{K_{tot}}\right)^2 + \left(\frac{\partial P_{0,3H}}{\partial P_C} b_{P_C}\right)^2} \\ &= \sqrt{\left(P_C\ b_{K_{tot}}\right)^2 + \left((K_{tot}+1) b_{P_C}\right)^2} \end{aligned} \tag{B.45}$$

$$\begin{aligned} \sigma_{P_{0,3H}} &= \sqrt{\left(\frac{\partial P_{0,3H}}{\partial K_{tot}} \sigma_{K_{tot}}\right)^2 + \left(\frac{\partial P_{0,3H}}{\partial P_C} \sigma_{P_C}\right)^2} \\ &= \sqrt{\left(P_C\ \sigma_{K_{tot}}\right)^2 + \left((K_{tot}+1) \sigma_{P_C}\right)^2} \end{aligned} \tag{B.46}$$

The coefficient K_{tot} is a function of both the flow angle and the Mach number. For the uncertainty calculation, the contribution of the Mach number is again neglected since it is very small. For the calculation of the SEE, a 4^{th} order polynomial fit has been used to establish the relation between α and K_{tot}. Both systematic and random uncertainties on K_{tot} are detailed below:

$$b_{K_{tot}} = \sqrt{b^2_{K_{tot},calib} + b^2_{K_{tot},test}} \tag{B.47}$$

$$\sigma_{K_{tot}} = \frac{\partial K_{tot}}{\partial \alpha}\sigma_\alpha \tag{B.48}$$

with,

$$b_{K_{tot},calib} = \frac{SEE}{\sqrt{N}} \tag{B.49}$$

$$b_{K_{tot},test} = \frac{\partial K_{tot}}{\partial \alpha} b_\alpha \tag{B.50}$$

The same procedure is applied to calculate the uncertainty on the static pressure retrieved by the three-hole probe.

$$P_{s,3H} = P_{av,LR} - K_{dyn}P_C \tag{B.51}$$

$$b_{P_{s,3H}} = \sqrt{\left(b_{P_{av,LR}}\right)^2 + \left(-K_{dyn}b_{P_C}\right)^2 + \left(-P_C b_{K_{dyn}}\right)^2} \tag{B.52}$$

$$\sigma_{P_{s,3H}} = \sqrt{\left(\sigma_{P_{av,LR}}\right)^2 + \left(-K_{dyn}\sigma_{P_C}\right)^2 + \left(-P_C \sigma_{K_{dyn}}\right)^2} \tag{B.53}$$

The calculation of the uncertainty on K_{dyn} is given below:

$$b_{K_{dyn}} = \sqrt{b^2_{K_{dyn},calib} + b^2_{K_{dyn},test}} \tag{B.54}$$

$$\sigma_{K_{dyn}} = \frac{\partial K_{dyn}}{\partial \alpha}\sigma_\alpha \tag{B.55}$$

with,

$$b_{K_{dyn},calib} = \frac{SEE}{\sqrt{N}} \tag{B.56}$$

$$b_{K_{dyn},test} = \frac{\partial K_{dyn}}{\partial \alpha} b_\alpha \tag{B.57}$$

B.3.3.6 Diffusion factor

The diffusion factor is defined as:

$$D = 1 - \frac{V_2}{V_1} + \frac{V_1 \sin(\alpha_1) - V_2 \sin(\alpha_2)}{2\sigma V_1} \tag{B.58}$$

The velocity ratio can be expressed in function of the Mach number and the speed of sound. Moreover, since there is no work exchange in a cascade and as the cascade is considered to be adiabatic, an assumption can be reasonably done

on the total temperature assumed constant across the cascade. This allows to make the following simplifications:

$$\begin{aligned} D &= 1 - \frac{M_2\sqrt{\gamma R T_{s,2}}}{M_1\sqrt{\gamma R T_{s,1}}} + \frac{\sin(\alpha_1) - \frac{M_2\sqrt{\gamma R T_{s,2}}}{M_1\sqrt{\gamma R T_{s,1}}}\sin(\alpha_2)}{2\sigma} \\ &= 1 - \frac{M_2}{M_1}\sqrt{\frac{1+\frac{\gamma-1}{2}M_1^2}{1+\frac{\gamma-1}{2}M_2^2}} + \frac{\sin(\alpha_1) - \frac{M_2}{M_1}\sqrt{\frac{1+\frac{\gamma-1}{2}M_1^2}{1+\frac{\gamma-1}{2}M_2^2}}\sin(\alpha_2)}{2\sigma} \end{aligned} \tag{B.59}$$

For the sake of clarity, the uncertainties have been calculated separately. All the equations for systematic and random uncertainties are given below.

$$b_D = \sqrt{\left(-(1+\frac{\sin(\alpha_2)}{2\sigma})b_{V_2/V_1}\right)^2 + \left(\frac{\cos(\alpha_1)}{2\sigma}b_{\alpha_1}\right)^2 + \left(\frac{-\cos(\alpha_2)}{2\sigma}\frac{V_2}{V_1}b_{\alpha_2}\right)^2} \tag{B.60}$$

$$\sigma_D = \sqrt{\left(-(1+\frac{\sin(\alpha_2)}{2\sigma})\sigma_{V_2/V_1}\right)^2 + \left(\frac{\cos(\alpha_1)}{2\sigma}\sigma_{\alpha_1}\right)^2 + \left(\frac{-\cos(\alpha_2)}{2\sigma}\frac{V_2}{V_1}\sigma_{\alpha_2}\right)^2} \tag{B.61}$$

$$\frac{V_2}{V_1} = \frac{M_2}{M_1}\sqrt{\frac{1+\frac{\gamma-1}{2}M_1^2}{1+\frac{\gamma-1}{2}M_2^2}} \tag{B.62}$$

$$b_{V_2/V_1} = \sqrt{\left(\frac{\partial V_2/V_1}{\partial M_1}b_{M_1}\right)^2 + \left(\frac{\partial V_2/V_1}{\partial M_2}b_{M_2}\right)^2} \tag{B.63}$$

$$\sigma_{V_2/V_1} = \sqrt{\left(\frac{\partial V_2/V_1}{\partial M_1}\sigma_{M_1}\right)^2 + \left(\frac{\partial V_2/V_1}{\partial M_2}\sigma_{M_2}\right)^2} \tag{B.64}$$

$$\frac{\partial V_2/V_1}{\partial M_1} = \frac{M_2}{\sqrt{1+\frac{\gamma-1}{2}M_2^2}}\left(\frac{\frac{\gamma-1}{2}}{\sqrt{1+\frac{\gamma-1}{2}M_1^2}} - \frac{\sqrt{1+\frac{\gamma-1}{2}M_1^2}}{M_1^2}\right) \tag{B.65}$$

$$\frac{\partial V_2/V_1}{\partial M_2} = \frac{\sqrt{1+\frac{\gamma-1}{2}M_1^2}}{M_1}\left(\frac{1}{\sqrt{1+\frac{\gamma-1}{2}M_2^2}} - \frac{\frac{\gamma-1}{2}M_2^2}{(1+\frac{\gamma-1}{2}M_2^2)\sqrt{1+\frac{\gamma-1}{2}M_2^2}}\right) \tag{B.66}$$

B.3.3.7 Loss parameters

Two loss parameters have been used:

$$\zeta_1 = \frac{\omega\cos(\alpha_2)}{2\sigma} \tag{B.67}$$

$$\zeta_2 = \frac{\omega\cos(\alpha_2)}{2\sigma}\left(\frac{\cos(\alpha_2)}{\cos(\alpha_1)}\right)^2 \tag{B.68}$$

The following equations gives the systematic and random uncertainties of both loss parameters.

$$b_{\zeta_1} = \sqrt{\left(\frac{\cos(\alpha_2)}{2\sigma} b_\omega\right)^2 + \left(-\frac{\omega \sin(\alpha_2)}{2\sigma} b_{\alpha_2}\right)^2} \tag{B.69}$$

$$\sigma_{\zeta_1} = \sqrt{\left(\frac{\cos(\alpha_2)}{2\sigma} \sigma_\omega\right)^2 + \left(-\frac{\omega \sin(\alpha_2)}{2\sigma} \sigma_{\alpha_2}\right)^2} \tag{B.70}$$

$$\begin{aligned} b_{\zeta_2} = \Bigg[& \left(\frac{\cos(\alpha_2)}{2\sigma} \left(\frac{\cos(\alpha_2)}{\cos(\alpha_1)}\right)^2 b_\omega\right)^2 + \dots \\ & + \left(-\frac{3\omega \cos^2(\alpha_2)\sin(\alpha_2)}{2\sigma} \frac{1}{\cos^2(\alpha_1)} b_{\alpha_2}\right)^2 + \dots \\ & + \left(\frac{\omega \cos^3(\alpha_2)}{2\sigma} \frac{\sin(\alpha_1)}{\cos^3(\alpha_1)} b_{\alpha_1}\right)^2 \Bigg]^{\frac{1}{2}} \end{aligned} \tag{B.71}$$

$$\begin{aligned} \sigma_{\zeta_2} = \Bigg[& \left(\frac{\cos(\alpha_2)}{2\sigma} \left(\frac{\cos(\alpha_2)}{\cos(\alpha_1)}\right)^2 \sigma_\omega\right)^2 + \dots \\ & + \left(-\frac{3\omega \cos^2(\alpha_2)\sin(\alpha_2)}{2\sigma} \frac{1}{\cos^2(\alpha_1)} \sigma_{\alpha_2}\right)^2 + \dots \\ & + \left(\frac{\omega \cos^3(\alpha_2)}{2\sigma} \frac{\sin(\alpha_1)}{\cos^3(\alpha_1)} \sigma_{\alpha_1}\right)^2 \Bigg]^{\frac{1}{2}} \end{aligned} \tag{B.72}$$

B.3.3.8 Axial Velocity Density Ratio

The AVDR is defined as:

$$AVDR = \frac{\rho_2}{\rho_1} \frac{V_{ax,2}}{V_{ax,1}} \tag{B.73}$$

Based on the same considerations as the diffusion factor, it can written as follows:

$$AVDR = \frac{p_{s,2}}{p_{s,1}} \left(\frac{1 + \frac{\gamma-1}{2} M_2^2}{1 + \frac{\gamma-1}{2} M_1^2}\right) \frac{\cos(\alpha_2)}{\cos(\alpha_1)} \frac{V_2}{V_1} \tag{B.74}$$

The systematic and random uncertainties are given by the following equa-

tions.

$$
\begin{aligned}
b_{AVDR} = \Bigg[& \left(\left(\frac{1+\frac{\gamma-1}{2}M_2^2}{1+\frac{\gamma-1}{2}M_1^2} \right) \frac{\cos(\alpha_2)}{\cos(\alpha_1)} \frac{V_2}{V_1} b_{p_{s,2}/p_{s,1}} \right)^2 \dots \\
& + \left(\frac{p_{s,2}}{p_{s,1}} \left(\frac{(\gamma-1)M_2}{1+\frac{\gamma-1}{2}M_1^2} \right) \frac{\cos(\alpha_2)}{\cos(\alpha_1)} \frac{V_2}{V_1} b_{M_2} \right)^2 \dots \\
& + \left(\frac{p_{s,2}}{p_{s,1}} \left(1+\frac{\gamma-1}{2}M_2^2 \right) \frac{(\gamma-1)M_1}{\left(1+\frac{\gamma-1}{2}M_1^2\right)^2} \frac{\cos(\alpha_2)}{\cos(\alpha_1)} \frac{V_2}{V_1} b_{M_1} \right)^2 \dots \\
& + \left(\frac{p_{s,2}}{p_{s,1}} \left(\frac{1+\frac{\gamma-1}{2}M_2^2}{1+\frac{\gamma-1}{2}M_1^2} \right) \frac{V_2}{V_1} b_{\cos(\alpha_1)/\cos(\alpha_2)} \right)^2 \dots \\
& + \left(\frac{p_{s,2}}{p_{s,1}} \left(\frac{1+\frac{\gamma-1}{2}M_2^2}{1+\frac{\gamma-1}{2}M_1^2} \right) \frac{\cos(\alpha_2)}{\cos(\alpha_1)} b_{V_2/V_1} \right)^2 \Bigg]^{\frac{1}{2}}
\end{aligned}
\tag{B.75}
$$

$$
\begin{aligned}
\sigma_{AVDR} = \Bigg[& \left(\left(\frac{1+\frac{\gamma-1}{2}M_2^2}{1+\frac{\gamma-1}{2}M_1^2} \right) \frac{\cos(\alpha_2)}{\cos(\alpha_1)} \frac{V_2}{V_1} \sigma_{p_{s,2}/p_{s,1}} \right)^2 \dots \\
& + \left(\frac{p_{s,2}}{p_{s,1}} \left(\frac{(\gamma-1)M_2}{1+\frac{\gamma-1}{2}M_1^2} \right) \frac{\cos(\alpha_2)}{\cos(\alpha_1)} \frac{V_2}{V_1} \sigma_{M_2} \right)^2 \dots \\
& + \left(\frac{p_{s,2}}{p_{s,1}} \left(1+\frac{\gamma-1}{2}M_2^2 \right) \frac{(\gamma-1)M_1}{\left(1+\frac{\gamma-1}{2}M_1^2\right)^2} \frac{\cos(\alpha_2)}{\cos(\alpha_1)} \frac{V_2}{V_1} \sigma_{M_1} \right)^2 \dots \\
& + \left(\frac{p_{s,2}}{p_{s,1}} \left(\frac{1+\frac{\gamma-1}{2}M_2^2}{1+\frac{\gamma-1}{2}M_1^2} \right) \frac{V_2}{V_1} \sigma_{\cos(\alpha_1)/\cos(\alpha_2)} \right)^2 \dots \\
& + \left(\frac{p_{s,2}}{p_{s,1}} \left(\frac{1+\frac{\gamma-1}{2}M_2^2}{1+\frac{\gamma-1}{2}M_1^2} \right) \frac{\cos(\alpha_2)}{\cos(\alpha_1)} \sigma_{V_2/V_1} \right)^2 \Bigg]^{\frac{1}{2}}
\end{aligned}
\tag{B.76}
$$

The quantities $b_{p_{s,2}/p_{s,1}}$, $\sigma_{p_{s,2}/p_{s,1}}$, $b_{\cos(\alpha_1)/\cos(\alpha_2)}$ and $\sigma_{\cos(\alpha_1)/\cos(\alpha_2)}$ are given below.

$$
b_{p_{s,2}/p_{s,1}} = \sqrt{\left(\frac{1}{p_{s,1}} b_{p_{s,2}} \right)^2 + \left(-\frac{p_{s,2}}{p_{s,1}^2} b_{p_{s,1}} \right)^2} \tag{B.77}
$$

$$
\sigma_{p_{s,2}/p_{s,1}} = \sqrt{\left(\frac{1}{p_{s,1}} \sigma_{p_{s,2}} \right)^2 + \left(-\frac{p_{s,2}}{p_{s,1}^2} \sigma_{p_{s,1}} \right)^2} \tag{B.78}
$$

$$
b_{\cos(\alpha_1)/\cos(\alpha_2)} = \sqrt{\left(\frac{-\sin(\alpha_1)}{\cos(\alpha_2)} b_{\alpha_2} \right)^2 + \left(\frac{\cos(\alpha_1)\sin(\alpha_2)}{\cos^2(\alpha_2)} b_{\alpha_1} \right)^2} \tag{B.79}
$$

$$\sigma_{\cos(\alpha_1)/\cos(\alpha_2)} = \sqrt{\left(\frac{-\sin(\alpha_1)}{\cos(\alpha_2)}\sigma_{\alpha_2}\right)^2 + \left(\frac{\cos(\alpha_1)\sin(\alpha_2)}{\cos^2(\alpha_2)}\sigma_{\alpha_1}\right)^2} \tag{B.80}$$

Appendix C

Experimental investigation - Complementary results

C.1 Spanwise distributions

Spanwise distributions of losses, turning, diffusion factor and AVDR are respectively given in Fig. C.1, Fig. C.2, Fig. C.3 and Fig. C.4 at 0°, 6° and 9° of incidence for M_1=0.60. The trends are very similar to the ones at M_1=0.45. The unexpected loss distribution obtained for the low solidity is also depicted and even more stressed. The losses at 20% are lower than at 30% and 50%. As explained in Chapter 4, this is most probably related to the AVDR distributions and the inlet profile of incidence. More detailed measurements along the span as well as at neighboring incidences are required to shed light on the origin of this loss distribution.

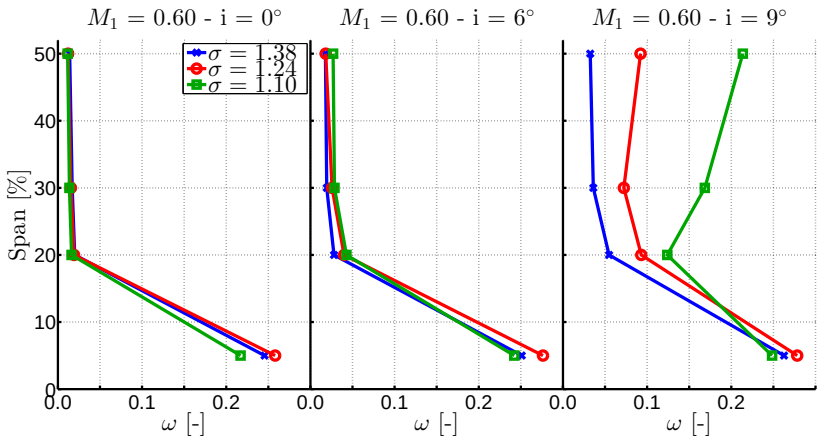


Figure C.1: *Spanwise total pressure losses distributions at M_1=0.60*

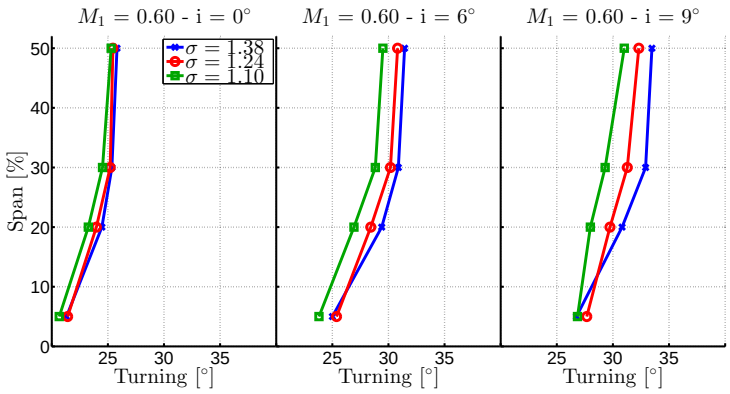


Figure C.2: *Spanwise turning distributions at M_1=0.60*

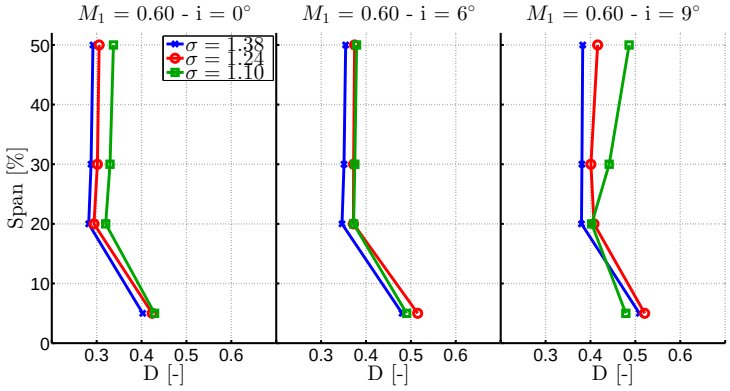


Figure C.3: *Spanwise diffusion factor distributions at M_1=0.60*

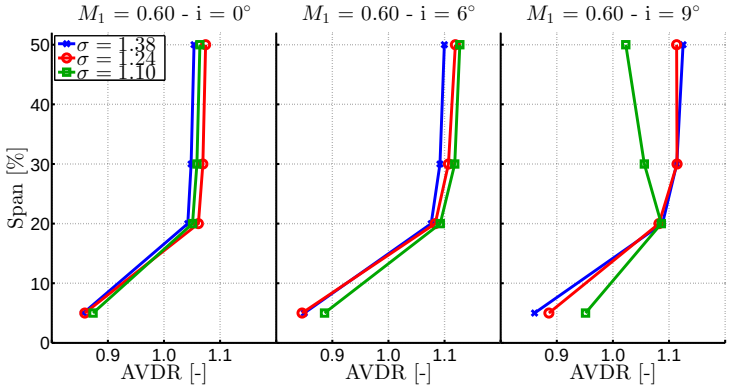
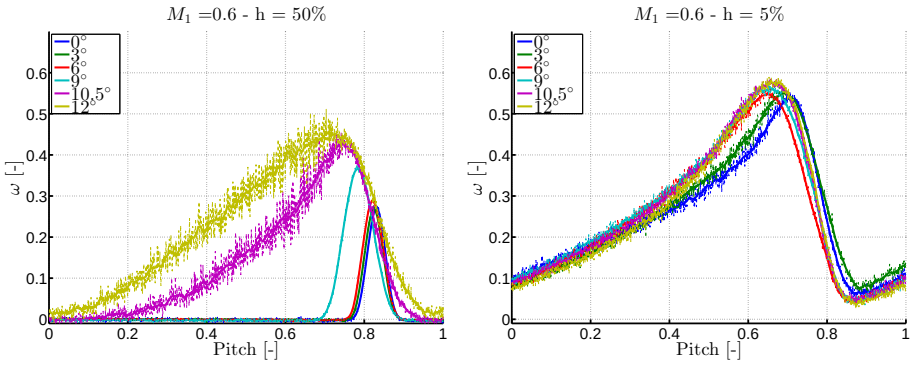


Figure C.4: *Spanwise AVDR distributions at M_1=0.60*

C.2 Wakes

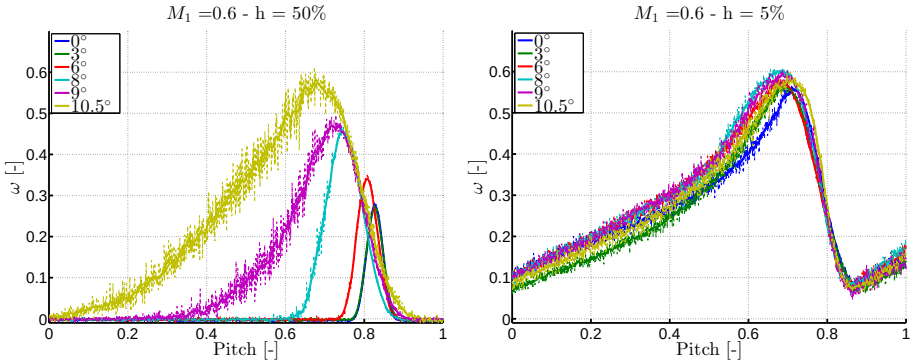
C.2.1 Total pressure loss wakes

Total pressure wakes at 50% and at 5% of the span are given at $M_1 = 0.60$ in Fig. C.5, Fig. C.6 and Fig. C.7 respectively for σ=1.38, 1.24 and 1.10. The wake evolution with the variation of incidence and solidity is analogous to the results of Chapter 4 at M_1=0.45.



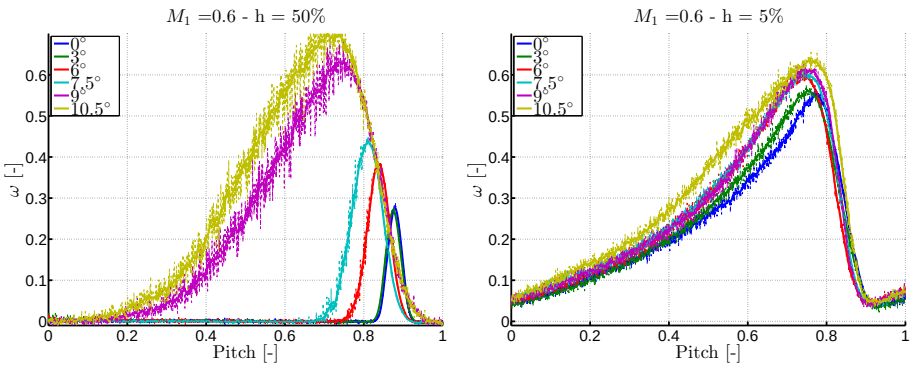
(a) *h=50%* **(b)** *h=5%*

Figure C.5: *Total pressure loss wakes at* $\sigma = 1.38$ *and* $M_1 = 0.60$



(a) *h=50%* **(b)** *h=5%*

Figure C.6: *Total pressure loss wakes at* $\sigma = 1.24$ *and* $M_1 = 0.60$

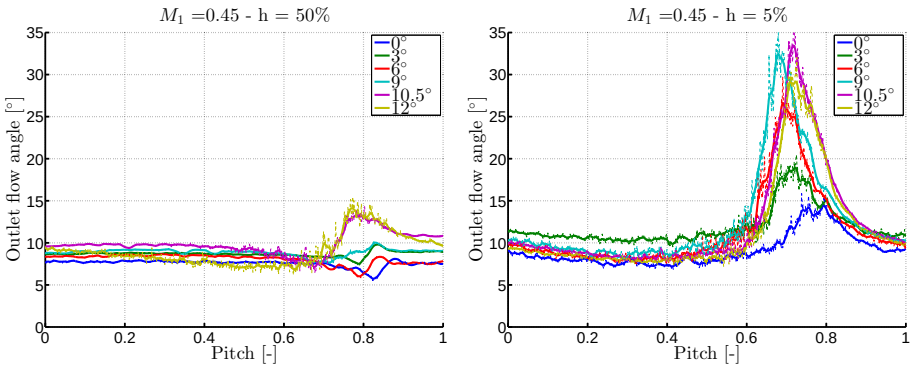


(a) *h=50%* **(b)** *h=5%*

Figure C.7: *Total pressure loss wakes at* $\sigma = 1.10$ *and* $M_1 = 0.60$

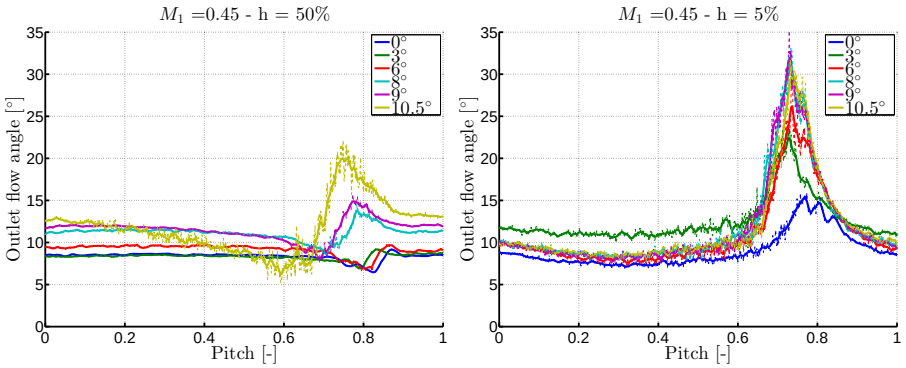
C.2.2 Yaw angle wakes

Yaw angle wakes are given at M_1=0.45 in Fig. C.8, Fig. C.9 and Fig. C.10 respectively for σ=1.38, 1.24 and 1.10. Similar plots are available at M_1=0.60 in Fig. C.11, Fig. C.12 and Fig. C.13. Since each pressure hole of the probe has a 0.6 mm diameter, all the holes are not simultaneously located at the exact same position. The measurements must then be corrected to virtually get the pressures measured by each of the three holes at the same pitch location. Nevertheless, the measure of a flow angle is not an easy task. It still represents a strong discontinuity where the flow from the suction side mixes with the flow of pressure side. The figures C.8 to C.13 typically illustrate blade wake flow angle measurements. Towards high incidences, the flow becomes more three-dimensional and unsteady. The discontinuity created by the wake yields an overshoot which may influence the final average value of the flow angle. At high incidences, flow angle measurements with a standard three-hole probe are maybe not anymore the most appropriate measurement technique.



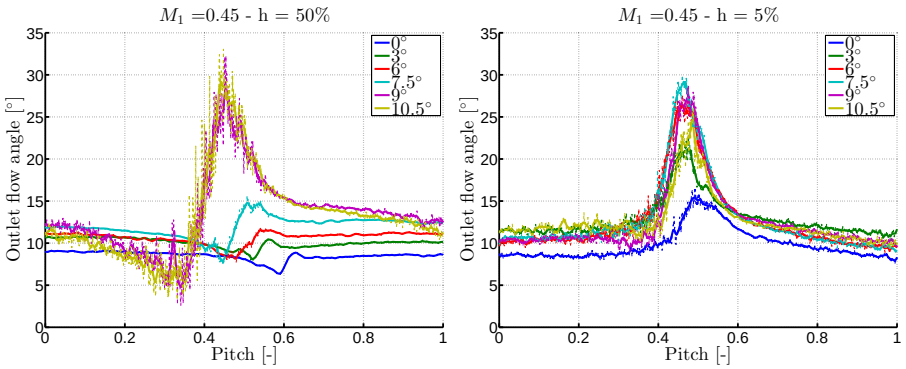
(a) *h=50%* **(b)** *h=5%*

Figure C.8: *Yaw angle wakes at* $\sigma = 1.38$ *and* $M_1 = 0.45$



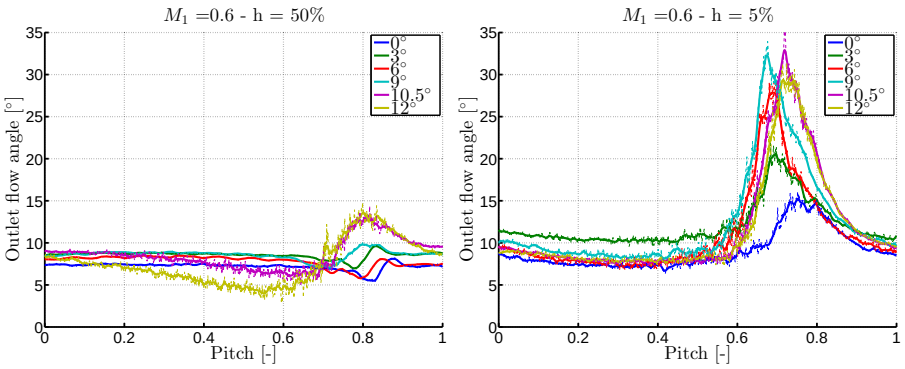
(a) *h=50%* **(b)** *h=5%*

Figure C.9: *Yaw angle wakes at* $\sigma = 1.24$ *and* $M_1 = 0.45$



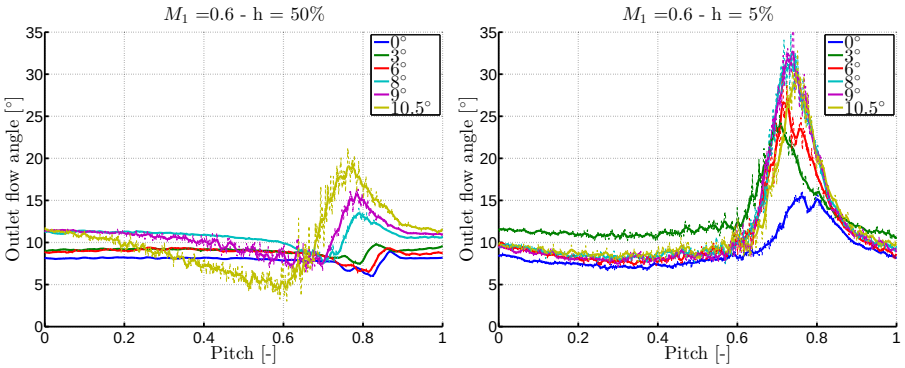
(a) *h=50%* **(b)** *h=5%*

Figure C.10: *Yaw angle wakes at* $\sigma = 1.10$ *and* $M_1 = 0.45$



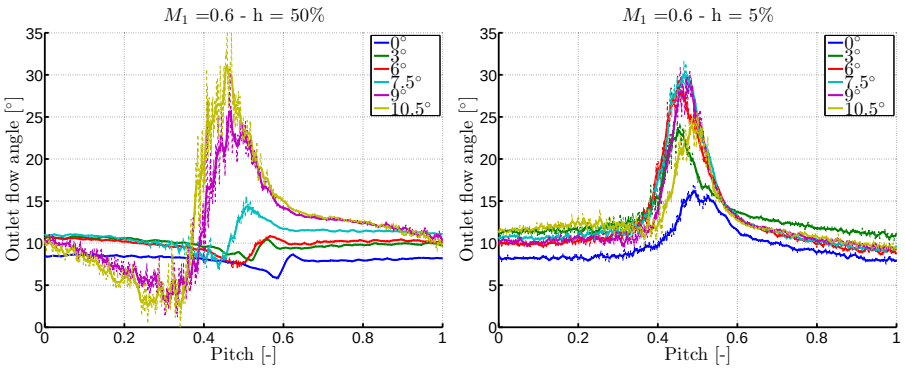
(a) *h=50%* **(b)** *h=5%*

Figure C.11: *Yaw angle wakes at* $\sigma = 1.38$ *and* $M_1 = 0.60$



(a) *h=50%* **(b)** *h=5%*

Figure C.12: *Yaw angle wakes at* $\sigma = 1.24$ *and* $M_1 = 0.60$



(a) *h=50%* **(b)** *h=5%*

Figure C.13: *Yaw angle wakes at* $\sigma = 1.10$ *and* $M_1 = 0.60$

C.3 Numerical parameter effects

C.3.1 Outlet flow topology

For the highest solidity, at 3° and 9° and $M_1 = 0.45$, computations have been performed with two turbulence models (Yang-Shih k-ϵ and Spalart-Allmaras) and two numerical schemes (central and upwind). For both turbulence models, while the turbulence intensity remains constant and equal to 1%, the turbulence length scale has been set to $0.1\,D_H$ and $0.0001\,D_H$ (with D_H standing for the hydraulic diameter). The experimental results are also given in Fig. C.22.

The wakes will be compared at 50% and at 20% in a following section and will offer a better overview of the various numerical effects but the analysis of the whole map already reveals big differences. Results at 3° and 9° are respectively given in Sec. C.3.1.1 and Sec. C.3.1.2 but the following discussion remains valid at both incidences.

First of all, with a threshold set at 1% of losses, most of the results present negative loss areas. Even using an upwind scheme does not always completely remove those nonphysical regions. Secondly, decreasing the length scale usually increase the area covered by the negative losses but decreases the wake width and intensity. This is especially visible for the Spallart-Allmaras turbulence model that seems more sensitive to the reduction of ℓ and the wakes directly appear thinner with $\ell = 0.0001\,D_H$.

Considering both incidences, although the $k-\varepsilon$ model seems to offer a better representation of the flow, from a designer perspective, no final conclusion can be drawn.

C.3.1.1 Outlet flow topology - $i = 3°$

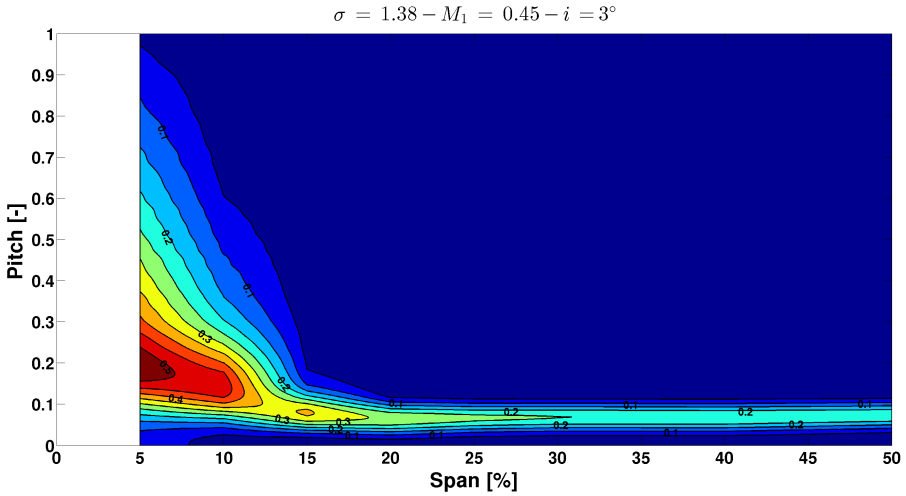


Figure C.14: *Experimental total pressure loss map*

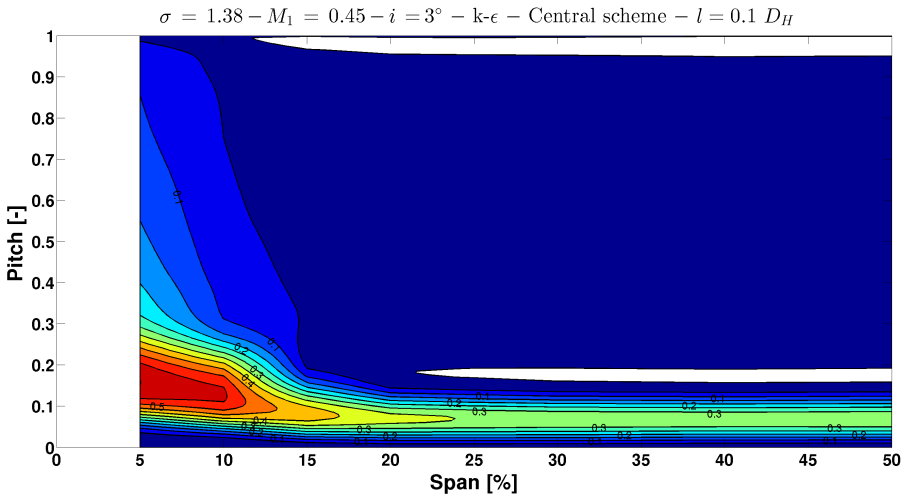


Figure C.15: *Numerical total pressure loss map using Yang-Shih k-ϵ turbulence model with $\ell = 0.1\, D_H$ and a central scheme*

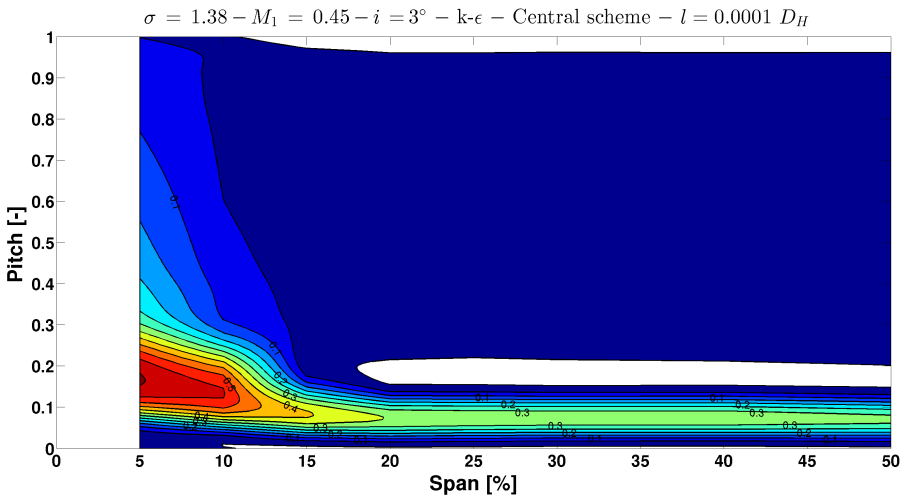


Figure C.16: *Numerical total pressure loss map using Yang-Shih k-ϵ turbulence model with $\ell = 0.0001\, D_H$ and a central scheme*

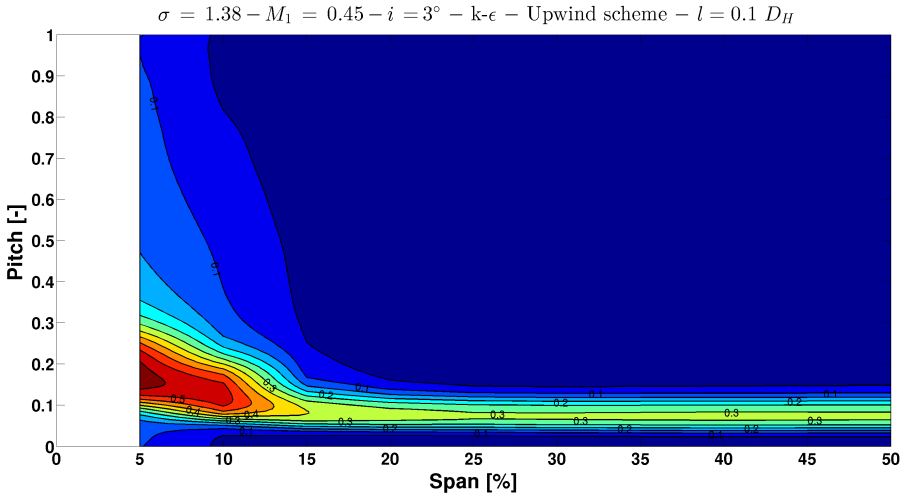


Figure C.17: *Numerical total pressure loss map using Yang-Shih k-ϵ turbulence model with $\ell = 0.1\, D_H$ and an upwind scheme*

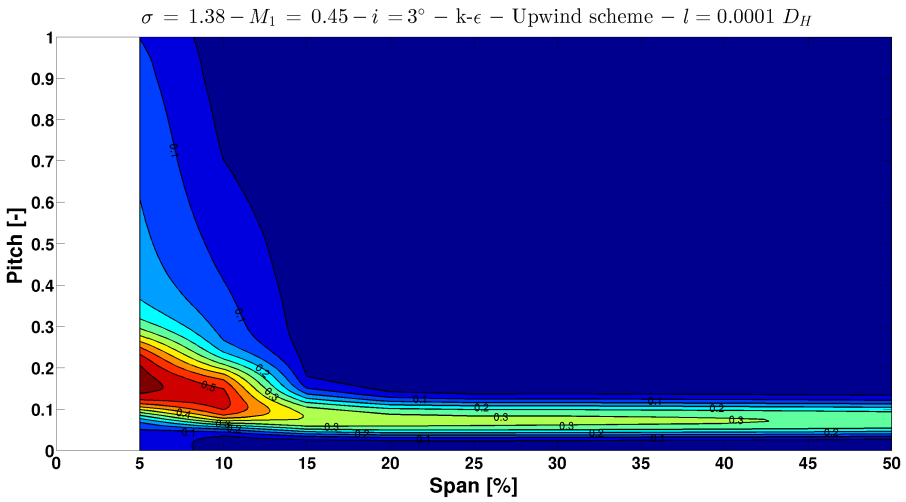


Figure C.18: *Numerical total pressure loss map using Yang-Shih k-ϵ turbulence model with $\ell = 0.0001\, D_H$ and an upwind scheme*

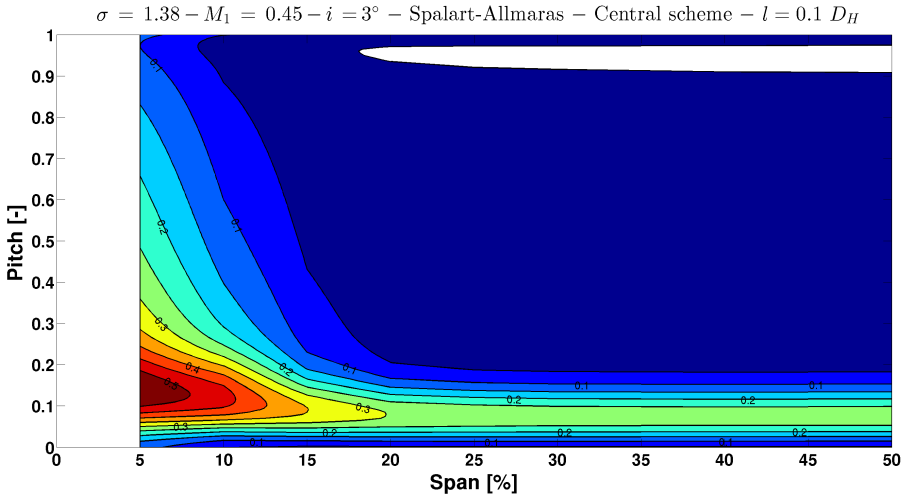


Figure C.19: *Numerical total pressure loss map using Spalart-Allmaras turbulence model with $\ell = 0.1\, D_H$ and a central scheme*

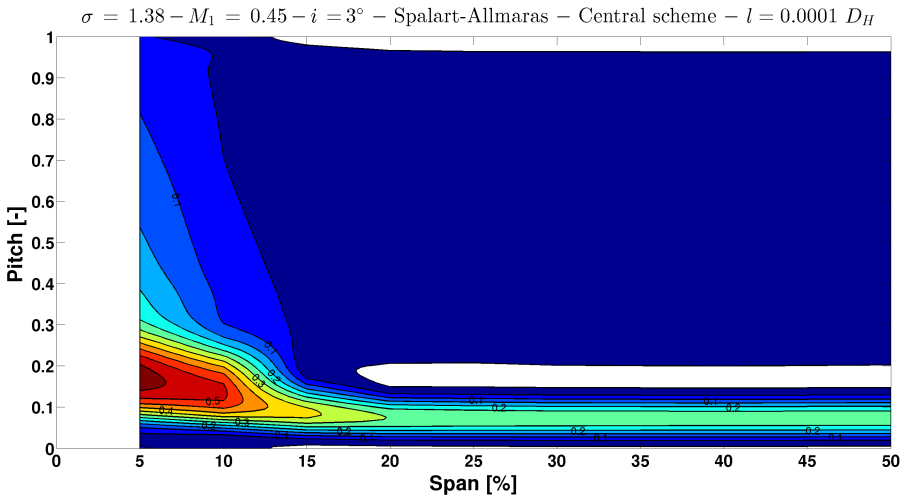


Figure C.20: *Numerical total pressure loss map using Spalart-Allmaras turbulence model with $\ell = 0.0001\, D_H$ and a central scheme*

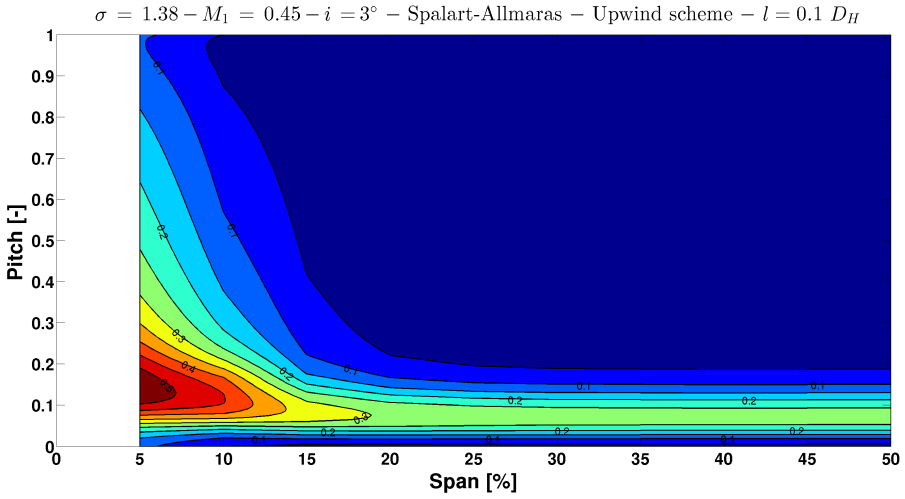


Figure C.21: *Numerical total pressure loss map using Spalart-Allmaras turbulence model with $\ell = 0.1\, D_H$ and an upwind scheme*

C.3.1.2 Outlet flow topology - $i = 9°$

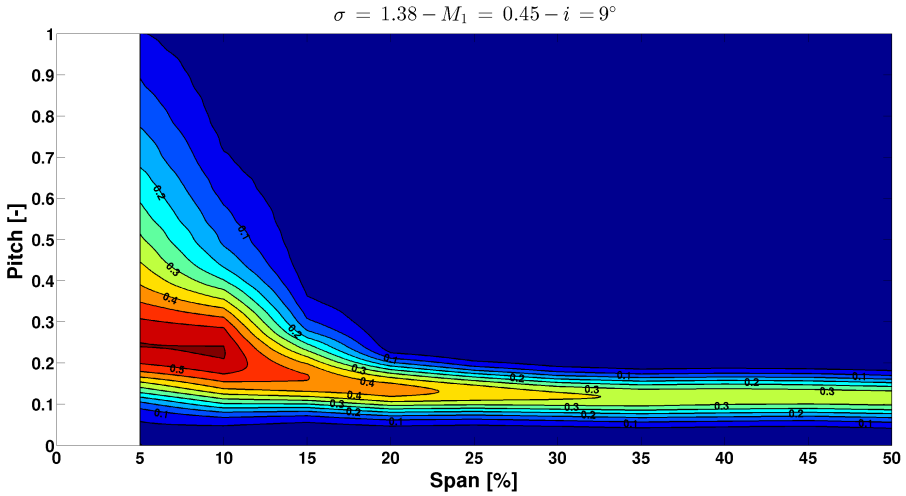


Figure C.22: *Experimental total pressure loss map*

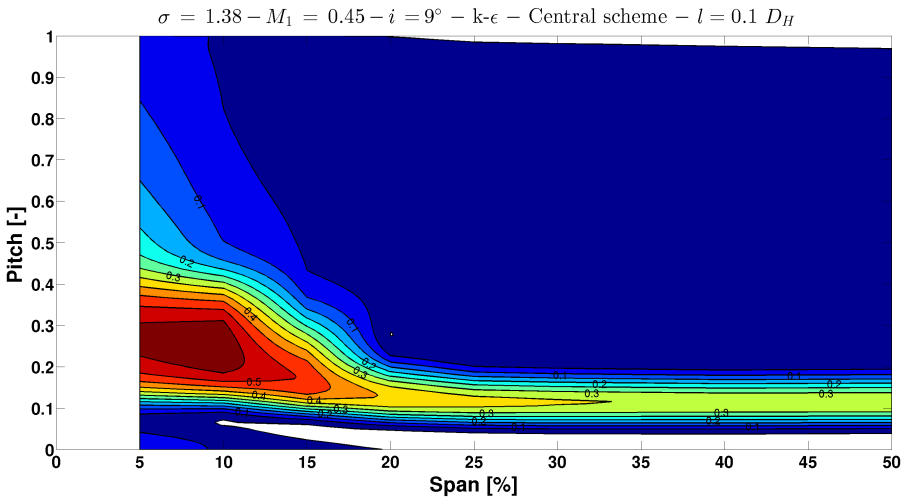


Figure C.23: *Numerical total pressure loss map using Yang-Shih k-ϵ turbulence model with $\ell = 0.1\, D_H$ and a central scheme*

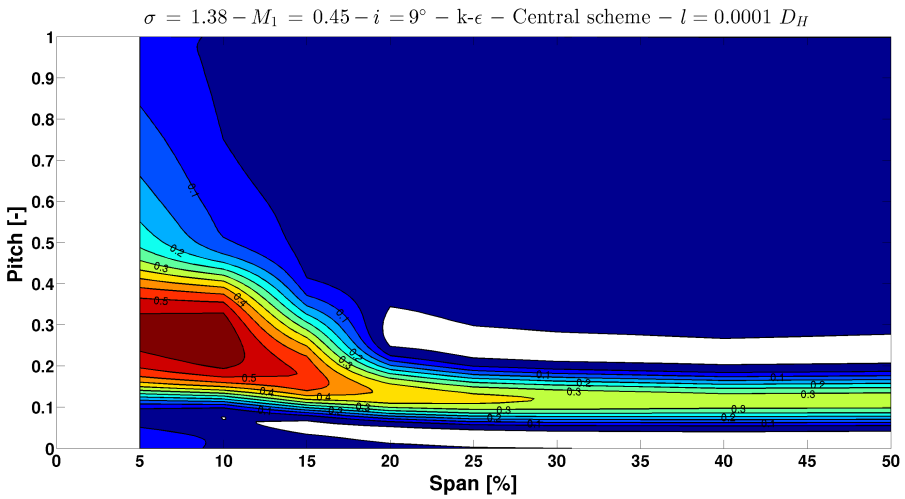


Figure C.24: *Numerical total pressure loss map using Yang-Shih k-ϵ turbulence model with $\ell = 0.0001\, D_H$ and a central scheme*

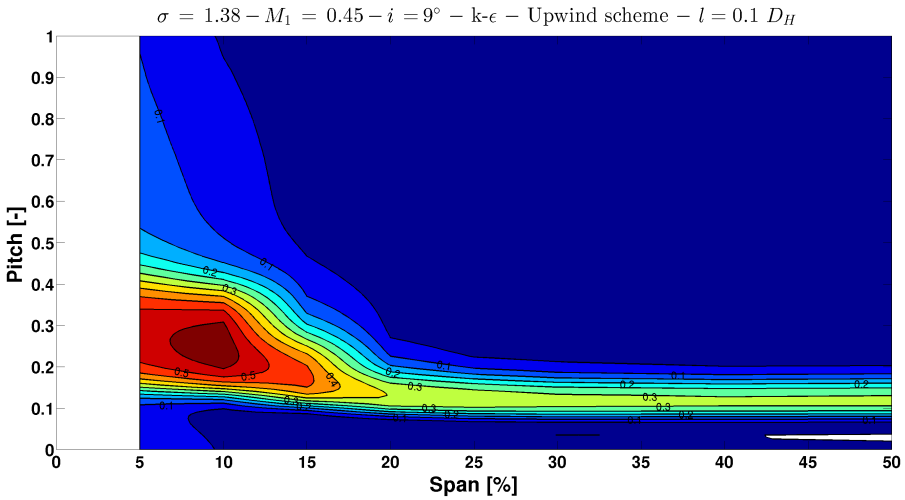


Figure C.25: *Numerical total pressure loss map using Yang-Shih k-ϵ turbulence model with $\ell = 0.1\, D_H$ and an upwind scheme*

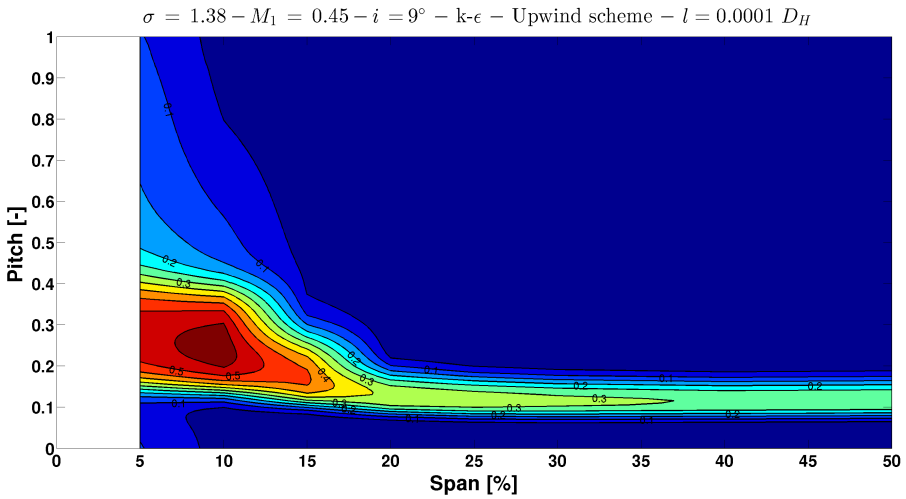


Figure C.26: *Numerical total pressure loss map using Yang-Shih k-ϵ turbulence model with $\ell = 0.0001\, D_H$ and an upwind scheme*

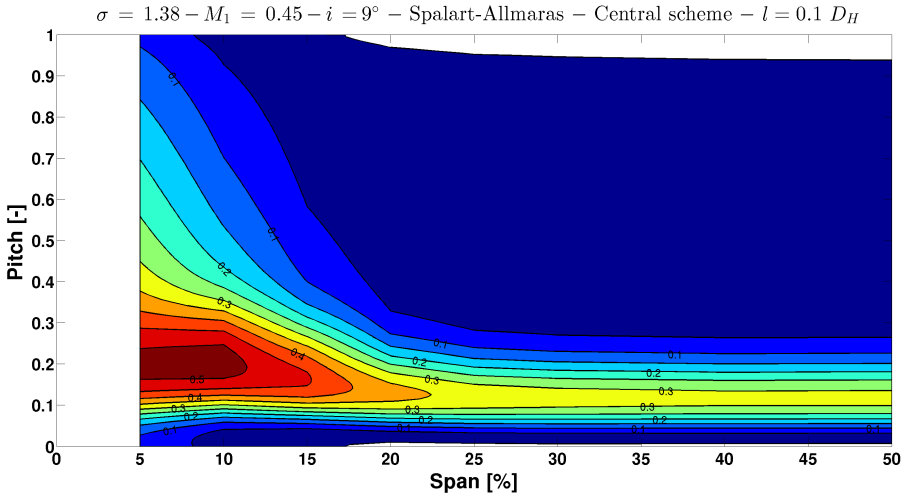


Figure C.27: *Numerical total pressure loss map using Spalart-Allmaras turbulence model with $\ell = 0.1\, D_H$ and a central scheme*

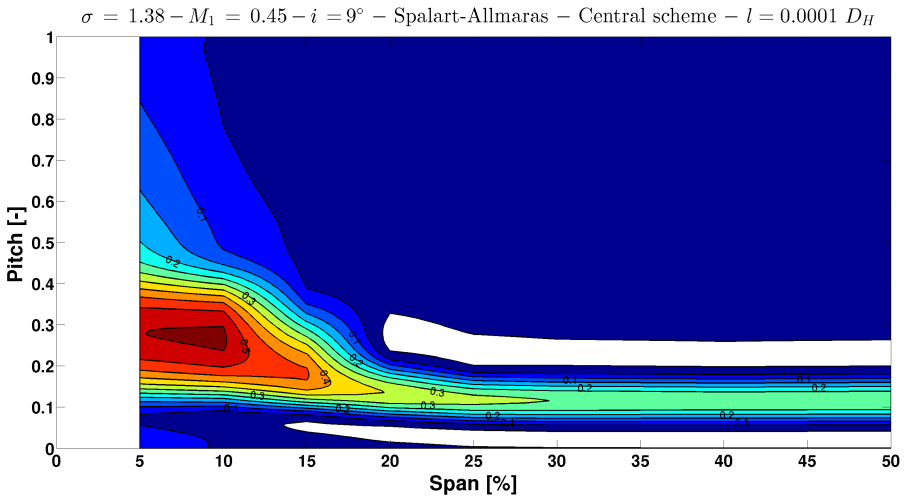


Figure C.28: *Numerical total pressure loss map using Spalart-Allmaras turbulence model with* $\ell = 0.0001\, D_H$ *and a central scheme*

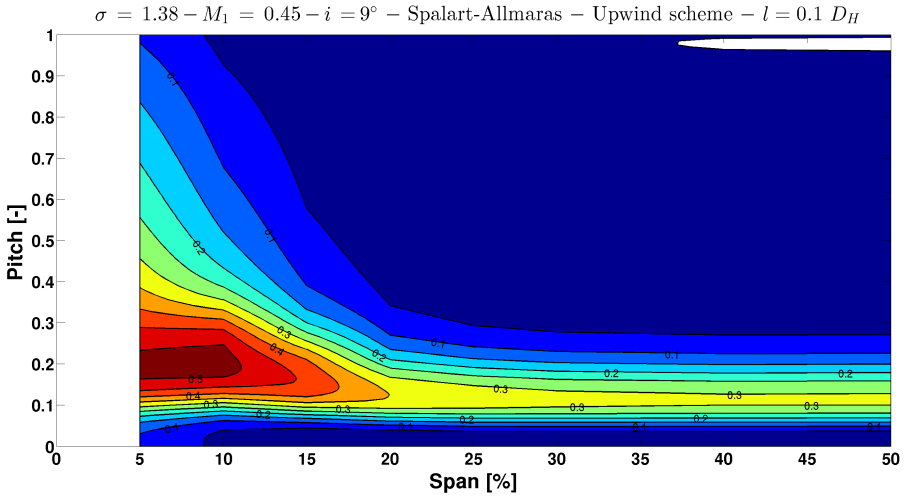


Figure C.29: *Numerical total pressure loss map using Spalart-Allmaras turbulence model with* $\ell = 0.1\, D_H$ *and an upwind scheme*

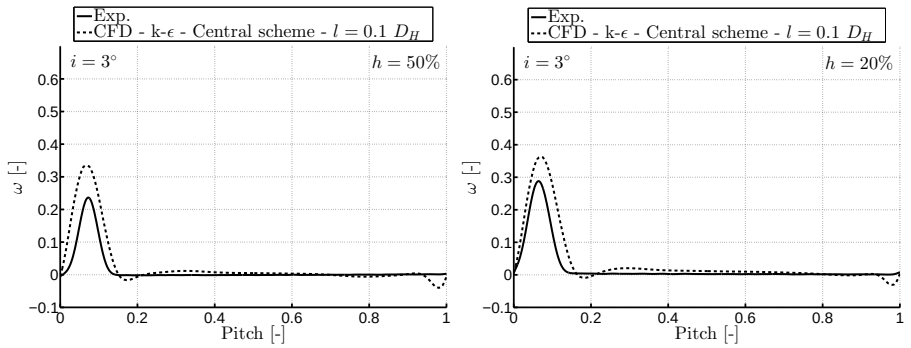
C.3.2 Total pressure loss wakes

The wakes are compared at 50% and 20%. This offers a more qualitative and quantitative comparison. However, since the position of the probe relatively to the trailing edge has not been measured and the motor displacements were not recorded during a traverse, the CFD wakes have been moved in order to set the maximum losses at the same location as the experiments.

The figures C.30 to C.43 distinctly show the difference between a central and an upwind scheme. The dispersive nature of the central scheme (leading to loss undershoots) is compensated by the more dissipative nature of the upwind scheme which always fails at capturing the right loss intensity. The influence of the turbulence length scale is higher than suggested in Chapter 3 and for both turbulence models, decreasing the length scale presents a much better agreement in terms of wake width and depth for both span heights.

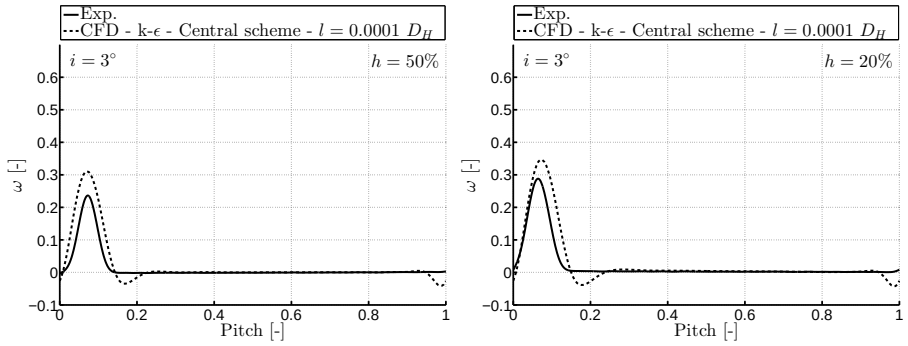
The wakes at 3° and 9° are respectively given in Sec. C.3.2.1 and Sec. C.3.2.2. If both incidence conditions are considered, it appears that the $k-\varepsilon$ model using $\ell = 0.0001\, D_H$ is a better option. The use of a central or an upwind scheme is more difficult to assess. Although it may not lead to the right wake intensity, the upwind scheme provides a more physical solution whereas the central scheme always predicts non-physical negative losses. In that prospect, an upwind scheme should most probably be preferred. However, the better numerical stability, the years of experience in the design of low-pressure compressors and the validated high accuracy in predicting global performance of real compressor geometries (cf. [75, 78]) are important points playing in favor of the central scheme.

C.3.2.1 Total pressure loss wakes - $i = 3°$



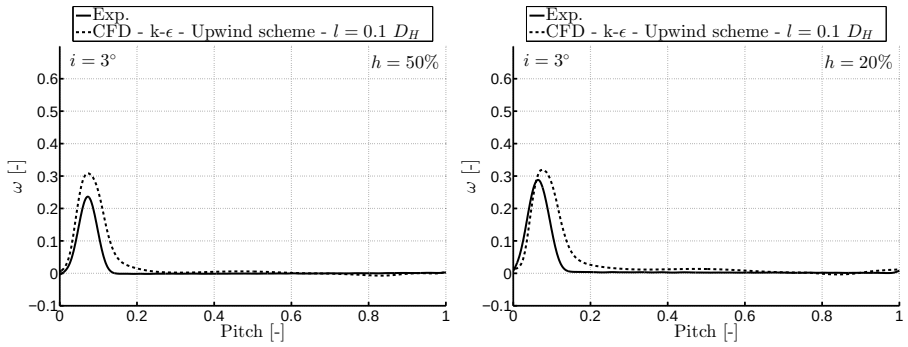
(a) *h=50%* **(b)** *h=20%*

Figure C.30: *Comparison of total pressure loss wakes using Yang-Shih k-ϵ turbulence model with $\ell = 0.1\, D_H$ and a central scheme*



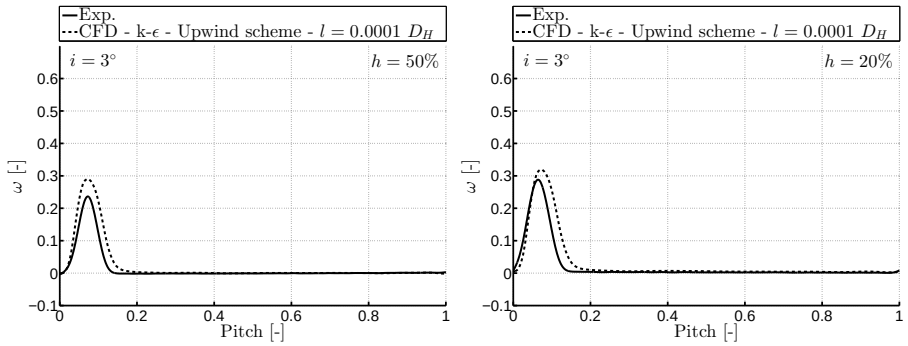
(a) *h=50%* **(b)** *h=20%*

Figure C.31: *Comparison of total pressure loss wakes using Yang-Shih k-ϵ turbulence model with $\ell = 0.0001\, D_H$ and a central scheme*



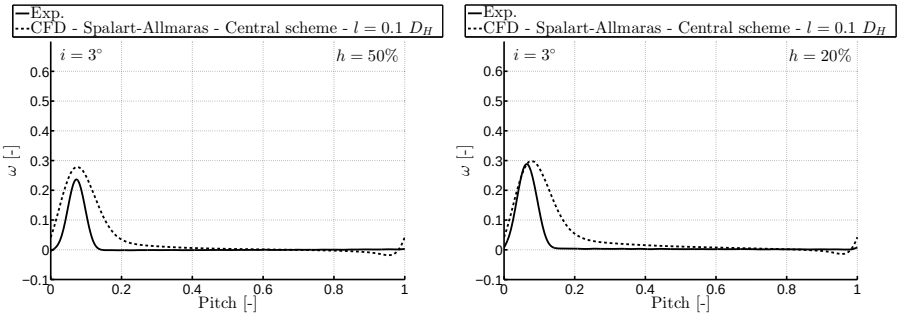
(a) *h=50%* **(b)** *h=20%*

Figure C.32: *Comparison of total pressure loss wakes using Yang-Shih k-ϵ turbulence model with $\ell = 0.1\, D_H$ and an upwind scheme*



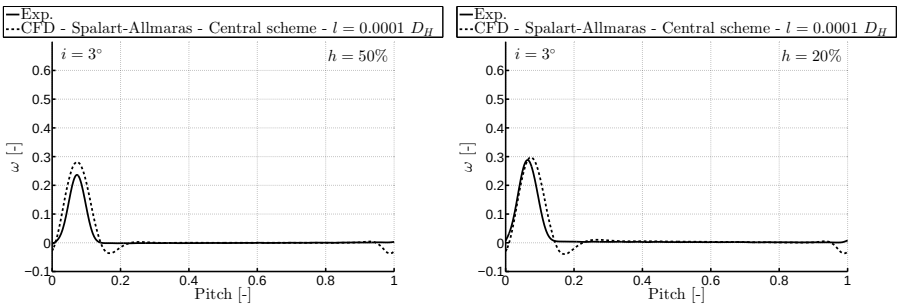
(a) *h=50%* **(b)** *h=20%*

Figure C.33: *Comparison of total pressure loss wakes using Yang-Shih k-ϵ turbulence model with $\ell = 0.0001\, D_H$ and an upwind scheme*



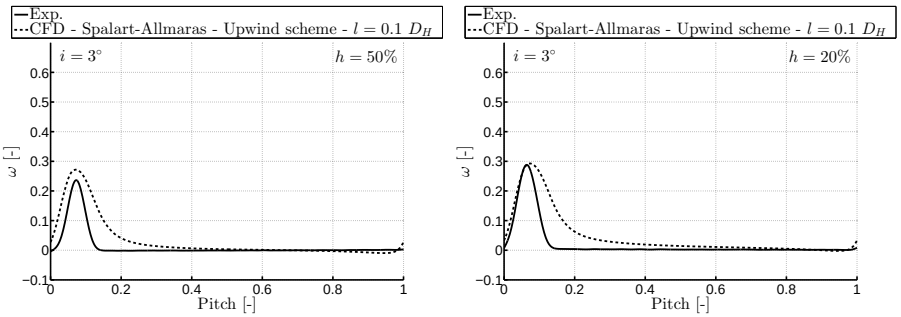
(a) *h=50%* **(b)** *h=20%*

Figure C.34: *Comparison of total pressure loss wakes using Spalart-Allmaras turbulence model with $\ell = 0.1\, D_H$ and a central scheme*



(a) *h=50%* **(b)** *h=20%*

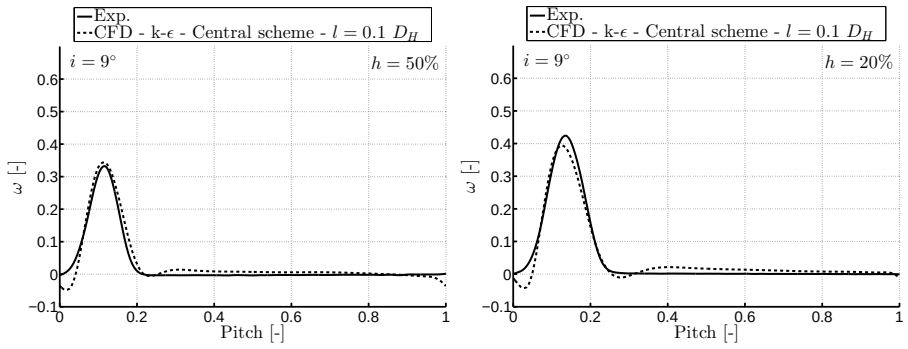
Figure C.35: *Comparison of total pressure loss wakes using Spalart-Allmaras turbulence model with $\ell = 0.0001\, D_H$ and a central scheme*



(a) *h=50%* **(b)** *h=20%*

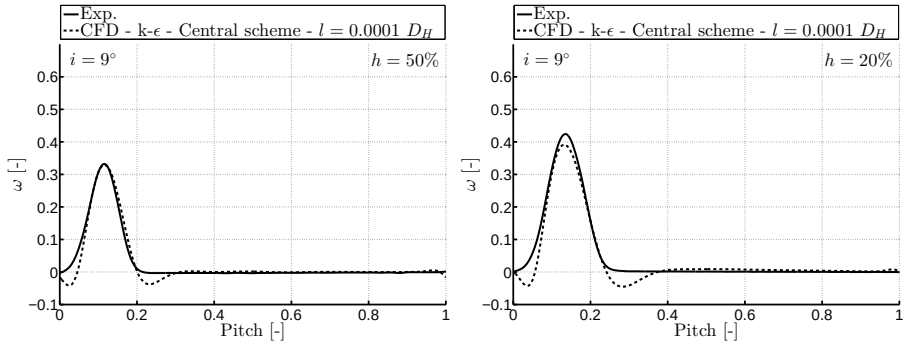
Figure C.36: *Comparison of total pressure loss wakes using Spalart-Allmaras turbulence model with $\ell = 0.1\, D_H$ and an upwind scheme*

C.3.2.2 Total pressure loss wakes - $i = 9°$



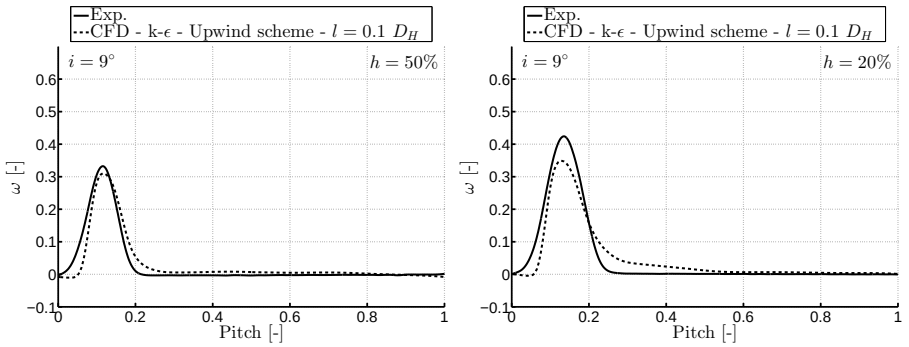
(a) *h=50%* **(b)** *h=20%*

Figure C.37: *Comparison of total pressure loss wakes using Yang-Shih k-ϵ turbulence model with $\ell = 0.1\, D_H$ and a central scheme*



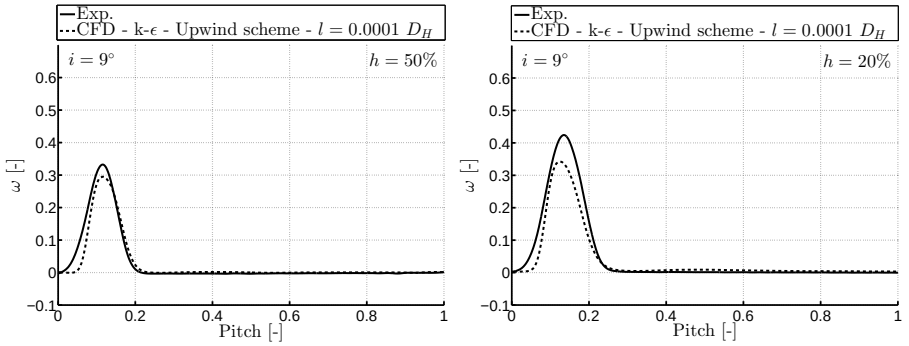
(a) *h=50%* **(b)** *h=20%*

Figure C.38: *Comparison of total pressure loss wakes using Yang-Shih k-ϵ turbulence model with $\ell = 0.0001\, D_H$ and a central scheme*



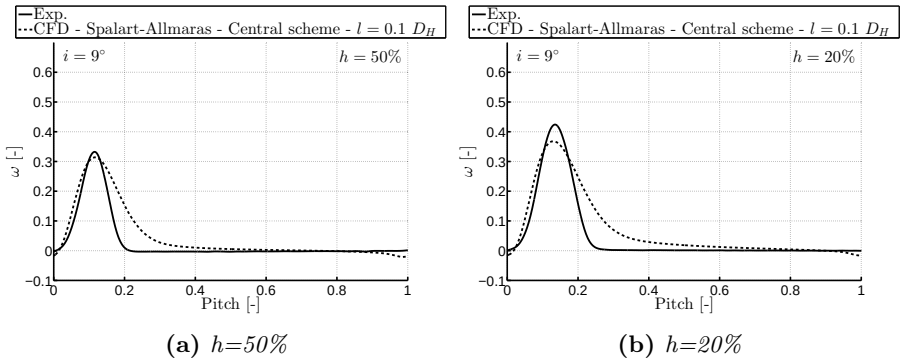
(a) *h=50%* **(b)** *h=20%*

Figure C.39: *Comparison of total pressure loss wakes using Yang-Shih k-ϵ turbulence model with $\ell = 0.1\, D_H$ and an upwind scheme*



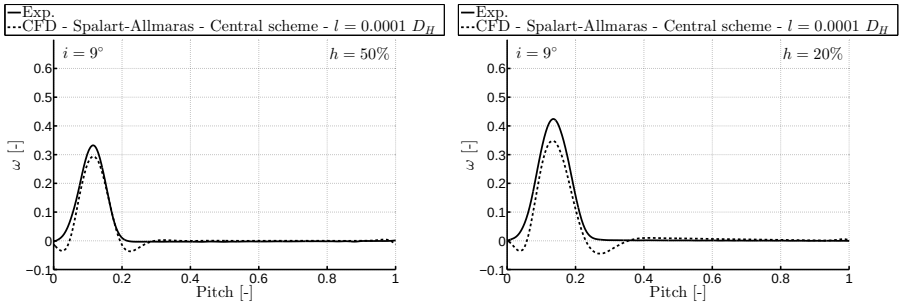
(a) *h=50%* **(b)** *h=20%*

Figure C.40: *Comparison of total pressure loss wakes using Yang-Shih k-ϵ turbulence model with $\ell = 0.0001\, D_H$ and an upwind scheme*



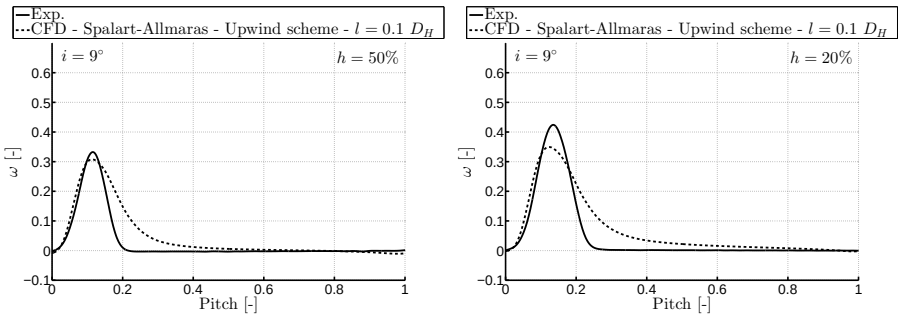
(a) *h=50%* **(b)** *h=20%*

Figure C.41: *Comparison of total pressure loss wakes using Spalart-Allmaras turbulence model with $\ell = 0.1\, D_H$ and a central scheme*



(a) *h=50%* **(b)** *h=20%*

Figure C.42: *Comparison of total pressure loss wakes using Spalart-Allmaras turbulence model with $\ell = 0.0001\, D_H$ and a central scheme*



(a) *h=50%* **(b)** *h=20%*

Figure C.43: *Comparison of total pressure loss wakes using Spalart-Allmaras turbulence model with $\ell = 0.1\, D_H$ and an upwind scheme*

Appendix D

Meridional Optimization - Complementary results

D.1 Additional optimization constraint

It may be required for various reasons that the solidity or the chord profile must have a specific slope or curvature. The following section gives the example of a positive solidity curvature and a chord distribution with a fixed slope at the hub. Those constraints may look arbitrary but they come from many evidences of solidity profiles found in the literature [39, 75] as well as from the distribution of the DREAM booster. However, without any mechanical calculation, such constraints have no reason to be applied.

Considering a 3-points Bezier parametrization, the solidity is given by

$$\sigma = A(1-t)^2 + 2Bt(1-t) + Ct^2 \tag{D.1}$$

where t is the span variable ($t \in [0,1]$) and the coefficient A, B and C are the 3 control points of the parametrization. It is possible to force a positive curvature by imposing:

$$\begin{aligned} \frac{\partial^2 \sigma}{\partial t^2} &> 0 \\ 2A - 4B + 2C &> 0 \\ \frac{A+C}{2} &> B \end{aligned} \tag{D.2}$$

Constraints may also be imposed on the chord or the slope of the chord. The chord is given by:

$$\begin{aligned} c &= \frac{2\pi}{Z} r(t)\sigma(t) \\ &= \frac{2\pi}{Z} \left(t(r_{tip} - r_{hub}) + r_{hub}\right) \left(A(1-t)^2 + 2Bt(1-t) + Ct^2\right) \end{aligned} \tag{D.3}$$

The first derivative of the chord with respect to the span is

$$\frac{\partial c}{\partial t} = \frac{2\pi}{Z} \left[(r_{tip} - r_{hub})\sigma(t) + r(t)\left(-2A(1-t) - 2B - 4Bt + 2Ct\right)\right] \tag{D.4}$$

If the slope is imposed at the hub ($t = 0$), it becomes

$$\begin{aligned}\frac{\partial c}{\partial t}_{|\,t=0} &= \frac{2\pi}{Z}\left[(r_{tip} - r_{hub})\sigma(0) + r(0)\left(-2A(1-0) - 2B - 0 + 0\right)\right] \\ &= \frac{2\pi}{Z}\left[-A\left(3 - \frac{r_{tip}}{r_{hub}}\right) + 2B\right]\end{aligned} \tag{D.5}$$

It is then possible to force the first derivative of the chord to be negative (or positive) at the hub as follows:

$$\begin{aligned}\frac{\partial c}{\partial t}_{|\,t=0} &< 0 \\ -A\left(3 - \frac{r_{tip}}{r_{hub}}\right) + 2B &< 0 \\ B &< \frac{A}{2}\left(3 - \frac{r_{tip}}{r_{hub}}\right)\end{aligned} \tag{D.6}$$

In some situations, such additional limitations may considerably help to avoid to make complementary mechanical iterations in the design process. However, as mentioned earlier, those are only examples and without a preliminary mechanical calculation, they should not be imposed.

D.2 Single rotor solidity optimization

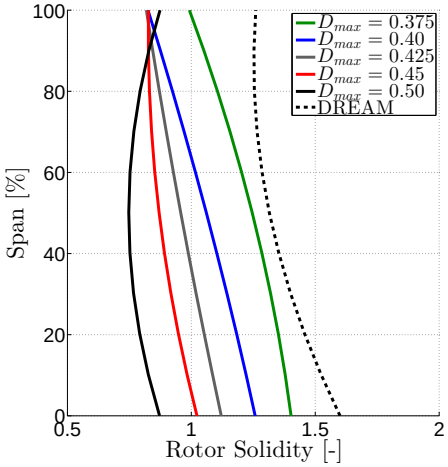


Figure D.1: *Optimum rotor solidity distributions for different values of D_{max} and for the DREAM rotor*

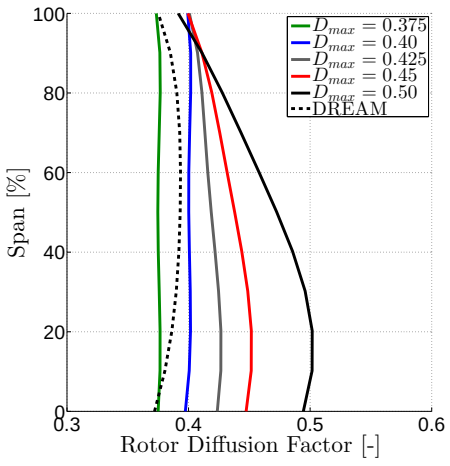


Figure D.2: *Rotor diffusion factor distributions for different values of D_{max} and for the DREAM rotor*

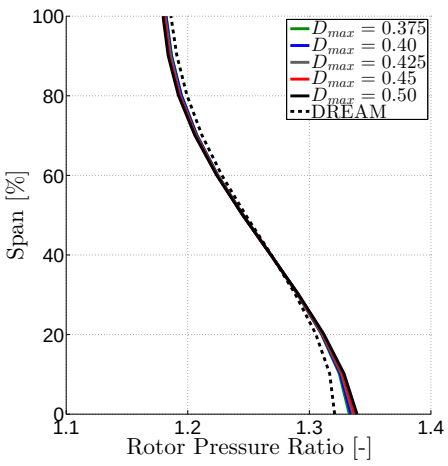


Figure D.3: *Rotor pressure ratio distributions for different values of D_{max} and for the DREAM rotor*

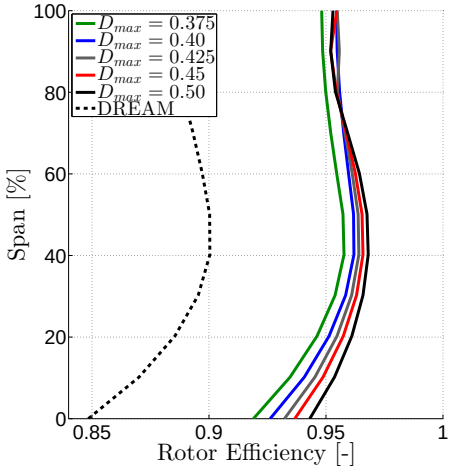
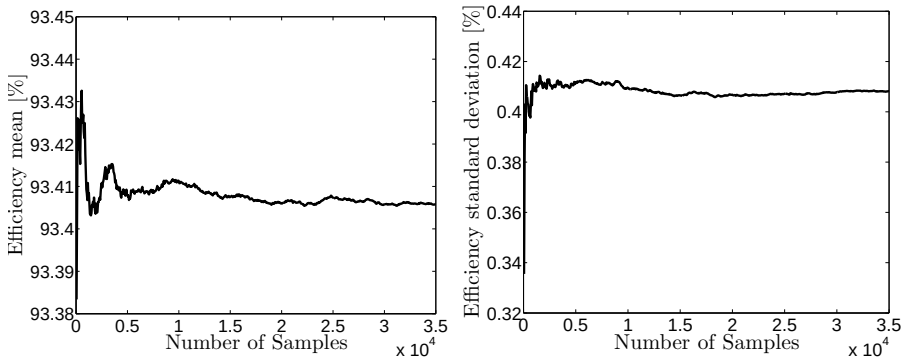


Figure D.4: *Rotor efficiency distributions for different values of D_{max} and for the DREAM rotor*

D.3 Uncertainty quantification

D.3.1 Full stage results with two uncertain parameters



(a) **(b)**

Figure D.5: *Evolution of the efficiency mean and standard deviation with the number of samples ($D_{max} = 0.45$)*

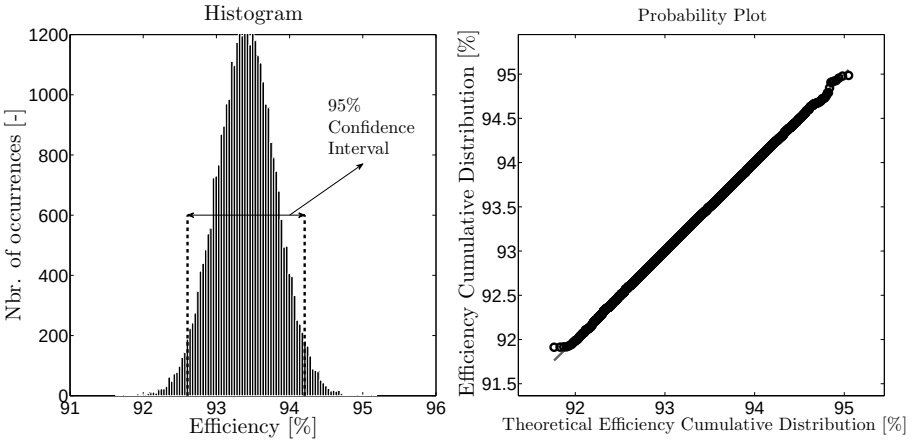


Figure D.6: *Efficiency histogram and probability plot ($D_{max} = 0.45$)*

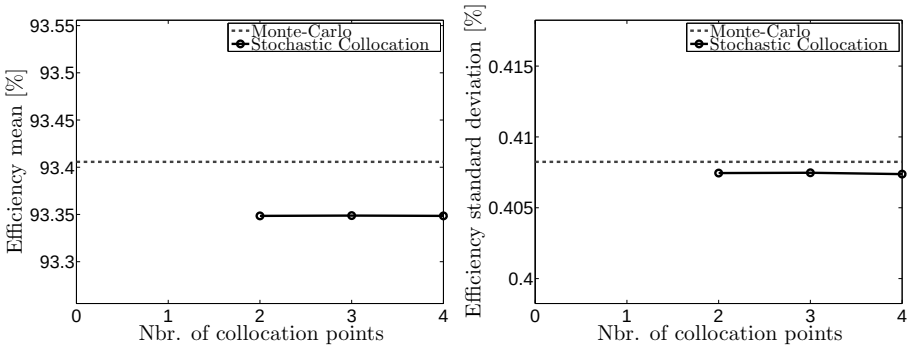
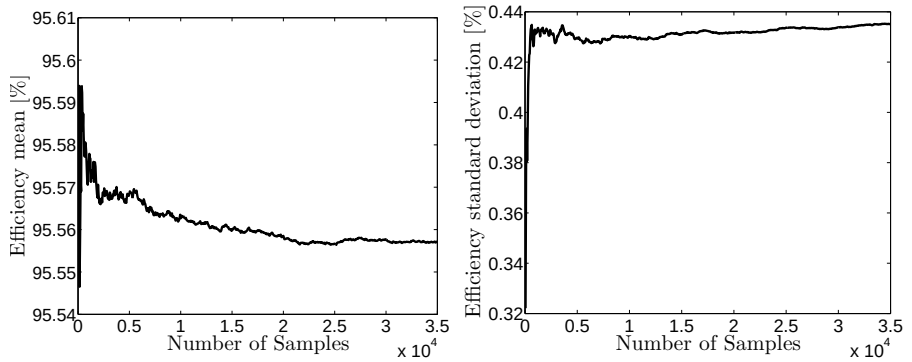


Figure D.7: *Efficiency mean and standard deviation in function of the number of collocation points ($D_{max} = 0.45$)*

D.3.2 Single rotor results with three uncertain parameters



(a) **(b)**

Figure D.8: *Evolution of the efficiency mean and standard deviation with the number of samples ($D_{max} = 0.40$)*

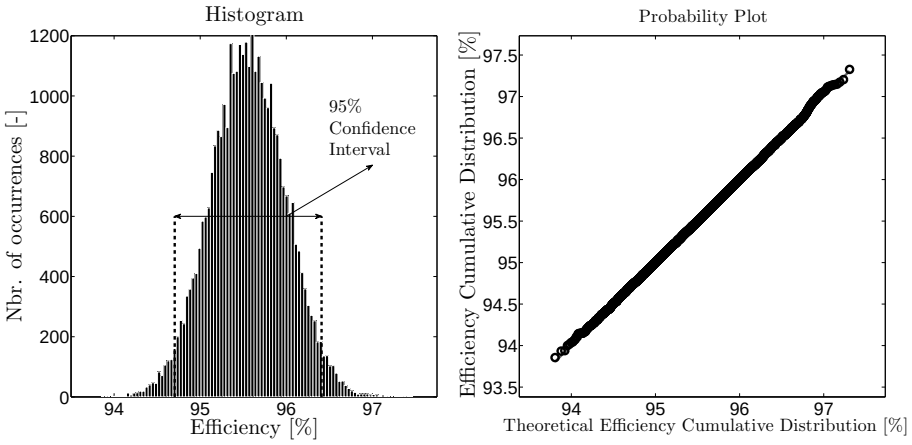


Figure D.9: *Efficiency histogram and probability plot ($D_{max} = 0.40$)*

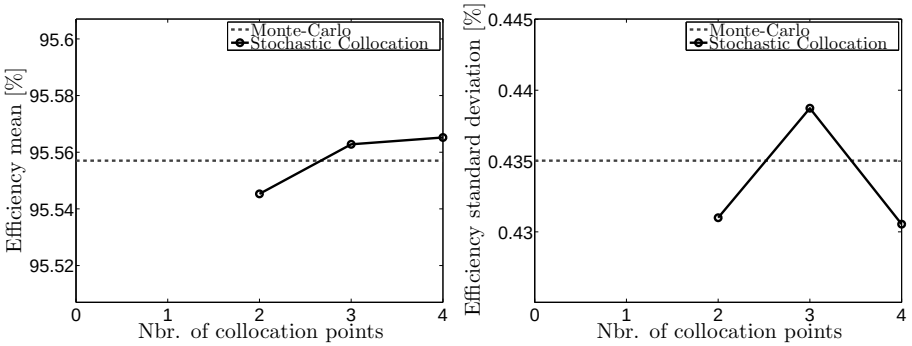
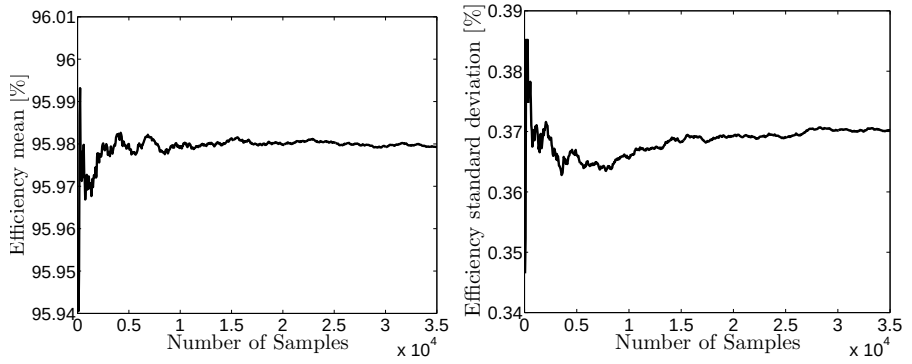


Figure D.10: *Efficiency mean and standard deviation in function of the number of collocation points ($D_{max} = 0.40$)*



(a) **(b)**

Figure D.11: *Evolution of the efficiency mean and standard deviation with the number of samples ($D_{max} = 0.45$)*

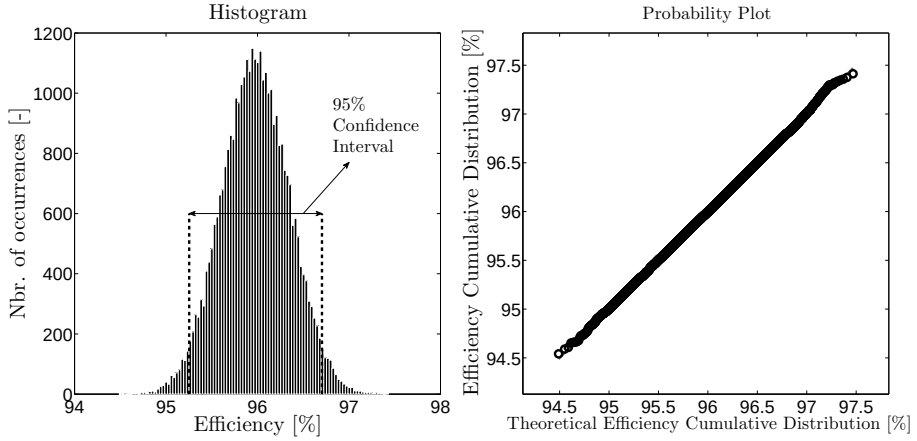


Figure D.12: *Efficiency histogram and probability ($D_{max} = 0.45$)*

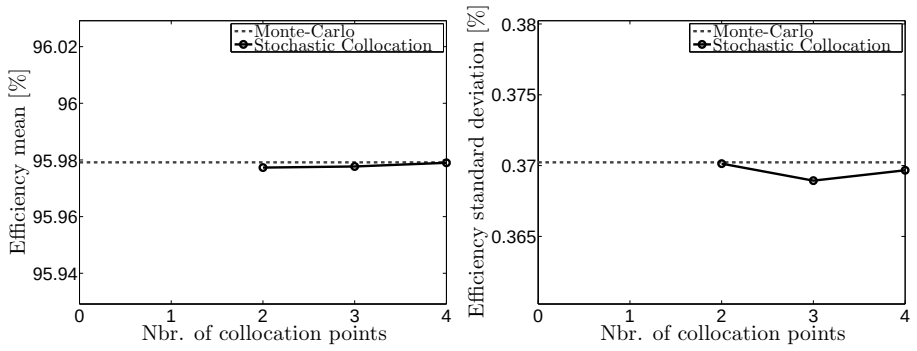


Figure D.13: *Efficiency mean and standard deviation in function of the number of collocation points ($D_{max} = 0.45$)*

Bibliography

[1] Obrecht, T., 2013. "HP compressor preliminary design". In Advances in axial compressor aerodynamics, von Karman Institute for Fluid Dynamics Lecture Series. VKI-LS 2013-03. 2, 19

[2] Howell, A. R., 1945. "Fluid dynamics of axial compressors". In Proceedings of Institution of Mechanical Engineering, Vol. 153, pp. 441–452. 3, 5, 8, 10, 47, 247

[3] Zweifel, O., 1945. "The Spacing of Turbo-Machine Blading, Especially With Large Angular Deflection". *The Brown Boveri Review, **32***, December, pp. 436–444. 3, 18, 47

[4] Carter, A. D. S., 1949. The Low-Speed Performance of Related Aerofoils in Cascades. A.R.C. Tech. Report, NGTE. Report No.R.55. 3, 5, 8, 10, 36, 79

[5] Lieblein, S., Schwenk, F. C., and Broderick, R. L., 1953. Diffusion Factor for Estimating Losses and Limiting Blade Loadings in Axial-Flow Compressor Blade Elements. NACA Research Memorandum, Lewis Flight Propulsion Laboratory, Cleveland, Ohio. RME53D01. 3, 5, 20, 23, 153, 155, 164, 176

[6] Lieblein, S., 1965. Aerodynamic design of axial-flow compressors - Chapter VI: Experimental Flow in Two-Dimensional Cascades. NASA SP-36. 5, 7, 10, 11, 13, 14, 16, 20, 21, 22, 26, 28, 29, 31, 65, 73, 79, 80, 82, 247, 248

[7] Horlock, J. H., 1973. *Axial flow compressors - Fluid mechanics and thermodynamics*. Robert E. Krieger Publishing Co. 9, 247

[8] Cumpsty, N. A., 1989. *Compressor aerodynamics*, First ed. Longman Scientific & Technical. 9, 16, 18, 35, 36, 38, 247

[9] Gostelow, J. P., 1984. *Cascade Aerodynamics*. Pergamon Press. 9, 101

[10] Herrig, L. J., Emery, J. C., and Erwin, J. R., 1957. Systematic two-dimensional cascade tests of NACA 65-series compressor blades at low speeds. Tech. rep., NACA, Langley Aeronautical Laboratory, February. 10, 20, 36, 136

[11] Eck, B., 1973. *Fans*. Pergamon Press. 19

[12] Wallis, R. A., 1983. *Axial flow fans and ducts*. John Wiley & Sons, Inc. 19

[13] Dixon, S. L., 1998. *Fluid mechanics, thermodynamics of turbomachinery*, Fourth ed. Butterworth-Heinemann. 19

[14] Arts, T., 1994. "Pressure Measurements". In Introduction to Measurement Techniques, von Karman Institute for Fluid Dynamics Lecture Series. 21, 56

[15] Lieblein, S., 1956. Theoretical Loss Relations for Low-Speed Two-Dimensional Cascade Flow. NACA Research Memorandum, Lewis Flight Propulsion Laboratory, Cleveland, Ohio. TN 3662. 22, 28, 82

[16] Lieblein, S., 1957. Analysis of Experimental Low-Speed Loss and Stall Characteristics of Two-Dimensional Compressor Blade Cascades. NACA Research Memorandum, Lewis Flight Propulsion Laboratory, Cleveland, Ohio. RME57A28. 22

[17] Lieblein, S., 1959. "Loss and Stall Analysis of Compressor Cascades". *Journal of Basic Engineering,* ***81***(4), September, pp. 387–400. 22, 23, 26, 27, 248

[18] Koch, C. C. and Smith, L. H., 1976. "Loss Sources and Magnitudes in Axial-Flow Compressors". *Journal of Engineering for Power,* ***98***(3), July, pp. 411–424. 23, 24, 25, 26, 27, 28, 48, 79, 247, 248

[19] Casey, M. V., 1987. "A Mean Line Prediction Method for Estimating The Performance Characteristic of An Axial Compressor Stage". In Turbomachinery: Efficiency Prediction and Improvement, Proceedings of Institution of Mechanical Engineering, pp. 273–281. C264/87. 23

[20] Wright, P. I. and Miller, D. C., 1991. "An Improved Compressor Performance Prediction Model". In Turbomachinery: Latest Developments in a Changing Scene, Proceedings of Institution of Mechanical Engineering, pp. 69–75. C423/028. 23, 24, 26, 28, 84, 247

[21] Dickens, T. and Day, I., 2009. "The Design of Highly Loaded Axial Compressors". In Proceedings of ASME Turbo Expo 2009. ASME Paper No. GT2009-59291. 23

[22] Boyce, M. P., 1967. "Design of Compressor Blades Suitable for Transonic Axial-Flow Compressors". In Proceedings of ASME Turbo Expo 1967. ASME Paper No. 67-GT-47. 28, 29, 84, 248

[23] Jansen, W. and Moffat, W. C., 1967. "The Off-Design Analysis of Axial-Flow Compressors". *Journal of Engineering for Power,* ***89***(4), October, pp. 453–462. 30, 84, 118

[24] Griepentrog, H., 1969. Transonic Compressor Cascades. Tech. rep., von Karman Institute for Fluid Dynamics Lecture Series, Rhode-Saint-Genese, Belgium, December. VKI-CN73. 30

[25] Heilmann, W., Starken, H., and Meyer, H., 1968. Cascade wind tunnel tests on blades designed for transonic and supersonic compressors. Tech. rep., Institut fuer Luftstrahlantriebe. AGARD-CP-34. 30, 31, 42, 90

[26] Schwenk, F. C. and Lewis, G. W. J., 1955. Experimental investigation of a transonic axial-flow compressor rotor with double-circular arc airfoil blade sections: III - comparison of blade element performance with three levels of solidity. NACA Research Memorandum, Lewis Fligh Propulsion, Cleveland, Ohio. RME55F01. 31, 42, 43, 44, 90, 248

[27] Tysl, E. R. and Schwenk, F. C., 1956. Experimental investigation of a transonic compressor rotor with 1.5-inch chord length and an aspect ratio of 3.0: III - blade element and over-all performance at three levels of solidity. NACA Research Memorandum, Lewis Fligh Propulsion, Cleveland, Ohio. RME56D06. 31, 42, 43, 44, 248

[28] Glassman, A. J. and Lavelle, T. M., 1995. Enhanced Capabilities and Modified Users Manual for Axial-Flow Compressor Conceptual Design Code CSPAN. Tech. rep., NASA, January. NASA TM 106833. 31

[29] Koch, C. C., 1981. "Stalling Pressure Rise Capability of Axial Flow Compressor Stages ". *Journal of Engineering for Power,* ***103***(3), October, pp. 645–656. 32, 33, 34, 35, 177, 248

[30] Sovran, G. and Klomp, E. D., 1967. "Experimentally Determined Optimum Geometries for Rectilinear Diffusers with Rectangular, Conical or Annular Cross-Section". In Fluid Mechanics of Internal Flow. 32, 33

[31] Starken, H., Breugelmans, F. A. E., and Schimming, P., 1975. "Investigation of the Axial Velocity Density Ratio in a High Turning Cascade". In Proceedings of ASME Turbo Expo 1975. ASME Paper No. 75-GT-25. 36, 37, 116, 131, 248

[32] Stark, U. and Hoheisel, H., 1981. "The Combined Effect of Axial Velocity Density Ratio and Aspect Ratio on Compressor Cascade Performance". *Journal of Engineering for Power,* ***103***, January, pp. 248–255. 36, 37, 116, 131, 248

[33] Kumaran, R. S., Swamy, K. M. M., Kamble, S., Nagpurwala, Q. H., and Bhat, A., 2013. "Effect of Axial Velocity Density Ratio on The Performance of a Controlled Diffusion Airfoil Compressor Cascade". In Proceedings of ASME Turbo Expo 2013. ASME Paper No. GT2013-94143. 38, 116, 131

[34] Ozgen, A., 2013. Effect of Aspect Ratio on Three Linear Cascades With Same Solidity and Hub Corner Stall Prediction. Tech. rep., von Karman Institute for Fluid Dynamics Lecture Series, Rhode-Saint-Genese, Belgium, September. VKI SR2013-33. 38

[35] Robbins, W. H., Jackson, R. J., and Lieblein, S., 1965. Aerodynamic design of axial-flow compressors - Chapter VII: Blade-element flow in annular cascades. NASA SP-36. 38, 39, 40, 41, 153, 155, 248

[36] Standahar, R. M. and Serovy, G. K., 1952. Some effect of changing solidity by varying the number of blades on performance of an axial flow compressor stage. NACA Research Memorandum, NACA, Lewis Flight Propulsion Laboratory, Cleveland, Ohio, April. RME52A31. 41, 248

[37] Turner, R. C. and Burrows, R. A., 1960. The low-speed performance of stagger compressors at three pitch/chord ratios. Memorandum, NGTE. M.336. 44, 248

[38] Moore, R. D., Osborn, W. M., and Urasek, D. C., 1972. Performance of a single stage transonic compressor with a blade-tip solidity of 1.3. Tech. rep., NASA, Lewis Research Center, Cleveland, Ohio, November. NASA TM X-2645. 45, 249

[39] Moore, R. D., Osborn, W. M., and Urasek, D. C., 1973. Performance of a single stage transonic compressor with a blade-tip solidity of 1.5 and comparison with 1.3- and 1.7-solidity stages. Tech. rep., NASA, Lewis Research Center, Cleveland, Ohio, November. NASA TM X-2926. 45, 229, 249

[40] Moore, R. D. and Reid, J., 1972. Performance of a single stage axial-flow transonic compressor with a blade tip solidity of 1.7. Tech. rep., NASA, Lewis Research Center, Cleveland, Ohio, December. NASA TM X-2658. 45, 249

[41] Britsch, W. R., Osborn, W. M., and Laessig, M. R., 1979. Effects of diffusion factor, aspect ratio and solidity on overall performance of 14 compressor middle stages. Tech. rep., NASA, Lewis Research Center, Cleveland, Ohio, September. NASA TP 1523. 45, 46, 249

[42] Houghton, T. and Day, I., 2010. "Stability Enhancement by Casing Grooves: The Importance of Stall Inception and Solidity". In Proceedings of ASME Turbo Expo 2010. ASME Paper No. GT2010-22284. 46, 90

[43] Hearsey, R. M., 1986. "Practical Compressor Aerodynamic Design". In Advanced Topics in Turbomachinery Technology, Concept ETI Principal Lecture Series. 48, 49, 249

[44] Liu, G. L., 1993. "Simple Formulae for Optimal Solidity of Two-Dimensional Compressor Cascades Based on Diffusion Concept". *International Journal of Turbo and Jet Engines,* ***10***, pp. 127–134. 48

[45] McKenzie, A. B., 1988. "The Selection of Fan Blade Geometry for Optimum Efficiency". *Proceedings of Institution of Mechanical Engineers, Part A: Journal of Power and Energy,* ***202***, February, pp. 39–44. 49, 50, 249

[46] Massardo, A., Satta, A., and Marini, M., 1990. "Axial Flow Compressor Design Optimization: Part II - Throughflow Analysis". *Journal of Turbomachinery,* ***112***, pp. 405–410. 52

[47] Joly, M., Verstraete, T., and Paniagua, G., 2012. "Full Design of Highly Loaded Fan by Multi-Objective Optimization of Throughflow and High-Fidelity Aero-Mechanical Performance". In Proceedings of ASME Turbo Expo 2012. ASME Paper No. GT2012-69686. 52, 154, 156

[48] Teichel, S., Verstraete, T., and Seume, J., 2013. "Optimized Preliminary Design of Compact Axial Compressors A Comparison of Two Design Tools". In 31st AIAA Applied Aerodynamics Conference. AIAA-2013-2651. 52, 154, 156

[49] Verstraete, T., 2008. "Multidisciplinary Turbomachinery Component Optimization Considering Performance, Stress and Internal Heat Transfer". PhD Thesis, von Karman Institute for Fluid Dynamics - Universiteit Gent, Rhodes-Saint-Genese, Belgium. 52, 153, 156

[50] Creveling, H. F. and Carmody, R. H., 1968. Axial Flow Compressor Design Computer Programs Incorporating Full Radial Equilibrium - Part I : Flow Path and Radial Equilibrium of Energy Specified. Tech. rep., NASA, June. NASA CR-54532. 52, 154, 155

[51] Creveling, H. F. and Carmody, R. H., 1968. Axial Flow Compressor Design Computer Programs Incorporating Full Radial Equilibrium - Part II : Radial Distribution of Total Pressure and Flow Path or Axial Velocity Ratio Specified. Tech. rep., NASA, June. NASA CR-54531. 52, 154

[52] Hurlbrink, J., 2013. Three-dimensional CFD Validation of Preliminary Axial Compressor Designs. Tech. rep., von Karman Institute for Fluid Dynamics Lecture Series, Rhode-Saint-Genese, Belgium, August. VKI SR2013-. 52

[53] Iaccarino, G., 2011. "Introduction to uncertainty representation and propagation". In Uncertainty quantification in computational fluid dynamics, RTO-AVT-VKI Lecture Series 2011/12 - AVT 193. 52, 153, 164

[54] Wheeler, A. P. S., Sofia, A., and Miller, R. J., 2009. "The Effect of Leading Egde Geometry on Wake Interactions in Compressors". *Journal of Turbomachinery,* ***131***. 041013. 55

[55] Goodhand, M. N. and Miller, R. J., 2011. "Compressor Leading Edge Spikes : A New Performance Criterion". *Journal of Turbomachinery,* ***133***. 021006. 55, 85

[56] Mesbah, M., Arts, T., Simon, J. F., and Geuzaine, P., 2009. "Numerical and Experimental Analysis of Surface Roughness Effects For Compressor Blades". In 19th Conference of the International Society for Air Breathing Engines. 56, 116

[57] Zhu, Z. W., Lacor, C., and Hirsch, C., 1993. "A New Residual Smoothing Method for Multigrid, Multi-stage Schemes". In 11th Computational Fluid Dynamics Conference. AIAA-93-3356-CP. 56

[58] Resmini, M., 2013. "Numerical Investigation of the Solidity Effect on a Linear Compressor Cascade Performance and Stability". Master's thesis, Politecnico de Milano - von Karman Institute for Fluid Dynamics. 56, 60, 61

[59] Sans, J., Resmini, M., Brouckaert, J. F., and Hiernaux, S., 2014. "The Impact of Turbulence Model and Numerical Scheme on The Performance of a Linear Compressor Cascade". In Proceedings of ASME Turbo Expo 2014. ASME Paper No. GT2014-25531. 56

[60] Dieck, R., 2004. *Measurement Uncertainty: Methods and Applications*, Fourth ed. ISA - The Instrumentation, Systems and Automation Society. 56, 193, 194, 196

[61] NUMECA International, 2010. *User Manual Autogrid5^{TM} v 8, Automated Grid Generator for Turbomachinery.* 57

[62] Biesinger, C. C. T., Galpin, P., and Braune, A., 2013. "Experimental and Computational Analysis of a Multistage Axial Compressor Including Stall Prediction by Steady and Transient CFD Methods". In Proceedings of ASME Turbo Expo 2013. ASME Paper No. GT2013-94639. 60

[63] Wilcox, D. C., 1993. *Turbulence Modeling for CFD.* DCW Industries, Inc. 60, 61

[64] Degrez, G., 2012. Two-dimensional boundary layers. Tech. rep., von Karman Institute for Fluid Dynamics, Rhode-Saint-Genese, Belgium, September. VKI CN. 60, 61

[65] Baldwin, B. and Lomax, H., 1978. "Thin Layer Approximation and Algebraic Model for Separated Turbulent Flows". In 16th AIAA Aerospace Sciences Meeting. AIAA-78-257. 60, 61

[66] Spalart, P. R. and Allmaras, S. R., 1992. "A One Equation Turbulence Model For Aerodynamic Flows". In 30th AIAA Aerospace Sciences Meeting. AIAA-92-0439. 61

[67] Yang, Z. and Shih, T. H., 1993. "A k-ε model for turbulence and transitional boundary layer". In *Near-Wall Turbulent Flows.* pp. 165–175. 61

[68] Launder, B. E. and Sharma, B. T., 1974. "Application of the Energy-Dissipation Model of turbulence to the Calculation of Flow Near a Spinning Disc". *Letters in Heat and Mass Transfer,* ***1***, pp. 131–138. 61

[69] Menter, F. R., 1993. "Zonal two equation k-ω turbulence models for aerodynamic flows". In 24th Fluid Dynamics Conference. AIAA-93-2906. 61

[70] Menter, F. R., 1994. "Two-Equation Eddy-Viscosity Turbulence Models for Engineering Applications". *AIAA journal,* ***32***, August, pp. 1598–1605. 61

[71] NUMECA International, 2010. *Theorethical Manual FINE^{TM}/Turbo v 8.7, Flow Integrated Environment.* 61, 62, 64, 115

[72] Menter, F. R., 1992. "Performance of popular turbulence models for attached and separated adverse pressure gradient flows". *AIAA journal,* ***30***(8), pp. 2066–2072. 62

[73] ANSYS, 2011. *ANSYS FLUENT User's Guide.* Release 14.0. 62

[74] Kiock, R., 1983. Boundary Layers on Turbomachinery Blades. Tech. rep., von Karman Institute for Fluid Dynamics Lecture Series, Rhode-Saint-Genese, Belgium, February. VKI-CN118. 65, 116

[75] Brouckaert, J.-F., de Wyer, N. V., Desset, J., Farkas, B., Perez, J. G., Capart, R., Thomas, J.-F., Isaac, N., and Hiernaux, S., 2009. "Experimental and Numerical Investigation of a Single Stage low Pressure Compressor for Counter-Rotating Turbofan Engine Architechtures". In The XVIIIth European Turbomachinery Conference. 66, 70, 89, 145, 222, 229

[76] Jameson, A., Schmidt, W., and Turkel, E., 1981. "Numerical Solutions of the Euler Equations by Finite Volume Methods using Runge-Kutta Time-Stepping Schemes". In 14th Fluid and Plasma Dynamic Conference. AIAA 81-1259. 68

[77] Yee, H. C., 1987. Upwind and symmetric shock-capturing schemes. Tech. rep., NASA. NASA TM 89464. 68, 70

[78] Sans, J., Desset, J., Dell'Era, G., and Brouckaert, J.-F., 2013. "Performance Testing of a Low-Pressure Compressor". In The Xth European Turbomachinery Conference. 70, 89, 99, 145, 185, 222

[79] AGARD, 1983. Mthodes d'Etablissement de Caractristiques Moyennes dans les Ecoulements Internes Htrognes. AGARD AR-182. 72

[80] Breugelmans, F. A. E., 1973. "The cascade and stator section performance of 48 degrees cambered DCA airfoil: comparison with 2D flow calculations in the compressible regime". In Transonic Flows in Turbomachinery, von Karman Institute for Fluid Dynamics Lecture Series. VKI-LS 59. 85

[81] Horlock, J. H. and Denton, J. D., 2005. "A Review of Some Early Design Practice Using Computational Fluid Dynamics and a Current Perspective". *Journal of Turbomachinery,* ***127***(1), January, pp. 5–13. 89

[82] Denton, J., 2010. "Some Limitations of Turbomachinery CFD". In Proceedings of ASME Turbo Expo 2010. ASME Paper No. GT2010-22540. 89

[83] Henault, N., 2014. "Experimental Investigation of a Linear Compressor Cascade Performance". Master's thesis, ESTACA - von Karman Institute for Fluid Dynamics. VKI SR 2014-. 95, 121, 122

[84] Anderson, J. D. J., 2001. *Fundamentals of aerodynamics*, Third ed. McGraw-Hill. 107, 251

[85] Arts, T., 2010. TATMo - Report on the effect of weld beat on aerodynamic performance for the high speed compressor cascade tests. Tech. rep., von Karman Institute for Fluid Dynamics Lecture Series, Rhode-Saint-Genese, Belgium, January. CONFIDENTIAL. 110, 141

[86] MATLAB Documentation : Zero-phase digital filtering. `http://nl.mathworks.com/help/signal/ref/filtfilt.html`. Last checked: 2015-04-03. 112

[87] Ma, W., 2012. "Experimental Investigation of Corner Stall in a Linear Compressor Cascade". PhD Thesis, Ecole Centrale de Lyon, Lyon, France. 116

[88] Çetin, M., Üçer, A. Ş., Hirsch, C., and Serovy, G. K., 1987. Application of Modified Loss and Deviation Correlations to Transonic Axial Compressors. AGARD R-745. 118

[89] Miller, D. C. and Wasdell, D. L., 1987. "Off-design prediction of compressor blade losses". In Turbomachinery: Efficiency Prediction and Improvement, Proceedings of Institution of Mechanical Engineering, pp. 249–260. C279/87. 118

[90] Gao, F., 2014. "Advanced Numerical Simulation of Corner Separation in a Linear Compressor Cascade". PhD Thesis, Ecole Centrale de Lyon, Lyon, France. 145, 146

[91] Verstraete, T., 2010. "CADO: a Computer Aided Design and Optimization Tool for Turbomachinery Applications". In 2^{nd} International Conference on Engineering Optimization. 156

[92] Price, K. and Storn, N., 1997. "Differential Evolution". *Dr. Dobb's Journal*, April, pp. 18–24. 156

[93] Pierret, S., 1999. "Designing Turbomachinery Blades by Means of the Function Approximation Concept Based On Artificial Neural Network, Genetic Algorithm and Navier-Stokes Equations". PhD Thesis, von Karman Institute for Fluid Dynamics - Faculté Polytechnique de Mons, Rhodes-Saint-Genese, Belgium. 156

[94] Hildebrand, F., 1974. *Introduction to Numerical Analysis*, Second ed. Dover Publications. 165

[95] Abramowitz, M. and Stegun, I., 1964. *Handbook of Mathematical Functions*, First ed. Dover Publications. 165

[96] Poloni, C., Pediroda, V., and Parussini, L., 2011. "Optimization under uncertainty". In Uncertainty quantification in computational fluid dynamics, RTO-AVT-VKI Lecture Series 2011/12 - AVT 193. 175

List of Figures

1.1 Evolution of solidity in compressor design over the last decades 2

2.1 Geometrical definition of a cascade 6
2.2 Optimum incidence definition [6]: (a) minimum loss incidence; (b) mid-range incidence 7
2.3 Nominal flow turning as a function of outlet flow angle and pitch-to-chord ratio[2] 8
2.4 Design curves for optimum conditions [7] 9
2.5 m_C factor for Carter's deviation rule (Eq. (2.4)) 9
2.6 Zero-camber incidence angle for blades of 10% maximum thickness [6] 11
2.7 Slope factor n for blades of 10% maximum thickness [6] 11
2.8 Thickness correction for the zero-camber optimum incidence angle [6] 11
2.9 Zero-camber deviation angle of Eq. (2.7) for blades of 10% maximum thickness [6] 13
2.10 Thickness correction for zero-camber deviation angle [6] 13
2.11 m factor of Eq. (2.7) [6] 14
2.12 b exponent of Eq. (2.7) [6] 14
2.13 Deviation angle slope at optimum incidence [6] 16
2.14 Sketch of the influence of the blade circulation on an incoming flow at zero incidence 17
2.15 Sketch of the influence of the solidity on incidence and deviation by potential flow theory 17
2.16 Position of the stagnation points around the leading edge computed using an incompressible singularity method for a NACA-65 airfoil with different solidities [8] 18
2.17 Drag-lift ratio in function of the Zweifel loading factor ψ for different types of bladings 19
2.18 Evolution of momentum thickness to chord ratio as a function of Lieblein diffusion factor of Eq. (2.13) [6] 21
2.19 Sketch of an outlet velocity wake for the calculation of the wake momentum thickness 21
2.20 Evolution of loss parameters ζ_1 and ζ_2 with diffusion factor [6] 22
2.21 Variation of wake momentum thickness to chord ratio as a function of the equivalent diffusion factor 23
2.22 Loss correlation of Wright and Miller [20] using D_{eq} of Eq. (2.22) 24
2.23 Theoretical velocity distribution and diffusion ratios considered by Koch and Smith [18] 25

2.24 Momentum thickness to chord ratio versus equivalent diffusion ratio at $M_1 = 0.05$ and AVDR=1 [18] 25
2.25 Evolution of losses as a function of solidity using Lieblein's correlation [6] and the mid-span DREAM booster data 26
2.26 Evolution of losses as a function of solidity using Koch and Smith correlation [18] and the mid-span DREAM booster data 27
2.27 Losses versus solidity for various inlet and outlet flow angles using Lieblein's correlation of [17] 27
2.28 Mach effect on deviation for various maximum thickness location Z [22] 29
2.29 Effect of Mach number on deviation on British C4 and DCA profiles [6] 29
2.30 Effect of Mach number on turning: (a) T1($18A_6I_{48}$)08 and (b) NACA 65-($12A_{10}$)10 [6] 29
2.31 Critical Mach number versus minimum pressure coefficient on suction side 31
2.32 Total pressure losses as a function of solidity and inlet Mach number 32
2.33 Sketch of Koch's diffuser analogy of a compressor passage with L as the diffuser length and g_2 as the diffuser outlet width . . . 33
2.34 Maximum diffuser static pressure rise for various values of inlet blockage in function of L/g_2 34
2.35 Koch's correlation of stalling effective static pressure rise [29] . 34
2.36 Koch's definition of effective dynamic pressure factor [29] . . . 35
2.37 Exit flow angle versus AVDR at various inlet flow angles and Mach numbers [31] 37
2.38 Total pressure losses versus AVDR at various inlet flow angles and Mach numbers [31] 37
2.39 Turning and losses versus AVDR at M=0.6 [32] 37
2.40 Turning and losses versus Mach number for various AVDR and aspect ratios [32] 37
2.41 Variation of loss parameter ζ_1 ($= \omega \cos\beta_2/2\sigma$) as a function of diffusion factors for linear and annular cascade tests [35] 39
2.42 Variation of ζ_1 with diffusion factor from annular cascade tests (fitted curves) [35] 40
2.43 Variation of optimum incidence between 2D and 3D tests versus Mach number (fitted curves) [35] 40
2.44 Variation of deviation at optimum incidence between 2D and 3D tests versus Mach number (fitted curves) [35] 41
2.45 Efficiency and pressure ratio for three rotors with different number of blades at nominal speed [36] 41
2.46 Efficiency and pressure ratio distributions along the span for three rotors with different number of blades at nominal speed (a) and 80% of nominal speed (b) [26] 43
2.47 Supersonic flow pattern through a cascade for two different solidities[27] 43
2.48 Performance and comparison of three rotors with different pitches[37] 44

2.49 Effect of solidity on rotor performance (results from NASA experimental investigations [38], [39] and [40]):(a) Pressure ratio and (b) adiabatic efficiency as a function of mass-flow 45
2.50 Effect of solidity on rotor performance (Britsch and al. [41]):(a) Diffusion factor ≈ 0.44 , rotor aspect ratio of 1 and 0.67; (b) Diffusion factor of 0.56 , rotor aspect ratio of 0.8 46
2.51 Optimum solidity for minimum losses as a function of inlet and outlet flow angles [43] 49
2.52 Efficiency contours as a function of the pitch-chord ratio s/c $(= 1/\sigma)$ and the ideal static pressure rise C_{p_i} [45] 50
2.53 Zweifel and Hearsey optimum σ and diffusion distributions compared with the distributions of the DREAM project booster: (a) Optimum solidity and (b) Diffusion factor (at optimum solidity) 51

3.1 Investigated CDB and DCA profiles (not to scale) 54
3.2 Picture of the linear cascade model 55
3.3 Blade-to-blade O4H grid topology 57
3.4 Mass-flow and total pressure ratio convergence curves for mesh B at $M_1 = 0.5$ for $i = 0°$ and $i = 10°$ 58
3.5 Outlet Mach number, outlet flow angle and losses grid independence at $i = 0°$ and $M_1 = 0.5$ 59
3.6 y^+ distributions for various turbulence models at mid-span on the blade suction (plain line) and pressure (dashed line) sides (mesh B - $i = 0°$ and $M_1 = 0.5$) 59
3.7 Influence of the turbulent eddy viscosity on the outlet Mach number, the outlet flow angle and the total pressure losses - i=0° and $M_1 = 0.5$ 63
3.8 Turbulence intensity and dissipation rate effects on the outlet Mach number, the exit flow angle and the losses for two-equation models ($i = 0°$ and $M_1 = 0.5$) 65
3.9 Turbulence model effect on operating range 66
3.10 Turbulence model effects on total pressure losses 67
3.11 Numerical scheme effects on incidence limits 68
3.12 Numerical scheme effects on total pressure losses at mid-span . 69
3.13 Numerical scheme effects on total pressure loss wakes 69
3.14 Numerical scheme effects on the loss distribution at $M_1 = 0.6$ - $k - \varepsilon$ Yang Shih - $i = 7°$ 71
3.15 Numerical scheme effects on the loss distribution at $M_1 = 0.6$ - Spalart Allmaras - $i = 8.5°$ 71
3.16 Total pressure losses versus incidence at M_1=0.4, 0.5, 0.6 and 0.7 73
3.16 Total pressure losses versus incidence at M_1=0.4, 0.5, 0.6 and 0.7 (continued) 74
3.17 Deviation versus incidence at M_1=0.4, 0.5, 0.6 and 0.7 75
3.17 Deviation versus incidence at M_1=0.4, 0.5, 0.6 and 0.7 (continued) 76
3.18 Diffusion factor versus incidence at M_1=0.4, 0.5, 0.6 and 0.7 . . 77

3.18 Diffusion factor versus incidence at M_1=0.4, 0.5, 0.6 and 0.7 (continued) 78
3.19 Minimum loss incidence versus solidity 79
3.20 Deviation at minimum loss incidence versus solidity 80
3.21 Diffusion factor at minimum loss incidence and at stall versus Mach number 81
3.22 Normalized outlet velocity wake of the high solidity CDB for the momentum thickness calculation (cf. Eq. (2.15)) 82
3.23 Loss parameter ζ_1 and wake momentum thickness to chord ratio versus diffusion factor compared with NASA correlation line of Fig. 2.20 (b) 83
3.24 Loss parameter ζ_2 and wake momentum thickness to chord ratio versus diffusion factor compared with NASA correlation line of Fig. 2.20 (a) 83
3.25 Updated loss correlation curve for the CDB (including compressibity effects) 84
3.26 Isentropic Mach number distributions at optimum incidence (M_1 = 0.40) 86
3.27 Isentropic Mach number distributions at optimum incidence (M_1 = 0.50) 86
3.28 Isentropic Mach number distributions at optimum incidence (M_1 = 0.60) 87
3.29 Isentropic Mach number distributions at optimum incidence (M_1 = 0.70) 87
3.30 Critical Mach number prediction of Eq. (2.26) using data at M_1=0.4 88
3.31 Critical Mach number prediction of Eq. (2.26) using data at M_1=0.6 88
3.32 Operating range versus Mach number 89
3.33 Losses (presented as $1-\omega$) and operating range versus solidity (CDB data) 91
3.34 Flow chart of a design process based on the choice of an optimum diffusion factor 93

4.1 Sketch of the high-speed cascade tunnel C3 facility 96
4.2 Views of the CAD model 97
4.3 Picture of the test section 98
4.4 Picture of the probes when mounted in the inlet groove (inlet view) 98
4.5 Picture of the three-hole probe used for traverse measurements 99
4.6 Picture of the kiel probe used for traverse measurements 100
4.7 Inlet kiel probe for inlet total pressure measurement 100
4.8 Effect of tailboard setting angle on outlet static pressure distribution 102
4.9 Inlet pressure distribution normalized by the settling chamber pressure 103

4.10 Inlet total pressure profile 104
4.11 Inlet incidence profile 104
4.12 Total pressure losses versus incidence 105
4.13 Normalized total pressure losses versus incidence 106
4.14 Turning versus incidence 107
4.15 Sketch of a typical evolution of the lift coefficient against the angle of attack [84] 107
4.16 Diffusion factor versus incidence 108
4.17 AVDR versus incidence 108
4.18 Two-dimensional diffusion factor versus incidence 109
4.19 Spanwise total pressure losses distributions at i=0°, 6° and 9° for M_1=0.45 110
4.20 Spanwise turning distributions at i=0°, 6° and 9° for M_1=0.45 111
4.21 Spanwise diffusion factor distributions at i=0°, 6° and 9° for M_1=0.45 111
4.22 Spanwise AVDR distributions at i=0°, 6° and 9° for M_1=0.45 . 112
4.23 Total pressure loss wakes at $\sigma = 1.38$ and $M_1 = 0.45$ 113
4.24 Total pressure loss wakes at $\sigma = 1.24$ and $M_1 = 0.45$ 113
4.25 Total pressure loss wakes at $\sigma = 1.10$ and $M_1 = 0.45$ 113
4.26 Geometrical model used for the post-test CFD computations . 114
4.27 Total pressure losses versus incidence for experimental data and both pre-test and post-test CFD models 115
4.28 Total pressure losses versus incidence for experimental data and both pre-test and post-test CFD models - Limited scale 116
4.29 Normalized total pressure losses versus incidence for experimental data and both pre-test and post-test CFD models 117
4.30 Total pressure loss 4^{th} order curve fit for σ =1.38, 1.24 and 1.10 - Experimental data 118
4.31 Total pressure loss 2^{nd} order curve fits for σ =1.38, 1.24 and 1.10 - Experimental data 119
4.32 Total pressure loss 2^{nd} order curve fits for σ =1.38, 1.24 and 1.10 - Post-test CFD data 120
4.33 Comparison of optimum incidence predictions 121
4.34 Picture of the instrumented blade 122
4.35 Total pressure losses versus incidence for the baseline and the low AR cascades - M_1=0.45 123
4.36 Total pressure losses versus incidence for the baseline and the low AR cascades - M_1=0.60 123
4.37 Experimental and numerical isentropic Mach number distributions ($M_1 = 0.45$ - scale-2 model) 124
4.38 Experimental and numerical isentropic Mach number distributions ($M_1 = 0.60$ - scale-2 model) 125
4.39 Comparison of experimental and numerical total pressure loss wakes at 9° and 12° for the scale-2 model ($M_1 = 0.45$) 126
4.40 Deviation versus incidence for experimental data and both pre-test and post-test CFD models 126

4.41 Deviation at optimum incidence for M_1=0.45 128
4.42 Deviation at optimum incidence for M_1=0.60 128
4.43 Diffusion factor versus incidence for experimental data and both pre-test and post-test CFD models 130
4.44 AVDR versus incidence for experimental data and both pre-test and post-test CFD models 130
4.45 Two-dimensional diffusion factor versus incidence for experimental data and both pre-test and post-test CFD models 130
4.46 Loss parameter ζ_1 versus diffusion factor at M_1=0.45 and M_1=0.60 132
4.47 Loss parameter ζ_2 versus diffusion factor at M_1=0.45 and M_1=0.60 133
4.48 Loss parameter ζ_1 versus 2D diffusion factor at (a) M_1=0.45 and (b) M_1=0.60 134
4.49 Loss parameter ζ_2 versus 2D diffusion factor at (a) M_1=0.45 and (b) M_1=0.60 135
4.50 Deviation at constant incidence for M_1=0.45 and M_1=0.60 . . 136
4.51 Two-dimensional diffusion factor at constant incidence for M_1=0.45 and M_1=0.60 137
4.52 Examples of design confidence regions based on the two-dimensional diffusion factor (M_1=0.45) 137
4.53 Off-design incidence correlations based on ζ_1 (top) or ζ_2 (bottom) and the diffusion factor at both Mach numbers. 138
4.54 Off-design incidence correlations based on ζ_1 (top) and ζ_2 (bottom) and the two-dimensional diffusion factor at both Mach numbers. 139
4.55 Incidence range versus solidity 140
4.56 Total pressure loss map for $\sigma = 1.38$ at i=3° and $M_1 = 0.45$ . . 142
4.57 Total pressure loss map for $\sigma = 1.38$ at i=9° and $M_1 = 0.45$ . . 142
4.58 Total pressure loss map for $\sigma = 1.24$ at i=3° and $M_1 = 0.45$ . . 143
4.59 Total pressure loss map for $\sigma = 1.24$ at i=9° and $M_1 = 0.45$ . . 143
4.60 Total pressure loss map for $\sigma = 1.10$ at i=3° and $M_1 = 0.45$ . . 144
4.61 Total pressure loss map for $\sigma = 1.10$ at i=9° and $M_1 = 0.45$ . . 144
4.62 Experimental total pressure loss map for $\sigma = 1.38$ at i=9° and $M_1 = 0.45$ 146
4.63 Numerical total pressure loss map for $\sigma = 1.38$ at i=9° and $M_1 = 0.45$ 146
4.64 Experimental total pressure loss map for $\sigma = 1.24$ at i=9° and $M_1 = 0.45$ 147
4.65 Numerical total pressure loss map for $\sigma = 1.24$ at i=9° and $M_1 = 0.45$ 147
4.66 Experimental total pressure loss map for $\sigma = 1.10$ at i=9° and $M_1 = 0.45$ 148
4.67 Numerical total pressure loss map for $\sigma = 1.10$ at i=9° and $M_1 = 0.45$ 148

5.1 Channel and axial station repartition 154
5.2 Rotor loss correlations of ACPreDesign 155

5.3 Stator loss correlations of ACPreDesign 155
5.4 Target normalized pressure ratio distribution 157
5.5 Comparison of pareto fronts and best efficiencies at $\pi = 1.25$ for various values of diffusion factors 159
5.6 Optimum rotor solidity distributions for different values of D_{max} and for the DREAM rotor 160
5.7 Rotor diffusion factor distributions for different values of D_{max} and for the DREAM rotor 160
5.8 Optimum stator solidity distributions for different values of D_{max} and for the DREAM stator 161
5.9 Stator diffusion factor distributions for different values of D_{max} and for the DREAM stator 161
5.10 Stage pressure ratio distributions for different values of D_{max} and for the DREAM stage 162
5.11 Stage efficiency distributions for different values of D_{max} and for the DREAM stage 162
5.12 Losses versus solidity for different inlet and outlet flow angles based on ACPreDesign rotor loss correlation curves 163
5.13 Sketch of the rotor loss parametrization with constant uncertain variable U_R 167
5.14 Sketch of the rotor loss parametrization with three uncertain variables U_{mean}, U_D and U_{stall} 168
5.15 Evolution of the efficiency mean with the number of samples ($D_{max} = 0.40$) 169
5.16 Evolution of the efficiency standard deviation with the number of samples($D_{max} = 0.40$) 169
5.17 Histogram and probability of the efficiency ($D_{max} = 0.40$) . . . 170
5.18 Efficiency mean and standard deviation in function of the number of collocation points ($D_{max} = 0.40$) 170
5.19 Evolution of the efficiency mean with σ_R (=σ_S) - $D_{max} = 0.40$ - 2 collocation points 173
5.20 Evolution of the efficiency standard deviation with σ_R (=σ_S) - $D_{max} = 0.40$ - 2 collocation points 173
5.21 Illustration of the *robust design* problem on an arbitrary function presenting two extrema 175
5.22 Comparison of pareto fronts with or without considering uncertainties 176

A.1 Three-dimensional view of the 1.5 DREAM booster stage . . . 185
A.2 Rotor pressure ratio versus mass-flow for three values of the rotor blade number of the DREAM stage 187
A.3 Rotor efficiency versus mass-flow for three values of the rotor blade number of the DREAM stage 187
A.4 Stage pressure ratio versus mass-flow for three values of the stator blade number of the DREAM stage 189

A.5 Stage efficiency versus mass-flow for for three values of the stator blade number of the DREAM stage 189
A.6 Stator outlet total pressure maps at near stall of the 80 stator blades configuration 190
A.7 Stator outlet total pressure maps at near stall of the 120 stator blades configuration 190

B.1 Kiel probe yaw calibration 191
B.2 Kiel probe pitch calibration 191
B.3 Yaw angle versus K_{yaw} 192
B.4 K_{tot} versus yaw angle 193
B.5 K_{dyn} versus yaw angle 193
B.6 K_{yaw} versus yaw angle for various pitch angles 193
B.7 K_{yaw} versus yaw angle for various pitch angles 193

C.1 Spanwise total pressure losses distributions at M_1=0.60 207
C.2 Spanwise turning distributions at M_1=0.60 208
C.3 Spanwise diffusion factor distributions at M_1=0.60 208
C.4 Spanwise AVDR distributions at M_1=0.60 208
C.5 Total pressure loss wakes at $\sigma = 1.38$ and $M_1 = 0.60$ 209
C.6 Total pressure loss wakes at $\sigma = 1.24$ and $M_1 = 0.60$ 209
C.7 Total pressure loss wakes at $\sigma = 1.10$ and $M_1 = 0.60$ 210
C.8 Yaw angle wakes at $\sigma = 1.38$ and $M_1 = 0.45$ 211
C.9 Yaw angle wakes at $\sigma = 1.24$ and $M_1 = 0.45$ 211
C.10 Yaw angle wakes at $\sigma = 1.10$ and $M_1 = 0.45$ 211
C.11 Yaw angle wakes at $\sigma = 1.38$ and $M_1 = 0.60$ 212
C.12 Yaw angle wakes at $\sigma = 1.24$ and $M_1 = 0.60$ 212
C.13 Yaw angle wakes at $\sigma = 1.10$ and $M_1 = 0.60$ 212
C.14 Experimental total pressure loss map 214
C.15 Numerical total pressure loss map using Yang-Shih k-ϵ turbulence model with $\ell = 0.1\, D_H$ and a central scheme 214
C.16 Numerical total pressure loss map using Yang-Shih k-ϵ turbulence model with $\ell = 0.0001\, D_H$ and a central scheme 215
C.17 Numerical total pressure loss map using Yang-Shih k-ϵ turbulence model with $\ell = 0.1\, D_H$ and an upwind scheme 215
C.18 Numerical total pressure loss map using Yang-Shih k-ϵ turbulence model with $\ell = 0.0001\, D_H$ and an upwind scheme 216
C.19 Numerical total pressure loss map using Spalart-Allmaras turbulence model with $\ell = 0.1\, D_H$ and a central scheme 216
C.20 Numerical total pressure loss map using Spalart-Allmaras turbulence model with $\ell = 0.0001\, D_H$ and a central scheme 217
C.21 Numerical total pressure loss map using Spalart-Allmaras turbulence model with $\ell = 0.1\, D_H$ and an upwind scheme 217
C.22 Experimental total pressure loss map 218
C.23 Numerical total pressure loss map using Yang-Shih k-ϵ turbulence model with $\ell = 0.1\, D_H$ and a central scheme 218

C.24 Numerical total pressure loss map using Yang-Shih k-ϵ turbulence model with $\ell = 0.0001\, D_H$ and a central scheme 219
C.25 Numerical total pressure loss map using Yang-Shih k-ϵ turbulence model with $\ell = 0.1\, D_H$ and an upwind scheme 219
C.26 Numerical total pressure loss map using Yang-Shih k-ϵ turbulence model with $\ell = 0.0001\, D_H$ and an upwind scheme 220
C.27 Numerical total pressure loss map using Spalart-Allmaras turbulence model with $\ell = 0.1\, D_H$ and a central scheme 220
C.28 Numerical total pressure loss map using Spalart-Allmaras turbulence model with $\ell = 0.0001\, D_H$ and a central scheme 221
C.29 Numerical total pressure loss map using Spalart-Allmaras turbulence model with $\ell = 0.1\, D_H$ and an upwind scheme 221
C.30 Comparison of total pressure loss wakes using Yang-Shih k-ϵ turbulence model with $\ell = 0.1\, D_H$ and a central scheme 222
C.31 Comparison of total pressure loss wakes using Yang-Shih k-ϵ turbulence model with $\ell = 0.0001\, D_H$ and a central scheme . . 223
C.32 Comparison of total pressure loss wakes using Yang-Shih k-ϵ turbulence model with $\ell = 0.1\, D_H$ and an upwind scheme . . . 223
C.33 Comparison of total pressure loss wakes using Yang-Shih k-ϵ turbulence model with $\ell = 0.0001\, D_H$ and an upwind scheme . 223
C.34 Comparison of total pressure loss wakes using Spalart-Allmaras turbulence model with $\ell = 0.1\, D_H$ and a central scheme 224
C.35 Comparison of total pressure loss wakes using Spalart-Allmaras turbulence model with $\ell = 0.0001\, D_H$ and a central scheme . . 224
C.36 Comparison of total pressure loss wakes using Spalart-Allmaras turbulence model with $\ell = 0.1\, D_H$ and an upwind scheme . . . 224
C.37 Comparison of total pressure loss wakes using Yang-Shih k-ϵ turbulence model with $\ell = 0.1\, D_H$ and a central scheme 225
C.38 Comparison of total pressure loss wakes using Yang-Shih k-ϵ turbulence model with $\ell = 0.0001\, D_H$ and a central scheme . . 225
C.39 Comparison of total pressure loss wakes using Yang-Shih k-ϵ turbulence model with $\ell = 0.1\, D_H$ and an upwind scheme . . . 226
C.40 Comparison of total pressure loss wakes using Yang-Shih k-ϵ turbulence model with $\ell = 0.0001\, D_H$ and an upwind scheme . 226
C.41 Comparison of total pressure loss wakes using Spalart-Allmaras turbulence model with $\ell = 0.1\, D_H$ and a central scheme 226
C.42 Comparison of total pressure loss wakes using Spalart-Allmaras turbulence model with $\ell = 0.0001\, D_H$ and a central scheme . . 227
C.43 Comparison of total pressure loss wakes using Spalart-Allmaras turbulence model with $\ell = 0.1\, D_H$ and an upwind scheme . . . 227

D.1 Optimum rotor solidity distributions for different values of D_{max} and for the DREAM rotor 231
D.2 Rotor diffusion factor distributions for different values of D_{max} and for the DREAM rotor 231

D.3 Rotor pressure ratio distributions for different values of D_{max} and for the DREAM rotor 231
D.4 Rotor efficiency distributions for different values of D_{max} and for the DREAM rotor 231
D.5 Evolution of the efficiency mean and standard deviation with the number of samples ($D_{max} = 0.45$) 232
D.6 Efficiency histogram and probability plot ($D_{max} = 0.45$) 232
D.7 Efficiency mean and standard deviation in function of the number of collocation points ($D_{max} = 0.45$) 233
D.8 Evolution of the efficiency mean and standard deviation with the number of samples ($D_{max} = 0.40$) 233
D.9 Efficiency histogram and probability plot ($D_{max} = 0.40$) 234
D.10 Efficiency mean and standard deviation in function of the number of collocation points ($D_{max} = 0.40$) 234
D.11 Evolution of the efficiency mean and standard deviation with the number of samples ($D_{max} = 0.45$) 234
D.12 Efficiency histogram and probability ($D_{max} = 0.45$) 235
D.13 Efficiency mean and standard deviation in function of the number of collocation points ($D_{max} = 0.45$) 235

List of Tables

2.1 Optimum incidence calculation for different solidities at constant camber (DCA blade, $t/c_{max} = 6.5\%$, $\beta_1 = 50°$ and $\phi = 30°$) . . 12
2.2 Optimum incidence calculation for different solidities at constant flow turning (DCA blade, $t/c_{max} = 6.5\%$, $\beta_1 = 50°$ and $\Delta\beta = 20°$) 12
2.3 NASA (a) and Carter (b) deviation predictions for DCA blade with $t/c_{max} = 6.5\%$ and $\beta_1 = 50°$ at constant camber 15
2.4 NASA (a) and Carter (b) deviation predictions for DCA blade with $t/c_{max} = 6.5\%$ and $\beta_1 = 50°$ at constant flow turning . . . 15
2.5 Solidity recommendations from Howell's, Zweifel's, Lieblein's, Hearsey's and McKenzie's methods 50

3.1 CDB and DCA geometrical parameters 54
3.2 Reference values for typical measurement uncertainties - $M_1 = 0.5$ 56
3.3 Grid characteristics 57
3.4 Values of turbulent eddy viscosity imposed for the Spalart-Allmaras model - i=0° and $M_1 = 0.5$ 62
3.5 Turbulence boundary conditions for two-equation models ($i = 0°$ and $M_1 = 0.5$) 64

4.1 Uncertainties of all measured quantities (given at 95%) 100
4.2 Uncertainties of derived quantities (given at 95%) 100
4.3 Test matrix in span, incidence and solidity 101

5.1 Mean and variance of U_R and U_S 167
5.2 Mean and variance of U_{mean}, U_D and U_{stall} 168
5.3 Monte-Carlo sampling results using two uncertain parameters (full stage configuration) 171
5.4 Stochastic collocations results using two uncertain parameters (full stage configuration) 172
5.5 Monte-Carlo sampling results using three uncertain parameters (single rotor configuration) 174
5.6 Stochastic collocations results using three uncertain parameters (single rotor configuration) 174

A.1 Rotor inlet and outlet velocity triangles of the DREAM project booster 186
A.2 Tested rotor blade numbers and solidities 186
A.3 Tested stator blade numbers and solidities 188

B.1 Systematic, random and total uncertainties of all measured pressures 197